



**HAL**  
open science

# Engineering of a viable artificial leaf for solar fuel generation

Duc Nguyen Ngoc

► **To cite this version:**

Duc Nguyen Ngoc. Engineering of a viable artificial leaf for solar fuel generation. Organic chemistry. Université Grenoble Alpes [2020-..]; Université des sciences et des technologies de Hanoï (Vietnam), 2021. English. NNT: 2021GRALV066 . tel-03917668

**HAL Id: tel-03917668**

**<https://theses.hal.science/tel-03917668>**

Submitted on 2 Jan 2023

**HAL** is a multi-disciplinary open access archive for the deposit and dissemination of scientific research documents, whether they are published or not. The documents may come from teaching and research institutions in France or abroad, or from public or private research centers.

L'archive ouverte pluridisciplinaire **HAL**, est destinée au dépôt et à la diffusion de documents scientifiques de niveau recherche, publiés ou non, émanant des établissements d'enseignement et de recherche français ou étrangers, des laboratoires publics ou privés.

## THÈSE

Pour obtenir le grade de

**DOCTEUR DE L'UNIVERSITE GRENOBLE ALPES**

**préparée dans le cadre d'une cotutelle entre  
l'Université Grenoble Alpes et l'Université des  
sciences et des technologies de Hanoï**

Spécialité: **Chimie inorganique et bio inorganique**

Arrêté ministériel: 25 mai 2016

Présentée par

**Duc NGUYEN NGOC**

Thèse dirigée par **Vincent ARTERO** et **Phong TRAN DINH**  
préparée au sein des **Laboratoire Chimie et Biologie des  
Métaux** et **Laboratoire de Chimie pour la Conversion et le  
Stockage d'Énergie**

dans l'École doctorale **Chimie et Sciences du Vivant** et l'École  
doctorale **USTH**

# Construction d'une feuille artificielle pour la production de carburants solaires

Thèse soutenue publiquement le **13 Decembre 2021**,  
devant le jury composé de:

**M. Hoang LUC HUY**

Professeur associé, HNUE, Président du jury

**Mme Christel LABERTY-ROBERT**

Professeure, Sorbonne Université, Rapportrice

**M. Bruno JOUSSELME**

Chercheur, CEA, Rapporteur

**Mme Catherine AMIENS**

Professeure, Université de Toulouse, Examinatrice

**Mme Fanny ALLOIN**

Directrice de recherche, CNRS, Examinatrice

**Mme Thu VU THI**

Maîtresse de conférences, USTH, Examinatrice

**M. Vincent ARTERO**

Directeur de recherche, CEA, Directeur de thèse

**M. Phong TRAN DINH**

Professeur associé, USTH, Directeur de thèse



# Acknowledgement

Throughout my life, I have been fortunate enough to have the chance to meet a lot of people, and the past three years of this PhD thesis helped me realize what a blessing that was. This work would definitely not be able to see the light of day without all the supports from many people, and even though I never managed to verbally express it, from the bottom of my heart, I am more thankful than anyone could be.

I am grateful to the Campus France for the unceasing assist, both financially through the Bourse d'Excellence 2018-2020 and administratively throughout my stay in France. I would also like to thank the financial support from LabEx Arcane and the PhotoCARB ANR project.

I would like to express my gratitude to Prof. Luc Huy Hoang, Prof. Christel Laberty-Robert, Dr. Bruno Jousselme, Prof. Catherine Amiens, Prof. Fanny Alloin and Dr. Vu Thi Thu for accepting to be members of the jury and evaluate this work. I am grateful for the interesting discussions and valuable suggestions during the defense.

To my two brilliant supervisors, Prof. Tran Dinh Phong and Dr. Vincent Artero, words are not sufficient to convey my appreciation for all the growth you have induced in me. Thank you very much for the chance to see the world, and to experience the true essence of collaboration through your long history of seamless cooperation. Your immense passion for science has always been a great beacon of motivation and encouragement as I scramble my way forward. Without your valuable advices, crystallized from vast experience and delivered through unwavering patience, I definitely would not have made it this far. For me, having your guidance during this first part on the way of science is truly a miraculous blessing and a great honor. I hope my work can make you proud.

My sincere thanks go to Prof. Ung Thi Dieu Thuy and Dr. Pascale Chenevier for the SEM/EDX measurements. I also want to thank Dr. Julien Pérard for the ICP-OES measurement, Dr. Truong Quang Duc for the XPS analysis, the Fab-Lab at Y.SPOT for the mechanical shear and laser cutter, and the CEA workshop for the wire cutting equipment.

To the SolHyCats, old and new, thank you so much for your warm welcome during my stay in Grenoble. The time we spent together will forever be a treasured memory for me. Adina, your valuable lessons in electrochemistry and your encouragement will no doubt boost my confidence in the future. Jennifer, I will never forget the first safety tour of the lab and all your help with the gas chromatography system. Murielle, your presence alone made my experience in the lab a pleasant one. Thank you very much for all your advices, support, and the opportunity to work with the dye-sensitized system. Matthieu, I am genuinely blessed to be able to meet and work with you. By following you around the lab, I was able to learn a lot about different machines and techniques as well as how to perform maintenance on them. Thank you for the awesome adventures and the ensuing discussions. May your garden grow ever more bountiful. Bertrand, I hope one day I would be able to become a cool scientist, and also a cool dad like you. To Christina and Manos, it has been a blast being able to combine our work and obtain something functional, I hope we can build more things together in the future. Mariam, thanks a lot for helping me with various experiments, and please never stop singing. Angelica, I really appreciate all your help, and wish you all the best in life. Andrew, Afridi, Ghislain, Kun and Louis, although with members scattered all over the world now, the TTeam will always be in my heart. I hope one day we can all go and take photos together again. Anthonin, Jingxian, Jonathan, Nabil, Nick, Seb, Tania and members of LCBM, thank you very much for the nice adventure.

I would also like to give special thanks to the former and current members of CECS research group for all the advices, discussion and support. Great appreciation goes to Dr. Le Van Hoang for his involvement in the creation of the tandem artificial leaf. I sincerely thank Dr. Le Thi Ly, Dr. Nguyen Duc Anh for the seamless transition to the group during my third year. I also thank Mrs. Nguyen Thi Chuc, Mr. Tran Duc Tien and Mr. Duong Minh Tuan for their friendship and emotional support.

The completion of this PhD thesis would not be possible without the peace of mind, the safe haven and unconditional supports from my family. And for that, I am eternally grateful.

And to you, my darling who brings warmth to my heart, thank you for joining and staying by my side on this journey.



# Table of Contents

Acknowledgement	
Abbreviation table.....	1
Grants, involved institutions, laboratories, collaboration .....	3
General introduction .....	4
<b>Chapter I.....</b>	<b>7</b>
<b>1. Where we are - World energy and environmental outlook.....</b>	<b>8</b>
<b>2. Where we want to go - Solar fuels as the energy vector of the future .....</b>	<b>10</b>
<b>2.1. Green hydrogen through solar water splitting.....</b>	<b>12</b>
<b>2.2. Solar fuels through CO<sub>2</sub> reduction .....</b>	<b>17</b>
<b>3. The means to get there – Current scientific progress on making solar fuels viable.....</b>	<b>19</b>
<b>3.1. The brute force PV-electrolyzer .....</b>	<b>21</b>
<b>3.2. The unstable mixed colloid.....</b>	<b>21</b>
<b>3.3. The compromise zone – where our interest lies.....</b>	<b>23</b>
<b>3.4. Some considerations moving forward .....</b>	<b>25</b>
<b>Chapter II .....</b>	<b>26</b>
<b>1. Introduction.....</b>	<b>27</b>
<b>1.1. Three broad classes of catalysts .....</b>	<b>27</b>
<b>1.2. Figures of merit for electrocatalysts.....</b>	<b>29</b>
<b>1.3. Overview of current state of solar fuels generating electrocatalysts .....</b>	<b>32</b>
<b>2. Experimental setup .....</b>	<b>38</b>
<b>2.1. Preparation of [Co(WS<sub>4</sub>)<sub>2</sub>]<sup>2-</sup> deposition solution .....</b>	<b>38</b>
<b>2.2. Electrochemical setup .....</b>	<b>38</b>
<b>3. Results and discussions.....</b>	<b>40</b>
<b>3.1. Electrochemical property of [Co(WS<sub>4</sub>)<sub>2</sub>]<sup>2-</sup>/KPi.....</b>	<b>40</b>
<b>3.2. Deposition of catalysts .....</b>	<b>43</b>
<b>4. Conclusions and perspectives.....</b>	<b>46</b>
<b>Chapter III.....</b>	<b>47</b>
<b>1. Introduction.....</b>	<b>48</b>
<b>2. Artificial leaf fabrication .....</b>	<b>49</b>
<b>2.1. The triple-junction amorphous silicon (3jn-a-Si) solar cell.....</b>	<b>49</b>
<b>2.2. Initial treatment for the 3jn-a-Si solar cell .....</b>	<b>52</b>
<b>2.3. Compatibility of the 3jn-a-Si solar cell with the dual catalysts.....</b>	<b>59</b>
<b>2.4. Artificial leaf fabrication through photo-induced assembly of dual catalysts.....</b>	<b>69</b>
<b>3. None-invasive investigation and evaluation of the monolithic artificial leaf .....</b>	<b>71</b>

3.1.	Optimization of 3jn-a-Si cutting method revisited.....	72
3.2.	Optimization of catalyst deposition.....	72
3.3.	Performance evaluation and investigations on catalysts.....	79
3.4.	Stability assessment.....	92
3.5.	Identifying the limiting component.....	93
4.	Invasive investigation and evaluation.....	94
4.1.	Half-cell assessment.....	94
4.2.	Full cell operando assessment.....	99
4.3.	<i>In-situ</i> assessment with tri-potentiostat and gas chromatography.....	106
5.	Conclusions and perspectives.....	111
Chapter IV.....		112
1.	Introduction.....	113
2.	The two photoelectrodes.....	115
2.1.	The BiVO <sub>4</sub>  CoPi photoanode.....	115
2.2.	The NiO RuP <sub>4</sub> -CoN <sub>4</sub> H photocathode.....	116
3.	Integration of the photoelectrodes into full cell.....	118
3.1.	Cell integration using the specially designed reactor.....	119
3.2.	Setup for individual electrodes assessment.....	123
3.3.	Setup for full tandem cell assessment.....	124
4.	Photoelectrochemical investigation coupled with gas chromatography.....	125
4.1.	Investigation for solar water splitting.....	125
4.2.	Investigation for solar CO <sub>2</sub> reduction.....	130
5.	Conclusions and perspectives.....	134
General conclusions and perspectives.....		135
References.....		137
Supporting information.....		148

## Abbreviation table

$\eta$	Overpotential
$\eta_{STF}$	Solar to fuels efficiency
$\eta_{STH}$	Solar to hydrogen efficiency
AM1.5G	Air mass 1.5 global
BI	Back-illuminated
CA	Chronoamperometry
CE	Counter electrode
CECS	Chemistry for Energy Conversion and Storage
CO <sub>2</sub>	Carbon dioxide
CO <sub>2</sub> RR	Carbon dioxide reduction reaction
CP	Chronopotentiometry
CV	Cyclic voltammetry
DFT	Density functional theory
DI	Deionized
DMSO	Dimethyl sulfoxide
EDX	Energy-dispersive X-ray spectroscopy
E	Potential
E <sub>oc</sub>	Open-circuit potential
FE	Faradaic efficiency
FI	Front-illuminated
FTO	Fluorine-doped tin oxide
GC	Gas chromatography
HEC	Hydrogen evolving catalyst
HER	Hydrogen evolution reaction
HNUE	Hanoi National University of Education
iAM	Ideal amperometer
ICP-OES	Inductively coupled plasma - optical emission spectrometry
IR	Infrared

ITO	Indium tin oxide
iVM	Ideal voltmeter
$j$	Current density
KCl	Potassium chloride
KPi	Potassium phosphate buffer
LSV	Linear sweep voltammetry
NHE	Normal hydrogen electrode
OCV	Built-in setting in the potentiostat for monitoring open-circuit voltage
OEC	Oxygen evolving catalyst
OER	Oxygen evolution reaction
PEC	Photoelectrochemical
PECVD	Plasma enhanced chemical vapor deposition
PEM	Proton exchange membrane
PV	Photovoltaic
RE	Reference electrode
RHE	Reversible hydrogen electrode
SEM	Scanning electron microscope
SFG	Solar fuels generator
STF	Solar to fuel
STH	Solar to hydrogen
SWS	Solar water splitting
$t$	Time
TCO	Transparent conducting oxide
UV	Ultraviolet
$V_{oc}$	Open-circuit voltage
WE	Working electrode
XPS	X-ray photoelectron spectroscopy

## Grants, involved institutions, laboratories, collaboration

This cotutelle doctoral thesis was formed and supervised through a close collaboration between Dr. Vincent Artero, Director of the Laboratoire de Chimie et Biologie des Métaux (University Grenoble Alpes (UGA), CNRS, CEA Grenoble, France) and Prof. Phong Tran Dinh, Director of the Department of Fundamental and Applied Sciences (University of Science and Technology of Hanoi (USTH), Hanoi, Vietnam). Financial supports for the first eighteen months were provided through the Bourse d'Excellence from the French government and a grant of LabEx Arcane from the University Grenoble Alpes. The remaining six months were financed by a work contract with CEA Grenoble under the PhotoCARB ANR project.

# General introduction

It is an undisputable fact that our existence and livelihood are inevitably dependent on the amount and characteristics of the energy sources that are accessible to us. Therefore, in order to survive, flourish and hopefully achieve greatness as a species, it is undoubtedly a natural decision to identify and make use of abundant and sustainable energy reserves while relinquishing aged and environmentally detrimental ones. The past two centuries have witnessed the birth of countless life-changing feats of wonder that were once considered to be mere fictions. However, the fossil fuels we abused to obtain them exacted a terrible toll to the stability of the environment. In hindsight, it was the blind pursuit of immediate profit and needless extravagances despite the pleas of climate researchers that ultimately put us in a race against time where defeat means the downfall of society as we know it, while victory will bring unimaginable alterations to our daily lives. Combined efforts from all fields and careful, methodological planning are essential for us to emerge triumphant as time is running short while the problem we have to solve is strikingly gargantuan.

A humongous problem requires gigantic solution, and many agree that our dream of sustainable future lies in the heart of the blazing star at the center of our solar system, which, for billions of years, has blasted the Earth with rays of pure energy. Taming such a beast through a Dyson sphere collar will no doubt be an inevitable goal in our quest to understand the universe and the meaning of life. However, it is also important to be rational and set out smaller, feasible objectives and steadily work our way forward while still be able to keep our heads above water. Our first milestone can be dialed down to the efficient capturing of the amount of sunlight reaching Earth, which, although meager in comparison to the total flux that the sun provides, is more than enough to satisfy our current energy demand. Accordingly, a suitable plan can be devised by working our way down and solving possible problems.

We begin with the largest demerit of solar energy, which is related to the various shading factors presented in the atmosphere, as well as the spherical shape and the revolving nature of our planet, leading to a disruptive irradiating duration for any given place (level 1 problem). This intermittent characteristic can be overcome by a form of storage in chemical bonds inspired by the natural photosynthesis. The process, termed artificial photosynthesis, can be achieved through solar water splitting (SWS) to get hydrogen or through reducing carbon dioxide (CO<sub>2</sub>) in the atmosphere to usable fuels that can be consumed at will, preferably when

sunlight is not available (level 1 solution). Those storage strategies, in turn, require conquering specific energy and kinetic barriers of the corresponding chemical reactions (level 2 problem). Currently, various research groups as well as companies around the world are putting forth resources on solving this problem through designing suitable devices with optimum catalysts and light harvesters (level 2 solution). However, among the myriad of designs, one capable of the ultimate balance between durability, scalability and performance has yet to be discovered (level 3 problem). In addition, such large quantity of devices gives rise to difficulties in comparing different designs with different mechanisms. Hence, a suitable experimentation is required to shed light to the inner-workings and provide commonly shared parameters of the devices for proper future optimization and benchmarking, respectively (level 3 solution). Afterwards, it is only the problem of building devices that work (level 4 problem).

In this dissertation, we aim to contribute a solution for level 4 problem and a pathway for level 3 solution, i.e. fabricating operational devices and find a suitable experimentation to examine their working mechanism. The thesis will be divided into four main chapters with special sections featuring details that are oft-times overlooked or left out of publications.

#### *Chapter I – Journey to a sustainable future*

Information on the current state of our energy reserve and demand, the finite capacity and the pollution created from over-usage of fossil fuels as well as the potential of solar energy as a sustainable source for the future will be presented. Basic knowledge on solar water splitting and CO<sub>2</sub> reduction will be introduced along with the thermodynamic/kinetic barriers and the requirements for suitable light harvesters and catalysts to overcome them. Finally, a general review on the different types of currently available solar fuels generators (SFGs) will be conducted with special attentions paid to the ones at the focal point of this work.

#### *Chapter II - Dual catalysts from a single deposition solution*

The chapter begins with a review on high performant catalysts for both water oxidation and proton reduction followed by the needs for a suitable pair that is able to not only work together, but also do that under similar pH to drive the overall water electrolysis. Afterwards, our work on simultaneous electrodeposition of such dual catalysts from a single precursor solution will be demonstrated in details. General performance assay is also presented.

### *Chapter III - The monolithic artificial leaf*

In this chapter, we employed the simultaneous formation of our aforementioned dual catalysts on a commercialized solar cell to fabricate, in a single step, an operational monolithic device capable of directing the overall solar water splitting without any external bias (the device is commonly referred to as an artificial leaf). After a brief introduction of this class of solar fuel generator, the whole experimental process will be reported in details followed by structural inspection utilizing various techniques.

Especially, we introduce our operando analysis which can allow us to extract multiple fundamental parameters of interest for this type of device using commonly found instruments in a photoelectrochemistry laboratory. The experimental setup is relatively versatile and potential application to other classes of solar fuel generators is possible with suitable reconfiguration.

### *Chapter IV – The tandem artificial leaf*

The fruit of the collaboration between the SolHyCat group in Grenoble and the CECS laboratory in Hanoi is conceived, ripened and delivered in this chapter. Through combined efforts, a dye-sensitized photocathode from SolHyCat and a BiVO<sub>4</sub>-based photoanode from CECS come together to form a fully functional, unassisted device capable of driving both the hydrogen evolution reaction (HER) and the CO<sub>2</sub> reduction reaction (CO<sub>2</sub>RR) under illumination. To begin, a brief introduction of this flexible class of solar fuel generator will be presented. Afterwards, through the employment of a custom-made specialized reactor and our aforementioned experimental setup, detailed study on the performance of the photoelectrodes, both individually as well as in combination will be demonstrated.

### *General conclusions and perspectives*

After a short reminder of the objectives of the project, notable remarks and potential outlook provided by this work will be discussed.



# Chapter I

## Journey to a sustainable future



## 1. Where we are - World energy and environmental outlook

The industrial revolution in the 19<sup>th</sup> century has brought along the most profound outburst of global population ever recorded in history. The immense boost to the quality of life has enabled the populace to increase sevenfold in size within a narrow timeframe from 1800 to 2011.<sup>1</sup> Even though annual growth rate has embarked on a downward trend since the 1970s, it is expected that the world will still need to provide for an additional four billion inhabitants by the end of the century,<sup>2</sup> leading to a natural increment in global energy demand. In its 2019 edition, the International Energy Outlook predicted that global energy demand will increase by 50% between 2018 and 2050.<sup>3</sup> However, the nature and scope of said increment will be subjected to changes in future energy policies as the world gradually realizes the downsides of the infamous “black gold”, upon which we are currently overly dependent.

Fossil fuels such as oil, coal and natural gas have been the major contributors to the energy mix available to us. Together, they persistently represented around 85% of the 360 Exajoules that the world consumed in 1995 up to the 581 Exajoules in 2019 (**Figure 1**).<sup>4</sup> This staggering domination is to be expected given their attractively high energy density,<sup>5</sup> huge reserve<sup>6</sup> and currently unbeatable ease of access and cost of extraction. However, counterbalancing all the goodness they bring, the downsides are monstrous enough to disqualify them as an energy source for a sustainable future.

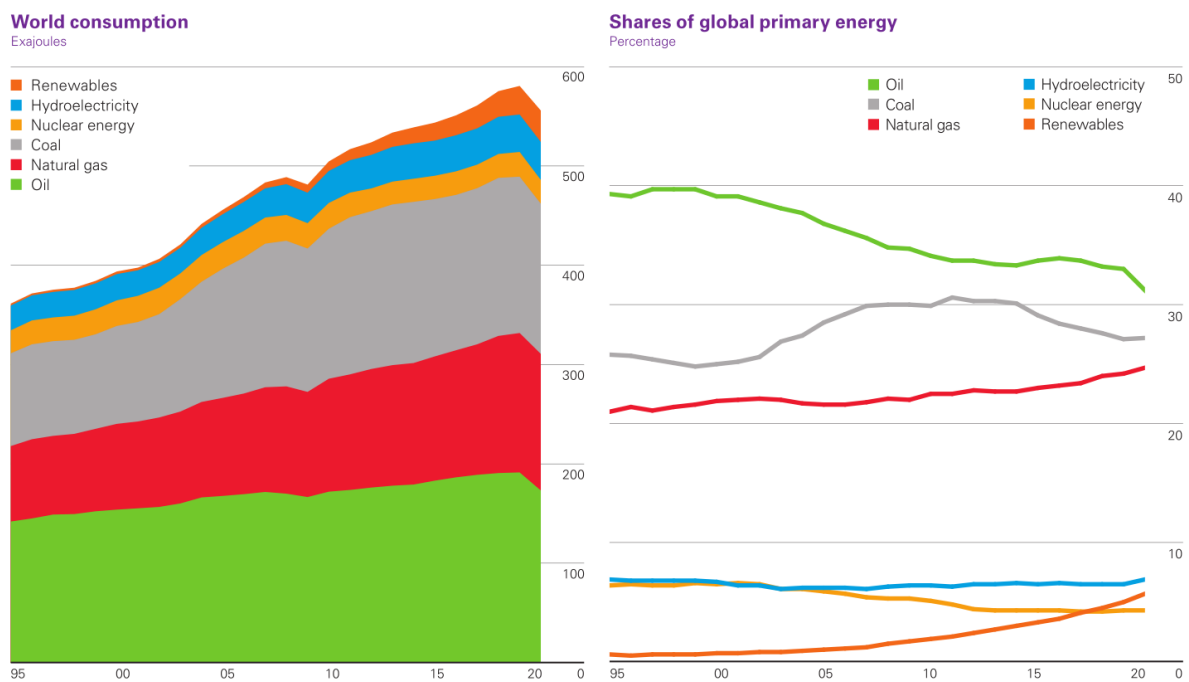
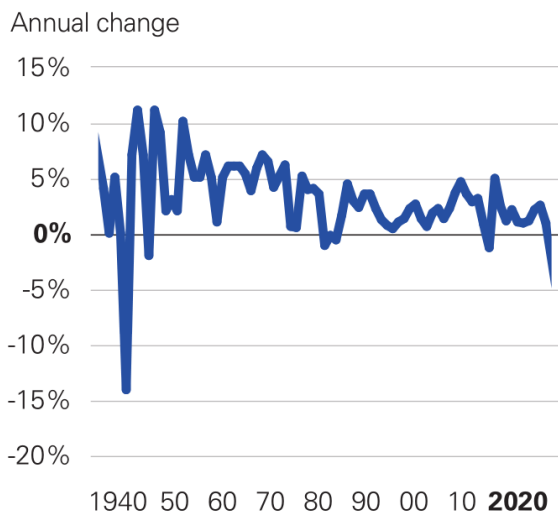


Figure 1: World energy consumption (left) and contribution from different sources (right) from 1995 to 2020<sup>4</sup>

The first demerit of fossil fuels lies in their formation mechanism from anaerobically decayed organisms. This process usually takes tens of millions of years to complete,<sup>7</sup> therefore, comparing the rate of formation and current rate of consumption, despite the immensely large quantity, fossil fuels are considered as finite and non-renewable. However, we probably will not see the day the last chunk of coal or the last barrel of oil get extracted from the ground, since long before then, the elevated cost of extraction would have rendered them economically unfavorable, and the environment would have been pulverized through their excessive utilization. Indeed, it has been evidenced that the consumption of energy is closely linked to the emission of CO<sub>2</sub> (**Figure 2**), the most prominent greenhouse gas responsible for long-term variations in global climate.<sup>8,9</sup> Even though the energy density has continuously been improved to reduce the ratio of CO<sub>2</sub> emitted per energy expended,<sup>10</sup> if the consumption rate does not decrease, it is estimated that global average temperature will increase by 4°C compared to the pre-industrial age by the end of the century,<sup>9</sup> bringing along devastating consequences to human life and the environment.<sup>11–16</sup>

#### Primary energy consumption



#### CO<sub>2</sub> emissions from energy use

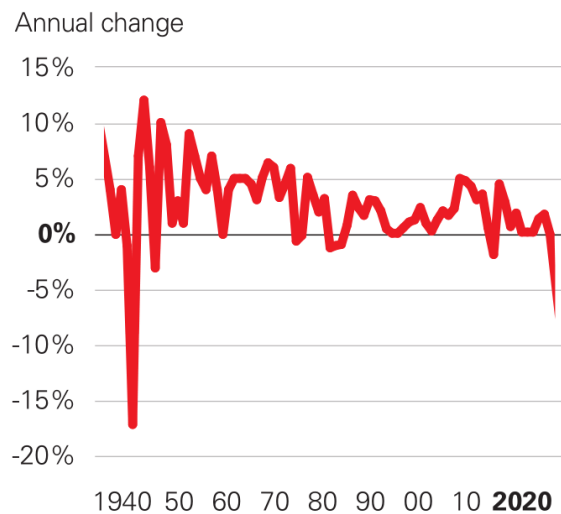


Figure 2: Global energy demand and CO<sub>2</sub> emissions<sup>4</sup>

The Paris agreement in 2015, the latest globally combined effort to a sustainable future at the time of writing, has set out an ambitious target to cut the greenhouse gases emission to limit the global temperature increment to below 2°C, preferably no more than 1.5°C.<sup>17</sup> This hefty task requires the realization of global net zero CO<sub>2</sub> emissions by 2050 coupled with a deep reduction in other greenhouse gases.<sup>18</sup> To be able to reach such goal while satisfying the energy demand of a growing population, careful planning and efficient allocation of our available resources to develop and migrate to renewable energy solutions are of paramount importance.

## 2. Where we want to go - Solar fuels as the energy vector of the future

Uprooting and abandoning fossil fuels, the lifeline of many of our already mature industries to embrace a new energy source is a big challenge. To be able to realize the transition, the new source needs not only to possess similar or greater capacity, but also to be renewable and safe for the environment. In addition, to make the switch from fossil fuels goes smoother, it would be ideal for the new source to be somewhat compatible with our existing infrastructures for transporting and utilizing energy. Considering all the major energy sources currently available to us (**Figure 3**), solar energy is unequivocally the winner.

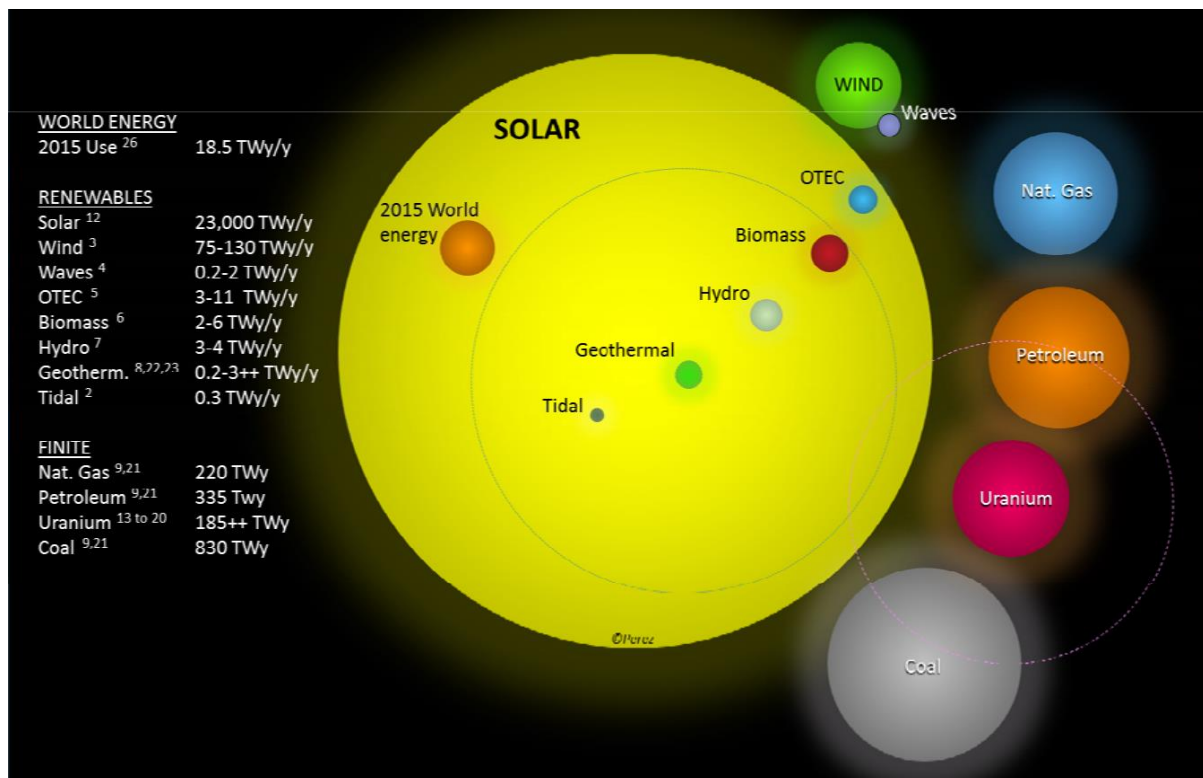


Figure 3: 2015 estimated finite and renewable planetary energy reserves (Terawatt-years). Total recoverable reserves are shown for the finite resources. Yearly potential is shown for the renewables.<sup>19</sup>

Every year, the Sun bombarded our planet with an overwhelming amount of energy that, if captured with one hundred percent efficiency on every land-covered surfaces, clocks at 23,000 TWy,<sup>19</sup> or nearly 726,000 Exajoules, the equivalent of roughly 1250 times the amount of energy we consumed in 2019. It is worth noting that even if as little as four percent of land were to be covered with twenty percent efficiency solar panels, the yearly collected energy would still be enough to power the world ten times over. This ridiculous capacity significantly dwarfed every known power source, though many of which are essentially solar-powered (wind, hydro, fossil fuels to name a few). In addition, sunlight's reliability is unparalleled as it requires no maintenance from our part, and we can still rely on it at least until the Earth leaves

the habitable zone of the solar system in a billion years.<sup>20</sup> However, even when that happens, if human could successfully colonize Mars, solar energy could again be relevant until the red planet, in turn, falls out of the Sun's favor.

Considering that various parts of our world today are powered by the flow of electric current, the transition from fossil fuels electricity, which is currently accounted for more than half of the electricity mix,<sup>4</sup> into its solar counterpart is expected to significantly reduce the CO<sub>2</sub> emission from this sector. Moreover, this approach would make use of the existing power grid, leading to a smoother transition all the while conserving our already limited available resources. Taking into account the rapid evolution of solar panel manufacturing technology,<sup>21–23</sup> the current growth in solar power generation despite the global pandemic<sup>4</sup> and the fact that solar photovoltaic devices are now the cheapest way to generate electricity,<sup>24</sup> the way forward is indeed promising, even more so if we can iron out all the bugs.

Solar panels can produce electricity as long as there are sunlight shining on them, which means they cease to function at night, or when the light path is obstructed by a number of reasons, be it geographically or environmentally. This significant variation in power generation is also usually misaligned with our energy demand. Therefore, in order to achieve an uninterrupted power solution, methods to store solar energy and release when required are essential. Luckily, the solution can be found in nature through the complex but fascinating process of photosynthesis which has been employed by plants, cyanobacteria and algae for their survival and growth since their first appearance on the planet. Employing the flawless operation of the photosynthetic machine, the photoautotrophs are able to capture light to oxidize water to oxygen then keep the photogenerated electrons for other purposes. Most organisms send these electrons to the Calvin cycle to reduce atmospheric CO<sub>2</sub> to biomass, while in some cases, to the hydrogenases to produce hydrogen (**Figure 4**).<sup>25–27</sup>

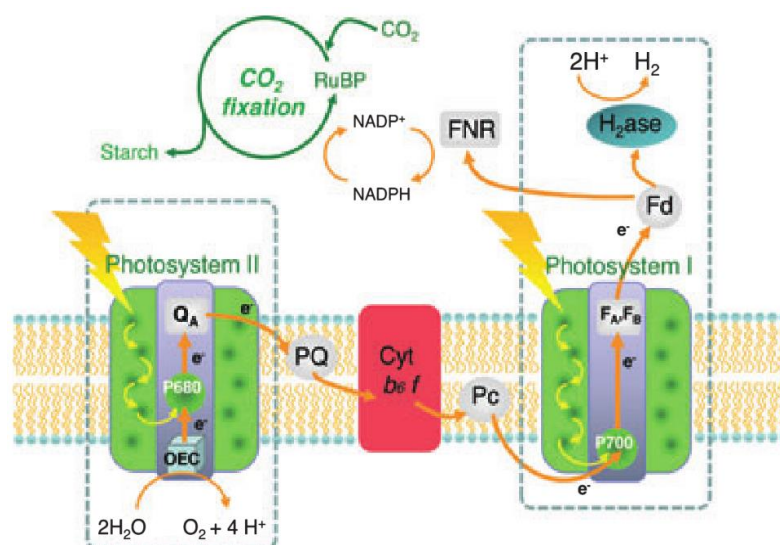


Figure 4: Schematic representation of the photosynthetic chain in the oxygenic photosynthesis <sup>27</sup>

Like a stroke of heavenly blessing, these two processes miraculously coincide with our goal and provide a pathway to spearhead two of our most pressing problems. Utilizing the hydrogen producing mechanism, we can perform solar water splitting to obtain a clean and powerful fuel, while the biomass producing mechanism gives us not only more fuel, but also a way to capture CO<sub>2</sub> and reduce its negative effects to our environment.

## 2.1. Green hydrogen through solar water splitting

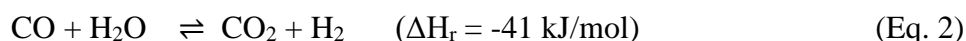
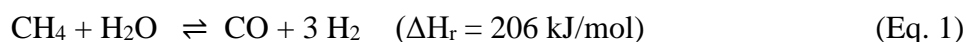
Despite having existed in nearly everything around us, it was not until 1766 that hydrogen was officially recognized as an element.<sup>28</sup> Possessing high reactivity, it is generally found bonded to other elements and notably is regarded as an important building block for virtually all organic molecules. However, its homonuclear diatomic form, dihydrogen (hereafter simplified to hydrogen), only exists in nature in much smaller quantity in comparison. Nevertheless, its usage has been observed in various aspects of our life, most widely in the industrial processes such as petroleum refinement, metal treatment, fertilizer production and food processing.<sup>29–31</sup> Even though hydrogen is also used to produce rocket fuel,<sup>32–34</sup> its contribution to the energy and powered transportation sector is still quite limited.<sup>35</sup>

At 120 MJ.kg<sup>-1</sup>, hydrogen possesses nearly three times as much gravimetric energy density than gasoline (44.4 MJ.kg<sup>-1</sup>). However, it loses by a nearly as much in term of volumetric energy density, even in its liquidized form (8.4 MJ.L<sup>-1</sup> vs. 31.1 MJ.L<sup>-1</sup>).<sup>36</sup> Nevertheless, researchers and engineers all over the world are currently putting forth massive efforts to find better storage methods for hydrogen, notably in solid state form to address this demerit.<sup>37,38</sup> Adding to the clean way it is consumed to release energy, either as heat through

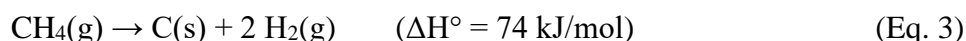


direct combustion in air or as electricity through the use of the technologically matured fuel cells, by leaving behind only water as by-product, hydrogen poses as an attractive energy carrier of the future. However, as the amount of naturally occurred hydrogen is too small for any practical purposes, it has to be produced from other sources and can only be truly considered as a clean source of energy if said production is also clean.

According to the IEA report this May, global low-carbon hydrogen production will need to reach 520 million tons annually by 2050 to realize a CO<sub>2</sub> neutral scenario.<sup>39</sup> Considering the yearly production of 90 million tons from all sources in 2020,<sup>39</sup> serious scaling up and restructuring must be realized to hit this goal. Throughout history, hydrogen was produced by various methods, each brings along its own economic and environmental advantages and detriments.<sup>40</sup> Nowadays, 96% of hydrogen is industrially produced from fossil fuels mainly through hydrocarbon reforming and pyrolysis.<sup>40</sup> The former method, responsible for 49% of the hydrogen generated,<sup>35</sup> is largely conducted through the well-established steam methane reforming (Eq. 1) to produce syngas which is usually further boosted by the water-gas shift reaction (Eq. 2) to achieve a higher yield. However, as a whole, it still spews out a plethora amount of CO<sub>2</sub> to the environment. Moreover, the CO remnant can passivate and reduce the efficiency of typical fuel cells.<sup>40</sup> Provided if the emitted CO<sub>2</sub> is re-captured, this type of hydrogen is normally regarded as “blue hydrogen”, otherwise, it is “grey hydrogen”.



The recently enhanced methane pyrolysis mediated by molten metals<sup>41–43</sup> introduced a CO<sub>2</sub>-free way to produce hydrogen from methane with solid carbon as by-product (Eq. 3). The hydrogen produced in this way bears the color of “turquoise”. Such an innovative method will be vital for our quest to move away from fossil fuels as it can revitalize the atmosphere and at the same time satisfy our hydrogen demand until other processes for producing clean and renewable hydrogen can mature.



Perhaps, one of the most promising methods for producing hydrogen is using renewable energies to power the water electrolysis. Indeed, this “green” color hydrogen can store the unused portions of any renewable energy sources then effectively release them on demand by

making use of the matured technology presented in fuel cells, now that the presence of CO has been removed. The newly acquired hydrogen can also be used for its various existing responsibilities. Afterwards, the byproduct of its consumption, which is usually water can be reintroduced and split again, thus complete the basic cycle of the famous hydrogen economy.<sup>44-</sup>

46

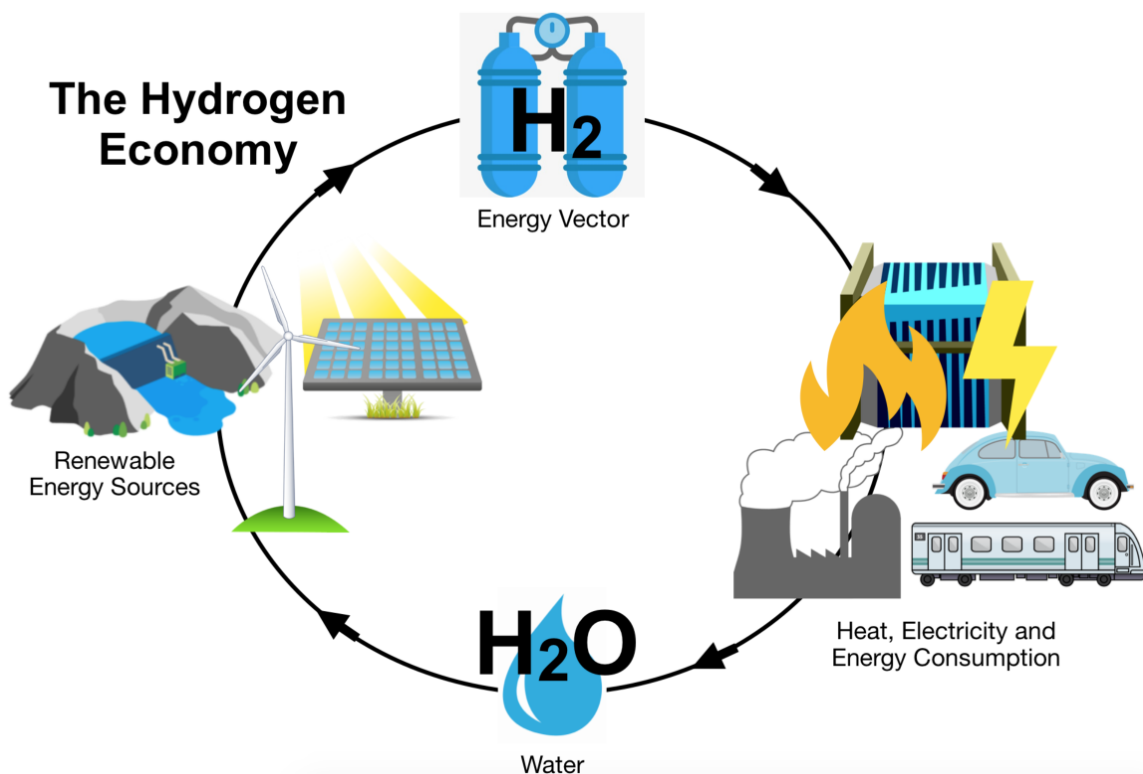


Figure 5: Schematic overview of a hydrogen-based energy economy<sup>37</sup>

As the world is largely covered by water, this hydrogen cycle (**Figure 5**), in combination with the existing PV industry, ultimately opens up the way to fully utilize the bountiful amount of solar energy available to us. When the sun shines, solar panels can generate electricity for our various needs. The excess amount, which is usually wasted, can now be used to perform water electrolysis (Eq. 4), or in other words, be stored in the chemical bonds of the resultant hydrogen. This stored energy can then be distributed by the existing infrastructure and release on demand, preferably when sunlight is not available. The realization of this scheme would effectively eliminate the biggest challenge of solar energy as a power source, thus providing us with a powerful, carbon-free and reasonably sustainable alternative to fossil fuels. However, the financial barrier from all sectors of the scheme must be overcome to generate sufficient driving force for us to make this life-changing transformation. As mentioned above, part of this

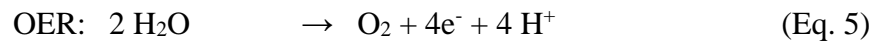


ambitious plan has been realized as the cost of electricity from PV panels has been brought down enough to rival that of fossil fuels. Moreover, across the board, massive efforts are being mobilized and new progress are being made, from the storage and transportation methods for green hydrogen, the matured and still evolving fuel cells technology for better utilization of said hydrogen, to the optimization of devices capable of the water splitting reaction that generates it.

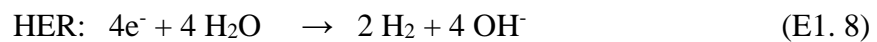
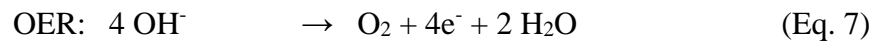


Being a thermodynamically up-hill reaction, energy input is required for water splitting to happen. When said input comes from solar electricity, the reaction is commonly referred to as solar water splitting, where the generated flow of electrons is used to drive its two half-reactions, namely the oxygen evolution reaction (OER – Eqs.5, 7) and the hydrogen evolution reaction (HER – Eqs.6, 8).

Acidic environment



Basic condition



The change in Gibbs free energy of the whole reaction suggested that, theoretically, application of 1.23 eV of external bias is enough for the reaction to start. However, considering various parameters such as activation energy barrier, kinetic barrier, diffusion limit, Ohmic drop, surface properties and entropy..., additional driving force is needed. In water electrolysis, this additional force comes in the form of overpotential ( $\eta$ ). The term is defined as the difference between the potential where the experiment is being conducted and the thermodynamically determined potential of the corresponded redox reaction. It is generally more negative than the reducing potential and more positive than the oxidizing potential. However, even when all the energy barrier is overcome, due to the OER requiring a whopping four proton-coupled electron transfers, the reaction rate is excruciatingly slow. Therefore, to increase the output to our desired value, which in this particular case, is the current density

generated and the amount of product formed, two approaches can be taken: to further increase the applied potential, or to somehow lower the energy barrier.

The first method can be achieved through improving the capability of the light harvesting system, either intrinsically through the choice of materials and fabricating technique, extrinsically through serial connection, or a combination of both. The spectrum of the sunlight reaching Earth's surface is mainly composed by visible (44.7%) and infrared (48.7%) irradiation.<sup>47</sup> However, the infrared light in theory can only generate less than 1.5 V worth of potential, which is not always sufficient to drive the overall water splitting. Therefore, visible light is arguably more attractive. Indeed, in the visible spectrum, the most energetic photon, with wavelength of 380nm, can theoretically induce 3.26 V potential. To get even more intrinsic potential out of a single semiconductor, one can make use of the 6.6% of more energetic UV light, however, performance is expected to drop significantly. This property of sunlight is a limitation to the kind of materials we can use. Connecting similar light harvesting units can also boost the driving force, or integrating layers of semiconductors with different bandgap can utilize more of the solar spectrum. However, elaborate system with complex technology can get expensive really fast. Fortunately, the burden laying on light harvesters can be partly eased by the addition of catalysts.

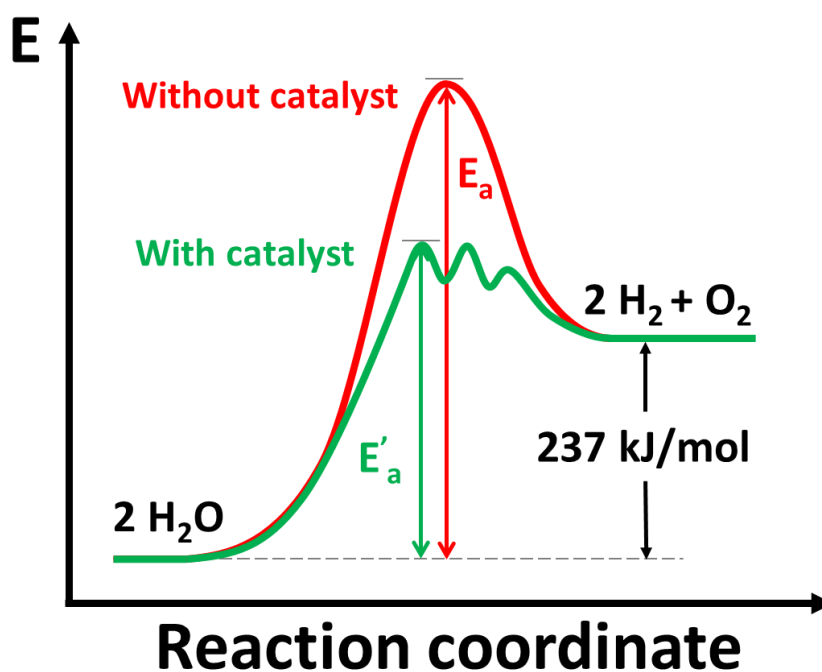


Figure 6: Energy diagram of water splitting reaction with and without the presence of catalyst

By providing a different reacting mechanism, catalysts are able to lead the reaction through a shortcut with lower activation barrier with the formation of additional intermediates (**Figure 6**). Their presence accelerates the reaction rate while keeping the same energy input. Hence, an optimum combination of suitable broad solar spectrum light harvesters and highly performant catalysts would be of utmost importance to achieve the highest possible solar energy storage efficiency.

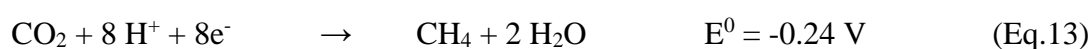
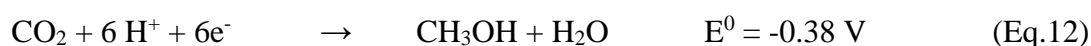
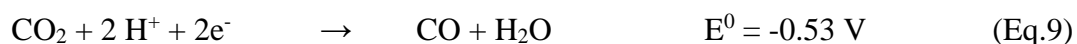
## **2.2. Solar fuels through CO<sub>2</sub> reduction**

While the quest to secure an environmental-friendly and sustainable energy source is indeed noble, reversing the negative consequences caused by abusing fossil fuels is also an urgent necessity. Ever since the industrial revolution, the amount of CO<sub>2</sub> released to the environment have been rising at an accelerated pace, chalking up to nearly 35.4 trillion tons in 2019 alone, overshadowing other more inherently potent greenhouse gases like methane by a large margin through the sheer quantity and persistent presence in the atmosphere. The global pandemic managed to dent this massive number by 6.3% in 2020, the largest decrement recorded since the end of the World War II.<sup>4</sup> However, the United Nations Environment Programme reported that if we were to meet the 1.5°C goal set by the Paris Agreement, the CO<sub>2</sub> emission has to be cut down further, e.g. to an annually 7.6% reduction for the remaining of this decade.<sup>48</sup> Nevertheless, even if we somehow managed to achieve such hefty task, dealing with the CO<sub>2</sub> amount already released would still need to be done.

There exist a handful of methods for capturing and storing CO<sub>2</sub> in the atmosphere.<sup>49-51</sup> However, as their performance is, to this date, quite miniscule compared to the gigantic size of the formidable enemy, significant upscaling is required. This creates a dilemma, since such systems are still currently being constructed mainly through fossil fuels-based resources. Nevertheless, until we can effectively shift our construction methods to renewable energy, efforts made to reduce CO<sub>2</sub> and its detrimental effects are all welcomed. Meanwhile, alternatives such as solar CO<sub>2</sub> electroreduction in aqueous solution to usable fuels is a promising approach inspired by natural photosynthesis and is gaining traction worldwide.

Converting CO<sub>2</sub> to fuels entails transforming it to its reduced carbon species. However, CO<sub>2</sub> reduction reactions (CO<sub>2</sub>RR) face serious kinetic hindrances. Right from the beginning, adding a single electron to the molecule requires a huge energy input due to the difficult reorganization between the linear structure and its bent radical anion one. As we descend the

depth of reduction, proton-coupled electron transfer is required and its number increases for each subsequent conversion. This leads to great technical challenges, but in return, more energetic fuels can be obtained (Eq. 9-14, potentials were quoted vs. NHE at pH 7).<sup>52</sup>



Researchers have been relatively successful at reducing CO<sub>2</sub> into less complex products like CO and HCOOH, reaching around 100-200 mA/cm<sup>2</sup> current density with the required overpotentials centered around 0.6 V and 1.0 V, respectively. The selectivity for these two products is also high with both possessing Faradaic efficiency around 90%.<sup>53</sup> However, more useful fuels, even the ones requiring comparable overpotentials, are still locked behind the door of low efficiency and selectivity due to the discouraging electro-kinetics. The key, once again, lies in the development and optimization of suitable devices containing efficient light harvesters coupled with catalysts boasting attractive performance and high selectivity. Only when the photoconverting part is working in optimum harmony with the fuel-converting one, and a competent cell design to facilitate charge and mass transfer is conceived, then the highest performance can be reached. In addition to that, one also need to consider the elevated difficulties in concentrating the dispersed CO<sub>2</sub> from the environment for the input and separating the various possible products from the resulting mix for their specific uses. However, once realized, this process has the potential to construct a miniature carbon cycle with enhanced regeneration rate that can contribute to our energy budget in a net-zero carbon emitting manner (**Figure 7**).

In this approach, solar energy can drive the electrochemical reduction of CO<sub>2</sub> to various fuels. These fuels, based on their physical state can be stored and transported accordingly through the existing distribution system for conventional fossil fuels. After having performed their purposes, the emitted CO<sub>2</sub> can be re-captured and introduced back into the cycle. If

sufficiently scaled with improved efficiency, its CO<sub>2</sub> intake can increase. Once we can finally shift away from fossil fuels, this scheme can shift its purpose to regenerating the damaged atmosphere.

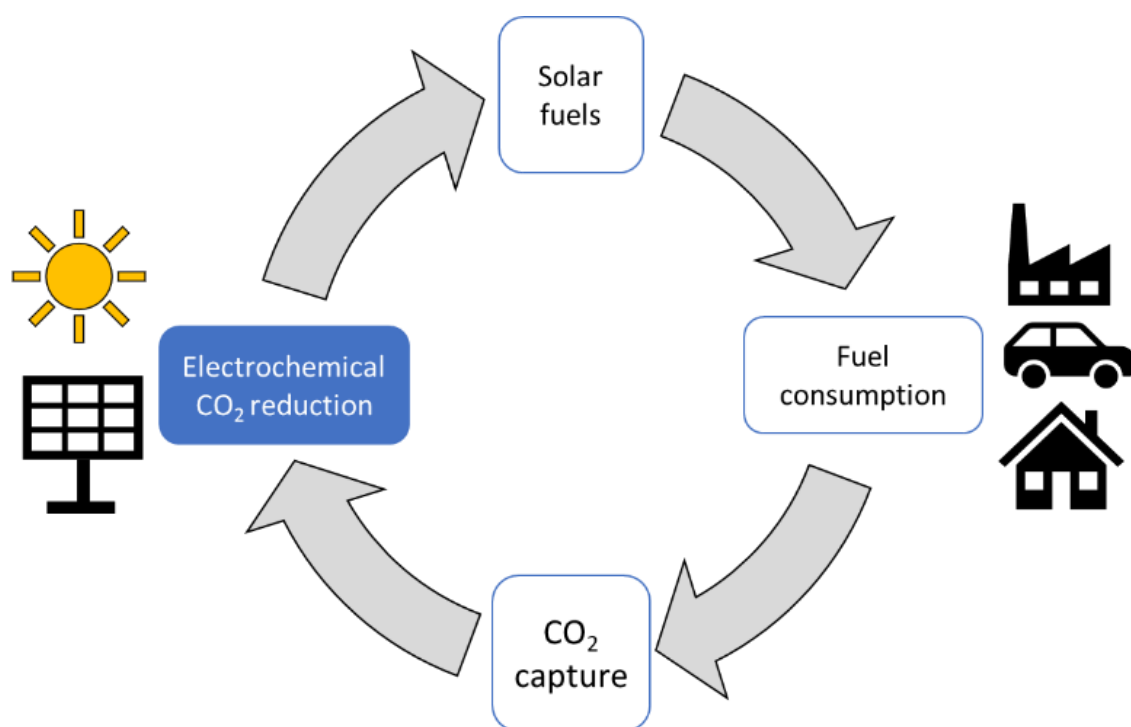


Figure 7: Schematic representation of a carbon neutral cycle

### 3. The means to get there – Current scientific progress on making solar fuels viable

Unleashing the potential of the clean and abundant solar energy to the fullest is undoubtedly a huge challenge. The process will require no less than an unprecedented rally of efforts from all related fields, be it political directives, financial campaigns, industrial reformations, cultural alterations or scientific and technological breakthroughs. These actions would also need to be performed as soon as possible, because the temporal window to reach net zero carbon emission is rapidly closing,<sup>18</sup> and we already crossed into the high risk zones for several planetary boundaries.<sup>54</sup> With that said, the science community, one of the first to realize the harm of climate change, has been hard at work to find possible technical solutions for the day the world can come together and the life changing agreement be formed.

The first demonstration of photovoltaic device, also the first photoelectrochemical (PEC) device was conceived in 1839 by French physicist Alexandre-Edmond Becquerel. However, it was not until 1972 when Fujishima and Honda discovered the solar water splitting effect of PEC<sup>55</sup> that it started to gain interest from researchers all over the globe as a promising candidate

for being the ultimate device. This is due to the fact that such device is capable of not only converting solar energy to electricity, but also providing a pathway to store said energy in chemical bonds. The resultant apparatus, at present normally referred in the broadest sense for its purpose as solar fuels generators, takes inspiration from the natural photosynthetic system. It functions with the minimum requirements of a light absorber, catalysts capable of driving the desired reactions, a conducting electrolyte and a way to separate the generated products.

Up to now, countless alterations, customizations and refinements have been designed and implemented to the device, sub-categorizing it to a wide range of classes with the aim to balance efficiency, cost, scalability, stability and durability. However, provided the large quantity and different underlying physics, this vast array of devices needs a logical classifying system so that methodological analysis and comparison can be performed, easing the path to future fine-tuning and optimization processes. Attempts from various researchers gave birth to several ways to group them together. However, as the inherent boundary is often blurred by relating mechanisms, it is currently a work-in-process. Nonetheless, it is necessary to establish a starting point. The taxonomy devised by Nathan S. Lewis and colleagues, although still questioned by some,<sup>56</sup> is widely embraced as one.<sup>57,58</sup> In this scheme, devices are sorted along the nuances of perceived development cost and the maturity of the underlying technology (**Figure 8**). One can also group the devices based on the mechanism through which the photogenerated electrons and holes are separated to perform meaningful work instead of recombining with each other.

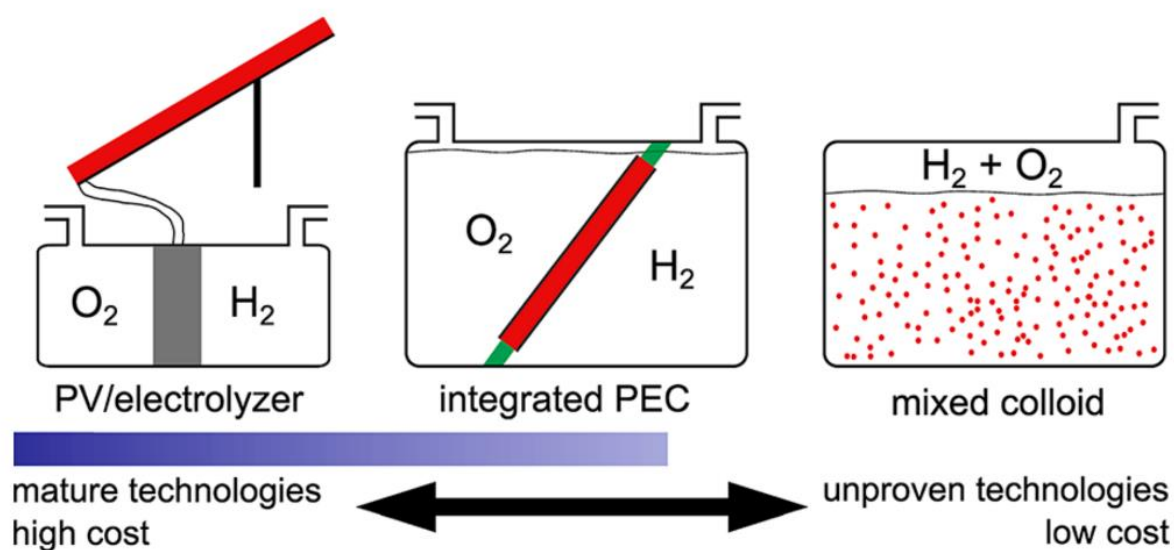


Figure 8: Schematic representation of three main solar-driven water splitting devices<sup>57</sup>

### **3.1. The brute force PV-electrolyzer**

Capping the left most end of the spectrum is a straightforward and intuitive approach where a photovoltaic (PV) device is directly wired to an electrolyzer, so that the electricity produced by solar irradiation can drive the splitting of water molecules. In a typical PV device, differently doped semiconductors are joined together. The interface between them is referred to as a junction. There are various types of junction. A p-n homojunction is formed between materials of the same element while p-n heterojunction is formed between materials of different elements. There is also p-i-n junction (with “i” referring to intrinsic or undoped semiconductor) which can also be heterogeneous or homogeneous in nature. Across these junctions in equilibrium state, there exists a difference in electric potential. This can prevent the recombination of photogenerated electron-hole pair by separating and sending them moving in opposite directions, thus yielding photocurrent. If being collected successfully at their respective terminals of the PV unit, these charged species can then move to the electrodes in the electrolyzer to do their job, provided that they are supplied with sufficient driving force. Thanks to the discrete modular architecture, the all-solid PV unit does not have to be in contact with the electrolyte, hence improving the stability of the system. Overall, this “brute force” method is backed with mature technologies and its high stability is also beneficial when concentrated sunlight is used to increase the output.<sup>59</sup> This family is currently hosting devices with best solar-to-hydrogen efficiency of more than 30% under concentrated illumination.<sup>60</sup> However, the device is normally bulky, and Ohmic drop from various connecting points is prominent. Moreover, the formation of the junction is costly due to the requirement of complex instruments and high vacuum.<sup>61,62</sup> The electrolyzers designed to work at high current density in the range of A/cm<sup>2</sup> also demand expensive materials.<sup>59</sup> Therefore, scaling up is a huge challenge, and even when realized, will only be suitable for centralized hydrogen production.

### **3.2. The unstable mixed colloid**

On the other extreme is the photocatalytic colloidal system. In this electrodes-less approach, the solar fuel production unit comes in the form of light harvesting nanoparticles coated with suitable co-catalysts, or molecules designed with specialized parts to fulfill both purposes. These units can either be dispersed or dissolved in solution, or affixed to a supporting porous scaffold. Here, once the incoming light is absorbed, the generated electrons and holes can diffuse to the adjacent catalytic centers and directly drive their designated reactions. This is an advantage over the photoelectrochemical system, since the charges generated are not

forced to go through large distance between the electrodes. Therefore, the burden in designing highly conducting electrolyte is lessened and distilled water can be used.

Although presently plagued by low efficiency compared to other approaches, photocatalytic colloid boasts unparalleled simplicity as well as economical predicted manufacturing cost, and is by far the most scalable. With the potential hydrogen price range estimated to be in the range of \$1.6 to \$3.2 per kilogram, this is currently the most promising candidate to meet the cost requirement of \$2.00 - \$4.00 per kilogram set by the United States Department of Energy for hydrogen to become a viable fuel.<sup>63,64</sup> Recently, Domen *et al.* demonstrated their photocatalytic hydrogen production setup of 100 m<sup>2</sup> using  $\text{SrTiO}_3:\text{Al}$  with co-catalysts, laying down an important milestone for the development of this class of device.<sup>65</sup>

Typically, the choice of materials is limited to large bandgap semiconductors that are only active under UV light. This highly energetic radiation only contributes to a bit more than 6% of the solar spectrum, hence the overall fuel conversion efficiency is quite modest (0.76% solar-to-hydrogen efficiency ( $\eta_{\text{STH}}$ ) for the aforementioned setup). However, to make up for that, the semiconductors are generally more chemically stable, environmentally benign and economically viable. In addition, with suitable additives, the bandgap can be tuned to accommodate additional wavelengths from sunlight and the undesired charge recombination can be suppressed. Domen's study also addresses the usual stability and safety concerns with their months-long test. Lacking inherent product separation mechanism, photocatalytic systems usually yield a stoichiometric mixture of hydrogen and oxygen, which, if poorly handled, can result in catastrophic explosion. Therein, it was shown that when confined to a sufficiently small volume, deliberate ignition of the mix resulted in no significant damage to the system.

Overall, with proper improvements in performance, cell designs and safety, photocatalytic water splitting systems will undoubtedly be an important contributor to the global green hydrogen production.



### 3.3. The compromise zone – where our interest lies

Finally, between those two distinct classes of device lies the remainder of the heap in an attempt to achieve the true balance between performance, stability and scalability while keeping the cost at a reasonable level. Though presented chiefly by the over-generalized apparatus called “integrated PEC” in **Figure 8**, this group of devices is the home to a huge number of designs with interesting working mechanisms. In short, this is the fun part of the spectrum.

Here, the basic structure of a PV-electrolyzer can be redistributed and compressed to a monolithic configuration as in the case of the famous artificial leaf from Nocera’s group (**Figure 9**).<sup>66,67</sup> Generally, a triple p-i-n junctions PV cell was coated with suitable catalysts on its respective faces, resulting in a super thin device resembling a natural leaf. Once dunked in an electrolyte and shined with light, the buried all-solid junctions guide the photogenerated charges to their respective catalysts, evolving bubbles of O<sub>2</sub> and H<sub>2</sub> from the two corresponding faces of the leaf. Since the gas production is tied to its specific side, separation can be easily achieved with a simple barrier. The elimination of excessive wirings and the size reduction also help promote better charges transfer across the device. However, the ion transfer pathway is elongated. Though the cost of the PV unit is still quite elevated, and its stability when immersed in the electrolyte is questionable, the possibility to integrate catalysts made from Earth-abundant elements and the structural enhancement to overall efficiency is a nice advantage.

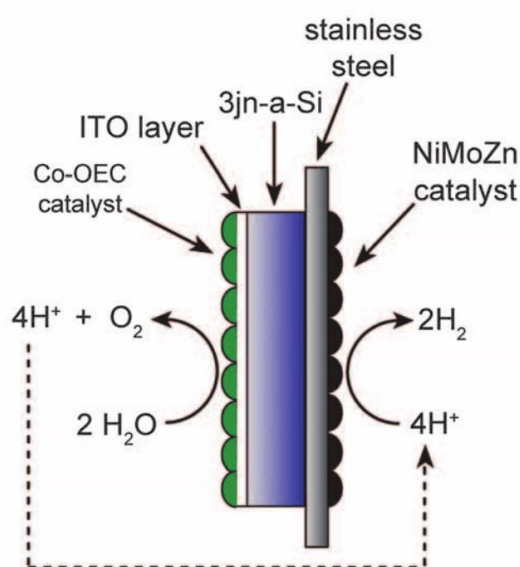


Figure 9: Schematic representation of a monolithic artificial leaf<sup>66</sup>

Aside from the solid-solid junction, there also exist a solid-electrolyte junction that can separate and vectorially guide the photo-generated charges. This type of junction can be seen in the typical tandem PEC device, where a p-type semiconductor is connected to an n-type semiconductor through an Ohmic contact, forming a Z-scheme configuration. Possessing different bandgaps but suitable band edges position, this scheme can employ a wide range of materials to efficiently use most of the sunlight spectrum. Once put inside the electrolyte, rectifying junctions are created across the semiconductors and the electrolyte interfaces. These junctions are capable of guiding the photogenerated minority charges out of their corresponding host through the circuit to their respective catalysts, driving the water splitting reaction. The formation of this type of junction is significantly simpler than the all-solid one, as the electrode surface just needs to be processed and put in a suitable electrolyte. The versatility in having two separate photoelectrodes that can be fine-tuned with different processes is also an attractive advantage. With the addition of a bipolar membrane, it is also possible to have the photoelectrodes working in different pH that are more beneficial to them.<sup>68</sup> The membrane can also act as a separator for the resulted gases. In addition, with the introduction of proton exchange membrane (PEM) such as Nafion, only the anode is required to be in contact with the electrolyte, hence alkaline solution can be used without negative effects to the hydrogen evolving side.<sup>69</sup> This type of device brings to the table a simple, yet versatile base system that allows in-depth (photo)electrochemical study of a wide range of new materials with interesting working mechanisms.

There are many more types of solar fuels generators targeting at various levels of compromises and employing components from other classes such as PV-biased photoelectrochemical cells, PEC-biased photoelectrosynthetic cell, etc.<sup>58</sup> However, in the scope of this PhD thesis, the two aforementioned sub-classes will be mainly focused as they align well with our existing resources and research interests.

### 3.4. Some considerations moving forward

As a rule of thumb for any type of machine, the best efficiency can only be achieved when all components are able to cooperate and reach a harmonically balance state with minimal losses, as an optimum condition for one part does not necessary be so for another. Nevertheless, some basic requirements should be made for each element in order to construct a viable device.

For the light harvesters:

- The bandgap should be sufficient for harvesting the visible light and the band edges positions suitable for the desired reactions.
- The material should be stable and photostable under aqueous condition, as the reactions of interest is in water. Alternatively, protective layers which do not affect its function can also be applied.
- The conductivity should be high to promote charge diffusion and reduce undesired recombination.

For the catalysts:

- The conductivity needs to be high to avoid impeding charge transfer.
- The surface should be suitable for reactant to adsorb.
- The altered mechanism should have efficient electron transfer to form intermediate states then the products.
- The desorption of the final product from the catalyst surface should also be efficient.

## Chapter II

### Dual catalysts from a single solution



## **1. Introduction**

It has been established that in a broad sense, the presence of catalysts is beneficial for chemical or biochemical reactions. Hence, researchers have been diligently trying to design these substances to find the best ones for their specific purposes. As a result, a huge number of catalysts with varying performance and characteristics have been created. Thus, once again, a classification method is required to get a broad picture of the field. This time, the state of the catalysts in comparison with the state of the reaction mixture can be used for the sorting process.

### **1.1. Three broad classes of catalysts**

When both the catalysts and reactants are in the same physical state or phase, the catalysts are called homogeneous catalysts. One of the key advantages of this type of catalyst lies in the highly increased interaction between the catalysts and the reactants to form intermediate compounds. The most common form of homogeneous catalysis is in liquid phase, where a nice balance between mobility and distance is achieved compared to its gas-gas or solid-solid counterparts. Moreover, as the molecular structure of such catalysts is often well-defined, precise analysis and optimization can be performed. However, the retrieval or recycling of the catalyst is usually challenging. It is the case for various organometal complexes which possess interesting mechanism and high activity but are difficult and expensive to design and synthesize in large amounts.

On the other hand, heterogeneously catalyzed reactions involve catalysts and reactants that are in different phases from each other. This type of process usually concerns catalysts in solid phase and reactants in liquid or gaseous phase. Unlike homogeneous catalysts, heterogeneous catalysts can be retrieved from the reaction mixture with relative ease. This can be achieved either through filtration in the case of particulate form, or straight up removal if they are embedded in a scaffold or made as electrodes. Hence, expensive catalysts can be recovered more easily, which is extremely important for sustainable development. In addition, once made into electrodes form, various electrochemical techniques can be used, giving valuable insights into the working mechanisms of the system. However, the degree of interaction is greatly dependent on the available surface area on the catalysts and the adsorption of the reactant thereon. Indeed, during reaction, a reactant needs to travel to the catalyst's surface, adsorb on it and get transformed to the product. When the catalyst's surface is fully

populated by the reactants, reaction can only continue when the products leave the surface and the cycle begins anew. In addition, structure analysis is a huge challenge due to their macroscopic scale, thus making improvement in selectivity and reactivity through structural modification difficult.

Nature since time immemorable evolved efficient, highly selective but super complex catalysts called enzymes. With a key-lock mechanism, these proteins exclusively catalyze their respective biochemical reactions by stabilizing the transition state, thus bringing down the activation energy. Though many argued their inclusion into the rank of homogeneous catalysts, their extreme specialization sets them apart as a class of their own, the biocatalysts. They skillfully employ the proton-coupled electron transfers<sup>70</sup> to dramatically speed up reactions, in some special cases, from a 78 million years to mere seconds.<sup>71</sup> They are also the inspiration for many organometallic complexes to accelerate a wide range of industrial processes. However, enzymes, being proteins, are sensitive to large changes in temperature and only function in a range of few degrees. Outside said range, denaturation or inhibition can occur, leading to performance degradation.

At the border of the broad classes also live the hybrid systems that provides different nuances of trade-offs with the aim to bring together the best qualities of each sides. Such system can be realized in the form of supported molecular catalysts.<sup>72</sup> This can be achieved though liquid-liquid biphasic system or solid-liquid system,<sup>73</sup> with the latter approach currently being favored by the scientific community.<sup>74-77</sup> Therein, the molecular catalysts are grafted on solid supports, effectively turning them into their heterogeneous counterparts. Thus, the high selectivity and activity of the former are overlapped with the robustness, stability and recoverability of the latter, provided if the grafting process does not negatively affect the catalytic centers.

Classification based on the reactions they catalyze is also a feasible approach. This can be seen in the case of the commonly studied electrocatalysts. These catalysts are used in electrochemical reactions, which is currently a distinct scientific field with unique applications.

For the purpose of solar fuels generation, catalysts belonging to all aforementioned classes have been employed in a wide range of systems. However, in the scope of this thesis, heterogeneous and supported molecular electrocatalysts will be focused on for their compatibility with our devices.

## 1.2. Figures of merit for electrocatalysts

With the huge number of electrocatalysts presently available, a unanimously agreed evaluation system is required to simplify comparison and induce meaningful development. The common figures of merit for general catalysts, namely activity, stability and selectivity are also relevant in electrocatalysts. However, they are expressed in a different way from other fields.

### *Activity*

In electrochemistry, the driving force is overpotential ( $\eta$ ), and the rate is represented by the obtained current. Thus, achieving the highest current from the least amount of overpotential means that the electrocatalyst possess optimum activity. Their relation depends on two main factors: the kinetic of the desired reaction and the mass transport efficiency. The coefficient of the latter can be obtained from the plateau region on a conventional I-V curve,<sup>78</sup> however, it only become prominent at relatively high current. The kinetic of an electrochemical reaction can be expressed with the more general Butler-Volmer equation when near the equilibrium (Eq.15).<sup>79</sup>

$$i = i_0 \left\{ \exp \left[ \frac{\alpha_{anode} n F \eta}{RT} \right] - \exp \left[ - \frac{\alpha_{cathode} n F \eta}{RT} \right] \right\} \quad (\text{Eq.15})$$

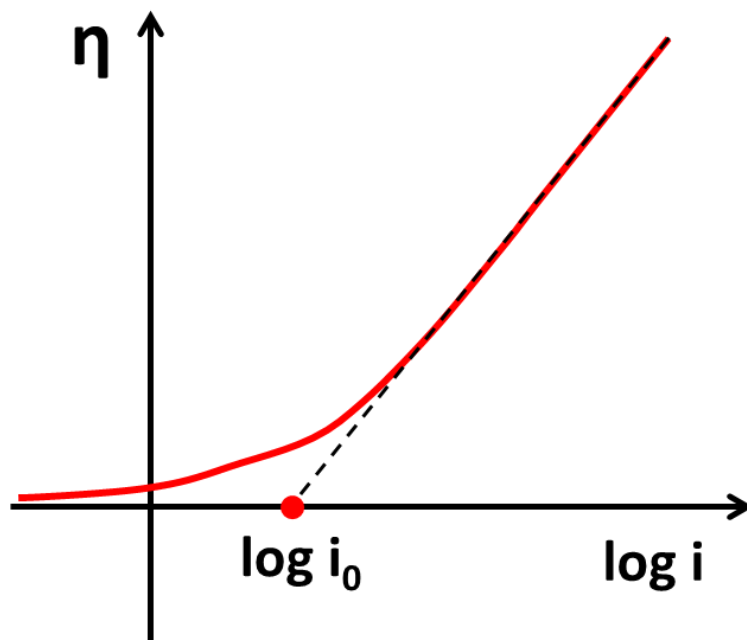
When the reaction is far from equilibrium, one term got cancelled out and the more simplified Tafel equation can be used (Eqs.16, 17).

$$i_{anode} = i_0 \exp \left( \frac{\eta}{b} \right) \quad (\text{Eq.16})$$

$$i_{cathode} = -i_0 \exp \left( - \frac{\eta}{b} \right) \quad (\text{Eq.17})$$

Herein, the various constants or parameters uniquely attached to the reaction like temperature (T), gas constant (R), Faraday's constant (F), transfer coefficient ( $\alpha$ ) and number of transferred electrons (n) is simplified to the parameter b, named Tafel slope. Thus, when reporting the activity of electrocatalysts, the common parameters that are often used are the exchange current  $i_0$  and the Tafel slope b. Indeed, catalysts with high exchange current show that at the equilibrium, the net measured current is at zero. However, it was the result of massive forward and backward reactions occurring at the same time, cancelling each other. Therefore, when even a small overpotential is applied, high current can be generated. This relation can be expressed by the Tafel slope, which shows the overpotential requirement to increase the

obtained current up by an order of magnitude. These two values can be extracted from a typical I-V curve by replotting it to the Tafel diagram (**Figure 10**).



*Figure 10: Representation of a Tafel diagram*

After a linear fit of the data points far away from the reaction equilibrium is obtained, the exchange current can be calculated from its intersection with the horizontal axis while the Tafel slope is its slope. In addition, to express the catalysts activity in comparison to a specific goal, values such as current density at a given overpotential or the overpotential needed to generate a specific current density are used. Commonly, for solar fuels generation, the overpotential required to yield  $10 \text{ mA/cm}^2$  worth of current density is often reported. This benchmarking current density corresponds to a solar fuel generator quoting at 12.3% efficiency.<sup>80</sup>

It is also worth noting that current density is often reported instead of only current for better comparison. However, there are different methods of measuring the area to which the current will be normalized. The geometrical surface area covered by the catalyst layer is the simplest for this purpose. Nevertheless, when porosity or topology is taken into consideration, the real surface area that will be in contact with the electrolyte will be more appropriate. Thus, a careful measurement of the area that are electrochemically active is required.



### ***Stability***

The stability of catalysts can be measured or monitored using different techniques. One frequently used in electrochemical study is chronoamperometry. The generated *current density vs. time* ( $j - t$ ) plot shows the evolution of obtained current density as the reaction progress. Degradation of the catalysts or their detachment from the electrode can be recorded by a decrease in current density over time. However, in certain specific circumstances, the catalyst continuously degrades, e.g. corroded, but still shows stable or even enhanced catalytic current density.<sup>81</sup> Thus, a careful analysis of potential corroded products is also required to convincingly conclude about the robustness of catalysts.

### ***Selectivity***

It is desirable that the supplied driving force is used by the catalysts to drive only the desired reaction. To measure this selectivity, Faradaic efficiency (FE) is employed. Generally, it is calculated from the ratio of total number of charges that are used to obtain the desired products over the total number of charges supplied. In solar fuels generation, the former can be acquired through the help of gas chromatography (for H<sub>2</sub>, O<sub>2</sub>, CO, etc.) or ion chromatography (for HCOOH), while the latter is recorded by the potentiostat (Eq.18).  $N_e$  is the number of electrons required to obtain a molecule of the product and  $F$  is the Faraday constant. Higher Faradic efficiency toward the same reaction indicates that the corresponding catalyst has higher selectivity.

$$FE = \frac{Q_{useful} (C)}{Q_{total} (C)} \times 100\% = \frac{n_{product}(mol) \times N_e \times F (C.mol^{-1})}{I (A) \times t (s)} \times 100\% \quad (Eq.18)$$

### 1.3. Overview of current state of solar fuels generating electrocatalysts

The famous Paul Sabatier once stated that an optimum catalyst should possess an ideal bond strength, i.e. not too strong and not too weak, with the substrate. Since then, the Sabatier principle has become an important guideline for developing new catalysts and thus, has been improved by researchers over the years. The first qualitative representation of the principle was developed by Roger Parsons in the shape of a volcano.<sup>82</sup> Later on, when combined with the power of modern theoretical studies, a quantitative rendering of said volcano plot can be achieved. With the large amount of electrocatalysts that have been developed for various different reactions, the plot is also a comprehensive way to introduce an initial view of the current state of research.<sup>83</sup> Although to get a more in-depth comparison, a three-dimensional plot including effects of electrolytes, such as pH variation, is required. However, such data is not always fully available due to stability issues in a wide range of pH.

#### 1.3.1. Catalysts for water electrolysis

##### *Hydrogen Evolution Reaction catalysts*

Introduction of suitable Hydrogen Evolving Catalysts (HEC) will minimize the overpotential requirement for HER, thus improving the fuel production efficiency.

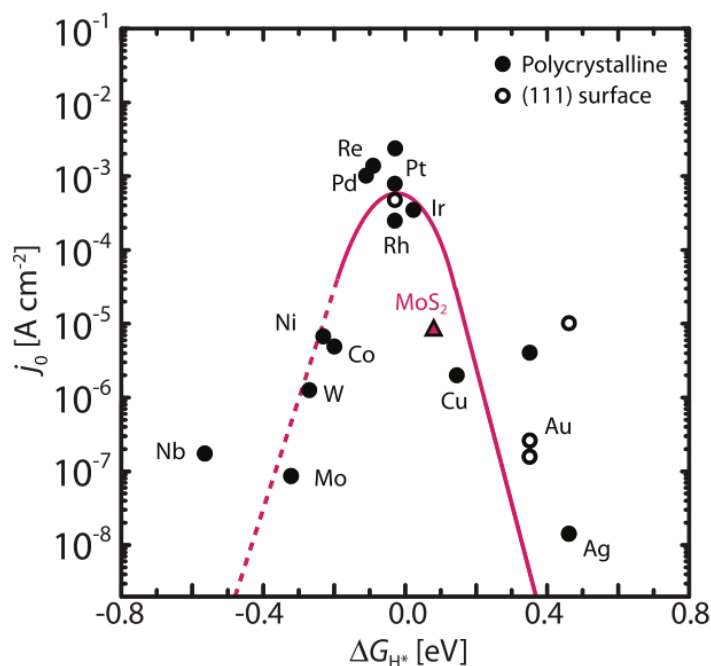


Figure 11: HER volcano plot for metals and MoS<sub>2</sub><sup>83</sup>

Having Gibbs free energy of  $\sim 0$  eV for the adsorption of hydrogen on its surface, platinum (Pt) is currently the most active catalyst for HER showing highest exchange current density ( $j_0$ ) (**Figure 11**).<sup>84</sup> It requires negligible overpotential to produce high current density. However, due to its scarcity and high cost, Pt is likely not an excellent candidate for the future large-scale production of H<sub>2</sub>. In this context, the search for more Earth-abundant alternatives with similar performance is being emerged. The usual trial-and-error approach is a good place to start, and has been employed at the initial stage of development. However, referencing from existing models from nature can give rise to promising research direction,<sup>85</sup> and progress can be significantly accelerated. Indeed, researchers utilized density functional theory (DFT) to study the catalytic active sites of natural hydrogenase and nitrogenase. MoS<sub>2</sub>, a material previously deemed inactive for HER, was shown to possess similar structure to those active sites. Having gained increased research interest, it was later found to be actually capable of driving the HER.<sup>86,87</sup> This was considered to be the event leading to the increment in research interest for the transition metal (notably Co, Fe, Ni, Mo, Cu...)<sup>88</sup> sulfides as HEC. The field later on extended to the transition metal chalcogenides family.<sup>84,89-93</sup> In addition, the introduction of another transition metal to the structure has been found to have positive effect to the catalytic performances.<sup>94,95</sup> The establishment of multi-metal chalcogenides materials provided another promising template for catalyst study and improvement. Similar systems based on carbides and phosphides also shows encouraging performance, some even coming very close to platinum (CoP).<sup>96-98</sup> More direct bio-inspired organometallic molecular catalysts mimicking the catalytic active sites of natural enzymes have also received a lot of research efforts.<sup>99-101</sup>

### ***Oxygen evolution reaction catalysts***

The sluggish four electrons transfer process is what made the OER the bottleneck of the overall water splitting. Development of effective Oxygen Evolving Catalyst (OEC) has thus been receiving a lot of attention from the research community. Among them, the transition metal oxides are perhaps the most investigated.

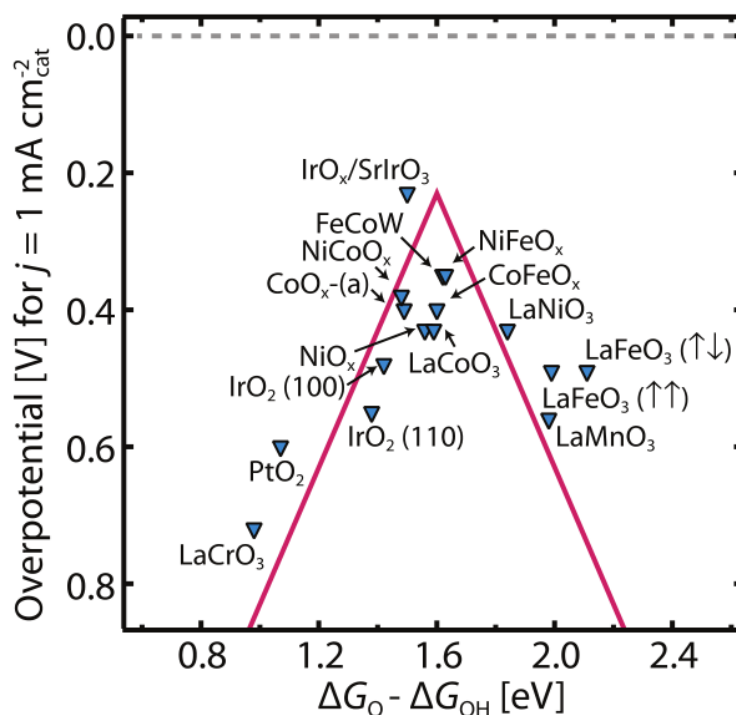


Figure 12: OER volcano plot for metal oxides <sup>83</sup>

In the initial stage of research, noble metals such as iridium or ruthenium and their oxides are widely investigated as OEC due to their high activity (**Figure 12**) in both acidic and basic conditions.<sup>102–104</sup> However, scaling up for these type of catalysts faces strong financial opposition. In addition, in the case of IrO<sub>2</sub> and RuO<sub>2</sub>, dissolution can occur under strong anodic condition.<sup>105,106</sup> To address these problems, alternatives based on non-precious metals are being researched due to their more generous reserve and inherently different chemistry. The amorphous cobalt-oxide-phosphate from Nocera's group is a notable example with attractive activity in a wide pH range from 4.5 to 9.5 and a proposed self-healing ability in analogy to that of enzymes in nature.<sup>107</sup> Interestingly, the addition of another transition metal into the structure can also alter the chemistry of the catalyst, thus promoting the catalytic activity. Indeed, development of multi metal oxides or hydroxide catalysts is a promising approach to improve the OER efficiency, with NiFeO<sub>x</sub> (Ni-Fe-OOH) under alkaline condition reaching performance very close to the precious metal oxide.<sup>108</sup> In particular, this class is also the home of the emerging perovskite material with elevated performance tunability through precise modification of the metals in the structure.<sup>109</sup> Some of these was reported to even outperform IrO<sub>2</sub> in alkaline environment.<sup>110</sup> Bioinspired approach by mimicking the oxygen evolving catalytic center (CaMn<sub>4</sub>O<sub>5</sub>) in the natural photosystem II through synthetic molecular catalysts is also being diligently studied. The combination of highly innovative synthetic ligands and inexpensive metal cores brings to the field another template for the pursuit of optimum performance.<sup>111</sup>

### 1.3.2. CO<sub>2</sub> reduction catalysts

Development of catalysts possessing high selectivity to the desired fuels is important for CO<sub>2</sub> reduction reactions given that it can produce different products ranging from C<sub>1</sub> to C<sub>n</sub> compounds. Especially, hydrogen evolution is a persistent contributor to poor selectivity in CO<sub>2</sub> reduction as proton reduction is more kinetically favorable. It has been shown that direct reduction of CO<sub>2</sub> can be achieved on metal surfaces with diverse selectivity, but mainly limited to the easier two electrons processes.<sup>112–114</sup> Moreover, high overpotential is usually required to overcome the kinetic barrier, and the generated products can also poison the catalyst's surface.<sup>115</sup>

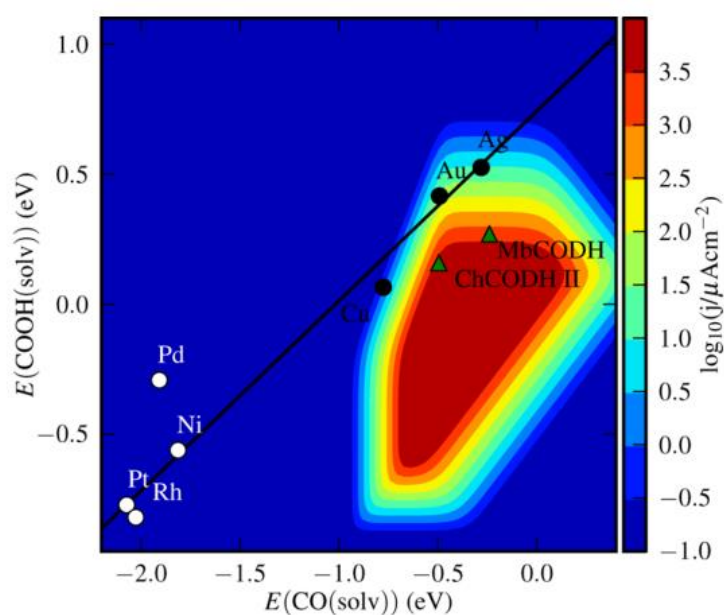


Figure 13: Three-dimensional kinetic volcano plot for CO evolution from the (211) step of transition metals and two enzymes models<sup>114</sup>

Though possessing lower CO-evolving activity than noble metals, copper is currently the only metal capable of generating hydrocarbons from CO<sub>2</sub> reduction with decent rate and thus has been widely studied and improved over the years.<sup>116</sup> However, the efficiency and selectivity of all of them are still far from natural enzymes. Indeed, in **Figure 13**, CODH enzyme models generated from studying bacteria such as *Methanosarcina barkeri* (MbCODH) and *Carboxydotherrmus hydro-genofmans* (ChCODH II) exhibit significantly higher current density than metals.<sup>114</sup> Hence, learning from the way multiple proton-coupled electrons reactions are simultaneously handled by enzymes and mimicking their structural features in artificially synthesized counterparts is a promising approach to obtain high performance.<sup>117</sup> Bioinspired molecular catalysts for CO<sub>2</sub> reduction in non-aqueous condition have been

designed and improved over the years, like the Tetraaza-macrocyclic cobalt (II) commonly known as  $[\text{Co}^{\text{II}}(\text{N}_4\text{H})]^{2+}$  from the 1980s.<sup>118</sup> More recent catalysts such as functionalized iron porphyrins also exhibit attractive activity, selectivity and robustness,<sup>119,120</sup> some can produce methane through a two-steps reaction with high selectivity.<sup>121</sup>

#### **1.4. Our attempt at cost reduction**

To induce sufficient financial incentive for the transferring away from fossil fuels to solar fuels, the final cost should be driven down as much as possible. In order to achieve that goal, efforts from all fronts should be mobilized, be it in researching inexpensive materials for the different components of solar fuel generators, or in engineering an optimum integration of those components.

Research on individual water splitting catalysts are blooming with new discoveries by the scientific community. However, top performance is usually achieved under the most favorable pH conditions, which are often near the extreme ends of the scale. Utilization of the immense amount of available sea water to replace specialized electrolytes would be a significant milestone for scaling up and cost reduction.<sup>122</sup> Thus, developing HECs and OECs capable of simultaneous operation in solution with neutral pH or in sea water is beneficial in the long term.

Even after the catalysts are developed, their activity in a device would often vary with the quality of the integration. There is often a general inverse relation between how well an assemblage is made and how inexpensive it is to do so. A method that can reach an optimum balance for these factors is highly desirable.

In an attempt to tackle those aforementioned obstacles, we propose a sole deposition solution that can concurrently lead to the electrodeposition of a dual catalysts for the overall water electrolysis. Indeed, the same  $[\text{Co}(\text{WS}_4)_2]^{2-}$  solution in phosphate buffer at pH 7 can result in the electrodeposition of CoWS-HEC<sup>123</sup> and CoWO-OEC<sup>124</sup> by applying an appropriate cathodic and anodic potential, respectively.

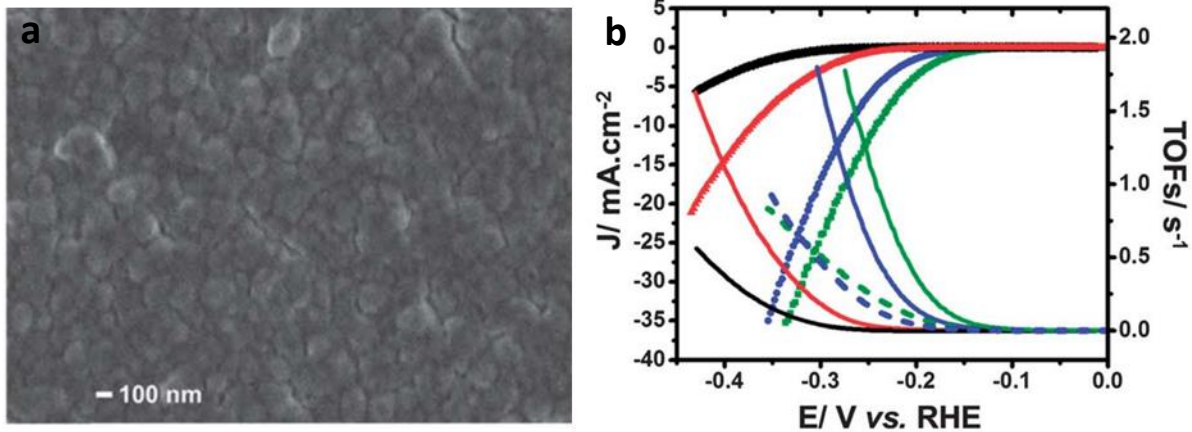


Figure 14: SEM image (a) and apparent catalytic current (b) of CoWS-HEC electrode<sup>123</sup>

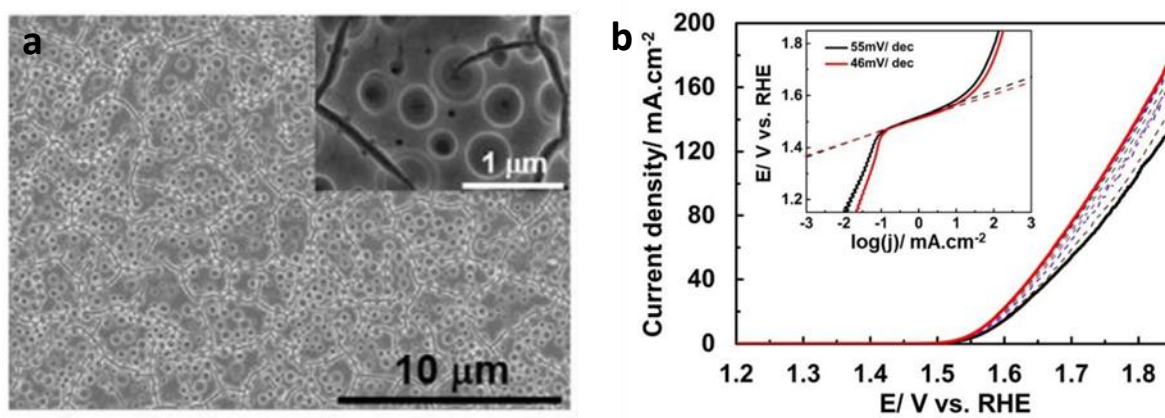


Figure 15: SEM image (a) and apparent catalytic current (b) of CoWO-OEC electrode<sup>124</sup>

Herein, we demonstrate the simultaneous deposition of these two catalysts onto two conducting electrodes, e.g. FTO, through the aid of a potentiostat.

## 2. Experimental setup

### 2.1. Preparation of $[\text{Co}(\text{WS}_4)_2]^{2-}$ deposition solution

To 30 mL of 0.1 M potassium phosphate buffer at pH 7 was added 4.36 mg of  $\text{Co}(\text{NO}_3)_2 \cdot 6\text{H}_2\text{O}$  (0.5 mM) and 5.22 mg of  $(\text{NH}_4)_2[\text{WS}_4]$  (0.5 mM). The yellow solution was then filtered through a hydrophilic PES membrane with 0.45  $\mu\text{m}$  pore size to remove any unwanted precipitates. After degassed by Argon for 15 minutes, the solution obtained was ready for electrochemical study and catalysts deposition.

We note that the chemical composition of the deposition bath can be easily altered by varying the  $\text{Co}(\text{NO}_3)_2:(\text{NH}_4)_2[\text{WS}_4]$  molar ratio, e.g. from 1:2 to 2:1. In all cases, homogeneous solution being stable for hours was obtained. It is in sharp contrast to the bath composed of  $\text{Co}(\text{NO}_3)_2$  and  $(\text{NH}_4)_2[\text{MoS}_4]$  which quickly precipitates in few ten minutes time even with proper degas.

For the sake of simplicity, the full name of the deposition solution, which was  $[\text{Co}(\text{WS}_4)_2]^{2-}$  in 0.1 M KPi (pH 7) would be shortened to  $[\text{Co}(\text{WS}_4)_2]^{2-}/\text{KPi}$ . The molar ratio between  $\text{Co}(\text{NO}_3)_2$  and  $(\text{NH}_4)_2[\text{WS}_4]$ , unless otherwise noted, would be 1:1.

### 2.2. Electrochemical setup

A SP-300 potentiostat from BioLogic was employed in the conventional three-electrode mode for bulk electrochemical study of  $[\text{Co}(\text{WS}_4)_2]^{2-}$  solution as well as catalyst deposition and performance evaluation. Cleaned fluorine-doped tin oxide on glass substrate (FTO) was used as the working electrode. Thermal tape with a circular hole (6 mm diameter) was used to ensure that the working area of 0.24  $\text{cm}^2$  is consistent between samples. The counter electrode was a platinum wire, and the reference electrode was a silver/silver chloride in 3 M KCl. Thereafter, this electrode would be shortened to just Ag/AgCl for the sake of simplicity. The reference electrode was calibrated daily to obtain  $E_{\text{Ag}/\text{AgCl}}^0$  and all recorded potentials were accordingly converted to reversible hydrogen (RHE) electrode through **equation 19**.

$$E_{\text{RHE}} = E_{\text{Ag}/\text{AgCl}} + E_{\text{Ag}/\text{AgCl}}^0 + 0.059 \times pH \quad (\text{Eq.19})$$

Current density was deduced from geometrical surface area of the working electrode. A typical 25 mL glass vial was used to contain the electrolyte. **Figure 16** shows a schematic representation of the setup.



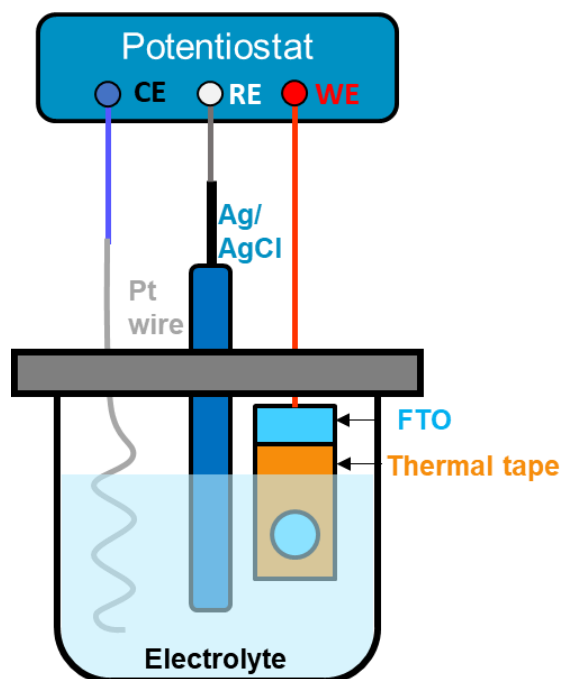


Figure 16: Schematic representation of conventional three-electrode electrochemical setup

The electrolyte level was adjusted to cover entirely the exposed circular area of the working electrode. The surface area of the counter electrode in contact with the electrolyte was also roughly adjusted to be larger than that of the working electrode to avoid possible electrical current bottle-neck.

Cyclic voltammetry (CV) was performed with potential scan rate of 10 mV/s starting from the open-circuit potential ( $E_{oc}$ ) to avoid undesirable electrical shock to the system. Linear sweep voltammetry was done with 2 mV/s scan rate and also started at  $E_{oc}$ .

### 3. Results and discussions

#### 3.1. Electrochemical property of $[\text{Co}(\text{WS}_4)_2]^{2-}/\text{KPi}$

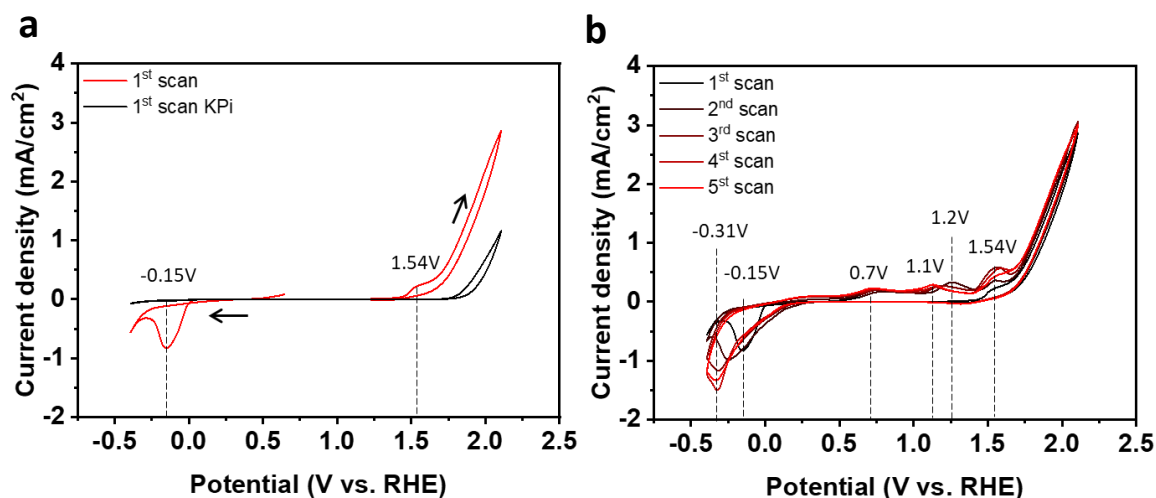


Figure 17: Survey anodic CV scans in  $[\text{Co}(\text{WS}_4)_2]^{2-}/\text{KPi}$  deposition solution

CV scans was conducted in  $[\text{Co}(\text{WS}_4)_2]^{2-}/\text{KPi}$  between -0.4 V and 2.1 V, starting from  $E_{oc}$  with anodic potential polarization direction to survey possible redox events in the solution (**Figure 17**). The first scan showed an oxidation event at 1.54 V previously being assignable to the oxidation of  $[\text{Co}(\text{WS}_4)_2]^{2-}$  precursor generating CoWO-OEC deposit,<sup>124</sup> prior to a catalytic wave at onset potential of 1.65 V being assignable to the catalytic water oxidation (**Figure 17a**, red trace). A reduction peak was observed at -0.15 V which was more cathodic than that reported for the reduction of  $[\text{Co}(\text{WS}_4)_2]^{2-}$  precursor generating CoWS-HEC layer (of 0.04 V vs. RHE)<sup>123</sup>. In subsequent potential scans, the current density of oxidation event at 1.54 V slightly increased, the reduction event at -0.15 V experienced a cathodic shift to -0.31 V together with the appearance of two new oxidation event at 0.7 and 1.1 V (**Figure 17b**).

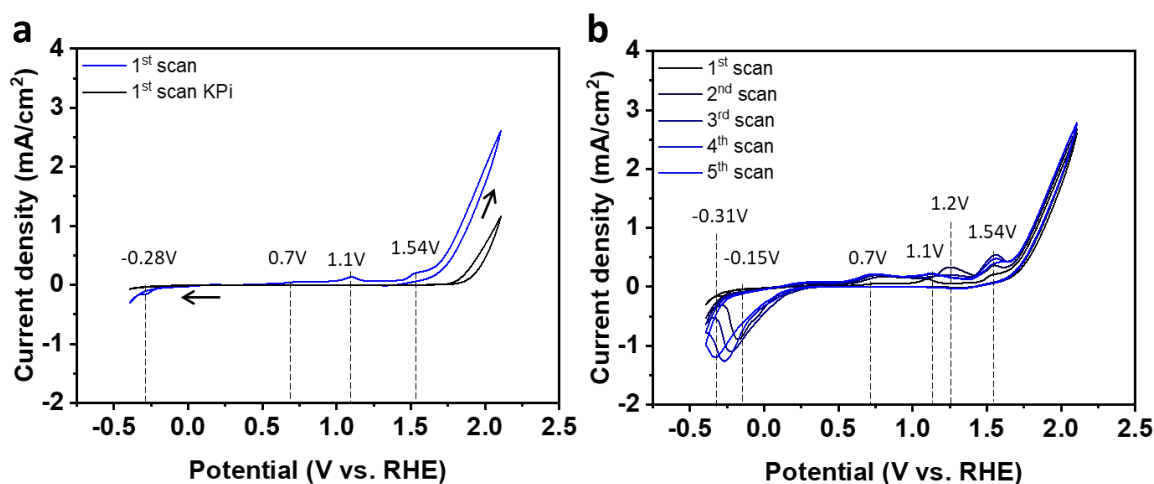


Figure 18: Survey cathodic CV scans in  $[\text{Co}(\text{WS}_4)_2]^{2-}/\text{KPi}$  deposition solution

Keeping the same potential window and starting from the same  $E_{oc}$ , but a potential polarization to the cathodic direction was conducted. In the first scan, the reduction event was observed at -0.28 V, being similar to that assigned to the reduction of  $[\text{Co}(\text{WS}_4)_2]^{2-}$  into CoWS deposit (**Figure 18**, blue trace).<sup>123</sup> Oxidation peaks were observed at 0.7, 1.1 and 1.54 V together with a catalytic peak at onset potential of 1.65 V vs. RHE. In subsequent scans, the reduction event experienced an anodic shift to -0.15 V (**Figure 18b**). Thus, we attribute the oxidation event at 1.54 V to the oxidation of  $[\text{Co}(\text{WS}_4)_2]^{2-}$  into CoWO deposit, and the reduction event at -0.28 V to the reduction of the same  $[\text{Co}(\text{WS}_4)_2]^{2-}$  into CoWS deposit on clean FTO electrode surface. The oxidation peaks at 0.7 and 1.1 V can be attributed to the oxidation of CoWS deposit readily grown on the FTO electrode. Whereas the reduction peak at -0.15 V can be attributed to the reduction of CoWO deposit readily grown or the reduction of  $[\text{Co}(\text{WS}_4)_2]^{2-}$  precursor onto a CoWO or CoWS surface that could be much favorable compared to the same reduction on a clean FTO surface.

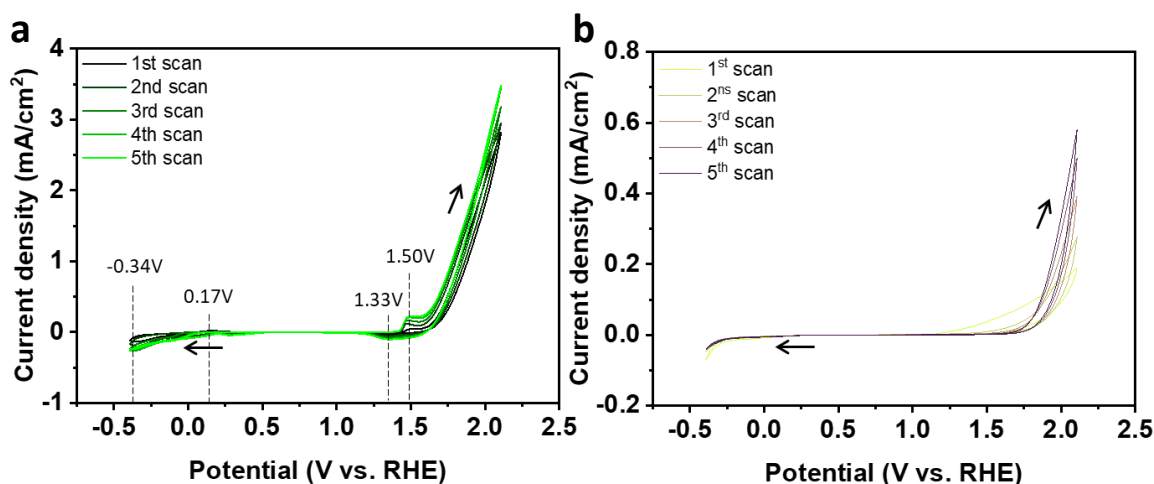


Figure 19: Survey anodic CV scans in  $\text{Co}(\text{NO}_3)_2/\text{KPi}$  (left) and  $(\text{WS}_4)^{2-}/\text{KPi}$  (right)

CV survey scans were also conducted for a 0.5 mM  $\text{Co}(\text{NO}_3)_2$  solution being free of  $(\text{NH}_4)_2[\text{WS}_4]$  as well as a 0.5 mM  $(\text{NH}_4)_2[\text{WS}_4]$  solution being free of  $\text{Co}(\text{NO}_3)_2$ , both in 0.1 M KPi (pH 7) buffer electrolyte. On FTO electrode, the  $\text{Co}(\text{NO}_3)_2$  showed an oxidation peak at 1.50 and a reduction peak at 1.33 V which can be assigned to the  $\text{Co}^{\text{III}}/\text{Co}^{\text{II}}$  redox couple<sup>107</sup> (**Figure 19a**). The catalytic water oxidation event was observed at onset potential of 1.65 V vs. RHE. No obvious events were observed in the cathodic potential range. There was, however, a possibility that a marginal amount of cobalt-based catalyst, named H2CoCat, with electrodeposition onset potential of -0.28 V vs. RHE was formed.<sup>125</sup> This could be the reason for the slight increment in anodic current density for subsequent scans near -0.5 V vs. RHE. Regarding the  $(\text{NH}_4)_2[\text{WS}_4]/\text{KPi}$  solution, no obvious redox events were observed, confirming its non-electrochemical active nature (**Figure 19b**).

Thus, the  $[\text{Co}(\text{WS}_4)_2]^{2-}/\text{KPi}$  solution possesses intrinsic electrochemical properties which are obviously different to a  $\text{Co}(\text{NO}_3)_2$  and a  $(\text{NH}_4)_2[\text{WS}_4]$  solutions. From the  $[\text{Co}(\text{WS}_4)_2]^{2-}/\text{KPi}$ , deposits can be obtained either at an appropriate anodic or cathodic potential. The deposits themselves are electrochemically active.

### 3.2. Deposition of catalysts

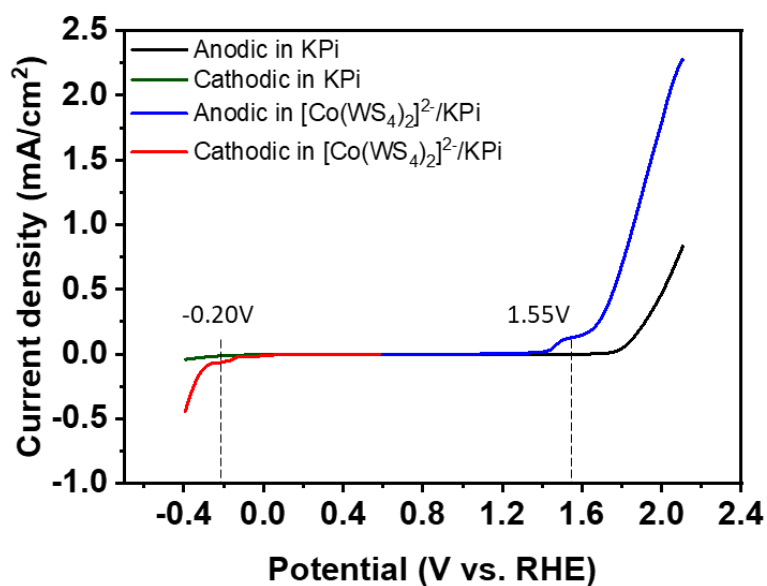


Figure 20: LSV scans in 0.5mM  $[\text{Co}(\text{WS}_4)_2]^{2-}/\text{KPi}$

LSV scans were then conducted with low potential scan rate of 2 mV/s in order to determine the onset potentials at which the electrodepositions of CoWS-HEC and CoWO-OEC started. The onset potential for deposition of CoWS-HEC and CoWO-OEC were determined to be -0.12 and 0.14 V vs. RHE (**Figure 20**). Indeed, holding the FTO electrode at -0.2 or at 1.55 V vs. RHE induced the deposition which were visible even with the naked eye after few minutes.

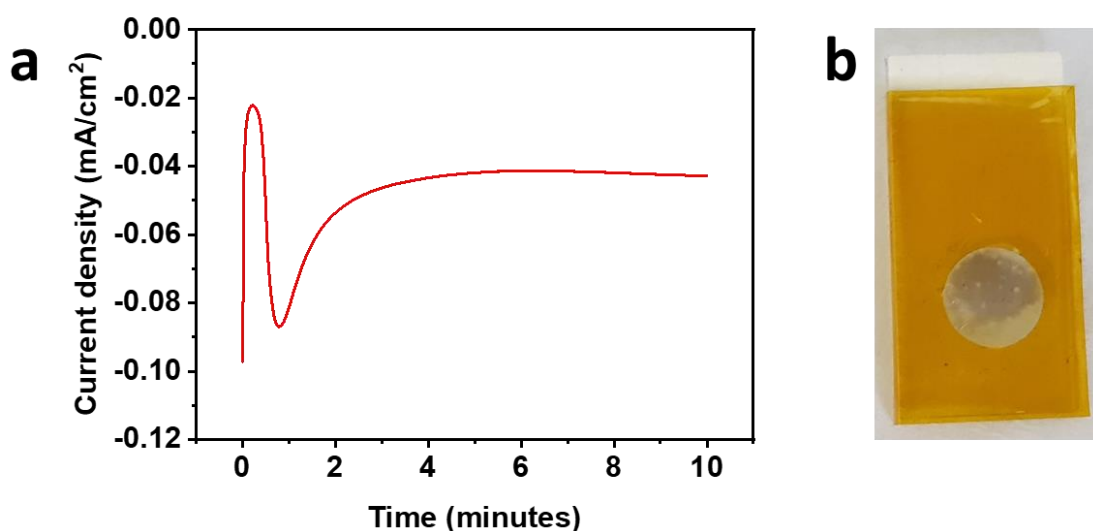


Figure 21: *j-t* plot at -0.2 V vs. RHE (a) and photo of the working electrode after 10 minutes (b)

Under -0.2 V vs. RHE, a  $j$ - $t$  plot was recorded with a distinctive dip at the 1-minute mark, which is characteristic for the nucleation step of a typical seed-growth mechanism (**Figure 21a**). After 10 minutes, an uneven light brown deposit layer was observed (**Figure 21b**) after having accumulated 28 mC/cm<sup>2</sup> worth of charges.

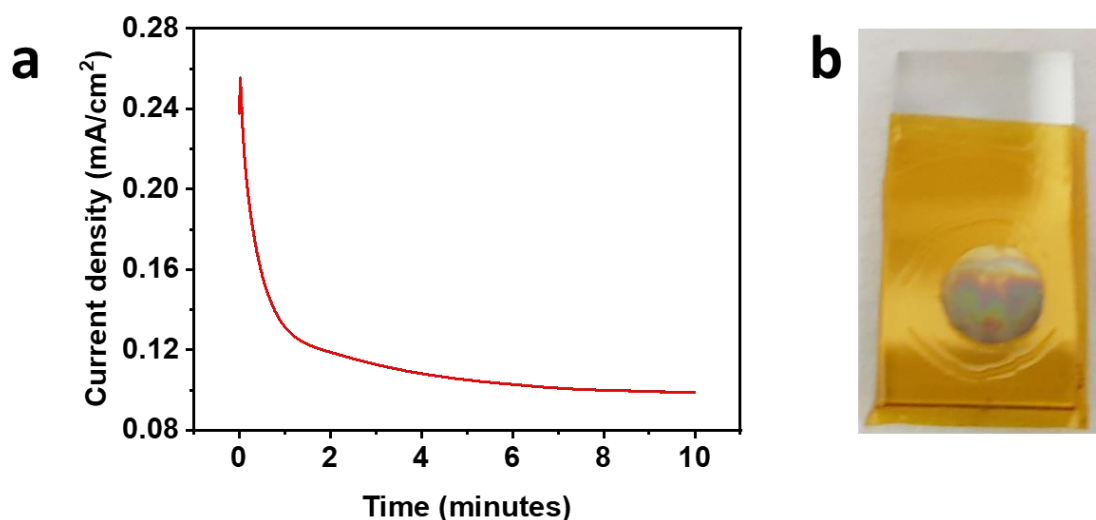


Figure 22:  $j$ - $t$  plot at 1.55 V vs. RHE (a) and photo of the working electrode after 10 minutes (b)

The  $j$ - $t$  plot acquired after holding the FTO at 1.55 V for 10 minutes (**Figure 22a**) showed a more straight-forward growth of a light-yellow layer (**Figure 22b**). When viewed at an angle, patches reflecting lights with different colors were observed, this could be the result of uneven thickness of the deposit. A total of 68 mC/cm<sup>2</sup> passed through the electrode during this time.

### 3.3. Performance verification of catalysts

The electrodes were retrieved, washed gently with a squirt bottle containing deionized (DI) water then dried under a stream of argon. Their electrochemical properties were then assayed in a 0.1 M KPi (pH 7) electrolyte solution being free of  $[\text{Co}(\text{WS}_4)_2]^{2-}$ ,  $\text{Co}^{2+}$  or  $[\text{WS}_4]^{2-}$  ion. The red trace in **Figure 23** shows the *current density vs. potential (j-E)* curve recorded for a CoWS-HEC film obtained after 10 minutes of electrodeposition. It shows a pre-catalytic peak at -0.03 V vs. RHE prior to the catalytic event at onset potential of -0.15 V vs. RHE. A catalytic current density of -1 mA/cm<sup>2</sup> was obtained at -0.40 V vs. RHE (**Figure 23**, red trace). Whereas the CoWO-OEC catalyzes the O<sub>2</sub> evolution at the onset potential of 1.55 V vs. RHE. It generates a catalytic current density of 1 mA/cm<sup>2</sup> at 1.80 V vs. RHE (**Figure 23**, blue trace). It is worth noting that activity assay on FTO was under mass-transport limitation, hence the current density recorded was much lower than that on rotating glassy carbon electrode in previous studies.<sup>123,124</sup> Apparently, the CoWO would express superior catalytic activity if it is assayed in an alkaline solution, e.g. higher catalytic current density at similar applied potential, as reported in previous work.<sup>124</sup>

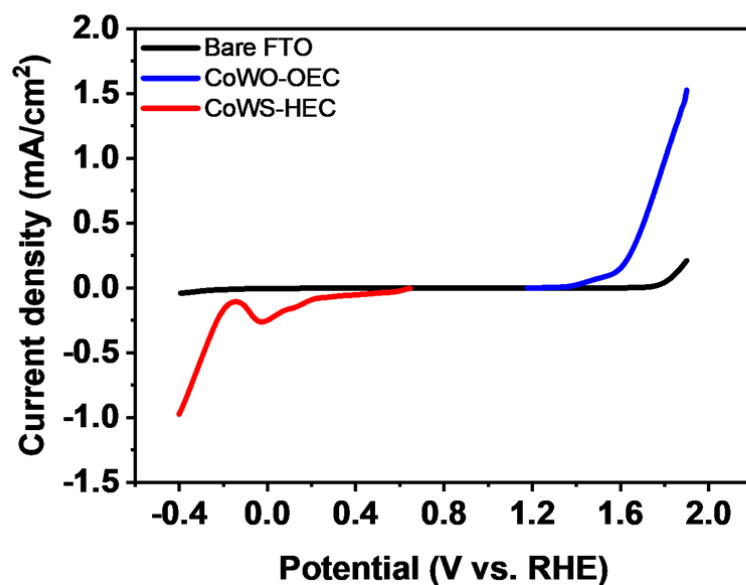


Figure 23: LSV scans for CoWS-HEC and CoWO-OEC in pure KPi 0.1 M (pH 7)

#### 4. Conclusions and perspectives

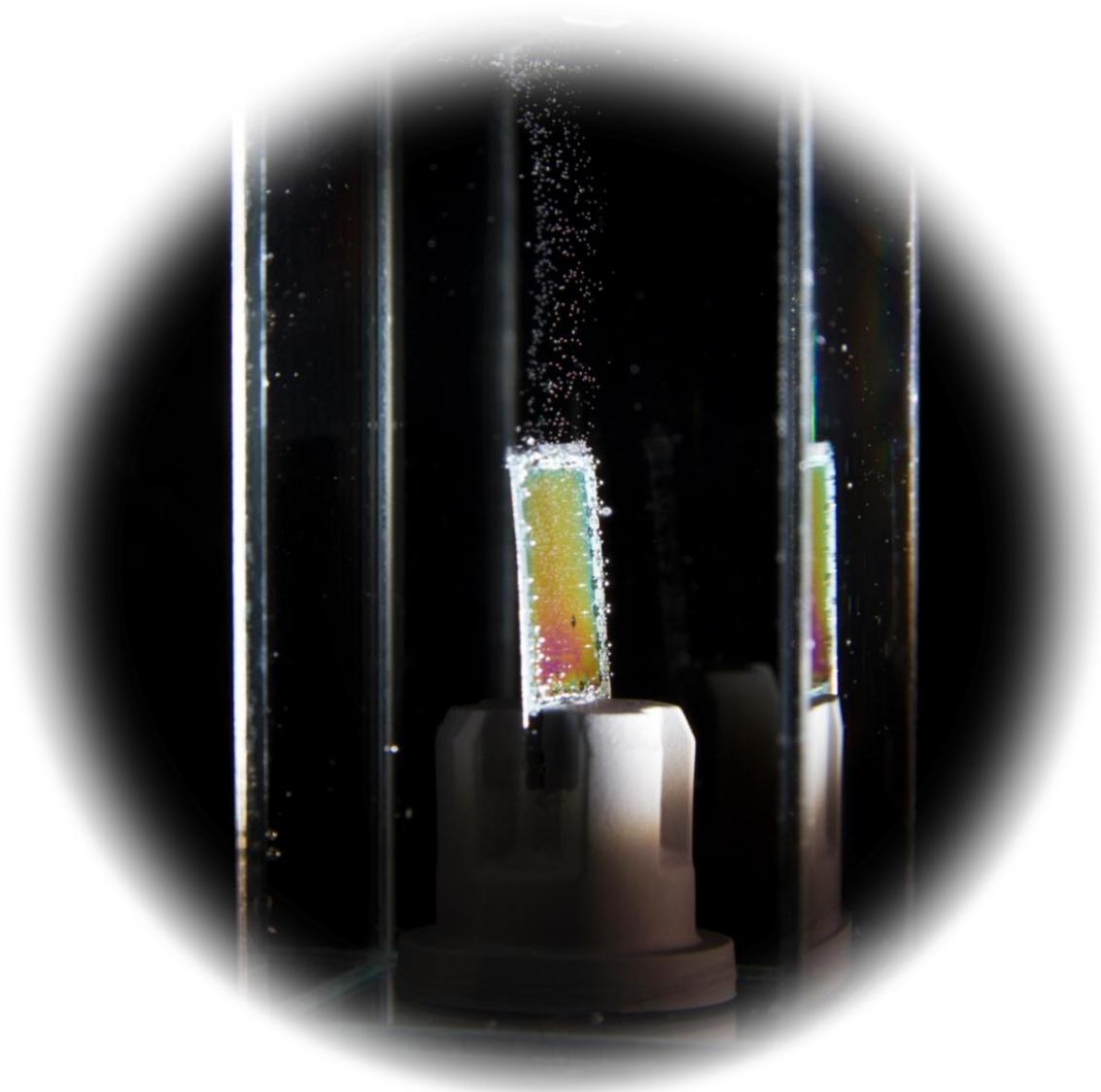
Through simple electrochemical assay and comparison to previous works from the group, it was shown that the reproduction of the two catalysts from a single solution was successful. Since the aforementioned catalysts were intensively investigated, further morphology and performance assay on FTO were omitted from this thesis in favor of integration into a solar fuel generator as well as device fabrication and evaluation.

Rather than chasing after high performance, this pair of catalysts was utilized as a proof-of-concept to a novel method to electrodeposit catalysts onto the surface of devices. It was shown in **Figure 20** that when a certain cathodic or anodic potential was applied to a conductive material submerged in the  $[\text{Co}(\text{WS}_4)_2]^{2-}/\text{KPi}$  solution, corresponding catalysts layers could be formed on its surface. With that said, it is reasonable to predict that when a PV device is capable of generating the required potentials, the catalysts will be readily and simultaneously electrodeposited, or in other words, self-assembled on its corresponding electrodes. This is a noteworthy advantage from the conventional electrodeposition which usually can only deposit one material on a substrate at a time. Moreover, when the potentials are supplied by the PV device, equipment such as potentiostat and specialized glassware are not required. With this concept, the benefits brought by the improved homogeneity and bonding quality to electrodes of electrodeposited catalysts can be achieved with reduced cost. In addition, such mild and non-invasive catalysts integration method is desirable for delicate substrate, as usually seen in thin film devices. The viability of this concept will be investigated in details in the next chapter.



## Chapter III

### The monolithic artificial leaf



## 1. Introduction

Recently, when the word “artificial leaf” is mentioned, it is almost certainly accompanied by the work of Daniel Nocera in 2012.<sup>67</sup> Belonging to the family of integrated PEC, this artificial leaf took great pride in its compactness in comparison to its inspiration, the traditional PV-electrolyzer system. Measured at a bit more than a hundred micrometers thick, yet the device boasted all the basic components required for a solar hydrogen generator to function in an aqueous environment. Therein, a commercialized triple-junction amorphous silicon solar cell (3jn-a-Si) from Xunlight Corp. was employed as the light harvester and different HEC and OEC were electrodeposited on its cathode and anode, respectively.

Apparatus utilizing similar structure had been previously demonstrated by G. H. Lin<sup>126</sup> and progressively investigated by E. L. Miller.<sup>127–130</sup> While their choice of amorphous triple silicon for the light harvesting unit is more cost effective than the highly active but less abundant gallium-based alternatives, the former employed precious metal oxides and the latter relied on sputtering to integrate the catalysts. Therefore, large scale production is challenging.

Aiming for decentralized energy generation and distribution, Nocera made modifications on these designs in a more cost-effective direction through employing more abundant elements and simpler engineering. It is perhaps the introduction of the newly developed earth abundant catalysts that gained the device its current fame. Indeed, the CoPi-OEC capable of self-healing during operation is undoubtedly valuable for device longevity.<sup>131</sup> The NiMoZn-HEC,<sup>67</sup> which improved on the powerful NiMo through the addition of Zn,<sup>132</sup> also contributed greatly to the overall activity and stability of the device. Through the relatively mild electrodeposition in ambient condition, the aforementioned catalysts were integrated on the surfaces of the solar cell. Given that the only element with questionable abundancy in the whole setup is germanium in the solar cell, and electrodeposition is friendly to surfaces with large areas, scaling up is indeed more feasible. The device implementation is also extremely straight-forward. Once put in a borate buffer at pH 9.2 under 1 Sun illumination, the device is capable of splitting water to generate bubbles of hydrogen and oxygen without any external bias.

In this chapter, we chose to employ this monolithic design along with our dual catalysts described from **chapter 2** and attempt on fabricating an artificial leaf with even lower engineering requirements. In addition, an experimentation setup was designed to assess the performance of the device in real-time by simultaneously monitoring various key operating parameters.

## 2. Artificial leaf fabrication

### 2.1. The triple-junction amorphous silicon (3jn-a-Si) solar cell

In 1961, William Shockley and Hans J. Queisser reported their calculation on the theoretical maximum solar energy conversion efficiency of 30% achievable for a single p-n junction made from semiconductor with 1.1 eV bandgap under unconcentrated light.<sup>133</sup> Later on, in 2016, the value was fine-tuned using more precise parameters to be 33.77% for device with 1.34 eV bandgap.<sup>134</sup> It is also worth mentioning that a semiconductor with a certain bandgap can only effectively capture photons with corresponding wavelength and energy. Indeed, the less energetic photons are ignored, while the ones with surplus energy loses the excess amount through phonon relaxation thermalization. Therefore, to achieve higher performance and optimal utilization of the solar spectrum, the incorporation of multiple semiconductors with varying bandgap is indispensable. It is generally expected that the more semiconductors are connected together, the higher efficiency can be reached. However, the theoretical upper limit was calculated to be 86.8% under concentrated sunlight, flawless engineering and perfect materials.<sup>135</sup> For instance, as recorded by the National Renewable Energy Laboratory,<sup>136</sup> the current highest cell efficiency of 47.1% was achieved using a six junctions device with III-V semiconductors under 143 suns illumination.<sup>137</sup> However, an optimum compromise is always more preferable for better financial incentive and sustainability.

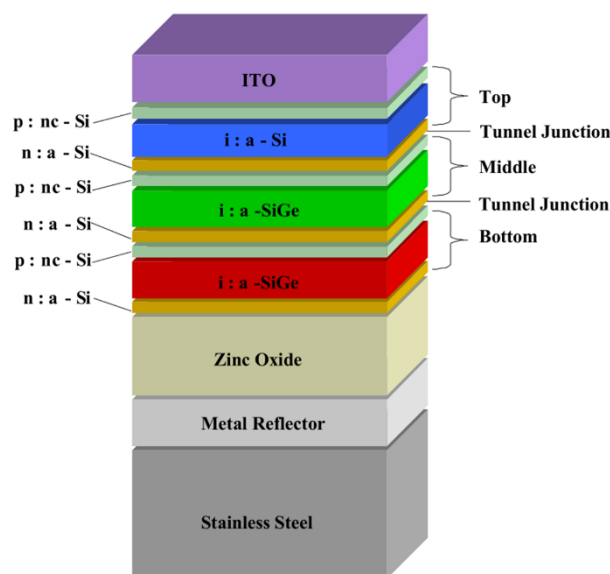


Figure 24: Structure of a 3jn-a-Si solar cell with the three p-i-n junctions (top, middle, bottom) separated by tunnel junctions, covered by transparent ITO and deposited onto a ZnO/metal reflector and supported by stainless-steel substrate <sup>138</sup>

The 3jn-a-Si (3jn: triple-junction, a-Si: amorphous silicon) solar cell represented an approach for such compromise. The detailed structure of the solar cell was demonstrated in a report from University of Toledo in 2005 (**Figure 24**).<sup>138</sup> The device came with a modest solar to electricity of only 7%.<sup>66</sup> Instead of the costlier III-V semiconductors like GaAs, silicon, being the second most abundant element in the Earth's crust, was used in this device. In addition, the amorphous structure in thin film configuration was chosen for more facile fabrication and less material consumption. Interestingly, the nature of the bandgap changed from indirect in the case of crystalline silicon to direct-like for the amorphous counterpart.<sup>139</sup>

However, it is well-known that the charge mobility is more impeded by amorphous silicon, especially when doped. Hence, instead of the traditional p-n junction, p-i-n junction (p: boron doped nano-crystalline silicon, i: intrinsic amorphous silicon and n: phosphorous doped amorphous silicon) was utilized. Indeed, when an intrinsic layer of the semiconductor was sandwiched between two doped ones, the charge depletion layer would be greatly enlarged, guiding the generated charges with more efficiency. This intrinsic layer also provided a larger absorption volume, helping the device capture more incoming irradiation, thus improving quantum efficiency.

The triple stacked p-i-n junctions generated 2.1 V under illumination, which is thermodynamically sufficient to supply the required overpotentials for many water electrolysis catalysts and thus to drive the overall water splitting. To achieve this, significant effort in engineering was mobilized. Firstly, the bandgap of the intrinsic amorphous silicon layers was fine-tuned through different degrees of germanium doping so that these layers can absorb the majority of the wavelength presented in the solar spectrum (**Figure 25**).<sup>67</sup> Although germanium is not considered as an abundant element, it is not rare. Furthermore, as it is used as a dopant, scalability should not be significantly affected. The sub-cells were then stacked with the one having the widest bandgap at the top with subsequent sub-cells in decreasing bandgap order.

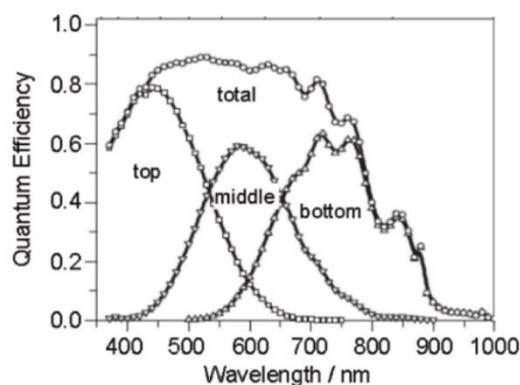


Figure 25: Absorption capability of the 3jn-a-Si<sup>67</sup>

Afterwards, to further facilitate light absorption, the encompassing p: nc – Si and n: a – Si doped layers were specially designed to be transparent to the wavelength that would be absorbed in their corresponding segments.

However, as the sub-cells were connected in series, current-matching is important so that none would become undesirable loads. To ensure that, the value of the semiconductor bandgaps and the thickness of the absorbing layers also need to be accordingly modified. To this end, precise thickness control as well as proper interfaces were provided through the employment of capacitively coupled plasma enhanced chemical vapor deposition (PECVD).

In addition, once the sub-cells were connected, the use of tunnel-junctions is also required to minimize electrical resistance. For this purpose, 1 nm thin interface layers of heavily p-doped (boron) and n-doped (phosphorous) silicon was deposited on the p:nc-Si and n:a-Si, respectively.<sup>138</sup> These layers helped ensure that the p-doped layer of the lower sub-cell cannot make a parasitic p-n junction with the n layer of the upper sub-cell. Indeed, the extremely thin depletion layer resulted from them allows electrons to tunnel through with relative ease.

As multiple junctions were used, the total distance that photo-generated charges need to travel in the bulk solid to get collected at a terminal becomes even more relevant. To this end, thinner semiconductor layers would facilitate charge collection at the cost of lower absorption volume. To address this, back-reflectors layers were utilized. The combination of sputtered zinc-oxide (ZnO) and sputtered metal (either Al or Ag) layers can bounce back unabsorbed photons, increasing the chance for them to be absorbed by the thinner semiconductors.<sup>139</sup>

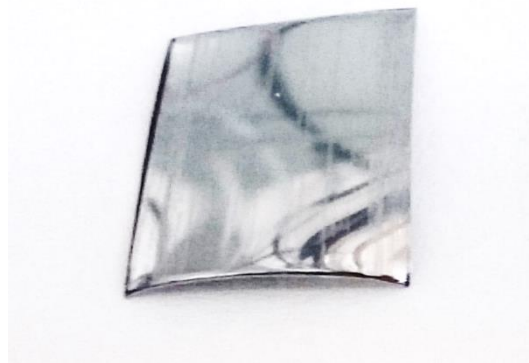
As the device was intended to be used in aqueous environment, corrosion of silicon is a major issue. Using magnetron sputtering, a layer of approximately 70 nm of ITO with sheet resistance of around 100-150  $\Omega$ <sup>139</sup> was deposited on the very top sub-cell as protection. Being inherently conductive and transparent to visible light, it can also act as an electrical terminal with minimal effect to the light absorption capability of the solar cell.

The whole assembly was deposited on a relatively flexible stainless-steel substrate for better mechanical stability. This layer also acts as the anodic terminal of the device. The final result was a super thin, moisture and corrosion resistant, all-solid triple junction amorphous silicon solar cell made chiefly from earth abundant elements that can potentially perform unassisted solar water splitting when incorporated with suitable catalysts.

## 2.2. Initial treatment for the 3jn-a-Si solar cell

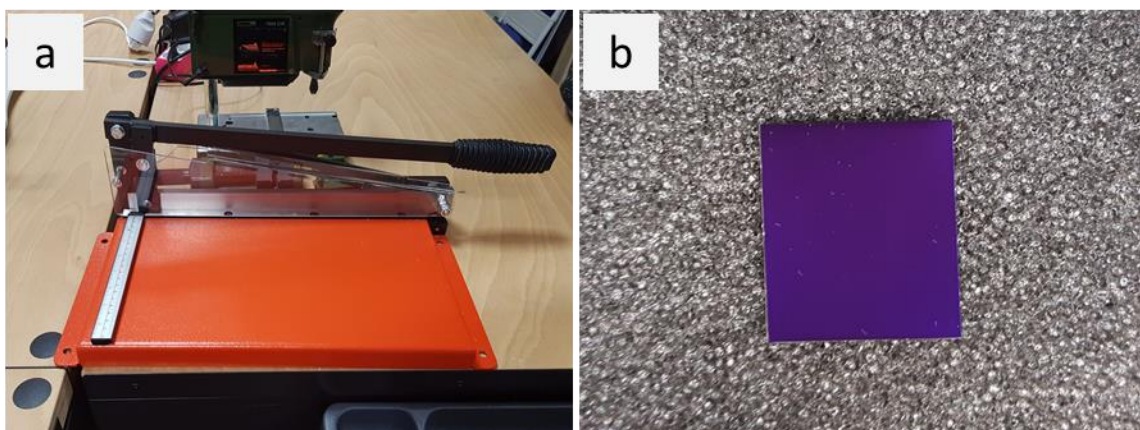
The same 3jn-a-Si solar cell from Xunlight corporation was utilized in this chapter. For practical purposes, 15 x 17 mm rectangular shaped pieces were cut from the originally received 300 x 400 mm sheet. Different cutting methods available within the institution were employed. The foremost accessible tool is a simple scissors.

Indeed, the thin stainless-steel substrate of the 3jn-a-Si solar cell was easily severed even with a typical art scissors. However, upon closer inspection, the edges of the solar cell were inelastically curved with the combined movement of the two blades of the scissors. For some samples, the bend was observed to extend a few millimeters deep to the center of the piece (**Figure 26**). Although the solar cell was advertised to be relatively flexible, permanent deformation caused by exceeding the elasticity threshold of the stainless-steel support would undoubtedly be detrimental to the micrometer-thin triple-junction layer deposited on it.



*Figure 26: Irreversible bending of the solar cell cut by typical scissors. The stainless-steel surface was shown to emphasize the affected area*

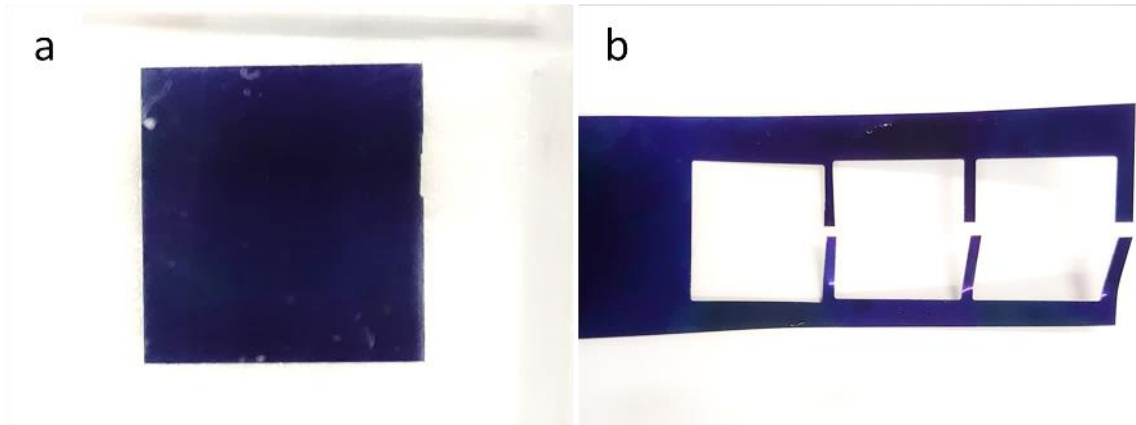
Next, a conventional table-top metal shear was employed, resulting in remarkable cutting quality and no significant bending of the edges (**Figure 27**).



*Figure 27: Metal shear (a) and the resulted cut of the 3jn-a-Si solar cell (b)*

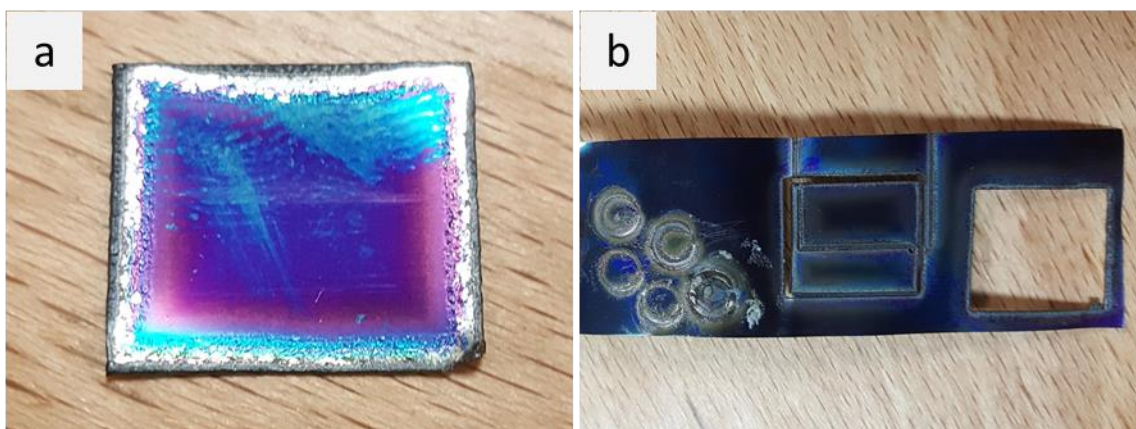


Heavy duty wire-cutting was also assayed. The quality of the cut is stellar with no bending of the resulted piece. However, as the bigger sheet needed to be clamped to the holder, a large portion of the 3jn-a-Si was badly scratched and thus no longer usable. The occasional error as can be observed from the right edge in **Figure 28a** happened with no negative effect to the piece. However, the entire amount of the left-over 3jn-a-Si solar cell shown in **Figure 28b** was unsalvageable, resulting in significant wastage.



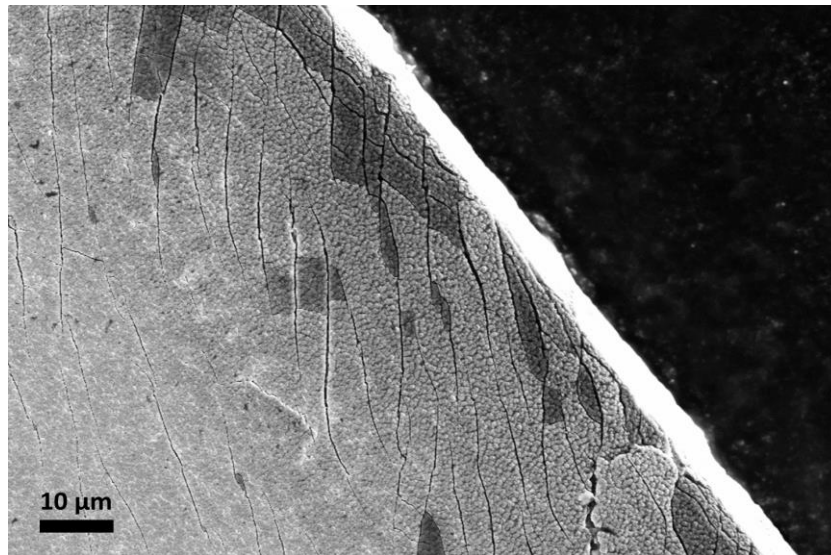
*Figure 28: Resulted 3jn-a-Si solar cell by wire-cutting (a) and the remaining waste (b)*

Lastly, laser cutting was used. The result was undesirable since the high temperature generated by the laser melted the steel substrate and damaged the 3jn-a-Si beyond recovery. Different speed, cutting shape and laser power were experimented with no perceivable improvement (**Figure 29**).



*Figure 29: resulted 3jn-a-Si solar cell by laser cutting (a) and attempts with varying parameters (b)*

In the end, the metal shear was determined to be the optimum choice for cutting the 3jn-a-Si solar cell, providing a desirable compromise between speed, quality and wastage. However, as with any mechanical shearing processes, local stress to the surrounding materials cannot be avoided, only minimized. Hence, closer inspection using scanning electron microscopy (SEM) was employed (**Figure 30**). Indeed, cracks were observed near the edge of the obtained triple-junction layer extending to around 100 micrometers to the center of the piece. The various darker areas caused by charging effect indicated that the stress has caused those layers to delaminate from the underlying support. These areas would result in moisture uptake or electric shorts during operation, possibly decreasing or fully suppressing the performance of the device.



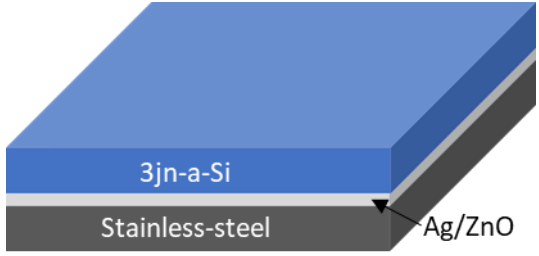

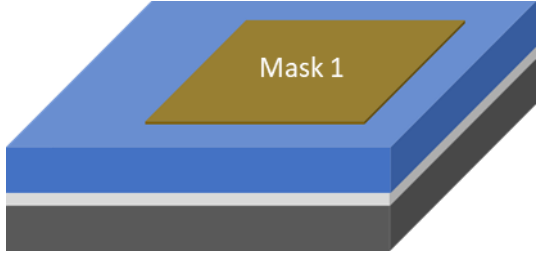

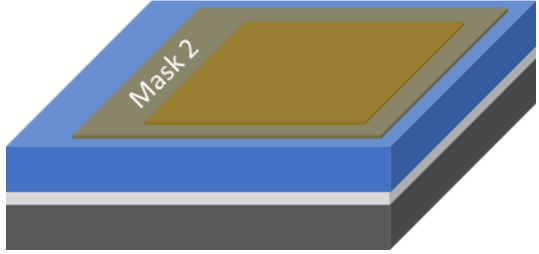
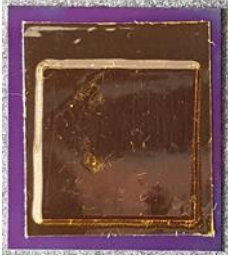
*Figure 30: SEM image showing the edge of the 3jn-a-Si solar cell cut by the metal shear*

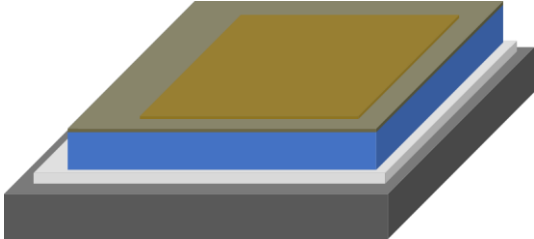
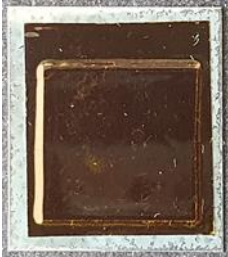
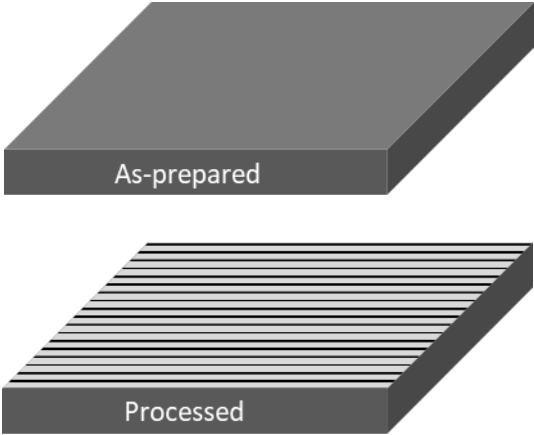

Therefore, to ensure the proper performance of the solar cell, one millimeter of the 3jn-a-Si from the edge of the piece would be removed by controlled etching using 1 M hydrochloric acid. However, as the top ITO layer can only protect the device from above, the vertical stack of various layers remained exposed to the environment after the etching process. Thus, proper protection should be implemented to improve the stability of the device.

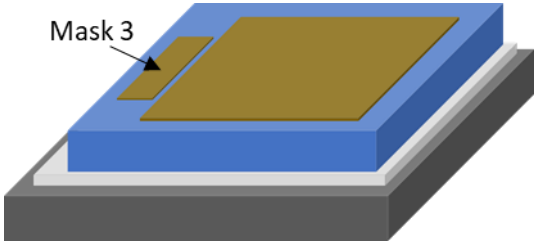
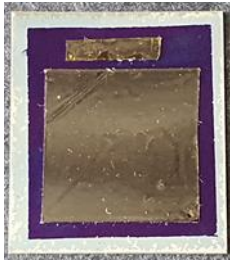
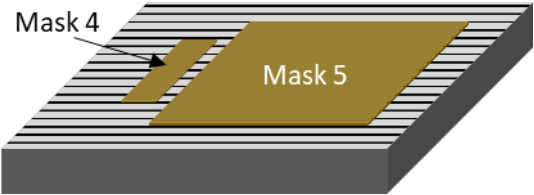

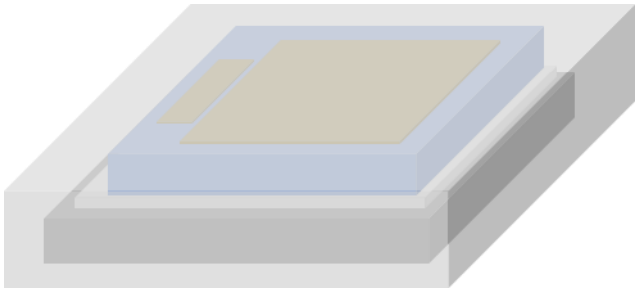

Herein, we devised a basic initial treatment protocol for the 3jn-a-Si solar cell prior to further experimentation using readily available materials and chemicals (see **Table 1**). This protocol can simultaneously provide a protective layer to components that are vulnerable to exposure to the environment, and improve the consistency between measurements through controlled limitation of working areas of the devices. Suitable openings for subsequent investigations were also included.

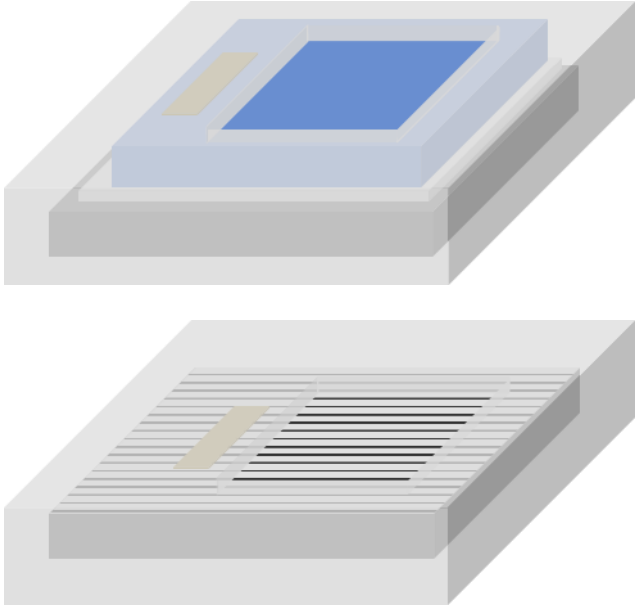
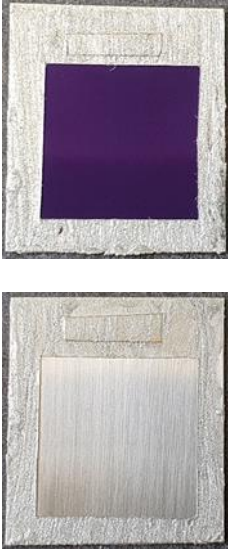


Table 1: Initial treatment protocol for the 3jn-a-Si solar cell

Step	Description	Schematic representation	Photo
1	A 15 x 17 mm piece of the 3jn-a-Si solar cell was cut with the metal shear.		
2	A 10 x 10 mm piece of thermal tape (mask 1) was put on the top surface as template for the anodic working area.		
3	A 12 x 15 mm piece of thermal tape (mask 2) was put on top and covered all the edges of mask 1 to determine the etching area.		

4	<p>The exposed 3jn-a-Si area was etched with a conventional cotton swab soaked in HCl 1M. Total etching time was approximately 10 minutes. The piece was washed with DI water and dried on a paper towel.</p>	 <p>A 3D schematic diagram showing a layered substrate. It consists of a grey base layer, a white middle layer, and a blue top layer. A central square area on the top surface is highlighted in a darker blue/grey color, representing the 3jn-a-Si area to be etched.</p>	 <p>A photograph of a square substrate with a dark, possibly etched, central square area. The substrate is mounted on a light-colored frame.</p>
5	<p>The stainless-steel surface was scratched with store-bought sandpaper of 600 or 1200 grit to improve the adherence of the catalyst. The surface was then wiped clean with a cotton swab and DI water to remove possible metal flakes.</p>	 <p>A 3D schematic diagram comparing two stainless steel surfaces. The top surface is labeled 'As-prepared' and is smooth. The bottom surface is labeled 'Processed' and shows a series of parallel horizontal lines, representing the surface after being scratched with sandpaper.</p>	 <p>Two photographs of stainless steel surfaces. The top photograph shows a smooth, reflective surface. The bottom photograph shows a surface with fine, parallel scratches, representing the 'Processed' state.</p>

6	<p>Mask 2 was removed. The piece was washed under a gentle stream of DI water and EtOH to remove possible contaminants then dried with compressed air. Optionally, mask 3 could be put in place to allow electrical contact for subsequent device investigations.</p>	 <p>A 3D schematic showing a blue rectangular mask (Mask 3) placed on a grey substrate. The mask covers a central area, leaving a smaller rectangular opening on the left side.</p>	 <p>A photograph of the physical Mask 3, which is a blue rectangular frame with a central opening, mounted on a grey substrate.</p>
7	<p>Similarly, mask 4 and mask 5 with the same size as mask 3 and mask 1, respectively, were placed on the processed stainless-steel surface to limit the cathodic working area to 1 cm<sup>2</sup> and establish future electrical contact.</p>	 <p>A 3D schematic showing two masks on a grey substrate. Mask 4 is a small rectangular mask on the left, and Mask 5 is a larger rectangular mask on the right. Both masks are yellowish-brown.</p>	 <p>A photograph of the physical masks. Mask 4 is a small yellowish-brown rectangle, and Mask 5 is a larger yellowish-brown rectangle, both on a grey substrate.</p>
8	<p>Conventional acrylic paint or steel paint was used to cover the entire solar cell.</p>	 <p>A 3D schematic showing a grey substrate with a blue rectangular area in the center. A layer of grey paint is being applied over the entire surface, including the blue area.</p>	 <p>A photograph showing two views of a solar cell. The left view shows the front of the cell, which is covered in a thick, textured grey paint. The right view shows the back of the cell, also covered in the same grey paint.</p>

9	<p>Mask 1 and mask 5 were removed to reveal the final working area. The piece was then washed gently under a stream of DI water, EtOH and dried with compressed air before use. Mask 3 and mask 4 will only be removed if electrical contacts are required for future (photo)electrochemical processes.</p>		
---	---	--	---

## 2.3. Compatibility of the 3jn-a-Si solar cell with the dual catalysts

### 2.3.1. Assaying the performance of the 3jn-a-Si solar cell

We first assayed the light harvesting capability of the treated 3jn-a-Si solar cell. **Figure 31** shows the schematic representation of the setup. The potentiostat was utilized in two-electrode configuration, i.e. the plugs for reference electrode and counter electrode were connected together. Steel wires secured by small pieces of conducting carbon tape were used to make electrical contacts to the stainless-steel and the ITO surfaces. The conductivity was further enhanced by a commercial gallium-indium eutectic.

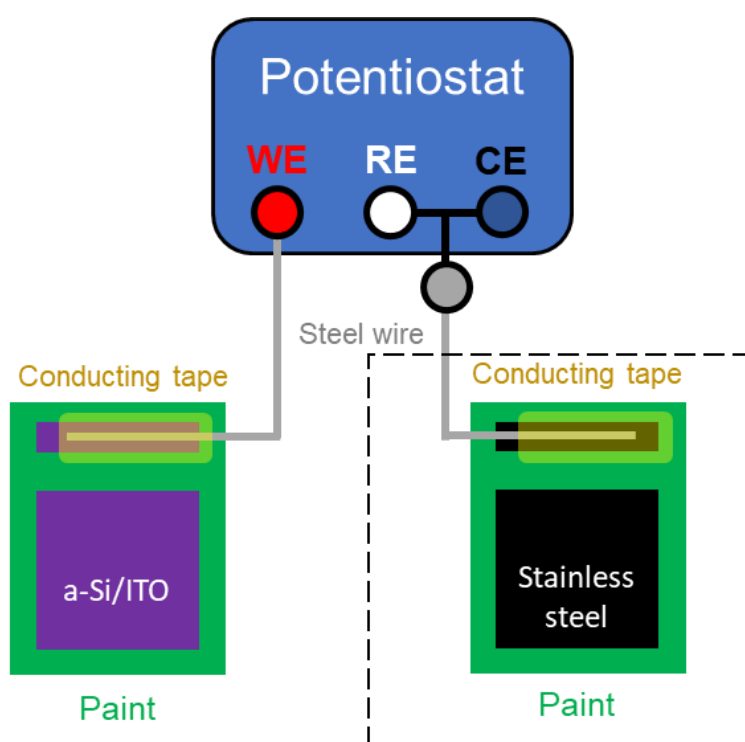


Figure 31: Setup for investigating the dry performance of a piece of 3jn-a-Si solar cell

### Typical performance assay through $j$ - $V$ plot

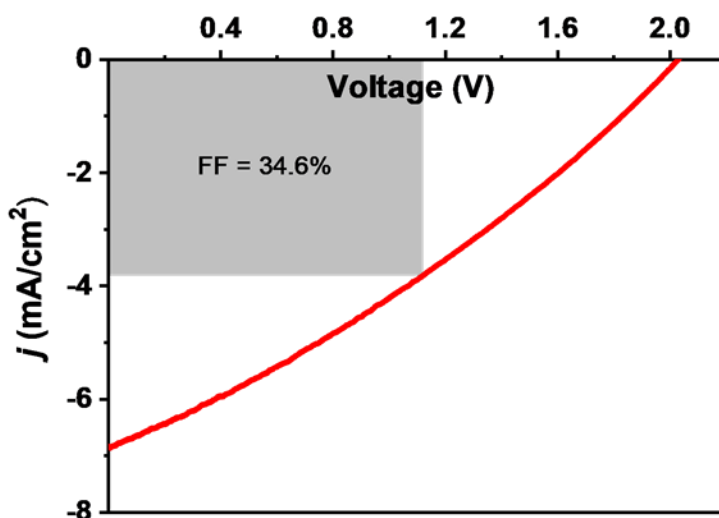


Figure 32: Current density versus voltage of a processed 3jn-a-Si solar cell

A typical *current density vs. photovoltage* ( $j$ - $V$ ) plot can be obtained with either a linear sweep voltammetry scan or the dedicated preset in the EC-Lab software as the settings were similar. A voltage sweep began from 0 V vs. ref to the open-circuit voltage ( $V_{oc}$ ) was conducted at 100 mV/s scan rate while the 3jn-a-Si solar cell was illuminated with 1 sun light (AM1.5G, 100mW/cm<sup>2</sup>) from a Xenon lamp. The resultant  $j$ - $V$  curve was shown in **Figure 32**. The  $V_{oc}$  was recorded at 2.02 V, which was slightly lower than the reported 2.32 V in the technical specification from the manufacturer. Similarly, the short circuit current density ( $j_{sc}$ ) was also inferior, e.g. 6.83 versus 7.56 mA/cm<sup>2</sup> as indicated in the technical specification. In addition, the fill factor was calculated to be only 34.6% compared to the reported value of 67.2%<sup>140</sup> which indicated a sub-optimal device. Indeed, the profile of the scan resembled that of a solar cell affected by electrical shunts in the bulk solid reported by Xunlight. Therefore, the shunt-passivation procedure proposed by Xunlight was followed in an attempt to improve the performance of the solar cell (**Figure 33**). The process involved photo-assisted selective electroreduction of the uppermost ITO layer to its insulating form. Thanks to this, the shunts would effectively be disconnected from the rest of the solar cell.<sup>139</sup> Indeed, under illumination, the shunt-free areas readily produced 2.1 V of photovoltage that opposed the applied reductive bias. Thus, unwanted conversion of ITO in these areas was limited or prevented. On the other hand, the shunted areas, unable to provide sufficient photovoltage to resist, were subjected to this reduction at a higher rate.

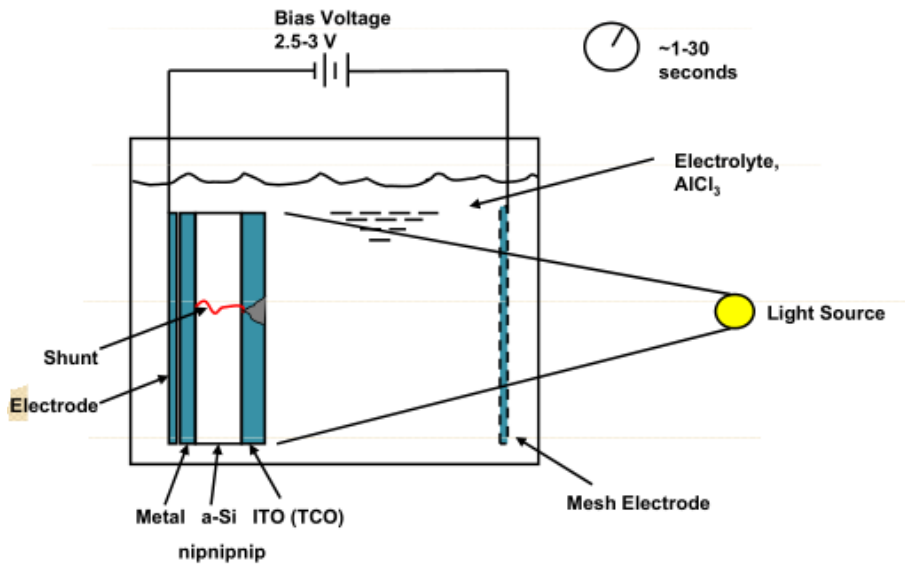


Figure 33: Shunt-passivation process for the 3jn-a-Si solar cell proposed by Xunlight <sup>139</sup>

In our attempt, a potentiostat in two electrodes mode was utilized. The working electrode was a 3jn-a-Si solar cell with electrical contact on the back stainless-steel surface. This connection was protected from the electrolyte by thermal tape. The counter electrode was a platinum wire. The electrolyte was constituted of 0.1 M  $\text{AlCl}_3$  solution in water. Chronoamperometry was employed to hold the solar cell at -2 V versus the counter electrode for 30 seconds. During this test, a small current density in the range of  $1 \mu\text{A}/\text{cm}^2$  was recorded. Afterwards, the  $j$ -V characteristic plot was recorded. However, negligible improvement was obtained.

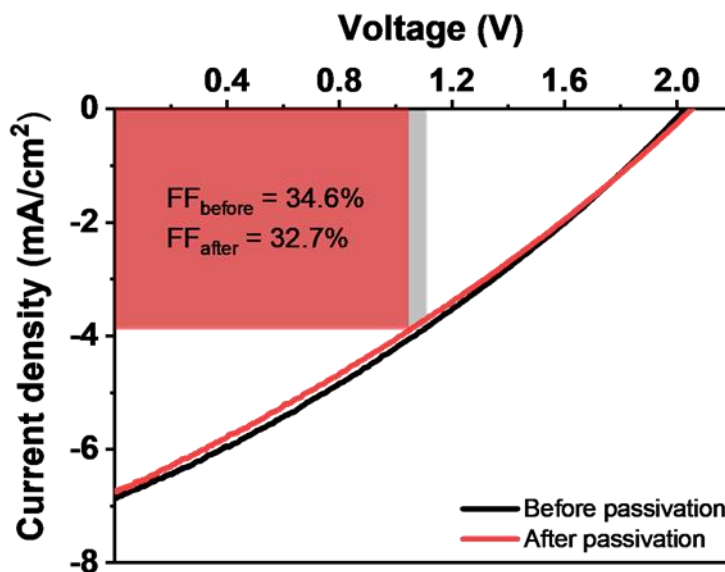


Figure 34: Current density versus voltage of a 3jn-a-Si solar cell and effect of shunt passivation

The shunt passivation process resulted in a slight improvement of  $V_{oc}$  from 2.02 V to 2.05 V at the cost of 1.9% fill factor (**Figure 34**). The procedure was repeated several times on the same piece of solar cell as well as freshly prepared ones with similar result. Nevertheless, it is worth noting that even though the fill factor was significantly inferior, the 3jn-a-Si solar cell delivered a photovoltage in the expected range of more than 2 V. This value was also significantly higher than the approximately 1 V of photovoltage typically reported for the shunted samples.<sup>139</sup> Therefore, it is possible that the shunt passivation was already performed by the manufacturer before shipment, and the  $j$ - $V$  characteristic plot recorded in **Figure 34** was due to the inherent nature of the sheet of 3jn-a-Si solar cell received. Unfortunately, additional samples were difficult to acquire from the manufacturer. Thus, it is decided that the available 3jn-a-Si solar cell samples would be used as received without performing further shunt passivation.

#### *Stability of the photovoltage when exposing the 3jn-a-Si solar cell in air*

Through the  $j$ - $V$  characteristic plot, the  $V_{oc}$  of the 3jn-a-Si solar cell was determined to be slightly more than 2 V. However, the inferior crystallinity of amorphous silicon could negatively affect the long-term stability of the solar cell, especially under elevated temperature caused by prolonged illumination. Therefore, employing the same setup illustrated in **Figure 31**, chronopotentiometry (CP) mode was utilized. Holding the 3jn-a-Si solar cell at 0 mA/cm<sup>2</sup>, the  $V_{oc}$  was thus continuously recorded under 1 Sun illumination over the period of 6 hours. After 3 hours, the  $V_{oc}$  slightly dropped from 2.02 V to 1.96 V (**Figure 35**). Afterward, a chop light mode was performed where the shutter of the Xe lamp was periodically closed and reopened. Even after 6 cycles, the photovoltage recorded was stable. After 6 hours, the photovoltage dropped to 1.93 V, resulted in a total performance drop of 4.4%.

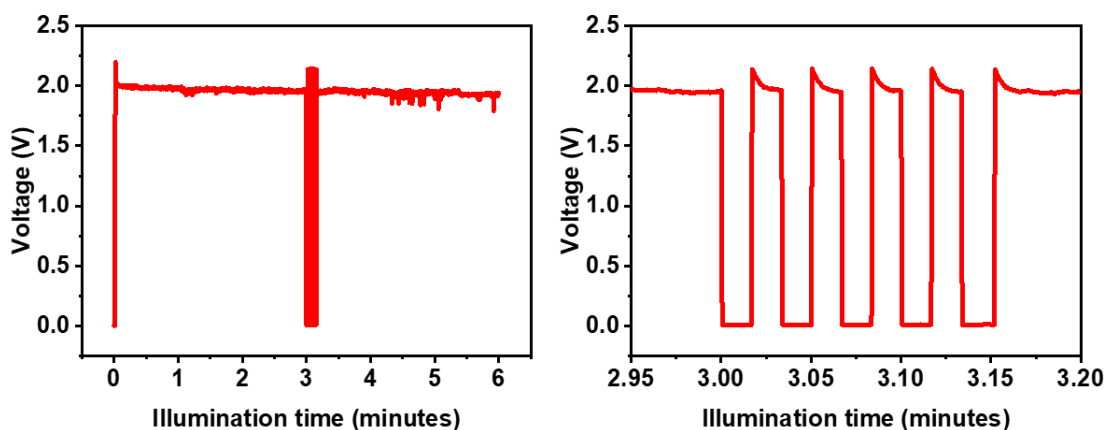


Figure 35:  $V$ - $t$  plot for a dry 3jn-a-Si (left) and chop light test (right)



### 2.3.2. Photo-potential provided by the 3jn-a-Si solar cell to electrodes in contact with electrolyte

When coupled with electrolyzer-equivalent components, the 3jn-a-Si solar cell is considered to be under load. The combined resistance from the electrolyte and various solid-electrolyte Helmholtz layers would result in a net reduction of generated photovoltage. Therefore, reevaluation of the photovoltage is desirable. Interestingly, the introduction of an electrolyte allowed the usage of a reference electrode. This addition would facilitate a precise measurement of photogenerated potentials, thus providing a more detailed perspective to the functioning mechanisms of the whole assembly.

A potentiostat in two-electrode configuration was utilized in the dedicated open-circuit-voltage (OCV) method. In this configuration, the potentiostat functions similarly to an ideal voltmeter (iVM) with infinite resistance. The two terminals of the 3jn-a-Si solar cell were respectively wired to two pieces of FTO glass by steel wire. Thermal tape with a 6 mm diameter circular hole was used to limit the area of FTO in contact with the 0.1 M phosphate buffer (pH 7) electrolyte. This thermal tape also acted as a protective layer for the electrical contact between the steel wire and the FTO from the electrolyte. The basic setup can be found in **Figure 36**.

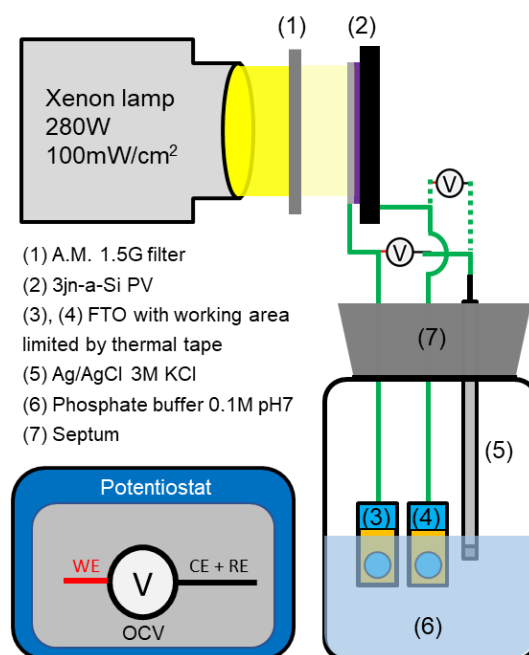
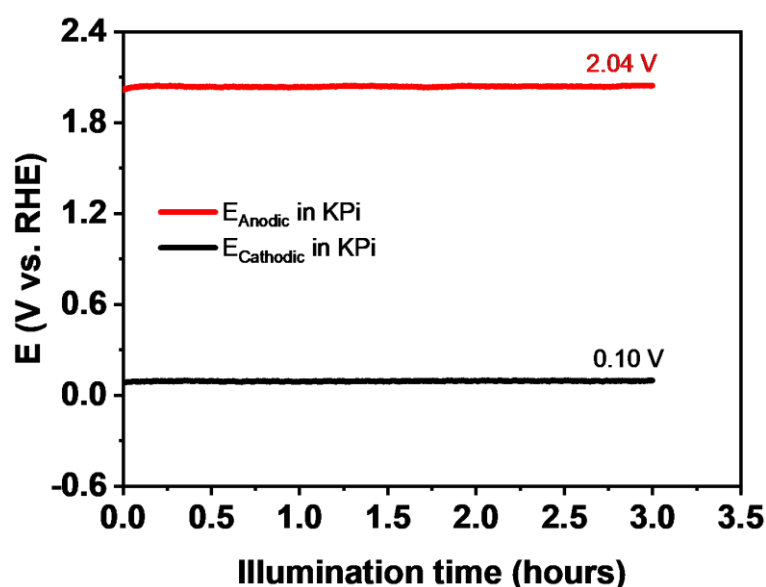


Figure 36: Schematic representation of the photoelectrochemical setup to determine the photo-potentials provided by the 3jn-a-Si solar cell

In essence, the photo-potentials versus the Ag/AgCl reference electrode at the anodic and cathodic terminals of the 3jn-a-Si solar cell under 1 Sun illumination would be measured. These values would later be converted to the RHE scale for easier comparison with the desired electrochemical processes. Two separated measurements were performed, where the terminals would take turn being the working electrode, while the Ag/AgCl acted as both reference and counter electrode. After each measurement, the FTO electrodes were replaced by freshly prepared ones. The combined result was presented in **Figure 37**.



*Figure 37: Photo-potentials provided by the terminals of the 3jn-a-Si solar cell under 1 Sun illumination in 0.1 M KPi (pH 7)*

Under 1 Sun illumination, the potential of the anodic terminal of the 3jn-a-Si solar cell was recorded at 2.04 V vs. RHE while the cathodic terminal was at 0.10 V vs. RHE. Thus, in total, the solar cell generated 1.94 V worth of photovoltage, representing a drop of 5% in compared to the photovoltage achieved in the conventional solar cell configuration (see **section 2.3.1**). Over the course of 3 hours, no significant changes in photo-potentials were recorded.

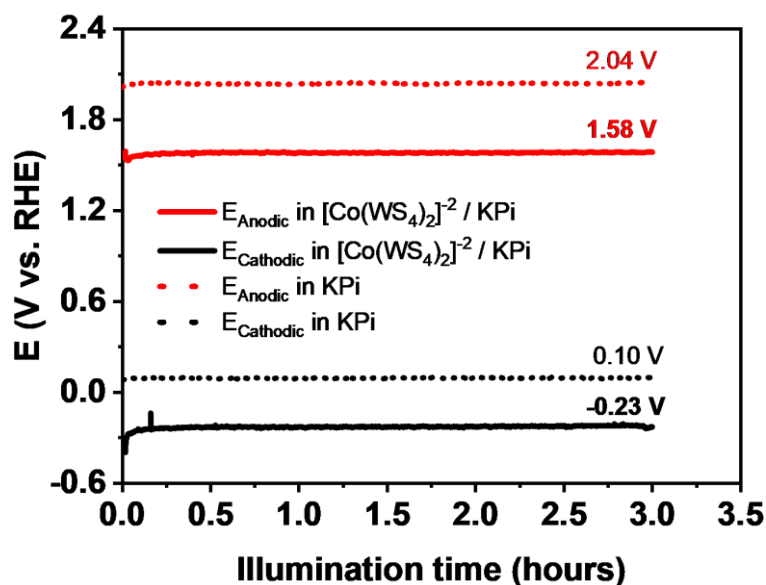


Figure 38: Photo-potentials provided by the terminals of the 3jn-a-Si under 1 Sun illumination in 0.5 mM  $[\text{Co}(\text{WS}_4)_2]^{2-}$  in 0.1 M KPi (pH 7)

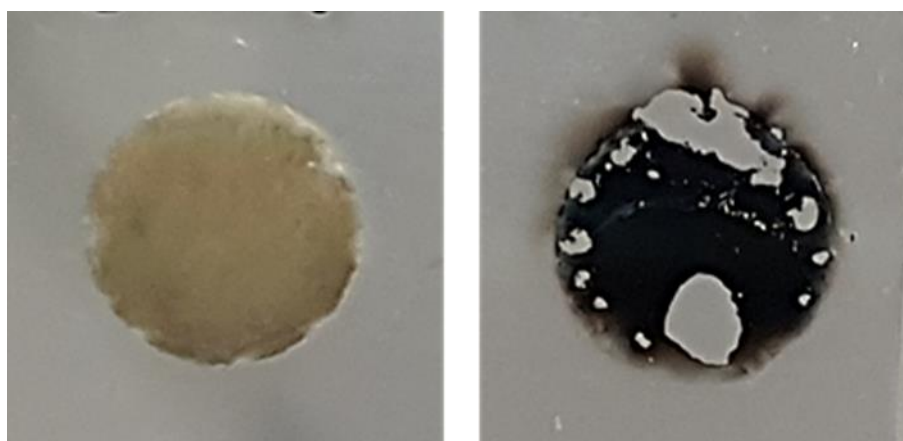
We repeated the measurement but immersing the two FTO electrodes in a 0.5 mM solution of  $[\text{Co}(\text{WS}_4)_2]^{2-}$  in 0.1 M KPi (pH 7). Stable anodic potential and cathodic potential of 1.58 and -0.23 V vs. RHE were recorded (**Figure 38**). The change at anodic and cathodic potential can be explained due to the change of chemical potential of the electrolyte that altered the equilibrium at FTO/electrolyte interface. The combined voltage of 1.81 V was recorded in this case, representing a drop of 100 mV in compared to that recorded with a blank KPi electrolyte. Indeed, in addition to the combined voltage staying in the expected range, the potentials provided by the two terminals of the 3jn-a-Si solar cell perfectly aligned with the deposition potentials of the dual catalysts, namely the CoWS catalyst for the  $\text{H}_2$  evolution and the CoWO for the  $\text{O}_2$  evolution (See **Chapter 2**).

We noted that during 3 hours of measurement using the  $[\text{Co}(\text{WS}_4)_2]^{2-}$  electrolyte solution, the color of the exposed FTOs changed and bubbles were also seen evolving from their surfaces (**Figure 39**). Single injection of the gas mixture into a Perkin-Elmer Clarus 580 gas chromatograph confirmed the presence of  $\text{H}_2$  and  $\text{O}_2$ , indicating the simultaneous deposition and operation of the catalysts.



*Figure 39: Simultaneous deposition and operation of the dual catalysts by a 3jn-a-Si under illumination*

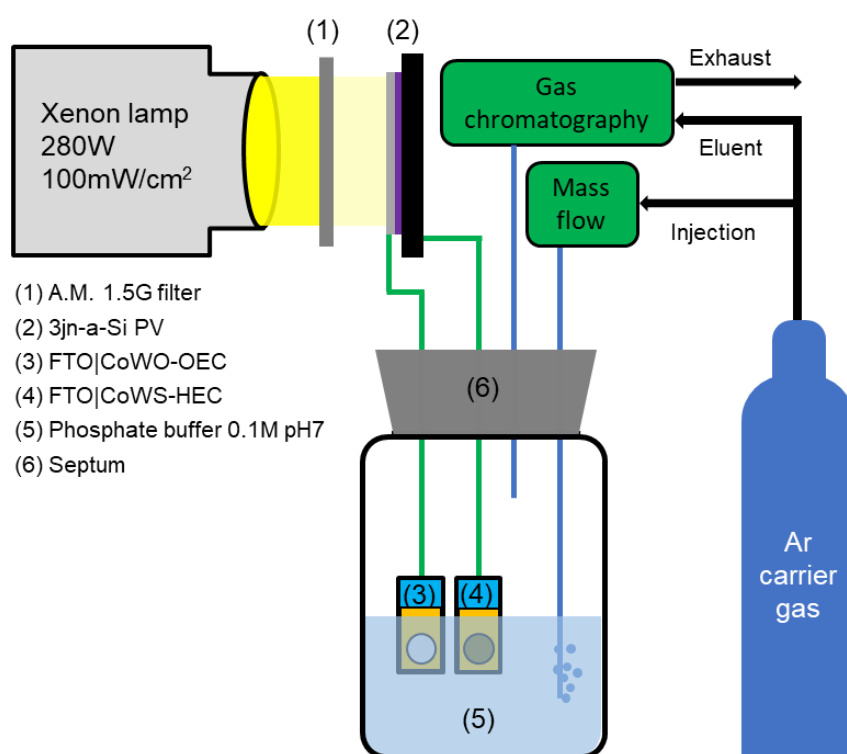
The FTOs were then retrieved from the solution, washed gently under a stream of DI water then dried under a stream of argon. The masking thermal tapes were removed and depositions were clearly observed on the exposed surfaces (**Figure 40**). The FTO connected to the anodic terminal of the 3jn-a-Si solar cell yielded a yellow deposit that turned light brown while the one wired to the cathodic terminal hosted a brown turned dark brown layer. The general colors of these layers were identical to that of the electrodeposited CoWO and CoWS layers in Error! Reference source not found. and Error! Reference source not found. in **chapter 2**, albeit being more vivid and uniform due to longer deposition duration. Some areas of the dark brown layer detached from the FTO surface. Upon closer inspection, the location of those areas matched perfectly to the positions where bubbles were formed in **Figure 39**. Therefore, the reason for this detachment was speculated to be the combined effect from elevated thickness of the deposited catalyst and gas bubbles formation.



*Figure 40: Deposits observed on the FTO wired to the anodic (left) and cathodic (right) terminals of the 3jn-a-Si solar cell*

### *Assaying the overall solar water splitting using the wired device*

We then decouple the photo-induced catalyst deposition and the photo-induced overall water splitting to measure the performance of the device. Here, the photo-induced catalyst was done for 10 minutes. The resulted electrodes were taken out of the  $[\text{Co}(\text{WS}_4)_2]^{2-}$  deposition solution, rinsed thoroughly with DI water and immersed in 0.1 M KPi (pH 7). In this case, the whole device was constituted of a 3jn-a-Si solar cell wired to a CoWO and a CoWS decorated FTO electrodes. The 3jn-a-Si solar cell was then illuminated by 1 sun (AM1.5G,  $100 \text{ mW/cm}^2$ ) illumination to power the overall water splitting process. To follow closely the evolution of gaseous products, a micro gas chromatography (microGC) model S3000 from SRA Instruments was introduced to the setup (**Figure 41**).



*Figure 41: Setup for gas chromatography monitoring of the overall water splitting of the device in PV-electrolyzer configuration*

Working in the automatic sampling mode, the machine utilized a steady flow of research grade argon regulated by a mass flow controller from Bronkhorst as carrier gas. For the sake of consistency, electrochemical test, illumination and gas chromatography were all started at the same moment. The evolved gaseous product would be swept along the carrier gas to the chromatograph, and a sample injection was made every 92 seconds. These data points when presented as-recorded would constructed a real-time presentation of the amount of gas produced in the reservoir. On the other hand, cumulative addition of the values of these data

points would yield an accumulated plot representing the total amount of gas generated up to the point of interest. For precise quantification, the machine was calibrated to a controlled response of platinum catalyst electrode during electrolysis in aqueous solution.

It was showed that hydrogen and oxygen gas were generated during the test. Indeed, as soon as the light was turned off at 150-minute mark, the generation of the gases immediately stopped. However, the low amount of O<sub>2</sub> was near the range where the background O<sub>2</sub> was significant (**Figure 42**, left), hence the stoichiometric ratio of 2 H<sub>2</sub> : 1 O<sub>2</sub> was not obtained. Solar water splitting performance dropped by half after 150 minutes, which was much steeper than the drop of photo-voltage of the 3jn-a-Si solar cell. Therefore, the main reason was more likely due to the catalyst degradation. Based on the accumulated amount of H<sub>2</sub> generated (2.87 μmol, **Figure 42**, right), the average solar-to-fuel efficiency (η<sub>STF</sub>) or in this case, solar-to-hydrogen efficiency (η<sub>STH</sub>) of the device calculated using Eq. 20 was found to be around 7.6 x 10<sup>-2</sup>%.

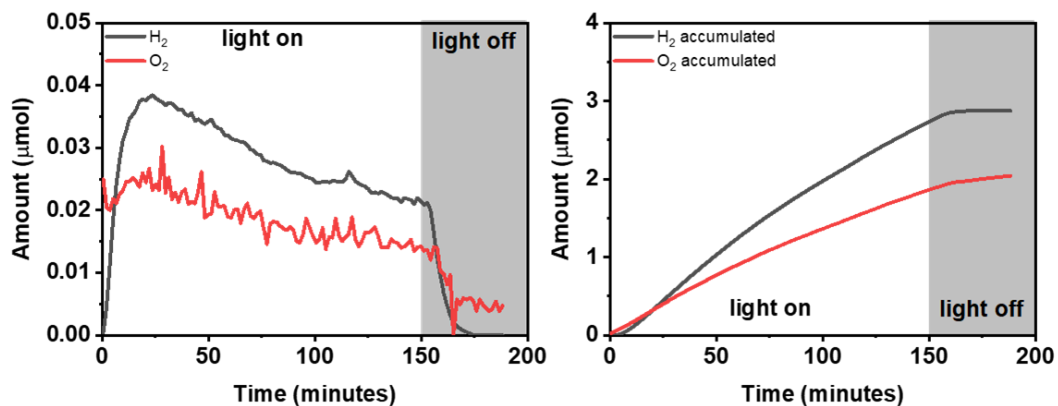


Figure 42: Real-time (left) and accumulated (right) result for gas chromatography monitoring of the overall water splitting of the device in PV-electrolyzer configuration

$$\eta_{STH} = \frac{\text{Energy stored in Hydrogen}}{\text{Total light Energy}} = \frac{\text{Amount of H}_2(\text{mol}) \times 237130 (\text{J} \cdot \text{mol}^{-1})}{\text{Light Power}(\text{J} \cdot \text{s}^{-1} \cdot \text{cm}^{-2}) \times \text{Area}(\text{cm}^2) \times \text{Irradiation time (s)}} \quad (\text{Eq.20})$$

Thus, we confirmed the compatibility of the 3jn-a-Si solar cell with the dual CoWO and CoWS catalysts. In other words, the 3jn-a-Si solar cell under illumination could provide sufficient driving force for the simultaneous deposition of the dual catalysts onto the corresponded FTOs wired to it. The resultant assembly, which resembled the PV-electrolyzer system, was capable of unassisted overall solar water splitting. Based on this, it is reasonable to expect that an integrated monolithic configuration with the catalysts deposited directly on the corresponding surface of the solar cell would produce similar or even better performance, especially when the overall Ohmic resistance has been improved through the elimination of excessive wirings.

## 2.4. Artificial leaf fabrication through photo-induced assembly of dual catalysts

Typical (photo)electrodeposition of catalysts onto the two opposite surfaces of a monolithic device was usually done separately in a stepwise “one side at a time” manner, like described in the work of Nocera.<sup>66,67</sup> This method provided certain flexibility to the choice of materials that could be used to build the catalysts for each side. Nevertheless, the increase in number of manipulation steps could also amplify the probability of inherent errors, especially for delicate thin film devices. In addition, the maximum deposition area was directly tied to the size of the openings presented in the clamp cell. Usually, glass was chosen as material for these clamp cells for its low gas permeability, chemical inertness as well as mechanical and thermal stability. However, apparatus with more complex structure often required precise glass manipulation, which is increasingly costly and time-consuming at large scale. Therefore, this is detrimental to the scalability of the fabrication process.

In comparison, when all required preparations were in place, our actual process to fabricate the monolithic artificial leaf could be completed with extreme simplicity. Here, any simple container with sufficient volume and a clear window to allow unimpeded illumination could be used as the reacting reservoir. In addition, as the setup required no clamping of the solar cell, the size limitation of the artificial leaf would depend on that of the container and the beam of the incoming light. This has greatly improved the scalability of the process. Moreover, since the required potentials were generated by the solar cell under light, the need for potentiostats was eliminated.

A first demonstration was conducted using a 15 x 17 mm piece of processed 3jn-a-Si solar cell and a commercially available 45 x 22.5 x 12.5 mm quartz cuvette containing 3 mL of 0.5 mM  $[\text{Co}(\text{WS}_4)_2]^{2-}$  solution in 0.1 M KPi (pH 7). The process began by simply dropping the 3jn-a-Si solar cell into the solution and open the shutter of the Xenon lamp. A piece of silicon septum with a small slit was used to keep the 3jn-a-Si solar cell in an upright orientation. Upon illumination, changes in color of the exposed terminals of the solar cell and formation of bubbles were immediately observed (**Figure 43**). The reflective cathode turned light brown while the violet color of the anode changed to light blue with a light shade of green. Initial visual inspection showed significantly higher evolution rate of bubbles than the deposition on FTO glass in the wired configuration (see this above), suggesting a superior performance of the integrated monolithic configuration. However, after 10 minutes, precipitation was observed floating near the interface between the anodic terminal and the electrolyte. This could be

attributed to the local drop in pH from the water oxidation reaction, which destabilized the  $[\text{Co}(\text{WS}_4)_2]^{2-}$  precursor. Attempts at stirring the deposition solution with a magnetic stirrer to counter this was unsuccessful because the magnet attracted the stainless-steel substrate. Alternatively, gentle agitation to the solution could be done with a plastic pipette. However, the added perturbation accelerated the formation of the precipitation, and the yellow deposition solution quickly turned opaque.

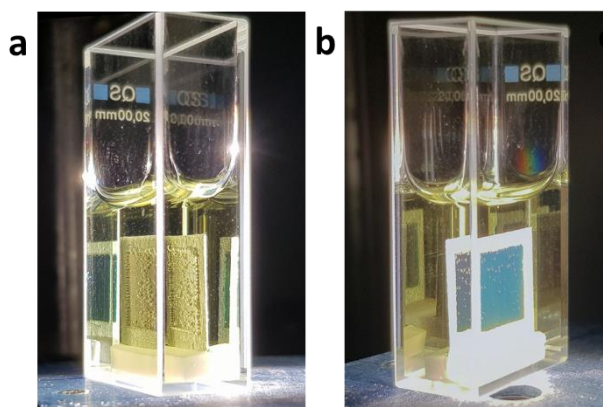


Figure 43: Photo-induced assembly of dual catalysts on 3jn-a-Si solar cell. View of the cathode (a) and view of the anode (b)

Our speculation for the mechanism of the process was presented through the expanded schematic representation in **Figure 44**. Here, the three p-i-n junctions effectively absorbed light with wavelength corresponding to their specific band gaps to generate electrons and holes. The most energetic ones, i.e. the holes from the top junction, and the electrons from the bottom junction were able to reach the solid-electrolyte interface to simultaneously oxidize and reduce the  $[\text{Co}(\text{WS}_4)_2]^{2-}$  precursor to form the respective CoWO and CoWS catalysts and drive their respective half-reactions of the overall water splitting. The remaining electrons and holes underwent recombination at the tunnel junctions to close the circuit.

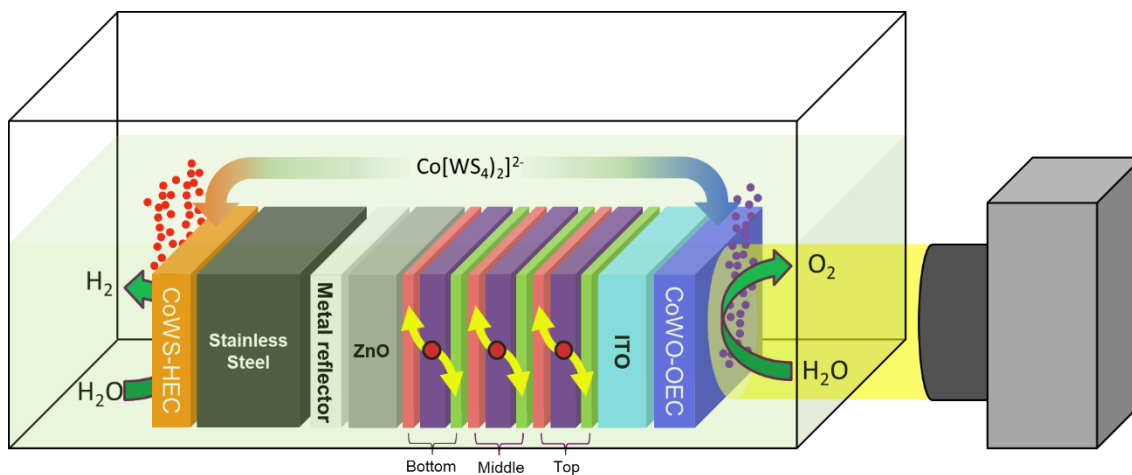


Figure 44: Schematic representation of the photo-induced assembly of dual catalysts on 3jn-a-Si solar cell



Thus, our novel approach to fabricate a functional monolithic artificial leaf with minimal engineering and attractive scalability using readily available equipment was viable. This appealing simplicity was largely contributed by the light-induced simultaneous assembly of the dual catalysts onto the surface of a commercialized 3jn-a-Si solar cell. The result was an artificial leaf capable of unassisted solar water splitting. This success was a good starting point for the following in-depth investigation and optimization.

### 3. None-invasive investigation and evaluation of the monolithic artificial leaf

The super thin 3jn-a-Si layer of the solar cell was easily damaged by physical contacts as demonstrated in **section 2.2**. Therefore, investigation through non-invasive methods would be more preferable. Adding to the fact that the resultant monolithic artificial leaf was capable of unassisted solar water splitting, initial evaluations with methods like gas chromatography, microscopy and spectroscopy would be a good start since they could avoid physical contacts with the instruments.

#### *Gas chromatography general setup for monolithic artificial leaf evaluation*

A general setup for gas chromatography was presented in **Figure 45**. Here, a conventional cylindrical glass vial was chosen as reaction reservoir for better integration with the gas chromatograph and superior gas impermeability of the whole setup. Indeed, coupled with a silicon septum, an air-tight and water-tight container was easily obtained. The system was left to degas for 15 minutes with the argon from the mass flow before evaluation. During this time, the sample was held out of the solution with the help of a magnet. The sample was then immersed in the 0.1 M KPi (pH 7) and illumination was performed with a Xenon lamp with intensity of 1 sun ( $100 \text{ mW/cm}^2$ ) after passing through an AM1.5G filter.

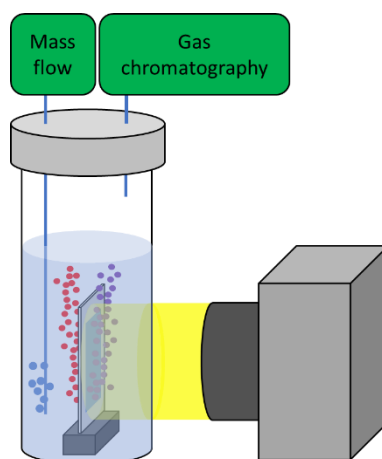


Figure 45: Gas chromatography general setup for monolithic artificial leaf investigation

### 3.1. Optimization of 3jn-a-Si cutting method revisited

Employing the aforementioned gas chromatography setup, the different cutting methods for the 3jn-a-Si could be reevaluated based on their effects on the performance of the resulting devices. To this end, artificial leaves prepared by metal shear and wire-cutting was assayed for three hours of continuous operation in 0.1 M KPi (pH 7). The cutting method using laser was not included since it resulted in a non-functioning device.

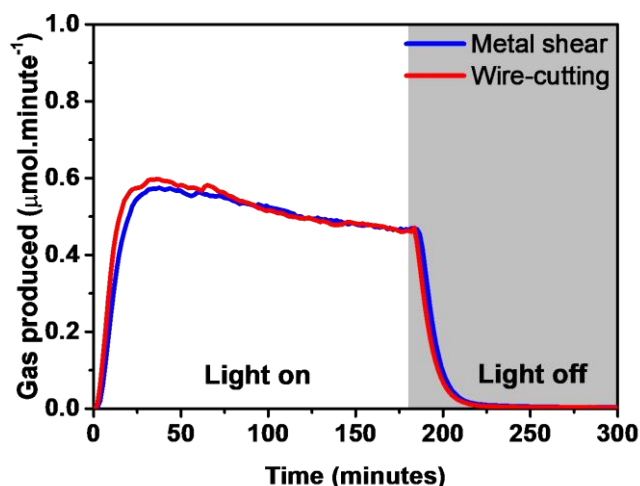


Figure 46: Evolution of hydrogen gas by artificial leaves prepared by metal shear and wire-cutting methods

As can be seen from the evolution of hydrogen monitored by gas chromatography (**Figure 46**), the two cutting methods resulted in devices with identical performance. Therefore, the choice of metal shear cutting method was evaluated to be optimum in terms of speed, quality, minimum wastage and performance of the resulting devices.

### 3.2. Optimization of catalyst deposition

It was observed that the thickness of the catalyst layers increased with prolonged illumination. It was generally agreed that higher amount of catalyst would often benefit overall activity, but only up to a certain point. Indeed, only the portion of material in direct contact with the electrolyte would be electrochemically active, while the parts shielded underneath had minimal contribution. Moreover, thicker layers block more incoming light. Therefore, tuning the thickness of the catalysts, especially the CoWO-OEC layer in our artificial leaf to reach a reasonable compromise between activity and light impedance was important. To this end, the non-invasive monitoring of the H<sub>2</sub> and O<sub>2</sub> amount generated during the catalyst deposition (using the gas chromatography setup in **Figure 45**) was used to optimize the catalyst deposition time as well as the chemical composition of the deposition bath.

### 3.2.1. An optimization of catalyst deposition time

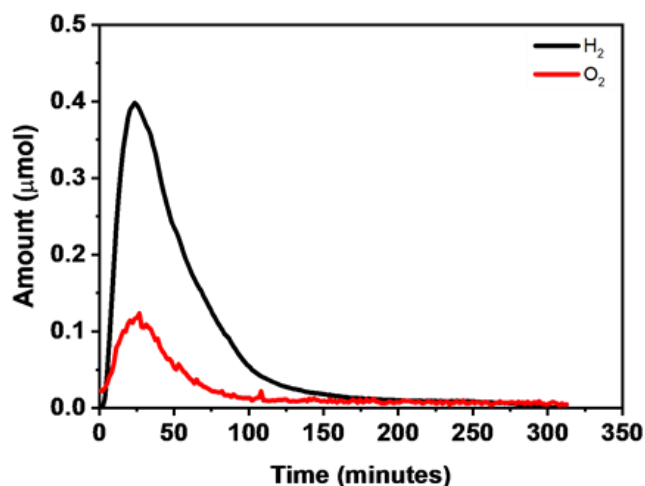


Figure 47: Evolution of gases during the photo-induced assembly of the dual catalyst

**Figure 47** shows the real-time profile of H<sub>2</sub> and O<sub>2</sub> gases evolved during the photo-induced deposition of CoWO and CoWS catalysts onto the two terminals of a 3jn-a-Si solar cell immersed in a 0.5 mM [Co(WS<sub>4</sub>)<sub>2</sub>]<sup>2-</sup> solution in 0.1 M KPi (pH 7). Initially, the amount of generated hydrogen and oxygen gases increased sharply as the deposition time elongated, thus higher amount of catalysts was deposited. However, the rate started decreasing from the 10-minute mark. The amount reached maximum at 25 minutes, after which, it gradually decreased and was fully suppressed after around 3 hours. Therefore, the sharp drop in gas production from the 25-minute mark was attributed to the light shielding effects from the thickness of the CoWO-OEC. Thus, the maximum duration for future catalysts deposition was determined to be inferior than 25 minutes.

This experiment also gave an insight on the formation of the catalysts. Here, the ratio between hydrogen and oxygen was recorded to be roughly 4:1 instead of the stoichiometric 2:1 as expected from the overall water splitting. This suggested that the formation of CoWO-OEC continued whereas CoWS-HEC already reached its best catalytic performance, hence, the H<sub>2</sub> evolution was more in favor than the CoWS catalyst deposition.

Interestingly, negligible amount of floating precipitation was observed during this test. It was possibly due to the continuous bubbling of argon in the deposition solution. Indeed, the stream of gas provided a mild form of agitation to the liquid phase, thus countering the local pH drop. In addition, depriving the environment of oxygen would reduce the rate of undesirable oxidation and improving the stability of the deposition solution.

We then decoupled the photo-induced catalyst deposition and the overall solar water splitting by assaying five functional artificial leaves obtained after different catalyst deposition time together with an as-prepared 3jn-a-Si solar cell hosting no catalyst as a reference sample. These leaves were assayed in a 0.1 M KPi (pH 7) electrolyte solution being free of  $[\text{Co}(\text{WS}_4)_2]^{2-}$  precursor using the same experimental setup (**Figure 45**). These leaves were illuminated for 60 minutes. Afterwards, the system was lightly shaken to dislodge the bubbles adhered to the surface of the leaves. The gas chromatograph was then left running for one additional hour to extract all the generated gases. The real-time profile of  $\text{H}_2$  gas produced was shown in **Figure 48**.

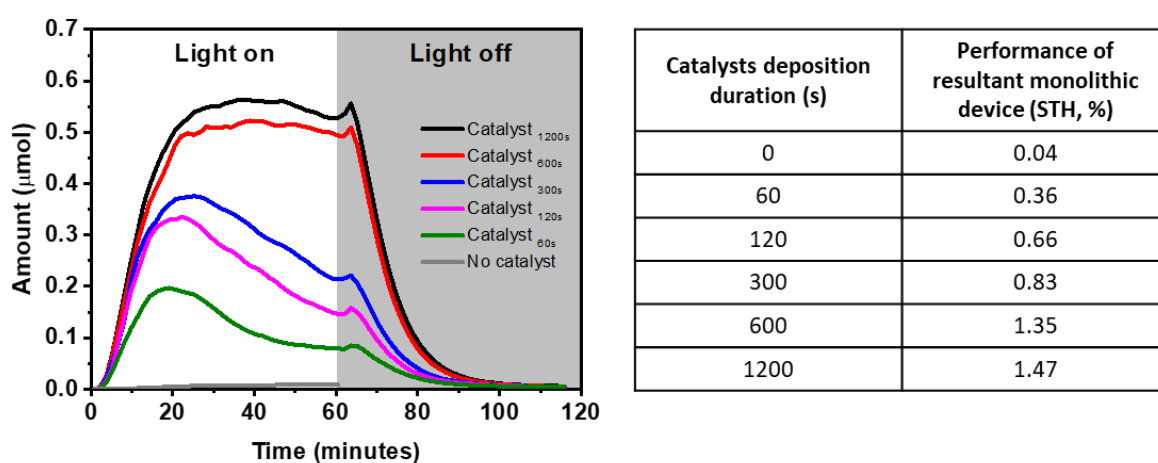
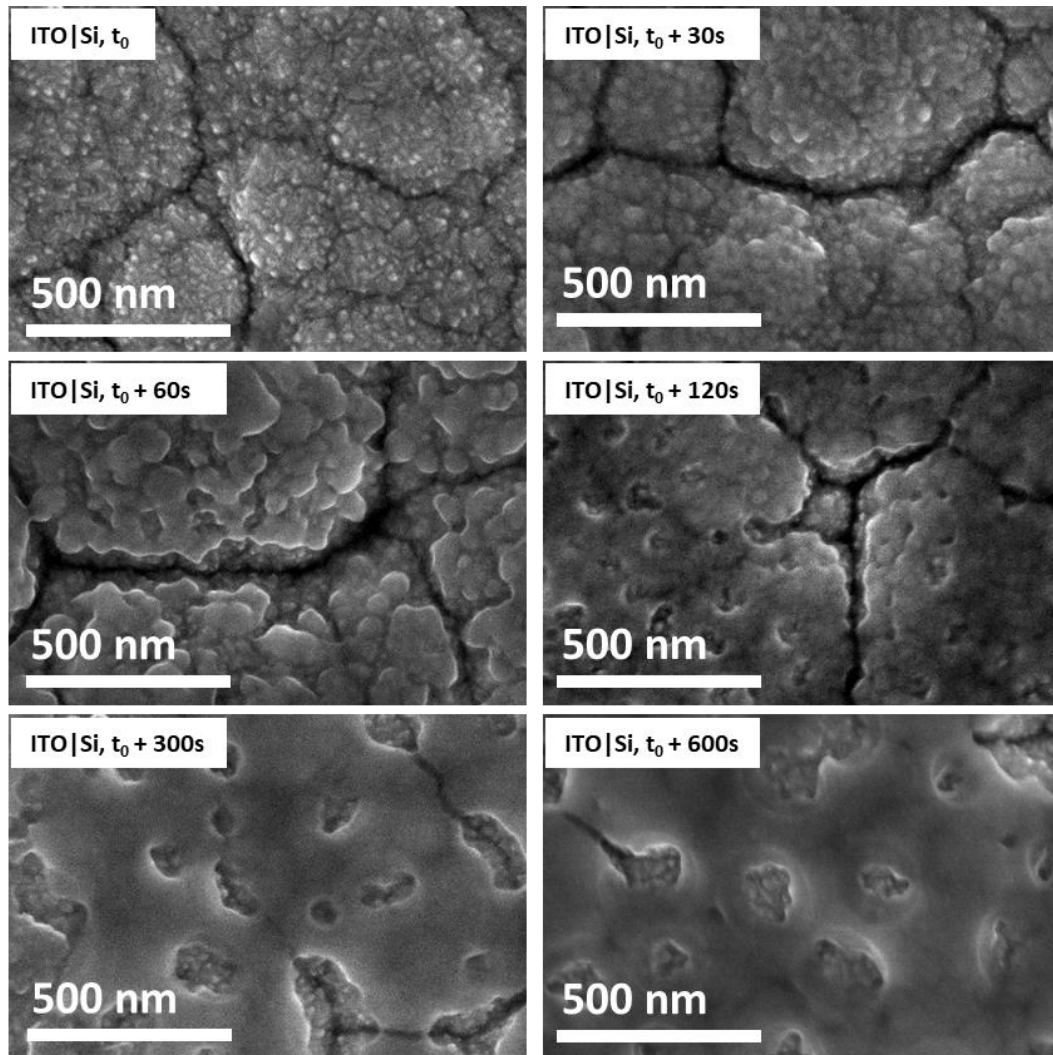


Figure 48: Real-time amount of hydrogen (left) and corresponding STH efficiencies (right) recorded from artificial leaves with catalysts deposited for various durations

Even though the 3jn-a-Si solar cell alone was more than able to provide sufficient photovoltage to drive the water splitting reaction, the lack of suitable catalysts to overcome the kinetic barrier severely hindered its performance. Indeed, negligible amount of  $\text{H}_2$  gas was detected in this case. Regarding other leaves having the dual CoWS and CoWO catalysts, the solar-to- $\text{H}_2$  conversion yield ( $\eta_{\text{STH}}$ ) increased when elongating the catalyst deposition time to 10 minutes. After that, the increment of  $\eta_{\text{STH}}$  was marginal. We speculated that the island growth mode was completed and the surface of the solar cell was largely covered by the catalysts after approximately 10 minutes of deposition. Indeed, leaves obtained after less than 10 minutes of catalyst deposition experienced a sharp decrease in performance over operation time. The reason could possibly be due to the incomplete formation of the catalyst layer which could be more easily subjectable to degradation. Microscopic technique would provide a more detailed insight for this process.

### *SEM inspection for the evolution of catalyst deposition over time*

Scanning electron microscopy (SEM) was employed to provide a more detailed inspection to the formation of the catalysts. Several artificial leaves hosting catalysts deposited for various durations were prepared to express the growing process of the catalysts over time. An as-prepared 3jn-a-Si solar cell was also included for reference.



*Figure 49: SEM images of CoWO-OEC deposited on the anodic terminal of the 3jn-a-Si solar cell for various durations*

As can be seen in **Figure 49**, the surface of the pristine anodic terminal was constructed from various islands of crystalline p-doped silicon with distinct pointy structure and clear boundaries. The thin layer of ITO covered and adapted closely to this structure. The initial growth of CoWO-OEC was observed after 30 seconds on the crystalline grains of silicon as small blobs measuring at around 30 nm. As the deposition progressed, these islands were enlarged, reaching nearly 100 nm in size after a minute and eventually merged to form a more compact layer. By the 5-minute mark, the entire surface was largely covered by a thin layer of



the catalyst. This layer was progressively thickened as observed after 10 minutes. Various crater-shaped holes were present in the layer exposing the underlying Si|ITO surface. These holes were characteristic to the spherical shape of the adhered gas bubbles on the surface, preventing its contact with the deposition solution. Therefore, no deposition was possible at those locations.

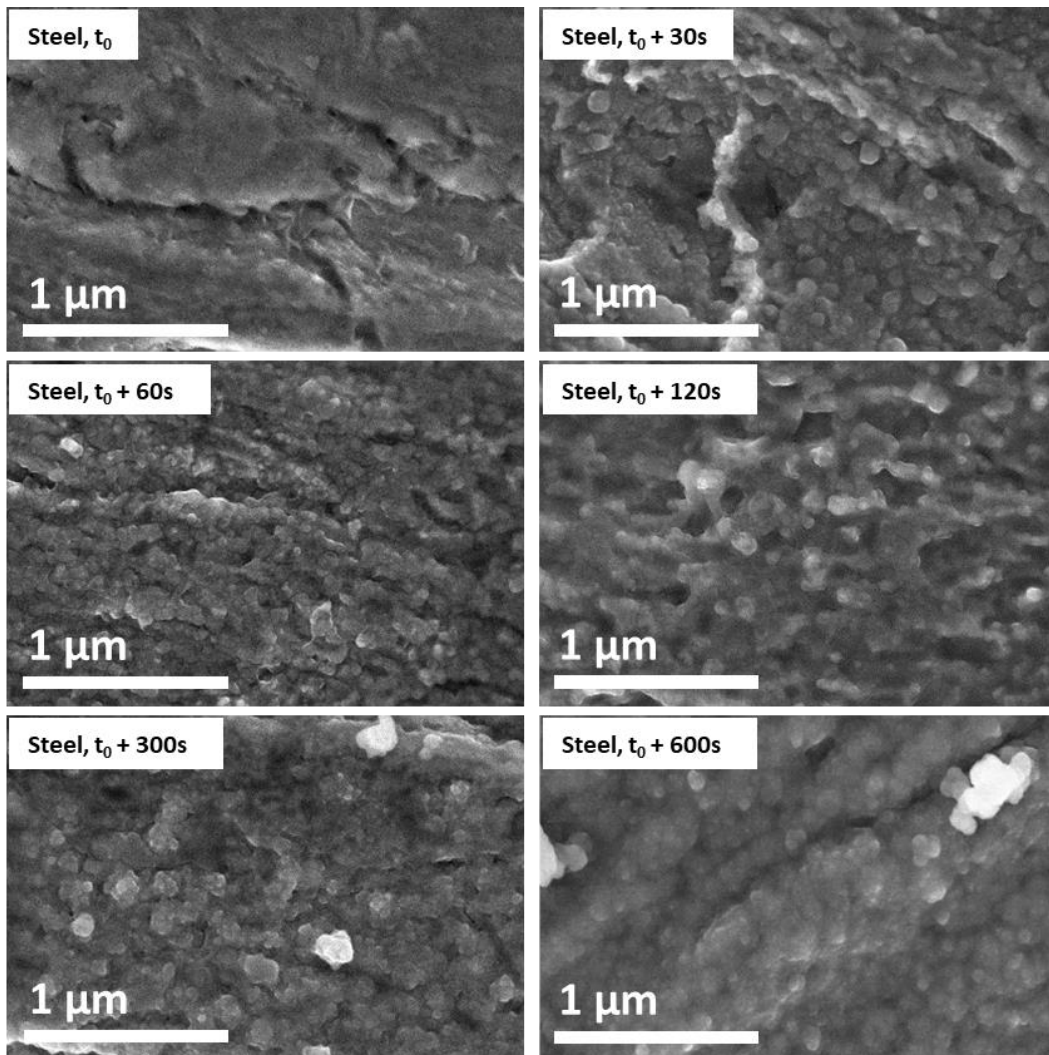
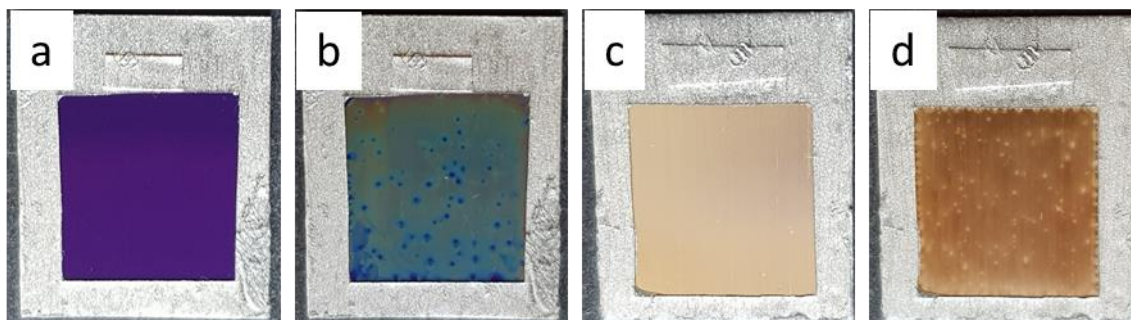


Figure 50: SEM images of CoWS-HEC deposited on the cathodic terminal of the 3jn-a-Si solar cell for various durations

Similarly, the growth of CoWS-HEC on stainless-steel was monitored (**Figure 50**). On the relatively smooth surfaces of the scratched stainless-steel, grains around 100 nm in diameter were readily formed after 30 seconds. Merging of the grains happened continuously and the stainless-steel surface was completely covered by the 2-minutes mark. As the deposition progress, new grains were observed growing on top of this layer after 5 minutes. Finally, the boundaries between those grains were covered completely, resulting in a compact layer of catalyst after 10 minutes. Interestingly, no microscopic holes caused by evolution of hydrogen were observed.

Zooming back out, the visual presentations of the sample before and after 10 minutes of catalyst deposition are shown in **Figure 51**. It can be seen that the exposed surfaces of the terminals were mostly covered by the catalysts, save for a few spots blocked by the gas bubbles. On this scale, the shielding effect of hydrogen gas could finally be seen, although the resulted holes were smaller in comparison to those caused by oxygen (**Figure 51d and b**, respectively).



*Figure 51: Photo of anodic terminal as-prepared (a) and with CoWO-OEC deposited for 10 minutes (b) and the cathodic terminal as-prepared (c) and with CoWS-HEC deposited for 10 minutes (d)*

Here, a compromise needed to be made. To elaborate, the local destabilization of  $[\text{Co}(\text{WS}_4)_2]^{2-}$  which was worsened with mechanical agitation could have unpredictable effects on the incoming illumination as well as the composition of the resulted catalyst. While continuous degassing with argon would provide improved stability, our interest lies in keeping the engineering at the minimum possible level. To this end, fabricating the artificial leaf for 10 minutes not only avoided the uncertainty in composition of the added layer of the catalyst, but also required no additional degassing or stirring. Therefore, it was decided to keep the catalyst deposition duration at 10 minutes for all samples used for further investigation. Through this, we chose to sacrifice a small gain in performance to favor a simpler and more consistent fabrication process.

### **3.2.2. An optimization of chemical composition of the deposition bath**

It was previously noted that the chemical composition of the deposition bath could be altered by modifying the molar ratio of the  $\text{Co}^{2+}$  and the  $[\text{WS}_4]^{2-}$ . Although the formation of  $[\text{Co}(\text{WS}_4)_2]^{2-}$  species was expected at any ratio,<sup>141</sup> excess amount  $\text{Co}^{2+}$  or  $[\text{WS}_4]^{2-}$  in the solution could potentially modify the performance of the deposited catalysts. Here, we employed the light-induced assembly method to fabricate artificial leaves in deposition baths with varying ratios of  $\text{Co}^{2+}$  and  $[\text{WS}_4]^{2-}$ . The deposition time was kept at 10 minutes. The resulted samples were then cleaned, dried and assayed for their overall solar water splitting performance in a 0.1 M KPi (pH 7) solution being free of  $\text{Co}^{2+}$  and  $[\text{WS}_4]^{2-}$ .

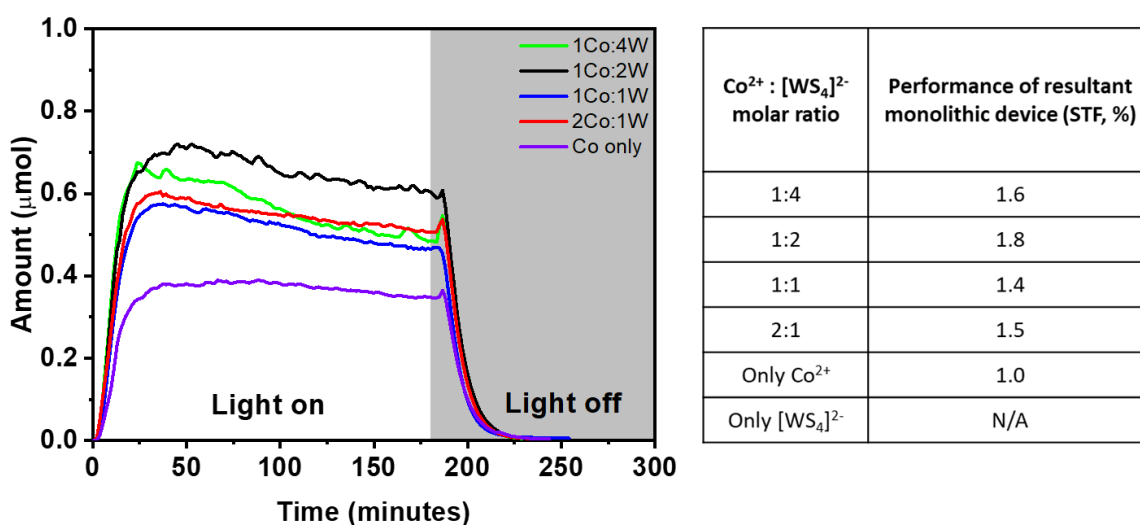


Figure 52: Real-time amount of hydrogen (left) and corresponding STH efficiencies (right) recorded from artificial leaves with catalysts deposited from chemical baths of various Co<sup>2+</sup> : [WS<sub>4</sub>]<sup>2-</sup> molar ratios

No deposition nor gas bubbles were observed on the 3jn-a-Si solar cell immersed in a 0.5 mM [WS<sub>4</sub>]<sup>2-</sup> solution being free of Co<sup>2+</sup>. This is within expectation, since [WS<sub>4</sub>]<sup>2-</sup> was not electroactive.<sup>123</sup> On the other extreme, solution containing only Co<sup>2+</sup> yielded an operational artificial leaf with a modest  $\eta_{\text{STH}}$  efficiency of 1%. Here, deposition of a Co-OEC (CoPi with onset deposition potential of 1.0 V vs. NHE)<sup>107</sup> and a Co-HEC (H<sub>2</sub>CoCat with onset deposition potential of -0.3 V vs. RHE)<sup>125</sup> could be expected on the anodic and cathodic terminals of the solar cell, respectively. The remaining deposition baths containing both Co<sup>2+</sup> and [WS<sub>4</sub>]<sup>2-</sup> gave out devices with  $\eta_{\text{STH}}$  efficiency in the narrow range of 1.4 to 1.8%. The highest efficiency of 1.8% was reached with the deposition bath with 1 Co<sup>2+</sup> : 2 [WS<sub>4</sub>]<sup>2-</sup> molar ratio. This value complied well with the original formula of [Co(WS<sub>4</sub>)<sub>2</sub>]<sup>2-</sup> species.

However, past the 1:1 ratio, further addition of [WS<sub>4</sub>]<sup>2-</sup> resulted in more rapid formation of precipitation even with equal degree of degas. In the case of 1 Co<sup>2+</sup> : 2 [WS<sub>4</sub>]<sup>2-</sup> molar ratio, local formation of precipitation on the anodic terminal was observed as soon as 5 minutes. Therefore, once again, a compromise was reached, and the composition of the chemical bath was kept with equimolar ratio between Co<sup>2+</sup> and [WS<sub>4</sub>]<sup>2-</sup>.



### 3.3. Performance evaluation and investigations on catalysts

#### 3.3.1. Overall solar water splitting capability assessment

We assayed in more detail the overall solar water splitting performance of the best leaf CoWO-OEC|ITO|3jn-a-Si|Steel|CoWS-HEC achieved with 10 minutes of catalyst deposition and using the 0.5mM  $[\text{Co}(\text{WS}_4)_2]^{2-}$  deposition bath with equimolar of  $\text{Co}^{2+}$  and  $[\text{WS}_4]^{2-}$ . The basic setup for gas chromatography presented in **Figure 45** was employed. The media was a 0.1M KPi (pH 7) solution being free of  $\text{Co}^{2+}$  and  $[\text{WS}_4]^{2-}$ .

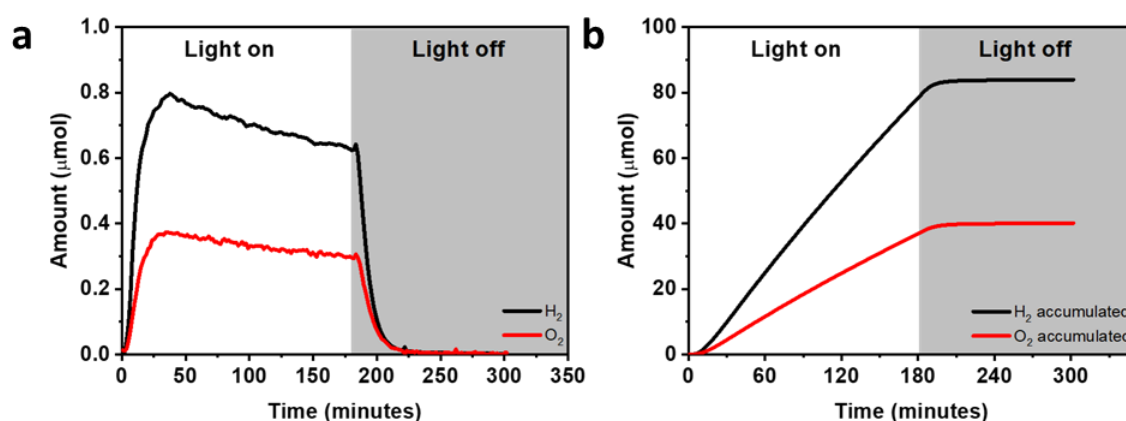


Figure 53: Gas chromatography result for the best artificial leaf in real-time (a) and accumulated (b) mode

In both the real-time profiles (**Figure 53a**) and the accumulated amount of gases produced (**Figure 53b**), the molar ratio of 2 H<sub>2</sub> : 1 O<sub>2</sub> was obeyed. The real-time profiles showed a sharp increase in the amount of gases produced up to 30 minutes. Afterwards, the performance gradually dropped, resulting in a relatively drop of 10%/ hour. This drop of performance could be the result of degradation of either the solar cell, the catalyst or a combination of them. It will be further discussed in the coming sections. As soon as the light was turned off after 3 hours of operation, the evolution of H<sub>2</sub> and O<sub>2</sub> immediately stopped. Combined with the consistently observed stoichiometric gas ratio, we conclude without any ambiguity that the H<sub>2</sub> and O<sub>2</sub> were products of the overall solar water splitting process driven by the CoWO-OEC|ITO|3jn-a-Si|Steel|CoWS-HEC monolithic device. The system was then left running for an additional 2 hours to extract all the gases produced. Over the course of 3 hours, the leaf was able to accumulatively generate 84 μmol of hydrogen and 41 μmol oxygen. The overall  $\eta_{\text{STH}}$  efficiency was then calculated by Eq. 20 to be 1.9%. This performance, although being in the same range, was lower than the 2.5% from the similar 3jn-a-Si solar cell loaded with CoPi-OEC and NiMoZn-HEC from Nocera and coll.<sup>66</sup> However, it was worth to

mention that our artificial leaf operated in a more benign condition of pH 7 phosphate buffer compared to the pH 9.2 borate buffer used by Nocera's group.

Due to the inconsistency between different areas on the big sheet of 3jn-a-Si solar cell received from the manufacturer, the efficiencies of the resulted artificial leaves were found to be generally in the range of  $1.7\% \pm 0.2\%$ . Therefore, to present the highest potential of our version of artificial leaf, subsequent performance studies would be normalized to the best value of 1.9% STH efficiency.

### 3.3.2. Investigation of the catalysts before and after solar water splitting

It has been observed that during the solar water splitting operation, the performance of the artificial leaf degraded. As the device is made of multiple elements, the reason could come from various factors. We decided to first investigate the catalyst layers for possible changes.

#### *SEM visualization for structural modification*

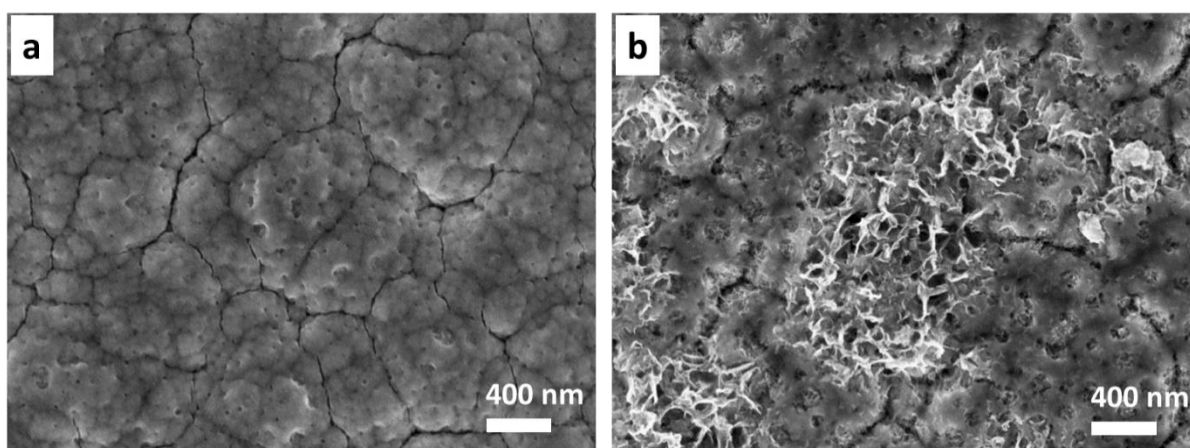
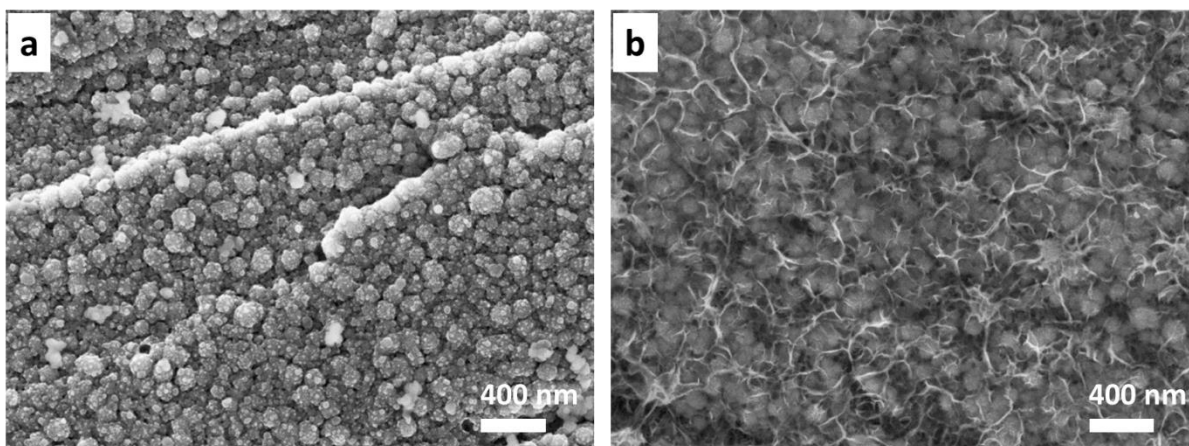


Figure 54: SEM images of CoWO-OEC on the anodic terminal of the artificial leaf before (a) and after (b) solar water splitting

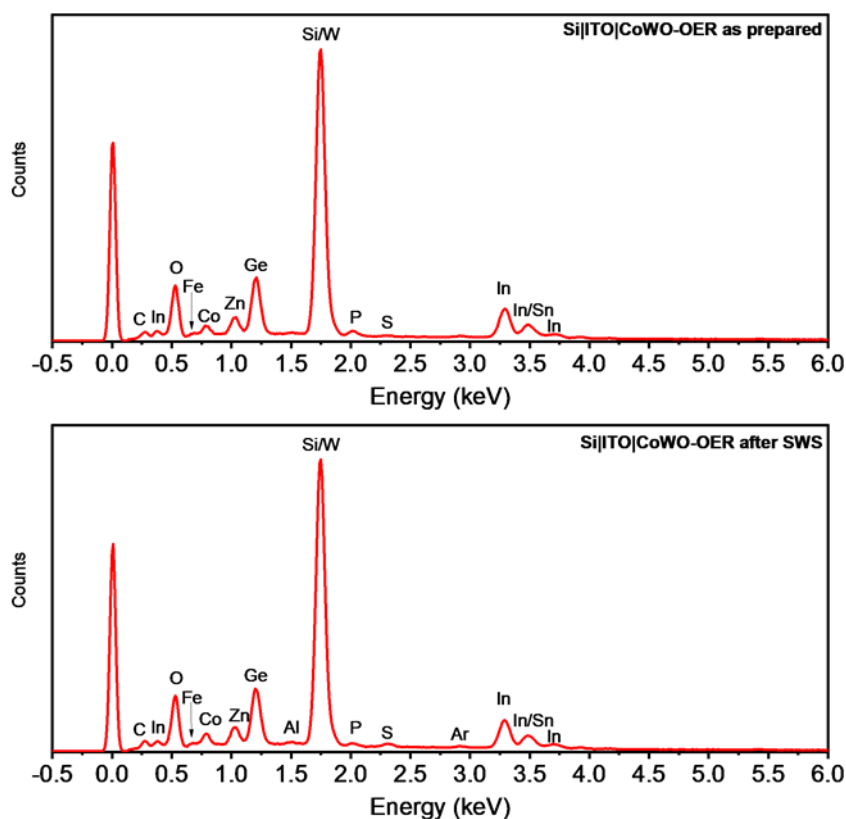
Before being used for the solar water splitting operation, the slimy CoWO-OEC was observed to completely cover the various domains of the underlying ITO|Si. However, after 3 hours of continuous photo-electrolysis, the layer was partly degraded, revealing the original ITO|Si structure underneath. New flaky material also formed with some structural resemblances to the cobalt phosphate crystal previously reported by Shao *et al.*<sup>142</sup> As potential was constantly supplied by the 3jn-a-Si, it was possible that when the CoWO-OEC degraded, it leaked  $\text{Co}^{2+}$  into solution which was then re-deposited onto the surface of the device in this flaky form.



*Figure 55: SEM images of CoWS-HEC on the cathodic terminal of the artificial leaf before (a) and after (b) solar water splitting*

On the cathodic terminal, a thin and compact film of material with layered structure was observed covering the surface at the end of the water splitting experiment. This could be similar to the structure conversion from amorphous to layer-like, previously reported for molybdenum sulfide.<sup>143,144</sup> As the grainy structure of CoWS-HEC was still present underneath, two possibilities were deduced. Either the very top layer of CoWS-HEC was converted to this layer, or an entirely new material was deposited. Nevertheless, more investigation was required before conclusions can be reached.

### *EDX measurement for composition modification*



*Figure 56: EDX investigation of CoWO-OER on the anodic terminal of the artificial leaf before (top) and after (bottom) solar water splitting*

To probe possible changes in chemical composition of the catalysts, Energy-dispersive X-ray spectroscopy (EDX) was employed. At probing voltage of 10 keV, aside from the catalyst layer, the whole thickness of the 3 $\mu$ m-a-Si layer was thoroughly reached. Elements originally belonging to the various layers of the solar cell were observed like In, Sn, O from ITO, Si, Ge from the junctions, Zn and Al from the reflector and low signal of Fe, C from the stainless-steel base. Regarding the CoWO-OER, Co, P and O was clearly recorded before and after the solar water splitting test with similar counts. However, the signal for W was too close to Si, thus its presence in the catalyst was not confirmed (that will be confirmed later by XPS analysis). The appearance of Ar could be expected from the prolonged degas during operation. Slight increment in signal of S could be contamination from the CoWS-HEC.

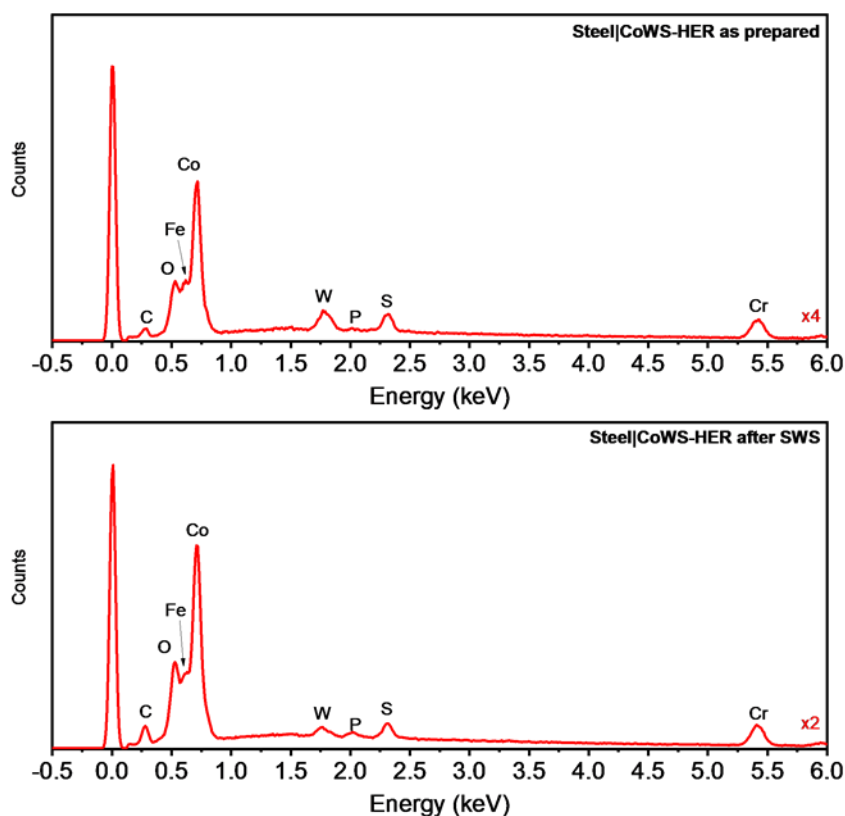


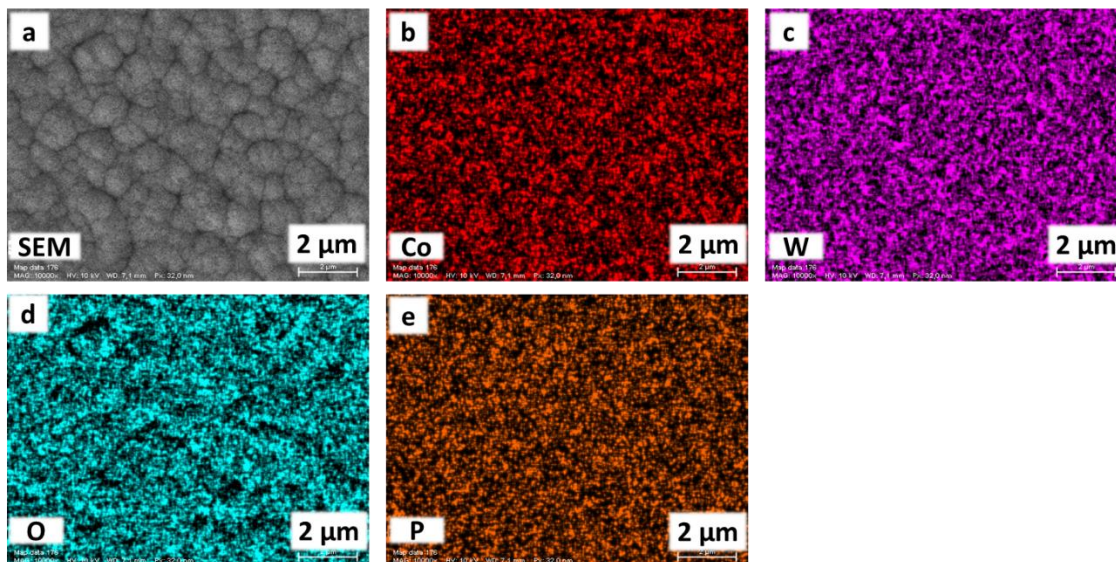
Figure 57: EDX investigation of CoWS-HEC on the cathodic terminal of the artificial leaf before (top) and after (bottom) solar water splitting

On the cathodic terminal, since the stainless-steel layer was significantly thicker, signal from the ITO, junctions and reflector were not recorded with probing voltage of 10 keV. Fe, C and Cr characteristic to stainless steel were clearly observed. The elevated signal of O could be the result of the addition from Cr. Similarly, the elevated signal of Co could be the result of the added signal from Fe. Regarding the CoWS-HEC, Co, W, and S were present, confirming the general composition of the catalyst. After water splitting test, Co and P signal increased, while W slightly decreased and S remained at the same level. This change in relative composition could be related to the new layer of material observed in the SEM images.



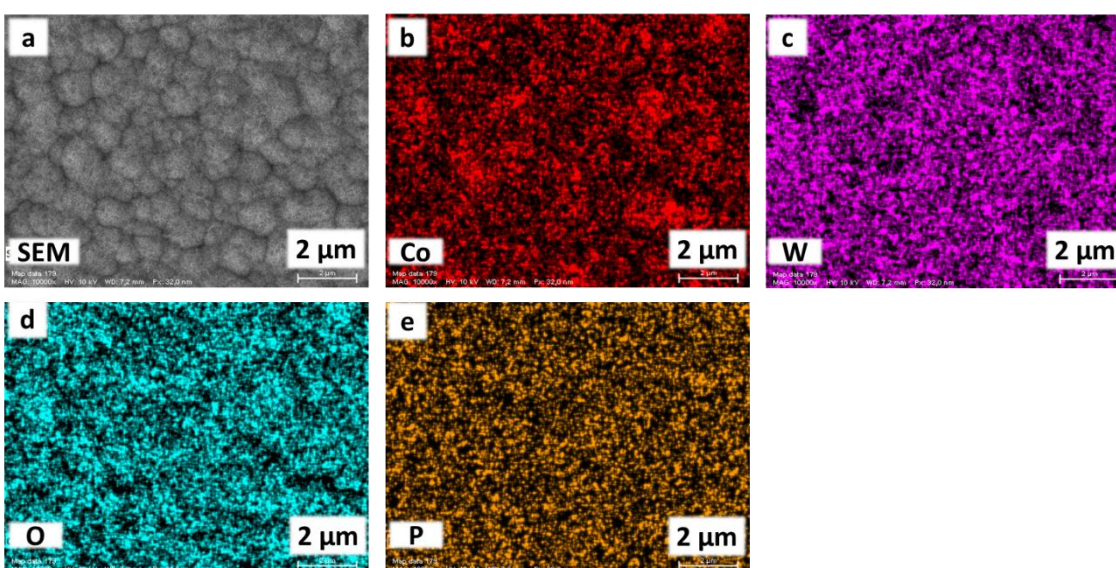
### *EDX mapping to investigate the distribution of various elements*

To visualize the distribution of the elements presented in the catalysts before and after solar water splitting, EDX mapping was utilized.



*Figure 58: EDX mapping for CoWO-OEC on the anodic terminal before solar water splitting*

Overall, the CoWO-OEC layer was homogeneous and the observed elements were distributed quite evenly across the whole surface. After solar water splitting, some redistributions were observed for Co, resulting in various areas with higher concentration (**Figure 59b**). This is consistent with the SEM visualization showing the appearance of newly Co-based domain after the solar water splitting operation.



*Figure 59: EDX mapping for CoWO-OEC on the anodic terminal after solar water splitting*



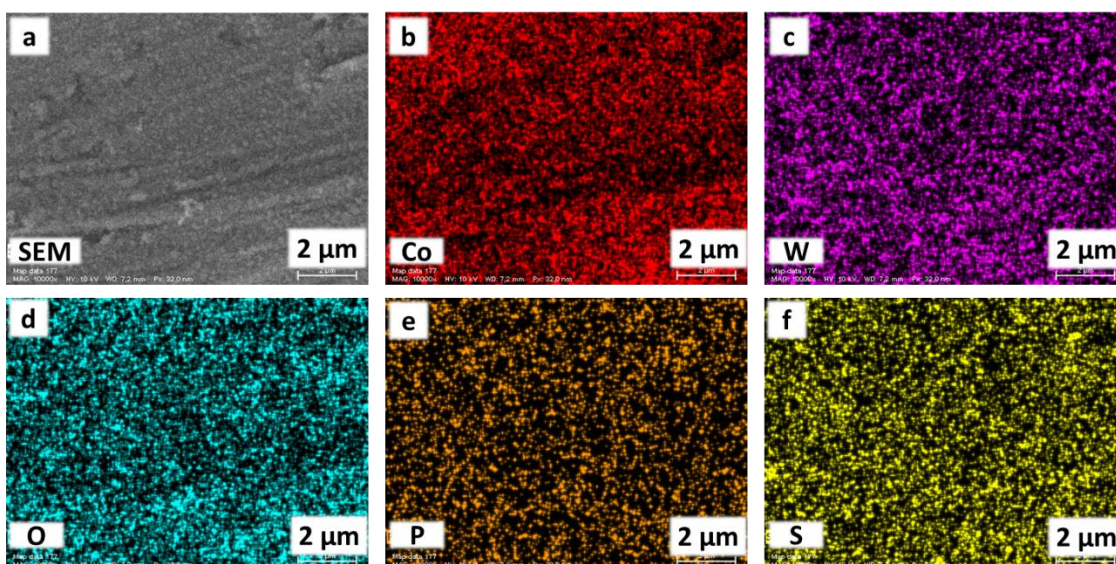


Figure 60: EDX mapping for CoWS-HEC on the cathodic terminal before solar water splitting

Similarly, the pristine CoWS-HEC layer was generally homogeneous with evenly distributed elements. After the solar water splitting operation, the appearance of some larger grains of material was observed. Upon close inspection, those grains contained higher amount of Co, P and O. However, generally, the elements were still distributed quite evenly across the surface.

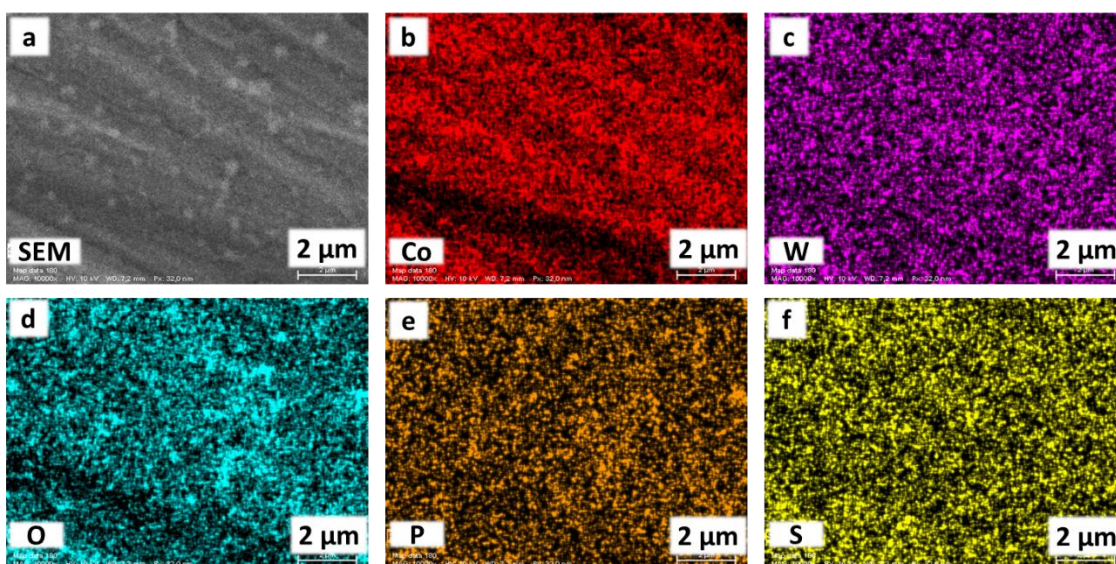


Figure 61: EDX mapping for CoWS-HEC on the cathodic terminal after solar water splitting

Through the EDX elemental mapping, we were able to witness to a certain degree the redistribution of the elements presented in both catalysts after the solar water splitting operation. This was within expectation, as the absence of a membrane and the continuous application of photo-potential from the solar cell could induce cross-contamination and redeposition of materials.

## XPS analysis of catalysts

To investigate further the oxidation states of the elements presented in the catalysts, as well as confirming the presence of W which was overlapped with Si in EDX measurement, X-ray photoelectron spectroscopy was utilized.

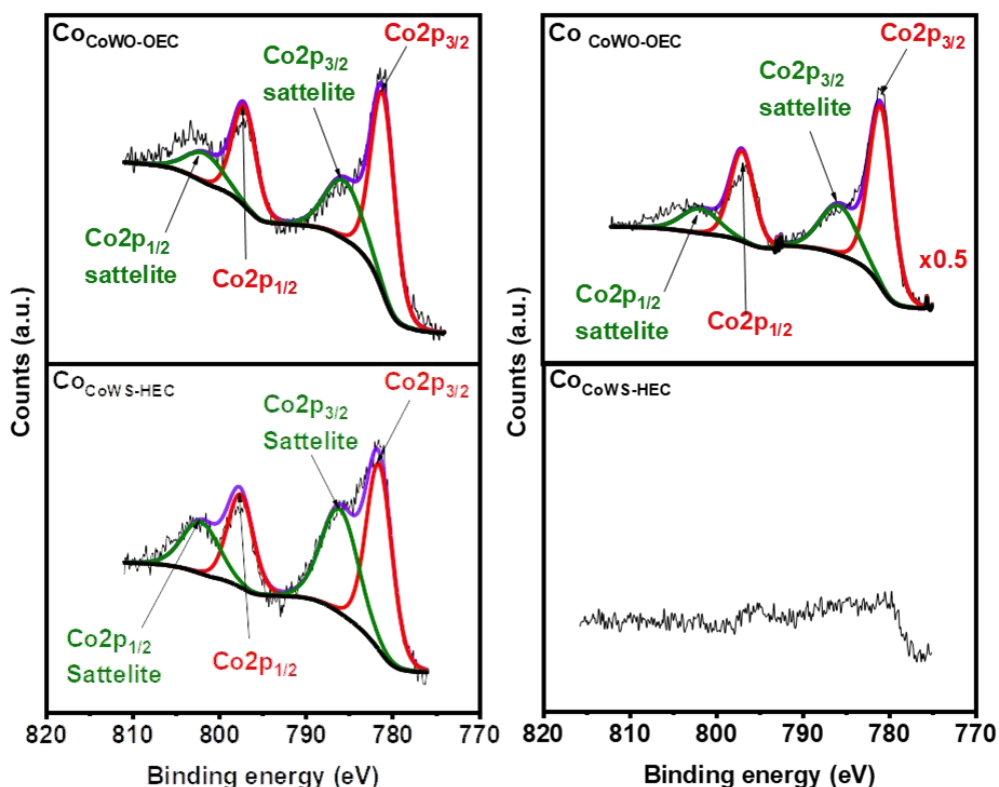


Figure 62: XPS result for Co in catalysts as-prepared (left) and after solar water splitting (right)

In the as-prepared leaf, the main and satellite  $\text{Co}2p_{3/2}$  were observed at binding energy (BE) of 781.2 and 785.6 eV suggesting the presence of  $\text{Co}^{2+}$  oxidation state.<sup>145,146</sup> Indeed, there was not an obvious difference in the  $\text{Co}2p$  signatures in the CoWO and CoWS catalysts (**Figure 62**, left). The amount of Co presented in both of these catalysts were similar. However, after the solar water splitting operation, the Co signal in CoWO-OEC nearly doubled while that in CoWS-HEC was significantly reduced (**Figure 62**, right). One can propose that Co from the CoWS catalyst dissolved, at least partially, into solution which was then re-deposited onto the CoWO side.



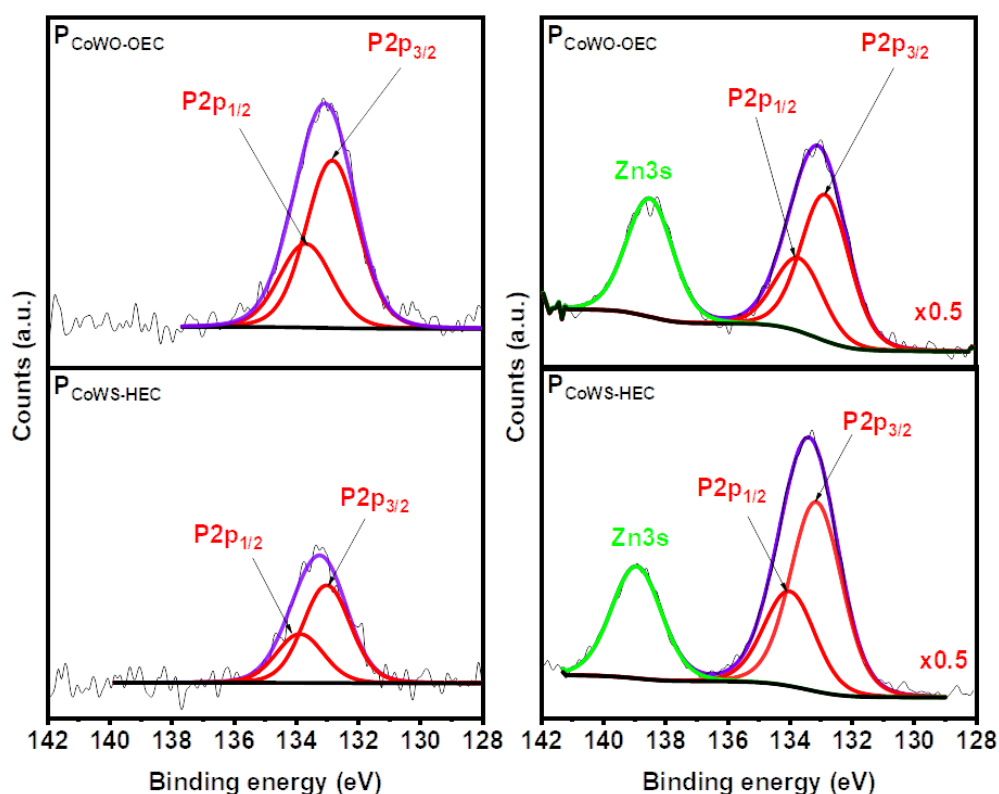


Figure 63: XPS result for P in catalysts as-prepared (left) and after solar water splitting (right)

In the as-prepared leaf, P2p<sub>3/2</sub> was found at 133.5 eV on both CoWO and CoWS layers (**Figure 63**, left). This binding energy is close to that reported for a phosphate species adsorbed onto cobalt oxide surface.<sup>124,125,147,148</sup> Overall, the intensity of P signals in both catalysts roughly doubled after the solar water splitting operation of the leaf. In addition, appearance of Zn3s signal was also observed (**Figure 63**, right). This could be the result of dissolution and redeposition of the ZnO reflector of the 3jn-a-Si solar cell.

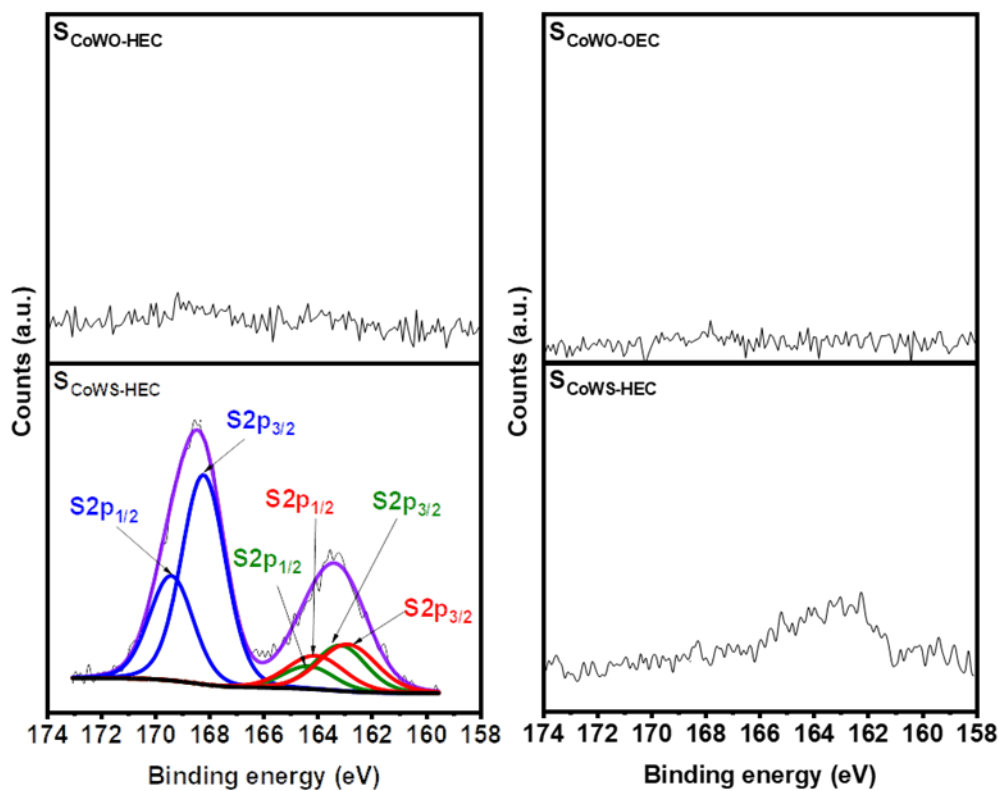


Figure 64: XPS result for S in catalysts as-prepared (left) and after solar water splitting (right)

S could only be observed in CoWS-HEC in both  $S^{2-}$  and highly oxidized state like  $SO_4^{2-}$  which were characterized by  $S2p_{3/2}$  peaks at 162.8 and 168.2 eV (**Figure 64**, left).<sup>123,149</sup> However, after the solar water splitting operation, the S amount significantly reduced (**Figure 64**, right).

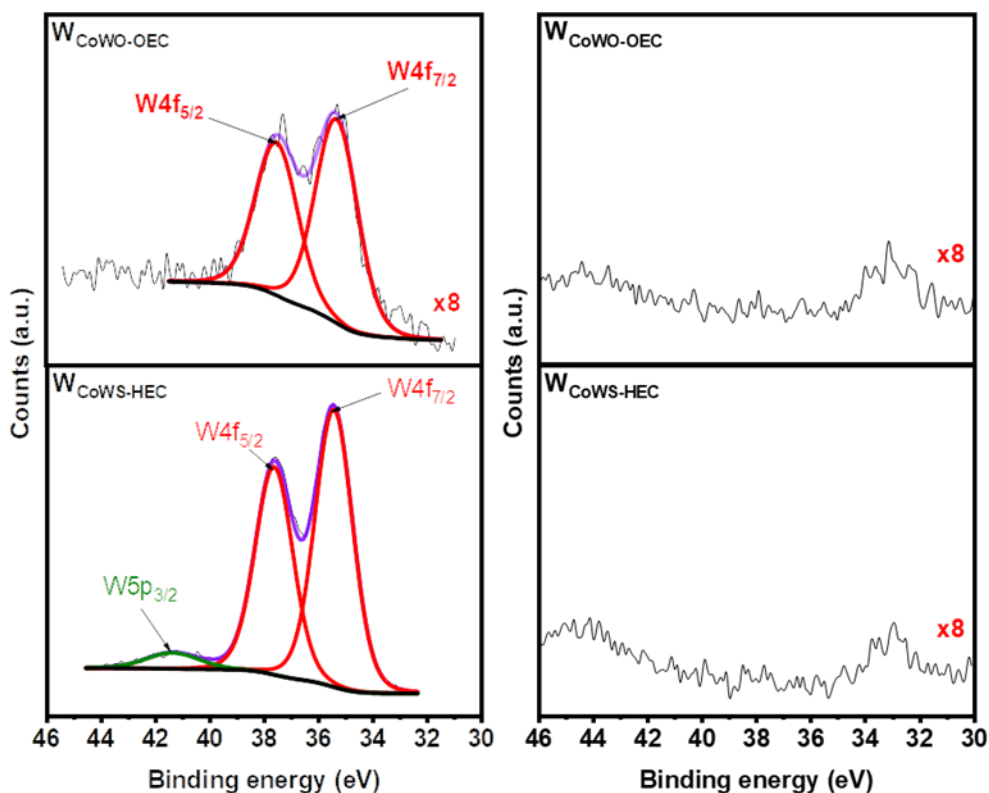


Figure 65: XPS result for W in catalysts as-prepared (left) and after solar water splitting (right)

In the W4f core spectrum, a doublet with W4f<sub>7/2</sub> binding energy of 35.36 eV was found, indicating the presence of the W<sup>6+</sup> oxidation state.<sup>124,150</sup> The W5p<sub>3/2</sub> at 41.30 eV characteristic to W<sup>6+</sup> was observed only in CoWS-HEC (**Figure 65**, left).<sup>151</sup> Before the solar water splitting operation, the amount of W presented in CoWS-HEC was much higher than in CoWO-OEC. This suggested that W is a major component of CoWS-HEC while being more like dopant in CoWO-OEC. However, after the solar water splitting, W was mostly removed from the outermost surfaces of both catalysts.

### *ICP-OES investigation of the electrolyte*

The above SEM, EDX elemental mapping and XPS analyses suggested a partial dissolution of CoWS and CoWO catalysts during the operation of the leaf. To gain more insight into this phenomenon, we employed Inductively coupled plasma - optical emission spectrometry (ICP-OES) to analyze the chemical composition of the phosphate buffer solution during the solar water splitting operation with the leaf. Specifically, a fixed volume of buffer was taken at various intervals for the measurement. The subsequent datapoints were adjusted to the missing portions of the total volume.

*Table 2: ICP-OES analysis for phosphate buffer during solar water splitting operation*

Time (minutes)	Cobalt in test solution ( $\mu\text{g/L}$ )	Tungsten in test solution ( $\mu\text{g/L}$ )	Co : W molar ratio
5	50.7	120.9	1 : 0.76
10	81.9	93.6	1 : 0.37
15	74.1	179.4	1 : 0.78
30	58.5	179.4	1 : 0.99
60	85.8	128.7	1 : 0.48
180	105.3	257.4	1 : 0.78

Presence of dissolved Co and W were recorded, clearly confirming the partial dissolution of the catalysts (**table 2**). However, it was difficult to determine the relative degree of dissolution between the CoWO-HEC and CoWS-HEC since the monolithic device functioned without the need of a membrane. Overall, the concentration of dissolved Co and W fluctuated over time without following any clear trend. This could be the result of the joint occurrence between dissolution and re-deposition processes.

### *General remarks*

The nature of pristine CoWO-OEC was consistent with the previous report from the group, being amorphous cobalt tungsten oxide with surface-bound phosphate.<sup>124</sup> CoWS-HEC also closely resembled to the past report from the group, containing both surface-bound phosphate and sulfate.<sup>123</sup>

Combining the structural changes observed through SEM images, the redistribution of different elements suggested by EDX mapping, the evolution of various elements in the catalysts by XPS analysis and the presence of Co and W in the buffer during operation by ICP-OES, a more detailed view of the whole process could be deduced. We speculated that during the solar water splitting, the catalysts were partly disintegrated and the resulted components were redeposited on the surface of the device. The dissolved  $\text{Co}^{2+}$  could be efficiently redeposited in phosphate buffer, effecting the self-healing capability of CoPi-OEC as can be seen in past demonstration.<sup>131</sup> The majority of W probably reacted with  $\text{O}_2$  in the solution and was not reintroduced to the structure. On the cathodic terminal, after the dissolution of the top-most layer, cobalt sulfide with surface-bound phosphate could possibly be redeposited. Similar to CoWO-OEC, W might not be reintroduced into the structure.

### 3.4. Stability assessment

Due to the partial dissolution of catalysts, one may think about the progressive degradation of the leaf when elongating the operation duration. To examine this, we first let the leaf operate for 3 hours in the 0.1 M KPi (pH 7) being free of  $\text{Co}^{2+}$  and  $[\text{WS}_4]^{2-}$  with AM1.5G 1 sun illumination. When the operation was over, the illumination was off and the leaf was kept standing in the dark while still being immersed in the KPi solution for the next 72 hours. The second operation was restarted for another 3 hours by sending the illumination. We repeated this assay for 4 cycles. In the fifth cycle, 1 mL of 0.5 mM  $[\text{Co}(\text{WS}_4)_2]^{2-}/\text{KPi}$  was added (to the initial solution volume of 20 mL). In the sixth cycle, 10 mL of the same 0.5 mM  $[\text{Co}(\text{WS}_4)_2]^{2-}/\text{KPi}$  was added.

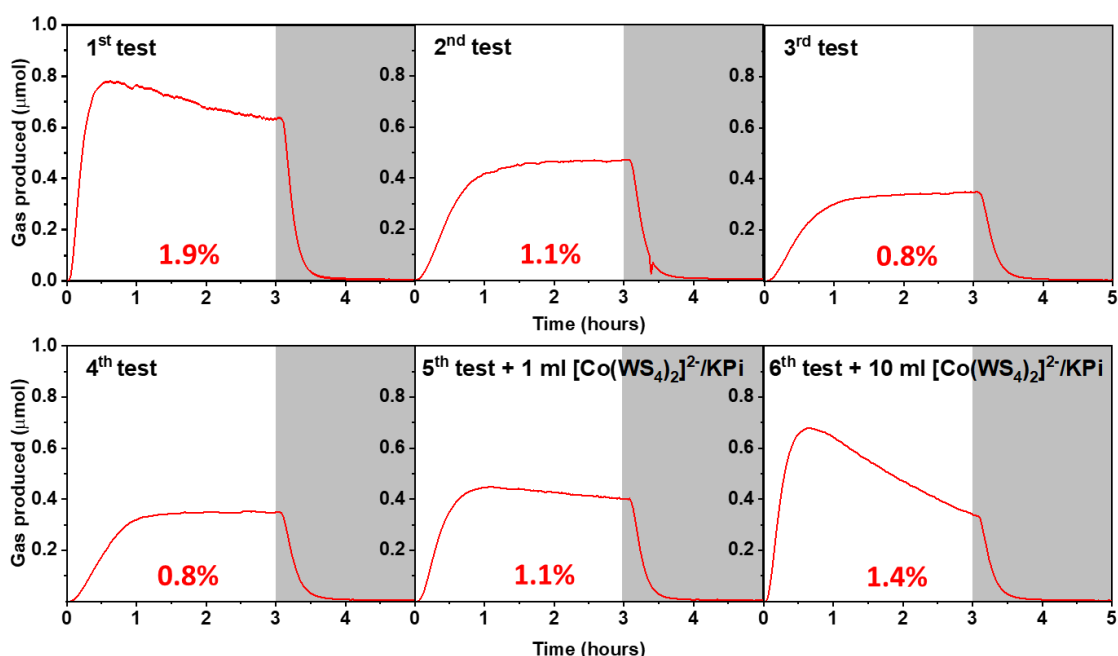


Figure 66: Real-time gas chromatography result of a single artificial leaf for various operating cycles and corresponding STH efficiency

The performance of the artificial leaf decreased over time, reaching  $\eta_{\text{STH}}$  of 0.8% after 4 cycles (**Figure 66**). We note that the most critical performance degradation occurred after the first test cycle. From the 2<sup>nd</sup> cycle to the 4<sup>th</sup> one, the degradation of performance over time was not significant. In these latter cases, the  $\eta_{\text{STH}}$  was rather stable during 3 hours of operation. The gas evolution profile as well as the performance also closely resembled that of an artificial leaf deposited in solution containing only  $\text{Co}^{2+}$  reported in **section 3.1**. In the 5<sup>th</sup> cycle, when 1 mL of 0.5 mM  $[\text{Co}(\text{WS}_4)_2]^{2-}/\text{KPi}$  was added, the performance of the device was slightly improved. Adding 10 mL of 0.5 mM  $[\text{Co}(\text{WS}_4)_2]^{2-}/\text{KPi}$  in the 6<sup>th</sup> cycle resulted in a sharp increase in

performance, reaching closely to that observed in the 1<sup>st</sup> test. However, the increased rate of degradation during the leaf operation was also observed. After 3 hours, the remained performance was in the range of the 4<sup>th</sup> cycle. These results demonstrated the progressive degradation of the monolithic device but also its capability to be healed by adding the catalyst precursor, namely the  $[\text{Co}(\text{WS}_4)_2]^{2-}$ .

### 3.5. Identifying the limiting component

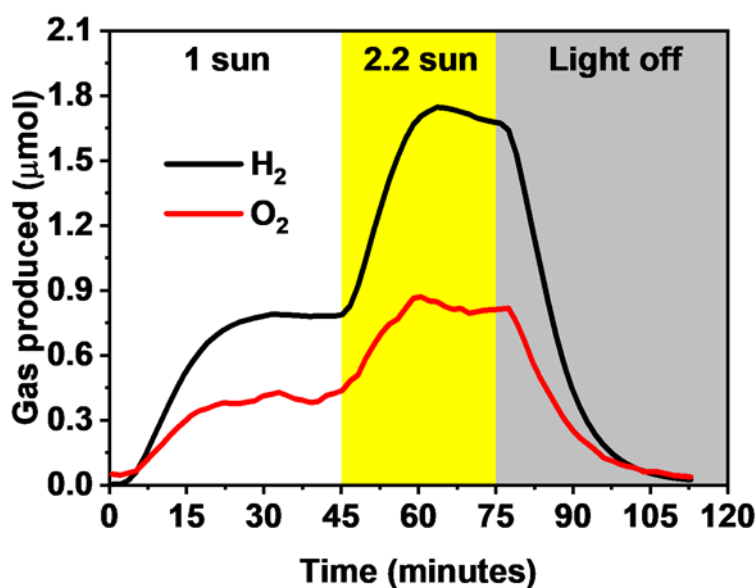


Figure 67: Real-time gas chromatography result for an artificial leaf operating in 0.1 M KPi (pH 7) and illuminated by different light power intensities

For proper improvement and optimization of devices composed of multiple components, identifying the limiting ones is desirable. We thus examined the operation of the 1.9% monolithic artificial leaf at different illumination power. To this end, the device was first conditioned under the standard 1 sun illumination until the actual gases evolution rate, quantified by an online gas chromatography, reached a steady value. Subsequently, a Fresnel lens was used to concentrate the light reaching the device to 2.2 sun. Immediately, the H<sub>2</sub> evolution rate increased, reaching a steady value which was 2.2 times higher than that obtained under 1 sun illumination (**Figure 67**). Thus, the identical  $\eta_{\text{STH}}$  of 1.9% was deduced for both 1 and 2.2 suns illumination. This result suggested that the operation of monolithic device was limited by the light harvesting capability of the 3jn-a-Si solar cell rather than the catalytic ability of the dual CoWO and CoWS catalysts nor the light harvester/catalysts interfacing.

#### 4. Invasive investigation and evaluation

The non-invasive investigation and evaluation were able to provide us insights on the general operation of the monolithic artificial leaf and the nature of the catalysts. However, many electrical/electrochemical parameters being highly valuable for better understanding of the 3jn-a-Si solar cell behavior were not obtained. Therefore, we decided to take on the risk and introduce more invasive electrochemical investigation where physical contacts would be made on the delicate surfaces of the 3jn-a-Si. With a careful manipulation to minimize damages, the return would definitely be worthy of the possible danger.

##### 4.1. Half-cell assessment

The general structure of the artificial leaf could be presented as CoWO-OEC|ITO|3jn-a-Si|Steel|CoWS-HEC. Thus, if the stainless-steel base was split in half and reconnected together using a conducting wire, then the monolithic artificial leaf became the equivalent of a tandem cell with a Steel|3jn-a-Si|ITO|CoWO-OEC photoanode and a dark Steel|CoWS-HEC cathode (**Figure 68**).

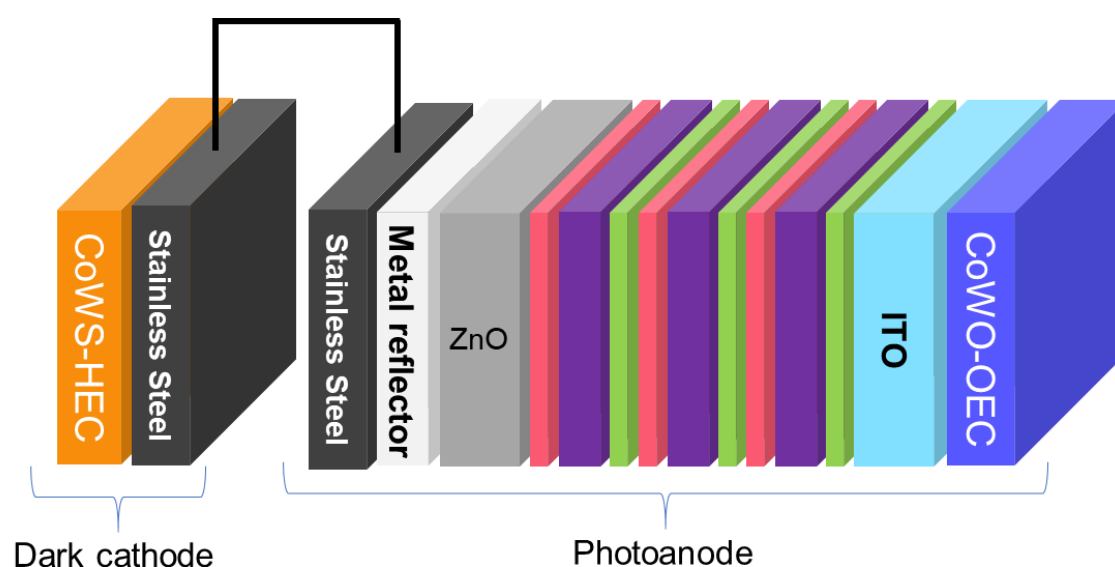


Figure 68: Expanded configuration of the artificial leaf featuring a dark cathode and a photoanode

Therefore, with a conducting wire electrically connected to the stainless-steel base and proper isolation of the opposite terminal from the electrolyte, a monolithic artificial leaf could be used safely as the working electrode for a conventional electrochemical assay. This way, the half-cell assessment could be realized with minimum damage to the 3jn-a-Si layer of the artificial leaf. The experimental setup was presented in **Figure 69**.



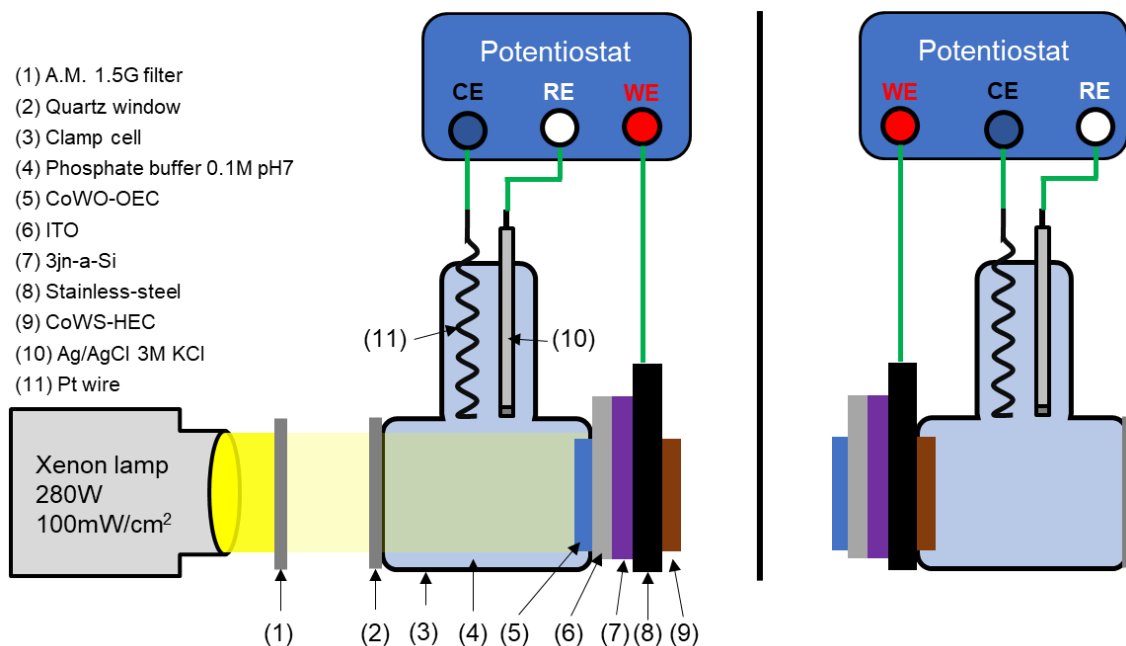


Figure 69: Experimental setup for half-cell assessment of Steel|3jn-a-Si|ITO|CoWO-OEC (left) and Steel|CoWS-HEC (right)

A potentiostat in the conventional three-electrode configuration was utilized. A Pt wire was used as counter electrode and a Ag/AgCl 3 M KCl was used as reference electrode. With the help of a typical glass PEC clamp cell, each half-cell could be assayed separately from the other. When the anodic terminal was in contact with the electrolyte, the Steel|3jn-a-Si|ITO|CoWO-OEC would act as the working electrode. Similarly, when the cathodic terminal was in contact with the electrolyte, the Steel|CoWS-HEC would act as the working electrode. Pristine 3jn-a-Si solar cell free of catalysts was also assayed as reference for the photoanode.

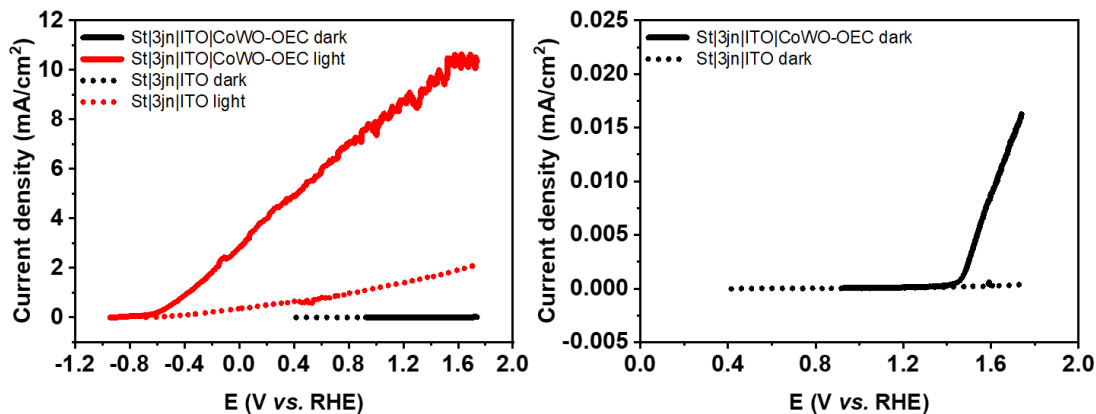


Figure 70: PEC assessment of the Steel|3jn-a-Si|ITO|CoWO-OEC photoanode (left) and zoomed view for the test without illumination (right)

For assessment of the Steel|3jn-a-Si|ITO|CoWO-OEC photoanode, linear sweep voltammetry (LSV) was conducted at the potential scan rate of 2 mV/s starting from  $E_{oc}$  to 1.8 V vs. RHE.

The dark measurement clearly depicted the activity improvement brought by the deposition of CoWO-OEC. At onset potential of 1.4 V vs. RHE, CoWO-OEC was able to catalyze the water oxidation with a modest onset overpotential of 170 mV (Figure 70, right, black straight trace). The activity without catalyst was negligible (Figure 70, right, black dotted trace). The low current density of less than  $20 \mu\text{A}/\text{cm}^2$  was recorded due to the inherent isolating characteristic of the 3jn-a-Si in the dark.

Upon illumination, the  $E_{oc}$  of the photoanode jumped to -0.94 V vs. RHE. Given that the  $E_{oc}$  of the photoanode in the dark was 0.92 V vs. RHE, a total photovoltage of 1.86 V was generated by the 3jn-a-Si. The photoanode was able to perform water oxidation with the onset potential of -0.67 V vs. RHE (Figure 70, left, red straight trace). The pristine Steel|3jn-a-Si|ITO also showed activity with similar onset potential, however, with much lower current density. Indeed, under 1 Sun illumination, the Steel|3jn-a-Si|ITO|CoWO-OEC was able to reach  $2 \text{ mA}/\text{cm}^2$  at only -0.16 V vs. RHE (Figure 70, left, red straight trace) while the Steel|3jn-a-Si|ITO required 1.65 V vs. RHE (Figure 70, left, red dotted trace).

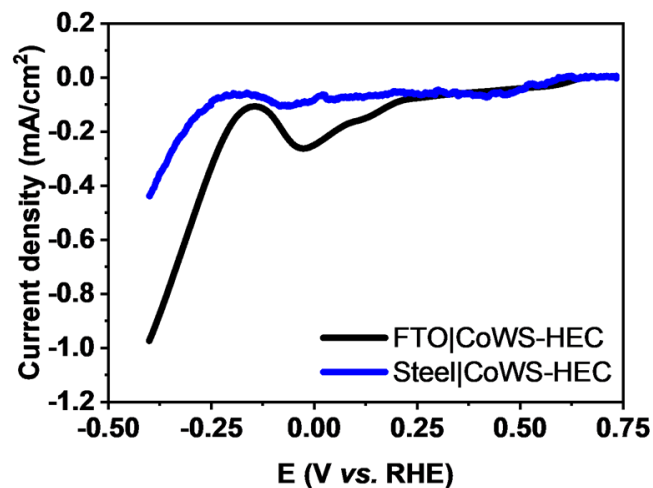


Figure 71: PEC assessment of the Steel|CoWS-HEC cathode

For assessment of the Steel|CoWS-HEC cathode, linear sweep voltammetry (LSV) was conducted at the potential scan rate of 2 mV/s, starting from  $E_{oc}$  to -0.4 V vs. RHE. The Steel|CoWS-HEC was catalytically active for the proton reduction reaction with an onset potential of -0.2 V vs. RHE, being close to that observed from a similar film deposited on FTO substrate (Figure 71).<sup>123</sup>

Thus, we conclude that the Steel|3jn-a-Si|ITO|CoWO-OEC photoanode was photocatalytically active for the photo-driven water oxidation and the Steel|CoWS-HEC cathode was catalytically active for the H<sub>2</sub>-evolution. These results demonstrated the capacity of the CoWO-OEC|ITO|3jn-a-Si|Steel|CoWS-HEC wireless device to drive the overall solar water splitting when being immersed in a pH 7 phosphate solution.

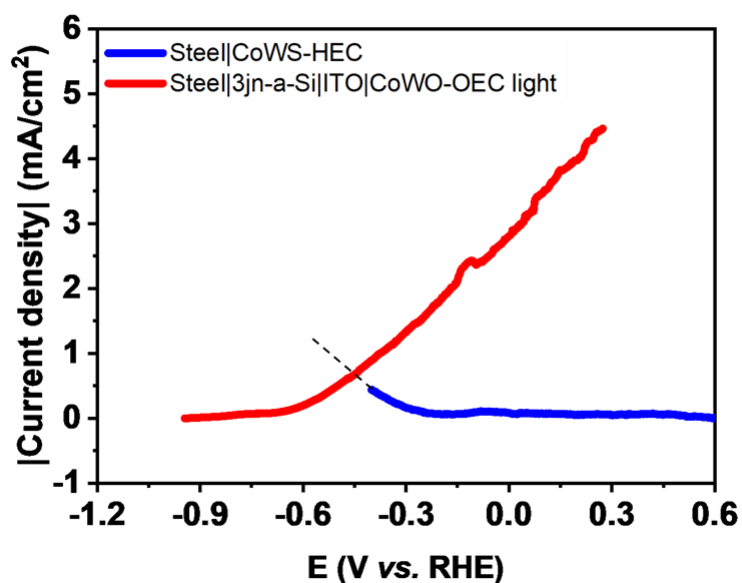


Figure 72: Prediction of the operating current density of the full cell

In an attempt to predict the operating current density of the full device, the *absolute current density vs. potential* ( $|j$ - $E$ ) curves of the two half-cells were overlapped. The operating current density would be deduced from their intersecting point. Though extrapolation of the Steel|CoWS-HEC, the current density value was determined to be around 0.7 mA/cm<sup>2</sup>. This would translate into an  $\eta_{\text{STH}}$  of 0.97% with a supposed Faradaic efficiency of 100% for the water splitting process.

## 4.2. Full cell operando assessment

As the monolithic artificial leaf functioned without the need of external bias, operando analysis was a challenging task. Herein, we aimed to probe the evolution of both the photovoltage and the photogenerated current circulating between the ITO|CoWO-OEC anodic terminal and the Steel|CoWS-HEC cathodic terminal of the monolithic device under illumination.

For this purpose, the use of a potentiostat was desirable instead of the conventional voltmeter or amperometer due to its unparalleled versatility and reliability. Indeed, a potentiostat in two electrodes mode could function as an ideal voltmeter (iVM) with infinite resistance with the built-in open-circuit-voltage (OCV) monitor method. Similarly, an ideal amperometer (iAM) with zero resistance could be obtained with the chronoamperometry (CA) method with zero applying bias. To this end, a special bi-potentiostat configuration was devised using an SP-300 equipped with two channels. This setup could enable simultaneous monitoring of the evolution of our two desired parameters, provided that proper integration was realized.

The photovoltage generated by the 3jn-a-Si could easily be measured with the iVM connecting to the stainless-steel base and the ITO layer like shown in **section 2.3**. However, introducing the iAM to the circuit of the monolithic artificial leaf was challenging. To this end, the expanded configuration of the artificial leaf in **section 4.1** was reemployed. This way, the Steel|CoWS-HEC cathodic terminal of the monolithic artificial leaf was simulated by the separated Steel|CoWS-HEC electrode. Thus, the iAM connecting to the two steel substrates would be capable of measuring the photocurrent circulating in the system during operation (**Figure 73**).

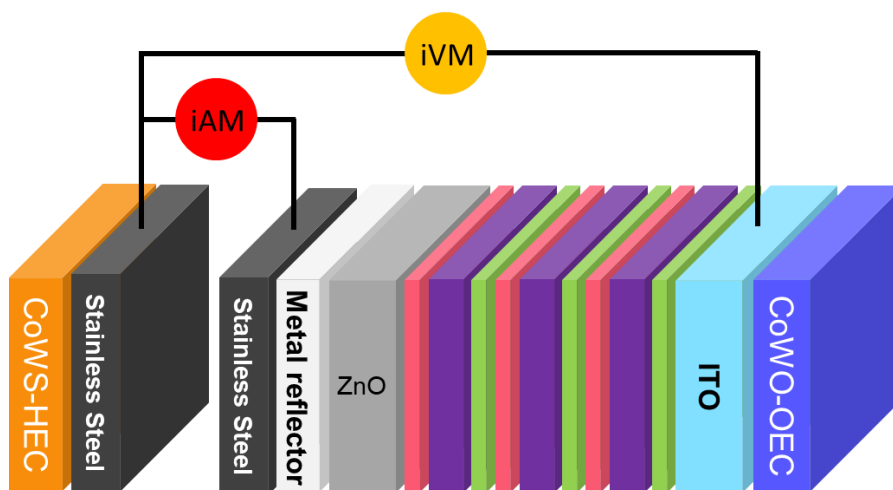


Figure 73: Integration of iAM and iVM to the expanded artificial leaf

We then proceeded to fabricate this expanded configuration. For the simulated Steel|CoWS-HEC electrode preparation, a stainless-steel base was obtained by the complete removal of the ITO, 3jn-a-Si, ZnO and metal reflector from a pristine solar cell through prolonged immersion in HCl 1 M. The piece was then connected to a piece of copper tape and covered thoroughly in thermal tape (intentionally made transparent in the schematic representation for better view), leaving an exposed working area of 1 cm<sup>2</sup> (**Figure 74**).

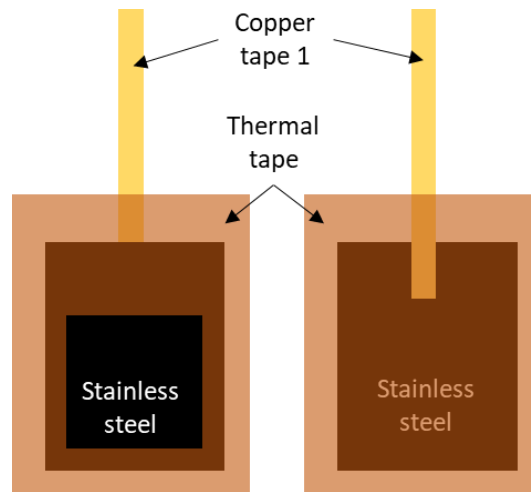


Figure 74: Preparation of the stainless-steel base for the dark cathode, front side with 1 cm<sup>2</sup> exposed stainless steel (left) and back side (right)

For the photoanode half, a piece of pristine 3jn-a-Si solar cell was used. The corresponding thermal tape masks were all removed to allow electrical contact with strips of copper tape. Thorough isolation of the contacts was done with a healthy amount of thermal tape. Only the 1cm<sup>2</sup> area of 3jn-a-Si|ITO was left uncovered (**Figure 75**).

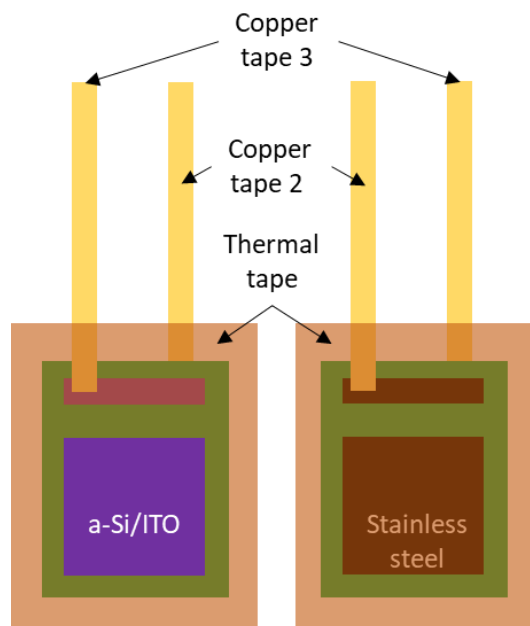


Figure 75: Preparation of the solar cell base for the photoanode, front side with 1 cm<sup>2</sup> exposed 3jn-a-Si|ITO (left) and back side (right)

Afterwards, the copper tape 1 was brought into electrical contact with the copper tape 2 to simulate the full solar cell. Photo-induced assembly of the dual catalysts in  $[\text{Co}(\text{WS}_4)_2]^{2-}$ /KPi was then conducted similarly to the monolithic configuration for 10 minutes (**Figure 76**).

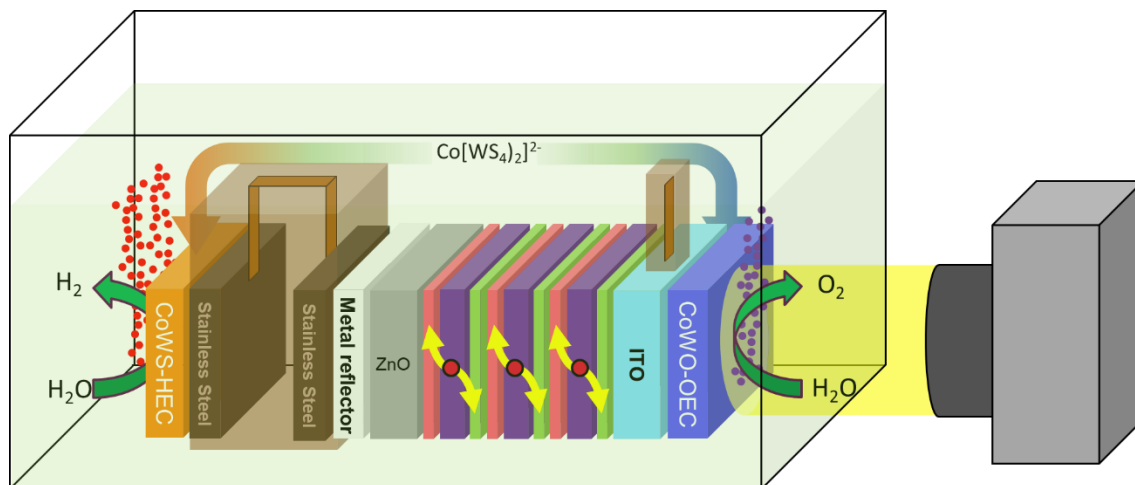


Figure 76: Photo-induced assembly of the dual catalysts on the expanded solar cell assembly

The connection between copper tape 1 and 2 was then disconnected and the two parts were rinsed with DI water, dried and introduced to a glass clamp cell. The assembly was then ready for bi-potentiostat assessment.

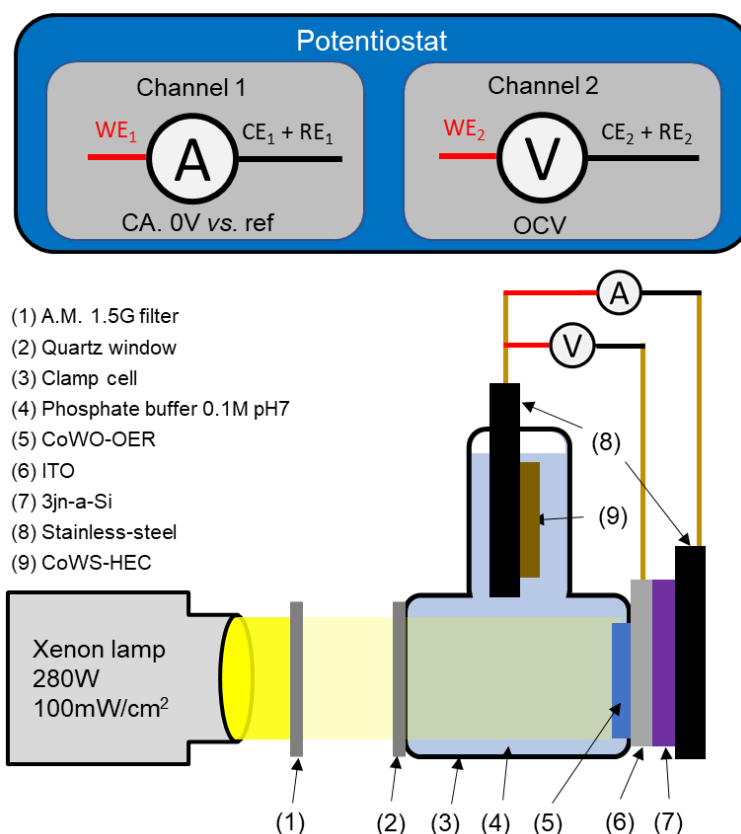


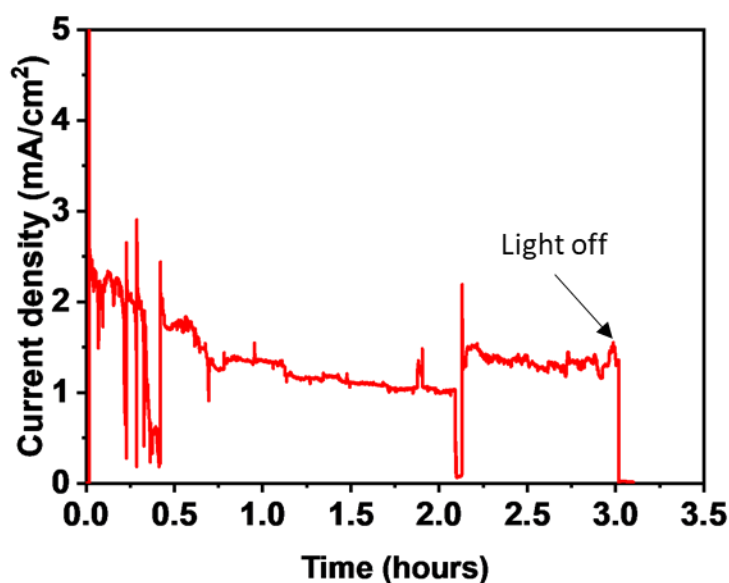
Figure 77: Bi-potentiostat setup for operando assessment of the expanded artificial leaf

The setup was represented in **Figure 77**. Here, the anodic terminal of the monolithic artificial leaf was interfaced with the pH 7 phosphate buffer and exposed to the light illumination whereas its corresponding cathodic terminal was isolated by the thermal tape. The separated Steel|CoWS-HEC electrode was immersed in the buffer but without being exposed to light illumination.

Channel 1 of the potentiostat was connected to the Steel|CoWS-HEC immersed in the electrolyte (copper tape 1) and the bare steel cathodic terminal of the solar cell (copper tape 2). This channel acted as an iAM to measure the current circulating between the two sides of the monolithic device, (e.g. by recording the current density at 0 V vs. the bare steel cathodic terminal reference electrode). Channel 2 of the potentiostat was connected to the ITO|CoWO-OEC electrode (e.g. connection was applied to the ITO area being free of CoWO-OEC layer through copper tape 3) and the Steel|CoWS-HEC electrode immersed in the electrolyte (copper tape 1). This channel acted as an iVM to measure the photovoltage generated between the anodic terminal and cathodic terminal of the monolithic device when it was illuminated, e.g. by recording the open-circuit voltage. The channels were synchronized through the controlling program so that they could start measuring at the same moment.



However, we note that the electrical connection to the ITO layer of the solar cell (i.e. with copper tape 3) could easily cause physical damages to the whole super thin ITO|3jn-a-Si layer. Therefore, prior to the full assessment using the bi-potentiostat, a similar assembly with no copper tape 3 attached to the ITO layer was fabricated and test with only the iAM by channel 1. Indeed, with this configuration, only the stainless-steel surfaces would be invasively probed, which, in theory could be scratched by the copper tape without any negative effect to the device's performance. The result is shown in **Figure 78**.



*Figure 78: Evolution of photocurrent generated by the CoWO-OEC|ITO|3jn-a-Si|Steel-Steel|CoWS-HEC assembly with no disturbance on the ITO layer under 1 sun illumination in 0.1 M KPi (pH 7)*

Upon light illumination, an initial current density of 2.5 mA/cm<sup>2</sup> was recorded circulating between the ITO|CoWO-OEC anode and the Steel|CoWS-HEC electrode. This value was higher than the 0.7 mA/cm<sup>2</sup> prediction in **section 4.1** of this chapter and would correspond to an  $\eta_{\text{STH}}$  of 1.6%, in line with the monolithic artificial leaf experiments in **section 3** when taking into account a Faradaic efficiency of 100%. Over the course of 3 hours of continuous operation, the current density experienced several steep declines, however, the performance was quickly restored afterwards. This observation provided the first insight about the instability of the artificial leaf during operation which could not be evidenced through the non-invasive gas chromatography with inherently long periods between injections. In addition, although the assembly remained functional after 3 hours, gradual decrement was observed for the recorded current density. This could be the combined result from catalysts and 3jn-a-Si degradation.

Nevertheless, with the successful monitoring of generated photocurrent, we continued with the bi-potentiostat assessment to gain additional insights on the evolution of photovoltage provided by the device.

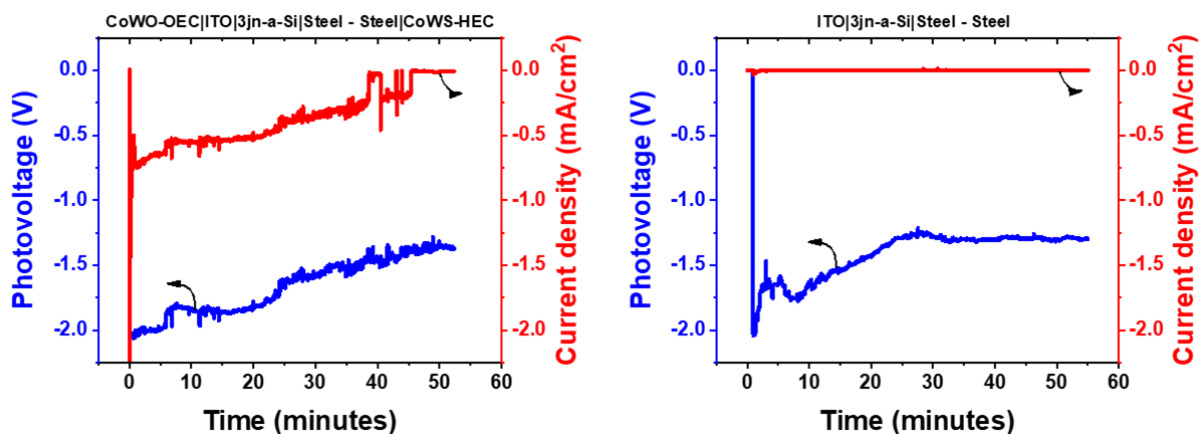


Figure 79: Evolution of photovoltage and photocurrent generated by the CoWO-OEC|ITO|3jn-a-Si|Steel-Steel|CoWS-HEC device (left) and a bare ITO|3jn-a-Si|Steel - Steel (right) solar cell under 1 sun illumination in 0.1 M KPi (pH 7)

Assessment of the CoWO-OEC|ITO|3jn-a-Si|Steel-Steel|CoWS-HEC assembly is shown in **Figure 79** left. Upon light illumination, an initial photovoltage of 2.0 V was recorded between the ITO|CoWO-OEC anode and the Steel|CoWS-HEC electrode. This value was similar to that generated when the pristine ITO|3jn-a-Si|Steel solar cell was illuminated in air (**Figure 35**). It indicated that the CoWO-OEC thin layer decorated on the anodic terminal had no negative impact to the light absorption of the ITO|3jn-a-Si|Steel solar cell. The photovoltage was largely sufficient to drive the overall water splitting on the ITO|CoWO-OEC and the Steel|CoWS-HEC electrodes. Thus, an initial current density of 0.75 mA/cm<sup>2</sup> circulating between these electrodes was recorded, which matched exceptionally well with our prediction in **section 4.1** of this chapter. However, the generated photovoltage and photocurrent were found to decrease over the device operation time (**Figure 79**, left). After nearly one hour of experiment, the photovoltage dropped to 1.25 V and the current density dropped to ~0 mA/cm<sup>2</sup>, indicating a full degradation of the device.

To confirm the effect of the dual catalysts, an ITO|3jn-a-Si|Steel - Steel assembly containing no catalysts was also assayed (**Figure 79**, right). Upon illumination, the same 2.0 V initial photovoltage was recorded. However, lacking the catalysts, no photocurrent was generated over the same duration of operation. The photovoltage also experienced similar decay to 1.25 V, albeit at significantly higher rate than when catalysts were deposited. This

could indicate that the CoWO-OEC did in fact provide protection to some extent to the underlying 3jn-a-Si.

Nevertheless, it was worth noting that a life-time of around 1 hour of the CoWO-OEC|ITO|3jn-a-Si|Steel-Steel|CoWS-HEC assembly was rather short comparing to the monolithic device, which could stand for more than 10 hours in the same electrolyte solution under light illumination. However, in the monolithic stability test, no connection to any voltmeter or amperometer was made. When repeating the bi-potentiostat measurement for several devices, reproducible results with the same short life-time of the device was obtained. Thus, we tentatively attributed this phenomenon to the application of electrical contacts to the anodic and cathodic terminals of the monolithic device which may have created physical damages leading to accelerated degradation of the device.

In any case, the degradation of the ITO|3jn-a-Si|Steel solar cell during the monolithic device operation of 50 minutes was evidenced. It caused a voltage drop and therefore a drop of the overall solar water splitting performance (**Figure 78**). In other words, the CoWO-OEC layer together with the built-in ITO layer could not perfectly protect the inner 3jn-a-Si light harvesting component against corrosion. Actually, the oxidative corrosion of a native Si electrode could occur at an extremely low O<sub>2</sub> dissolved concentration, e.g. 15 ppb.<sup>152</sup> Thus, if a crack, a pin-hole or even just a non-perfect coverage was present on the ITO|CoWO-OEC layer, the underlying Si layer would be quickly oxidized by the O<sub>2</sub> evolved on the surface of the same ITO|CoWO-OEC layer.

### 4.3. *In-situ* assessment with tri-potentiostat and gas chromatography

The accelerated degradation of the 3jn-a-Si when immersed in the electrolyte prevented in-depth photoelectrochemical study of the artificial leaf. Thus, the more stable PV-electrolyzer configuration where the 3jn-a-Si solar cell was kept outside of the electrolyte would be beneficial for our purpose. Indeed, since the monolithic artificial leaf was an integrated PV-electrolyzer, studying the fully expanded configuration could also provide insights on its operation. Granted, the expansion came at the cost of increased Ohmic resistance and risk of physical damages. However, with the more elaborated structure, more electrical contacts could potentially be made, opening new possibilities for designing assessment system.

Conventionally, the  $\eta_{\text{STH}}$  conversion yield assessment for PV-electrolyzer devices was usually deduced by overlapping the I-V curve of the solar cell and that of the electrolyzer to identify the ideal operation current.<sup>59</sup> Such a deduction ignored all Ohmic drops that might present in the system. The actual  $\eta_{\text{STH}}$  value could be calculated by quantification of the desired products like H<sub>2</sub> for solar water splitting. However, none of these approaches provided insights about the individual electrodes during operation, e.g. the actual potential provided by the solar cell to each electrode, the actual catalytic current circulating within the system or the Faradaic yield. To fill this gap, we devised an *in-situ* assessment setup employing tri-potentiostat and gas chromatography to simultaneously monitor the behavior of the solar cell and the electrolyzer during the operation of the whole system in relation to the performance.

We then attempted on fabricating the extended PV-electrolyzer configuration of the artificial leaf (CoWO-OEC|ITO – [ITO|3jn-a-Si|Steel]<sub>air</sub> – Steel|CoWS-HEC). First, an extended configuration of the 3jn-a-Si solar cell (ITO – [ITO|3jn-a-Si|Steel]<sub>air</sub> – Steel) was required. We realized that it could be achieved through slight modification of the setup used in **Figure 36** in **section 2.3.2**. Specifically, the FTO glass connected to the anodic terminal of the 3jn-a-Si solar cell was replaced by an ITO glass electrode while the FTO glass connected to the cathodic terminal of the 3jn-a-Si solar cell was replaced by a bare stainless-steel electrode. Thermal tape was used to secure and isolate the electrical connection as well as to limit the exposed area of those electrodes to 1 cm<sup>2</sup>, which was equal to that of the monolithic artificial leaf. Afterwards, standard photo-induced assembly of the CoWO-OEC and CoWS-HEC on the ITO and stainless-steel would yield the extended configuration of the artificial leaf that we desired (**Figure 80**).

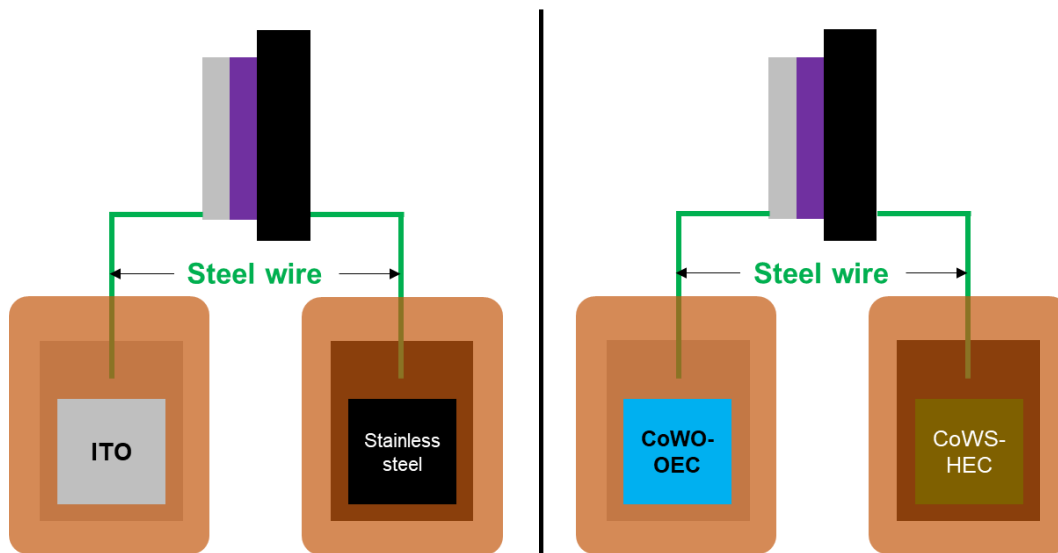


Figure 80: The extended 3jn-a-Si solar cell (left) and extended artificial leaf (right)

The device was then ready for assessment. A schematic representation of the experimental setup is presented in **Figure 81**.

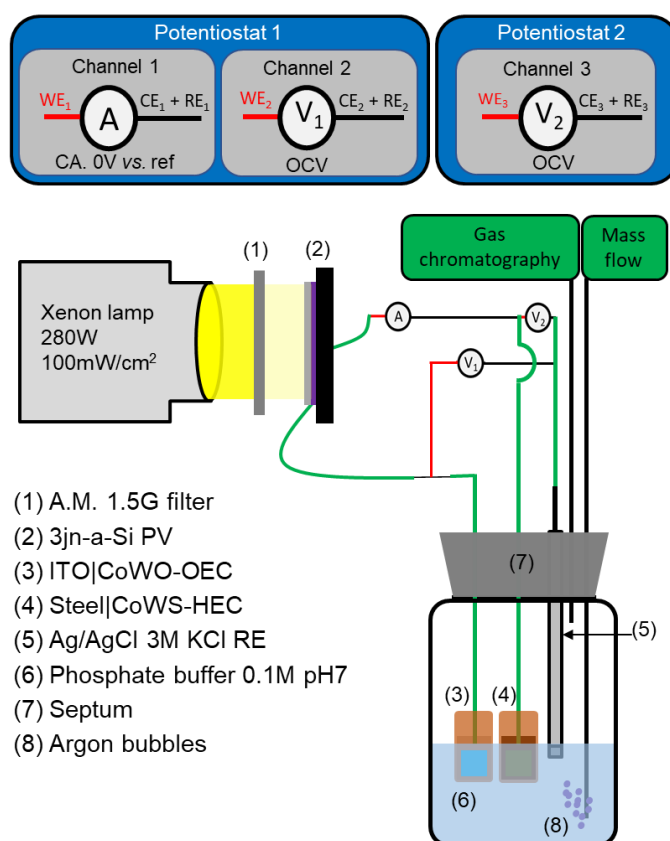


Figure 81: Schematic representation of tri-potentiostat configuration coupled with gas chromatography to assay the extended artificial leaf

Here, the ITO|CoWO-OEC and Steel|CoWS-HEC electrodes were immersed in 0.1 M KPi (pH 7) solution with extending steel wires to respectively connect to the anodic and cathodic terminals of the 3jn-a-Si solar cell which was kept out of the electrolyte. Channel 1 working as an iAM was inserted to the circuit through the connection between the Steel|CoWS-HEC electrode and the steel cathodic terminal of the 3jn-a-Si solar cell. This way, the photogenerated current circulating through the whole system could be monitored through zero applied-bias chronoamperometry method. The remaining channel 2 and 3 were used as two iVMs to record the potential of the ITO|CoWO-OEC and the Steel|CoWS-HEC versus a Ag/AgCl 3M KCl reference electrode, e.g. by recording their respective open-circuit potential when the solar cell was illuminated. Gas chromatography working in continuous automatic sampling mode was utilized to monitor *in-situ* the gaseous products generated during operation. All potentiostat channels and gas chromatograph were started at the same moment.

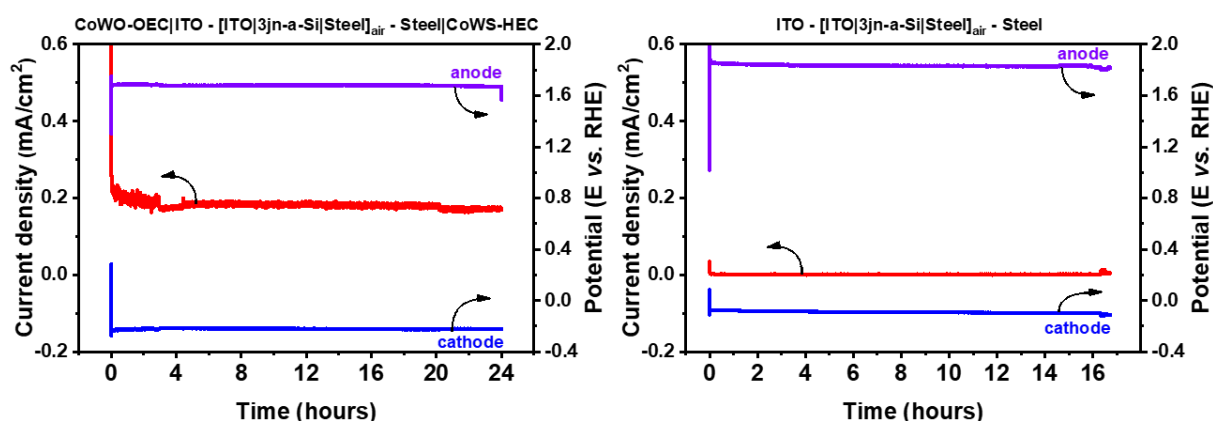


Figure 82: Evolution of anodic potential, cathodic potential and catalytic current density generated by the extended artificial leaf (left) and the extended 3jn-a-Si solar cell (right) over time

Upon illumination by 1 sun light, an anodic potential of 1.65 V and a cathodic potential of -0.25 V vs. RHE were recorded on the ITO|CoWO-OEC and Steel|CoWS-HEC electrodes, respectively. These potentials were found to be stable over 24 hours of experiment (**Figure 82**, left, purple and blue traces). In total, the 3jn-a-Si solar cell generated a stable photovoltage of 1.9 V between the ITO|CoWO-OEC and Steel|CoWS-HEC electrodes. This photovoltage was identical to that recorded during the dry assessment of the 3jn-a-Si solar cell using the conventional two electrodes configuration in **section 2.3**. Regarding the photogenerated catalytic current circulating through the system, an initial current density of  $\sim 0.2$  mA/cm<sup>2</sup> was recorded. It was then slightly dropped during the first 3 hours of operation before reaching a steady stable current density of  $\sim 0.18$  mA/cm<sup>2</sup>. After 24 hours of operation, a total of  $\sim 10\%$  performance loss was recorded.

An extended 3jn-a-Si without catalyst was also assayed. Upon illumination by 1 sun light, slightly different anodic potential of 1.83 V and a cathodic potential of -0.09 V *vs.* RHE were recorded on the ITO and Steel electrode, respectively. These values were also stable over 16 hours of experiment (**Figure 82**, right, purple and blue traces) and added up to 1.92 V, which was in the same range with the extended artificial leaf assessment as well as the dry test of the 3jn-a-Si solar cell mentioned above. However, lacking the catalysts, the catalytic current density measured was  $\sim 0$  mA/cm<sup>2</sup>, which was logical and also fitting with the bi-potentiostat investigation in **section 4.2**.

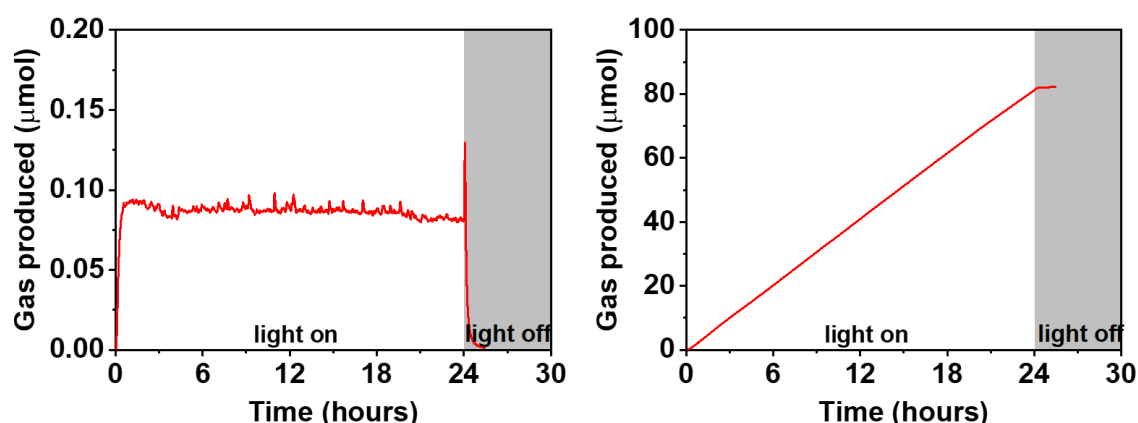


Figure 83: In-situ gas chromatography monitoring of H<sub>2</sub> generated during the tri-potentiostat assessment of the extended artificial leaf in real-time (left) and accumulated (right) mode

Getting back to the extended leaf, *in-situ* gas chromatography monitoring showed a stable evolution of hydrogen over time (**Figure 83**, left), which fit well with the stable current density recorded above (**Figure 82**, left, red trace). On the basis of 24 hours analysis, a total of 82  $\mu$ mol of hydrogen was generated (**Figure 83**, right), corresponding to an  $\eta_{\text{STH}}$  of 0.23%. A Faradaic efficiency of  $\sim 100\%$  was calculated using Eq.18, confirming the photogenerated current was solely used to drive the overall solar water splitting.

However, we note that this performance was much lower than the 1.9% obtained with the non-invasive method reported in **section 3.2.1**. The reason for this huge difference could be the price of the invasive assessment causing undesirable perturbation on the ITO and the underlying 3jn-a-Si through physical contact during the wiring step. Indeed, when the ITO layer was not disturbed, the current density circulating the device was recorded to be around 2 mA/cm<sup>2</sup> (**Figure 78**), which is 10 times higher than that recorded during the tri-potentiostat assessment. Thus, the difference of nearly 10 times in  $\eta_{\text{STH}}$  from 1.9% of the monolithic artificial leaf to 0.23% of the extended artificial leaf could be largely attributed to this invasive assessment.

We also note that both the aforementioned  $\eta_{\text{STH}}$  are significantly lower than the 4.7% reported by Nocera's group for the decoupled system using the same 3jn-a-Si solar cell to power a pair of Co-OEC and NiMoZn-HEC.<sup>66</sup> This low performance could be the combined effects from several factors. The first could be the inferior batch of 3jn-a-Si solar cell we received that inherently possesses low fill factor. The second might be related to the fact that in Nocera's work, the NiMoZn-HEC was grown on a Ni mesh electrode having high specific surface area while ours were grown on planar electrodes.

Nevertheless, given that the 3jn-a-Si solar cell provided stable anodic and cathodic potentials to the ITO|CoWO-OEC and the Steel|CoWS-HEC electrodes, we attributed the slight performance degradation of the extended artificial leaf system to a partial corrosion of the catalysts. Indeed, as reported in **section 3.2.2**, dissolved Co and W species were found in the phosphate electrolyte during the system operation by the ICP-OES analysis.



## 5. Conclusions and perspectives

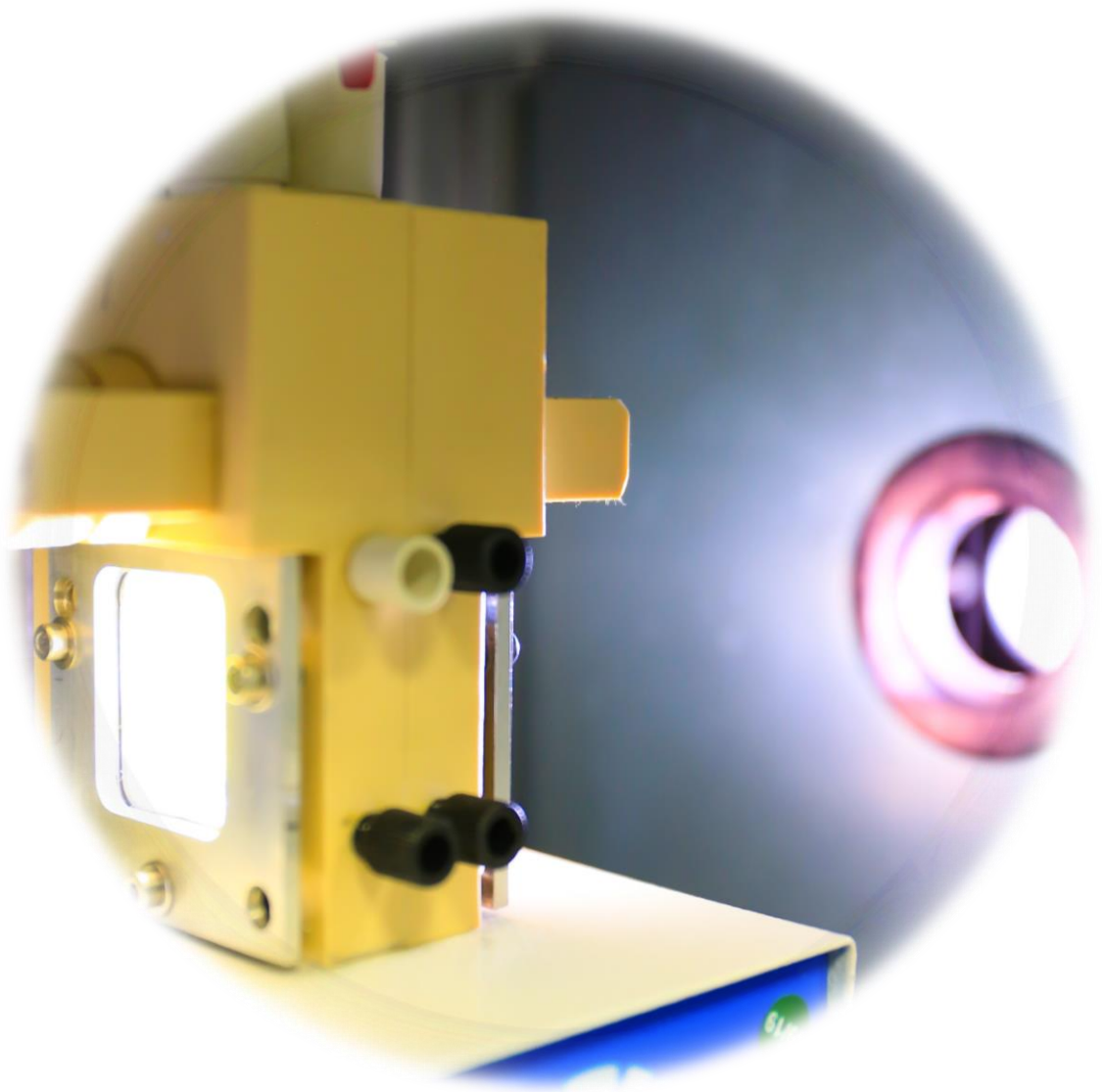
Employing a sole  $[\text{Co}(\text{WS}_4)_2]^{2-}/\text{KPi}$  solution, we were able to drive the assemblage of a pair of  $\text{O}_2$ -evolving and  $\text{H}_2$ -evolving catalysts onto the respective anodic and cathodic sides of an amorphous triple junction Si solar cell when the latter is illuminated by solar light. This rather simple solution process, requiring no high-tech facilities, enabled the creation of a complete CoWO-OEC|ITO|3jn-a-Si|Steel|CoWS-HEC monolithic artificial leaf for the overall solar water splitting application. The current best device offered an honorable solar-to- $\text{H}_2$  conversion yield of 1.9% when operating under benign conditions, e.g. in a pH 7 phosphate buffer solution. The performance of the device was found to be limited by the light harvesting capability of the ITO|3jn-a-Si|Steel solar cell. Thus, higher solar water splitting rate was achieved with higher light power intensity. The device performance decreased over few hours of operation time due to the partial dissolution of the catalysts that caused changes in their chemical composition and morphology. A device suffered from this degradation was healable as its initial performance could be almost recovered by adding the  $[\text{Co}(\text{WS}_4)_2]^{2-}$  catalyst precursor into the operating phosphate buffer. However, the device was not fixable if the 3jn-a-Si light harvester component which was sandwiched between the ITO|CoWO-OEC and Steel|CoWS-HEC layers was degraded, e.g. due to a chemical corrosion. As such, in a bi-potentiostat measurement, the 3jn-a-Si solar cell showed a photovoltage drop from 1.9 to 1.23 V and therefore a violent drop of photogenerated current from 0.75 to 0 mA/cm<sup>2</sup> after just 1 hour of experiment. It seems that the electrical contact made on the ITO surface of the 3jn-a-Si solar cell is largely responsible for this degradation of performance. In order to achieve an efficient and stable monolithic device, it would require:

- (i) The identification of novel OER, HER dual catalysts which are efficient and robust against the (electro)chemical corrosion.
- (ii) An innovative strategy to deposit the catalysts onto the 3jn-a-Si solar cell surface to perfectly protect this extremely sensitive component, e.g. suffered from chemical corrosion even with very low  $\text{O}_2$  concentration.

The novel tri-potentiostat setup coupled with *in-situ* gas chromatography would possibly have valuable contribution to fulfill those requirements provided if a correct engineering of the contact on the delicate ITO surface that does not lead to degradation of the solar cell could be achieved. Indeed, simultaneous monitoring of various parameters of not only the device as a whole but the individual components would undoubtedly be useful when assaying various devices made of different materials. Its application would also be of extreme importance for the tandem artificial leaf in the next chapter.

## Chapter IV

### The tandem artificial leaf



## 1. Introduction

Ever since their respective foundation, the SolHyCat and CECS research groups have been diligently developing and investigating catalysts and light-harvesters for solar fuels generation. As a result, considerable progress has been made on designing and synthesizing or fabricating highly active components as well as on their optimum integration into highly functional photoelectrodes. However, progress on constructing a complete and operational solar fuel generator was still rather limited. Therefore, to strengthen the long-established collaboration between the two groups, as well as demonstrating and emphasizing on the paramount importance of cooperation to reach a common goal, we decided to combine the latest photoelectrodes from each laboratory to build a viable artificial leaf capable of unassisted solar fuels generation. For this purpose, the superior flexibility and simplicity of the tandem was chosen.

Indeed, as previously introduced, tandem photoelectrochemical cell (PEC) takes advantage of the simple formation of solid-liquid junction to significantly drive down the complexity and cost of the fabrication process. Moreover, the solar spectrum can also be utilized to a higher extent when light harvesters with complementary bandgaps are combined. In addition, with the spatial separation of the component electrodes, which greatly facilitates their individual tuning and optimization using various materials, the tandem configuration has been shown to be an ideal base structure for integrating electrodes of different origins. All that required to form a complete device is simply connecting suitable electrodes and/or photoelectrodes in series.<sup>153</sup>

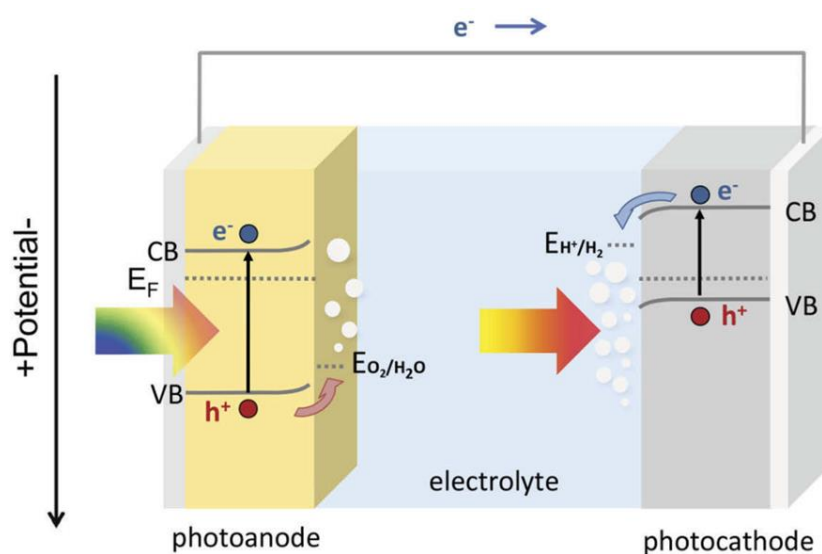


Figure 84: Schematic representation of a PEC tandem cell<sup>153</sup>

Truly, using the tandem configuration, as long as the band gaps and band positions are suitable, a vast array of electrodes or photoelectrodes can be combined. In the early stage of development, inorganic photoelectrodes of similar nature like hematite ( $\text{Fe}_2\text{O}_3$ ) were frequently studied<sup>153,154</sup> with  $\eta_{\text{STH}}$  reaching 0.11% as reported by Khan's group in 2006.<sup>155</sup> Recently, advancement in material design has brought about combination of inorganic photoelectrodes of different nature with improved performance like  $\text{BiVO}_4$  photoanode and  $\text{Cu}(\text{In}, \text{Ga})\text{Se}_2$  photocathode boasting  $\eta_{\text{STH}}$  of as much as 1.01%.<sup>156</sup> In addition, hybrid configuration between inorganic and organic systems was also intensively studied like the  $\text{TaON}|\text{CoO}_x$  photoanode coupled with  $\text{CuGaO}_2|\text{RBG-174}|\text{CoHEC}$  photocathode.<sup>157</sup> Although the  $\eta_{\text{STH}}$  was considerably lower at only  $5.4 \times 10^{-3}\%$ , the integration of the versatile molecular system brings increased degree of freedom for designing novel noble-metal-free components, potentially aiding the discovery of revolutionary operating mechanisms.

In this chapter, the hybrid tandem configuration will be employed. The photocathode was a dye-sensitized  $\text{NiO}|\text{RuP}_4\text{-CoN}_4\text{H}$  from SolHyCat. The photoanode was a  $\text{BiVO}_4$ -based from CECS. The result was the creation of a hybrid dye-sensitized photoelectrosynthetic cell. A specialized reactor designed by SolHyCat was employed to aid the formation of the complete device as well as to facilitate its performance evaluation down the line. Especially, using the bi-potentiostat assessment setup presented in **chapter 3**, in-depth study of the resultant tandem device was also conducted.

## 2. The two photoelectrodes

### 2.1. The BiVO<sub>4</sub>|CoPi photoanode

The semiconductor-based photoanodes generally are fabricated with layer-based structure. On a conducting support like FTO, a layer of semiconducting material is deposited, followed by the co-catalyst layer(s). Upon illumination, the incoming photons with suitable energy are absorbed by the semiconductor, knocking electrons out of the valence band (VB) to the conduction band (CB), effectively causing the generation of the electron (e<sup>-</sup>) - hole (h<sup>+</sup>) pairs. The electrons are then guided to the back contact, and the holes to the catalyst due to the formation of a rectifying solid-liquid junction between the semiconductor-catalyst assembly and the electrolyte. If the valence band of the semiconductor is at higher energy than the water oxidation redox equilibrium, the guided holes can be transferred and the reaction can happen.

With bandgap of 2.4 eV, BiVO<sub>4</sub> is capable of absorbing a large portion of visible light and is stable in aqueous condition with pH close to neutrality. Coupling with suitable band edges, it has been receiving substantial attention as material for photoanodes in tandem PEC cells for solar water splitting.<sup>158-160</sup> At CECS, research efforts have been mobilized to improve the performance of BiVO<sub>4</sub> through the structural improvement brought by electrochemical deposition as well as intrinsic activity enhancement from doping.

Following the recent work from CECS group,<sup>161</sup> which built on the work of Choi's group,<sup>159</sup> a base photoanode consisting of crystalline BiVO<sub>4</sub> nanoplates was fabricated. First, a film containing a fixed amount of BiOI was electrodeposited on FTO glass substrate through careful control of the amount of charges passing through the electrode. The main structure of this 900 nm thick layer is composed of intertwined thin blades of BiOI with occasional formation of over-deposited domains resembling a flower on top (**Figure 85a**). Then, excess amount of vanadium precursor was brought to the BiOI surface through drop-casting and thermal evaporation of the DMSO solvent. Afterwards, a modified annealing process with extra drying time and milder overall temperature was conducted to form BiVO<sub>4</sub>. The porous structure of BiOI limited the growth of BiVO<sub>4</sub>, thus, similar porous structure of BiVO<sub>4</sub> was obtained, drastically improving the surface area of the layer (**Figure 85b**) compared to flat substrates. The excess amount of vanadium was removed through immersion in NaOH 1 M.

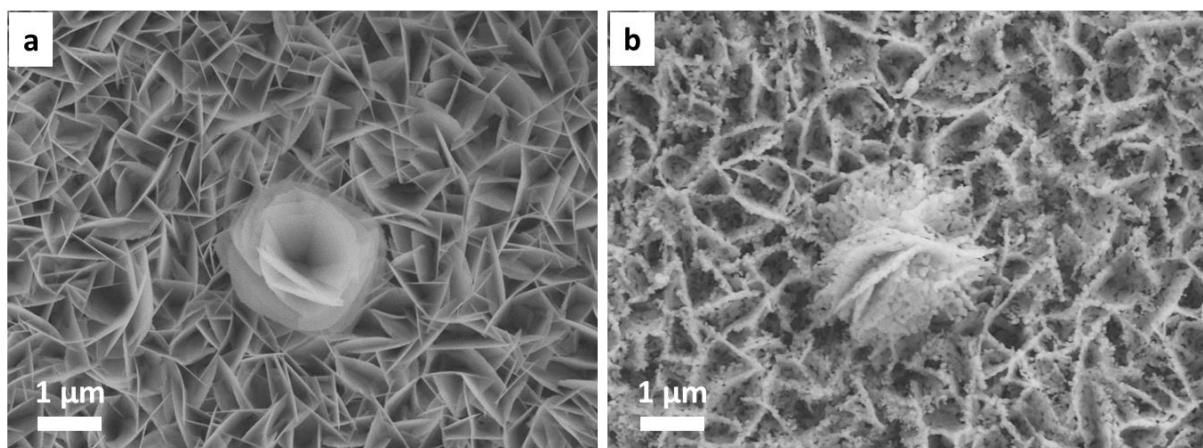
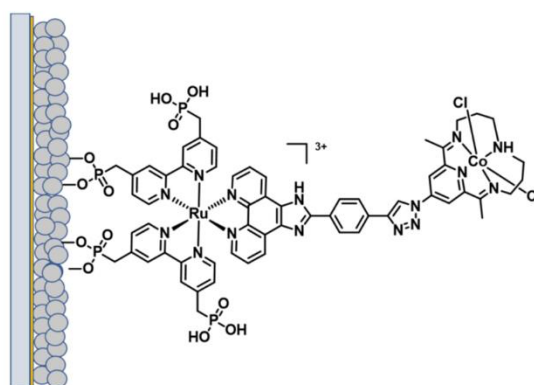


Figure 85: SEM images of BiOI (a) and resultant BiVO<sub>4</sub> (b) on FTO glass

To further boost the performance of the photoelectrode, we opted for the addition of a layer of CoPi cocatalyst onto the BiVO<sub>4</sub> layer following an electrodeposition method adapted from Nocera's group.<sup>131</sup> To this end, the BiVO<sub>4</sub> electrode was held at 1.1 V vs. Ag/AgCl in a 0.5 mM solution of Co(NO<sub>3</sub>)<sub>2</sub> in 0.1 M phosphate buffer (pH 7) until a charge density of 50 mC/cm<sup>2</sup> passed through the electrode.

## 2.2. The NiO|RuP<sub>4</sub>-CoN<sub>4</sub>H photocathode

Solar fuels generation using bio-inspired approach has always been the strong point of SolHyCat research group. Through the extremely versatility brought by organic synthesis, organometallic compounds with interesting working mechanism and high activity were created. This elevated degree of freedom could significantly broaden the possibilities for discovery of novel pathways to better understand and improve the photocathode, which is currently the limiting factor in fabricating full tandem setup.<sup>162</sup> Here, the recent progress from SolHyCat on developing functional dye-sensitized photocathode using supported molecular assembly of light harvester and catalyst was nominated for the construction of the tandem cell.



F108-templated NiO films

Figure 86: Schematic representation of The NiO|RuP<sub>4</sub>-CoN<sub>4</sub>H photocathode (courtesy of Dr. Emmanouil Giannoudis)

The photocathode features dyads composed of the recently reported ruthenium tris-diimine complex (RuP<sub>4</sub>) photosensitizer<sup>163</sup> (dye) and the well-studied cobalt tetraaza-macrocyclic (CoN<sub>4</sub>H) catalyst<sup>118</sup> grafted onto the wide bandgap p-type NiO base semiconductor (**Figure 86**). The photocathode was shown to be capable of both proton reduction to generate H<sub>2</sub> and CO<sub>2</sub> reduction to yield CO. Indeed, previous reports showed that the CoN<sub>4</sub>H catalyst has been used either in HER or CO<sub>2</sub>RR in aqueous<sup>118</sup> and non-aqueous<sup>164</sup> conditions. The samples were kindly prepared and provided by Dr. Emmanouil Giannoudis, former PhD candidate in the SolHyCat group, following the procedure described in his PhD thesis.

The working mechanism of a photocathode in a full dye-sensitized photoelectrosynthetic cell can be seen in **Figure 87**. Unlike their conventional semiconducting counterpart, in dye-sensitized photoelectrodes, it was the dye molecule that absorbs the incoming photons and as a result is brought to its excited state. If a suitable semiconductor with valence band at a higher energy level than the highest occupied molecular orbital (HOMO) of the dye is present, an electron is then “injected” from the valence band of this semiconductor to fill the vacant position made upon excitation in the HOMO level of the dye molecule. Thus, a hole (h<sup>+</sup>) is left behind in the semiconductor and will concurrently diffuse to the back contact, which is a FTO on glass substrate in this case. The excited dye, now contains an additional electron, off-loads this electron to the adjacent catalyst to “regenerate” itself back to the lower energy state. When two of such electrons are accumulated successfully without any undesired recombination, the reduction of proton to hydrogen or CO<sub>2</sub> to its corresponding fuels can happen.

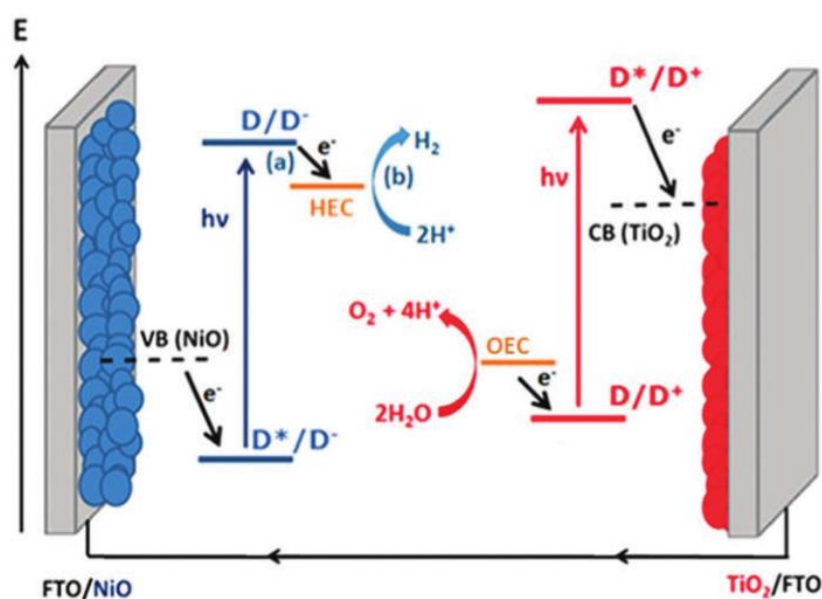


Figure 87: Schematic representation of a dye-sensitized photoelectrosynthetic cell <sup>162</sup>

### 3. Integration of the photoelectrodes into full cell

Although possessing different working mechanisms, as long as a matching flow of sufficiently energetic charge carriers is achieved, the two photoelectrodes can be combined to make an operational tandem cell. This combination can be done simply by making an Ohmic contact between the FTOs of the two photoelectrodes (**Figure 88**). In a true tandem configuration, the two photoelectrodes are positioned along the incoming light path so that the unabsorbed photons from the one in the front can be absorbed by the other in the back. Thus, more portions of the light spectrum can be useful. Upon illumination, the photogenerated holes from BiVO<sub>4</sub>/CoPi photoanode are used to drive the water oxidation reaction, while the electrons from NiO/RuP<sub>4</sub>-CoN<sub>4</sub>H photocathode are used to drive the fuel-forming reaction(s). Their respective halves of the photogenerated pair (i.e. electrons from BiVO<sub>4</sub>/CoPi photoanode and holes from NiO/RuP<sub>4</sub>-CoN<sub>4</sub>H photocathode) diffuse to the back contact then recombine with one another, thus closing the circuit.

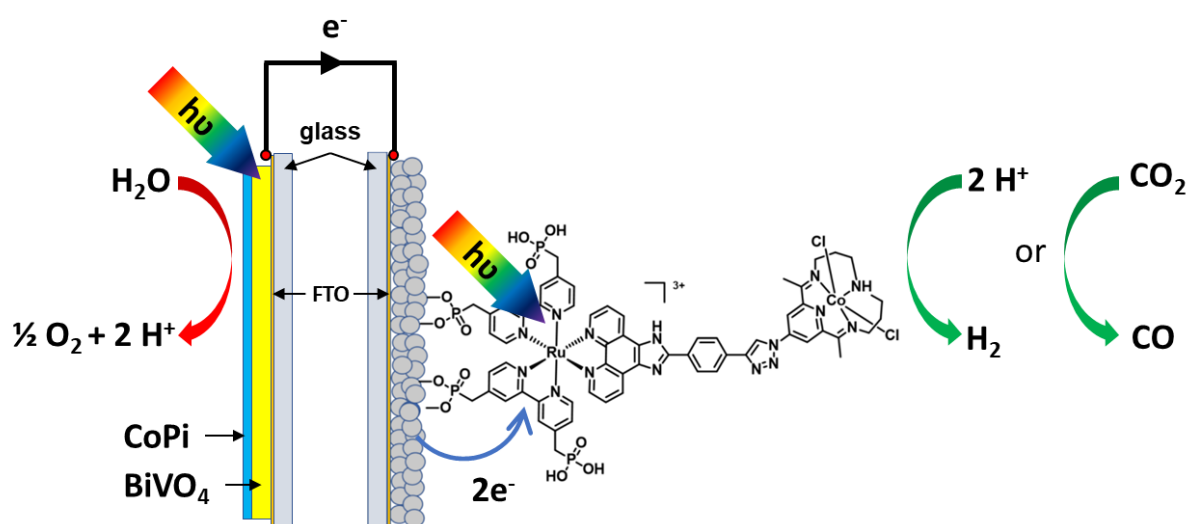


Figure 88: Schematic representation of the full CoPi|BiVO<sub>4</sub>|FTO–FTO|NiO|RuP<sub>4</sub>-CoN<sub>4</sub>H tandem cell



### 3.1. Cell integration using the specially designed reactor

The formation of the full tandem cell from two photoelectrodes is simple. However, if precise and consistent assessment is the goal, then a carefully designed environment with fixed or preferably controllable parameters is desired. To this end, a specialized reactor designed by SolHyCat is employed.

Polyvinyl chloride (PVC) was chosen as the material for the reactor for various reasons. First, the material is rigid, but also ductile enough to resist the formation of cracks while being drilled or cut. In addition, it is only damaged by organic solvent, and is stable in most aqueous environment, including inorganic acids, alkalines, and salt, covering a wide range of pH operation. Plus, it has low gas permeability to a large variety of gas, including H<sub>2</sub>, O<sub>2</sub> and CO<sub>2</sub>.<sup>165</sup>

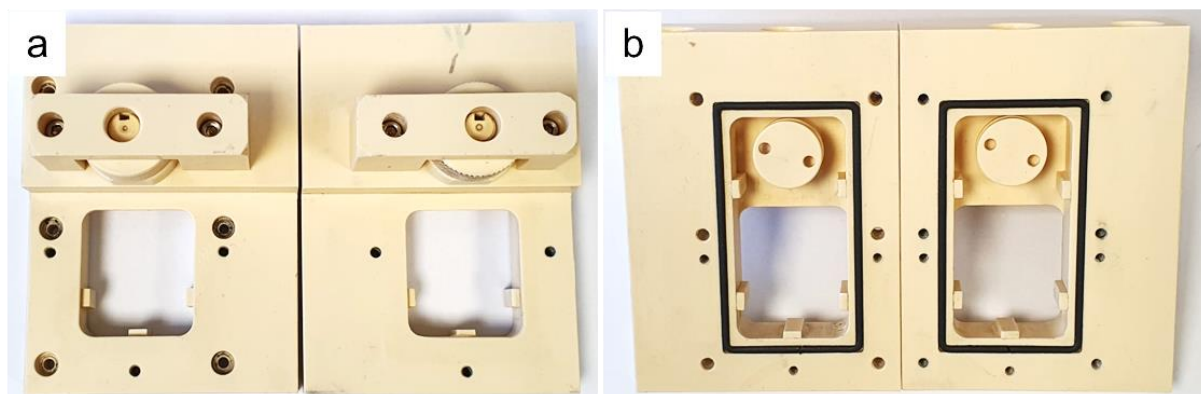
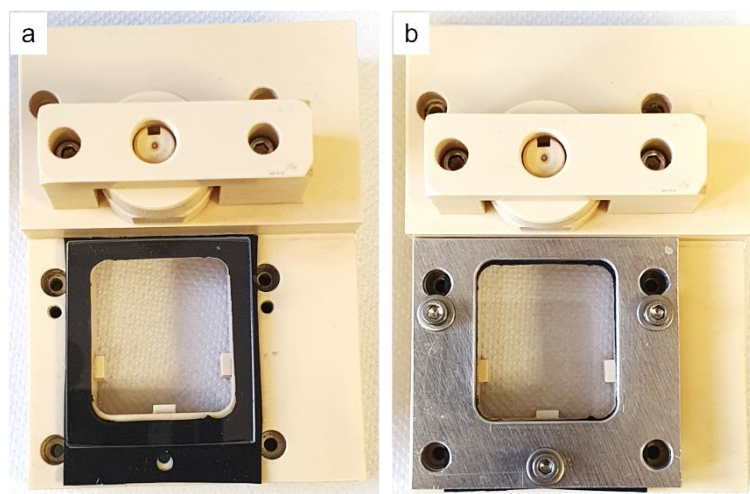


Figure 89: Photos showing the outer (a) and inner (b) view of the specialized reactor designed by SolHyCat

The reactor consists of two main halves which can be joined together by metal screws. Rounded-corner rectangular holes with size of 30 x 35 mm were made to establish the light path going through the system. On the outer side of these holes, screw threads were added for the subsequent integration of quartz windows (**Figure 89a**). A view of the inner side of the two halves shows 11-mm-deep rounded-corner rectangular cavities measured at 30 x 67 mm (**Figure 89b**). When the two halves are joined together, these cavities will form the reacting compartment of the system. Two round-shaped holders were also included to secure the photoelectrodes. Rubber strips were also placed around the cavities to avoid electrolyte leakage after assembly. Along the top and the sides of the reactor, various round-shaped holes were made to facilitate electrical contacts and gas/electrolyte in/outlets. For the integration of reference and counter electrodes, small separated compartments were also made in the reactor

and connected with the main compartment through porous ceramic frits. To prevent gas/electrolyte leakage from these connecting points, silicon septa were also employed.

With the help of aluminum plates, quartz windows were secured to the cell by metal screws, ensuring unimpeded light transmission. To avoid possible damage caused by the hard materials in contact with each other (i.e. quartz – aluminum and quartz – PVC), rubber gaskets were added in between. The rubber gaskets also improved the water-tightness of the integration (**Figure 90**).



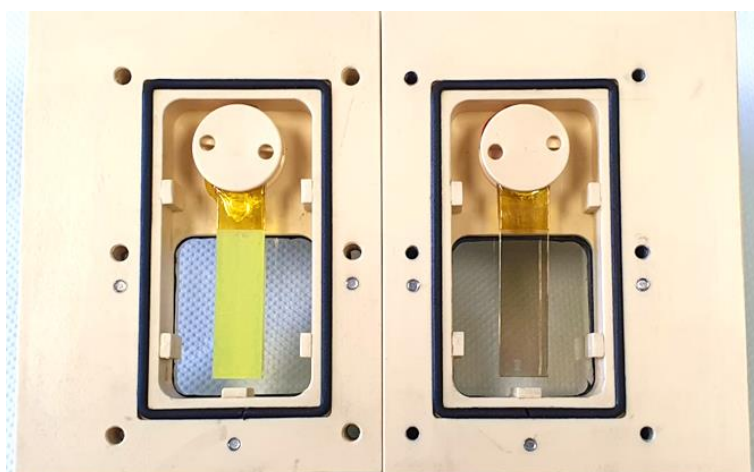
*Figure 90: Integration of quartz window to the reactor. (a) view of the rubber gasket and (b) completed integration*

Subsequently, the photoelectrodes, each measured at 10 x 40 mm with active area of 10 x 30 mm were secured to the round-shaped holders. The photoelectrodes were carefully positioned so that they would be completely overlapping each other when the two halves of the reactor joined together, forming a true tandem configuration.

We note that in a true tandem setup with two photoelectrodes, there are totally 8 possible ways to arrange them based on their positions relating to the incoming illumination and to each other. When the glass substrate is facing the light, the photoelectrode is considered back-illuminated (BI), while the reverse is considered front-illuminated (FI). In addition, the first photoelectrode to receive the light is considered in the front (F) while the remaining photoelectrode is considered in the back (B). However, we also notice that the BiVO<sub>4</sub> layer of the photoanode was highly porous, thus diffraction of the incoming illumination would be a problem if it was placed in the front. In comparison, the photocathode was noticeably more transparent. Therefore, the FTO|BiVO<sub>4</sub>|CoPi photoanode was decided to be put in the back. Relating to the relative position of the photoelectrodes with the incoming light, it was known that photogenerated charges collection of BiVO<sub>4</sub> was better under back-illumination.<sup>166</sup>

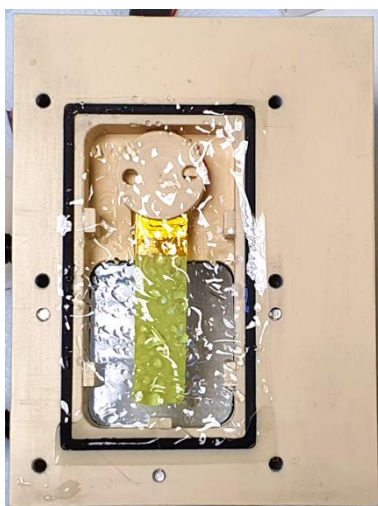
However, the combination of back position and back-illumination would elongate the mass transfer distance between the two photoelectrodes, thus overall performance would be negatively impacted. Therefore, the eventual configuration of the tandem setup was decided to be with the FTO|NiO|RuP<sub>4</sub>-CoN<sub>4</sub>H photocathode positioned in the front and with back-illumination (F-BI), while the FTO|BiVO<sub>4</sub>|CoPi photoanode was put in the back with front-illumination (B-FI).

Prior to the integration to the reactor, steel wires were connected to the remaining 10 x 10 mm bare FTO part of each photoelectrode and extended to their respective holes in the reactor for photoelectrochemical assessment. These electrical contacts were enhanced by silver paste and isolated from the electrolyte by thermal tape (**Figure 91**).



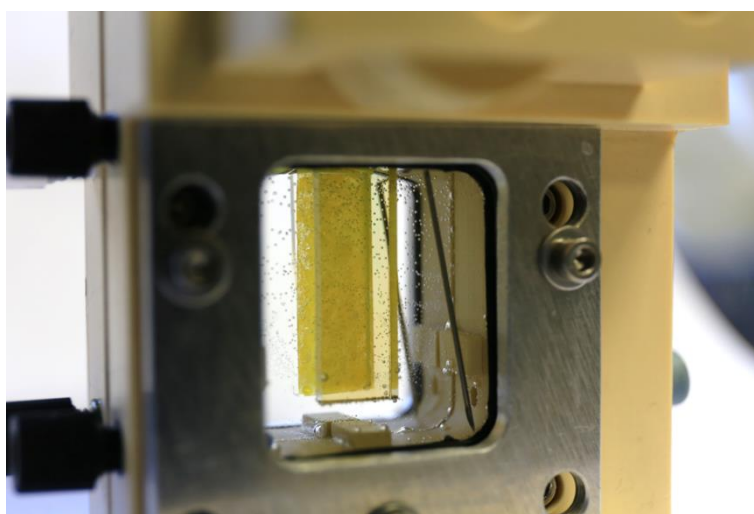
*Figure 91: Side-by-side view of the FTO|BiVO<sub>4</sub>|CoPi photoanode (left) and FTO|NiO|RuP<sub>4</sub>-CoN<sub>4</sub>H photocathode (right) secured to their respective halves of the reactor*

To limit the cross contamination while retaining the diffusion of proton between the two photoelectrodes, a 50  $\mu\text{m}$  thick Nafion proton exchange membrane (PEM) was added in between. As the membrane expands when in contact with aqueous solution, to prevent undesired deformation during operation, it was thoroughly soaked in DI water before the integration (**Figure 92**).



*Figure 92: Integration of a Nafion membrane to the reactor*

Afterwards, the two halves of the reactor were screwed together, forming two air-tight and water-tight compartments separated by the Nafion membrane, each containing one photoelectrode in full tandem configuration. The addition of 0.05 M  $\text{NaHCO}_3$  (pH 6.6) electrolyte as well as subsequent degassing by argon or introduction of  $\text{CO}_2$  to the two compartments were done by two long needles penetrating the top silicon septa (**Figure 93**).



*Figure 93: The fully assembled reactor containing the photoelectrodes in true tandem configuration*

### 3.2. Setup for individual electrodes assessment

While being kept in the true tandem configuration, the individual performance of each photoelectrode was assayed separately using a potentiostat in the typical three-electrode configuration. Each photoelectrode would take turn being the working electrode. A Pt wire was used as counter electrode and a Ag/AgCl 3 M KCl was used as reference electrode. The latter two were introduced to the system through the aforementioned separated compartments in the reactor. The schematic representation of the setup is shown in **Figure 94**.

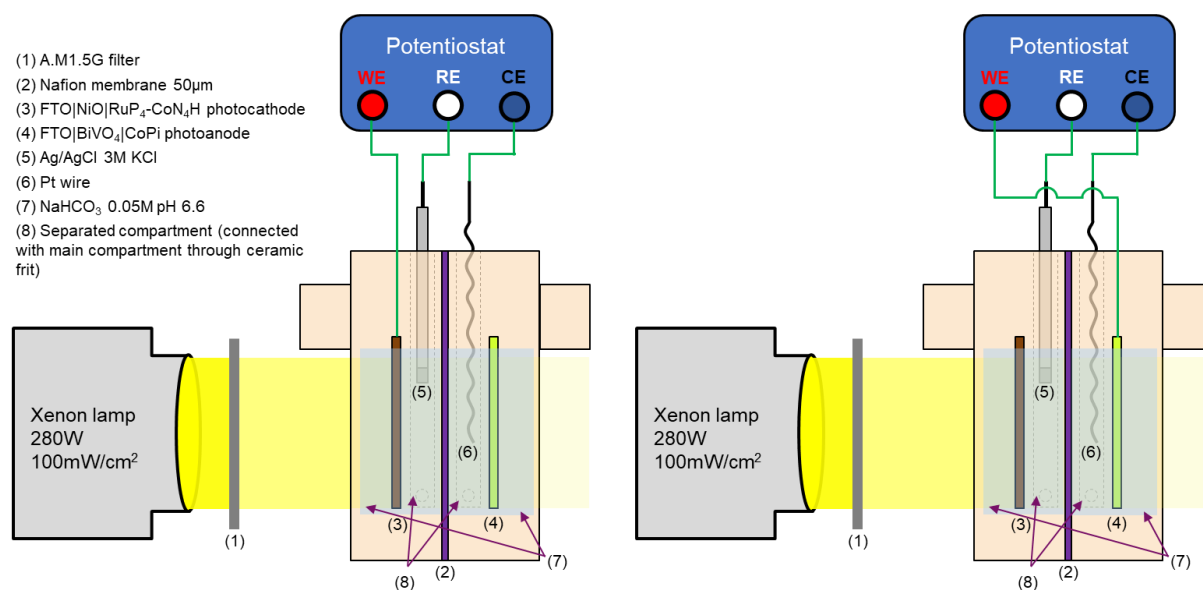


Figure 94: Schematic representation of experimental setup for individual photoelectrochemical assessment of FTO|NiO|RuP<sub>4</sub>-CoN<sub>4</sub>H photocathode (left) and FTO|BiVO<sub>4</sub>|CoPi photoanode (right)

For the samples used in HER operation, the NaHCO<sub>3</sub> electrolyte in both compartments was degassed with research grade argon for 15 minutes before the assessment. For the CO<sub>2</sub>RR, the electrolyte in both compartments was saturated with CO<sub>2</sub> for 15 minutes before the assessment. In both cases, the electrolyte was stirred with a magnetic bar during measurement.

This assessment serves to both confirm the individual activity of the two photoelectrodes as well as predicting the operating parameters of the resulted tandem device. Indeed, after the individual *current density vs. potential* (*j*-E) plots for the two photoelectrodes are obtained, the operating current density and potential of the whole tandem cell can be predicted through the intersecting point of their corresponding *absolute current density vs. potential* (*|j*|-E) plots. To this end, linear sweep voltammetry with potential scan rate of 2 mV/s was utilized. To avoid having to resort to extrapolation like in **Figure 72 (chapter 3, section 4.1)**, the scan range was decided to be the same for both photoelectrodes. The sweeping direction would be from 0.3 to 1.1 V vs. RHE for the photoanode, and from 1.1 V to 0.3 V vs. RHE for the photocathode.

### 3.3. Setup for full tandem cell assessment

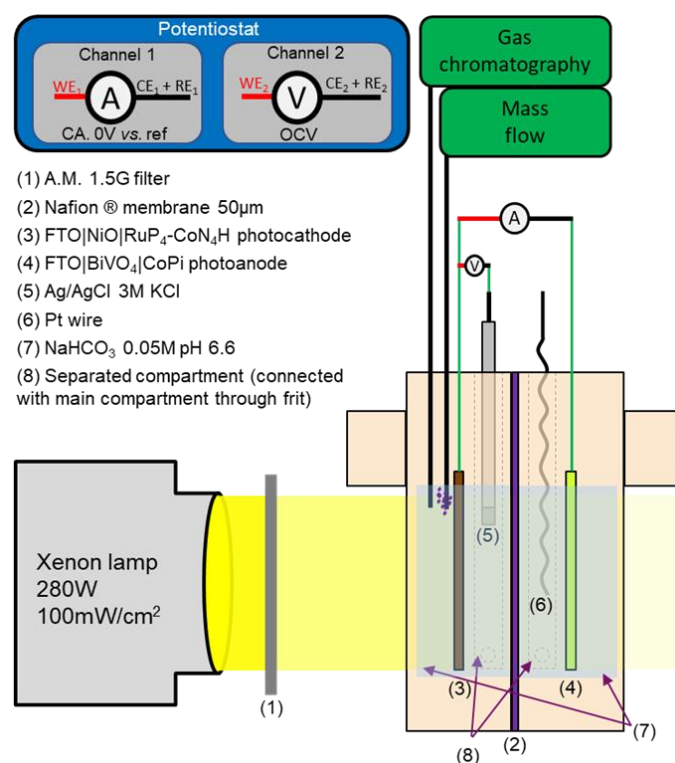


Figure 95: Schematic representation of experimental setup for full tandem cell assessment

When the two photoelectrodes are connected in series, their electrical potential would be at the same value. Therefore, the bi-potentiostat configuration would be sufficient to simultaneously probe the shared potential of the two photoelectrodes and the photogenerated current circulating between them. To this end, Channel 1 acting as an ideal amperometer (iAM) was inserted into the circuit through the Ohmic contact between the two photoelectrodes. Thus, the working current density of the tandem cell could be monitored over time. Channel 2 acting as an ideal voltmeter (iVM) was connected to the photocathode and the Ag/AgCl 3 M KCl reference electrode. By this way, the working potential of the full tandem setup could be recorded during the operation.

For the proton reduction operation, hydrogen gas generation was monitored using the automatic sampling micro gas chromatography setup (see **chapter 3** for details). For the CO<sub>2</sub> reduction operation, as the electrolyte was saturated with CO<sub>2</sub> before the experiment, the same method was not feasible because the continuous Ar degassing would quickly remove all the CO<sub>2</sub> in the electrolyte. Therefore, manual injection to a Perkin Elmer Clarus 580 gas chromatograph at the end of the operation was done instead to quantify the amount of gaseous products generated.



## 4. Photoelectrochemical investigation coupled with gas chromatography

### 4.1. Investigation for solar water splitting

#### 4.1.1. Individual assessment of the photoelectrodes and their compatibility

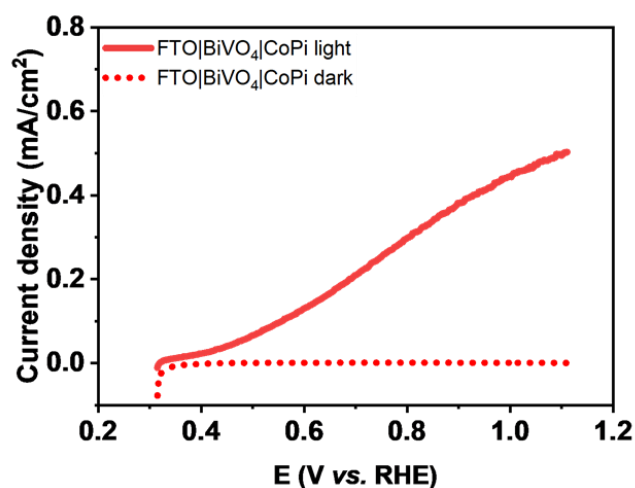


Figure 96: Photoelectrochemical assessment of FTO|BiVO<sub>4</sub>|CoPi photoanode

Under the remaining irradiation from 1 sun light passing through the photocathode and the Nafion membrane, the front-illuminated FTO|BiVO<sub>4</sub>|CoPi was able to catalyze the water oxidation reaction with an onset potential of 400 mV vs. RHE (Figure 96, red straight trace). The activity in the dark was negligible in comparison (Figure 96, red dotted trace).

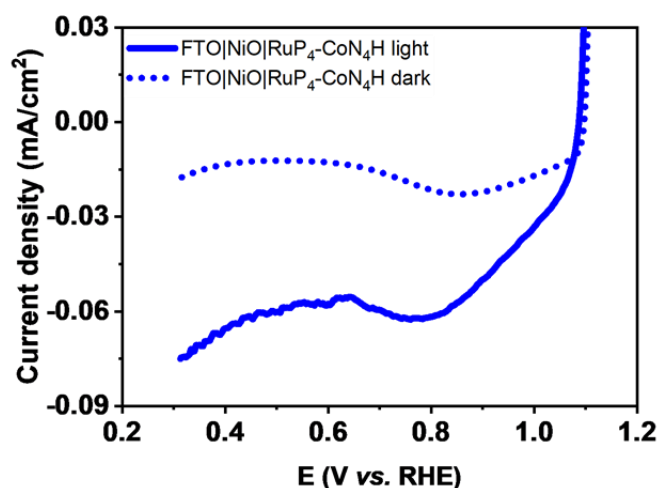


Figure 97: Photoelectrochemical assessment of FTO|NiO|RuP<sub>4</sub>-CoN<sub>4</sub>H photocathode

Under full 1 sun irradiation, the back-illuminated FTO|NiO|RuP<sub>4</sub>-CoN<sub>4</sub>H photocathode exhibited photoactivity with an onset potential of around 450 mV vs. RHE (Figure 97, blue straight trace). The activity in the dark was significantly lower (Figure 97, blue dotted trace). A reduction event characteristic to the NiO base was observed at around 0.8 V vs. RHE

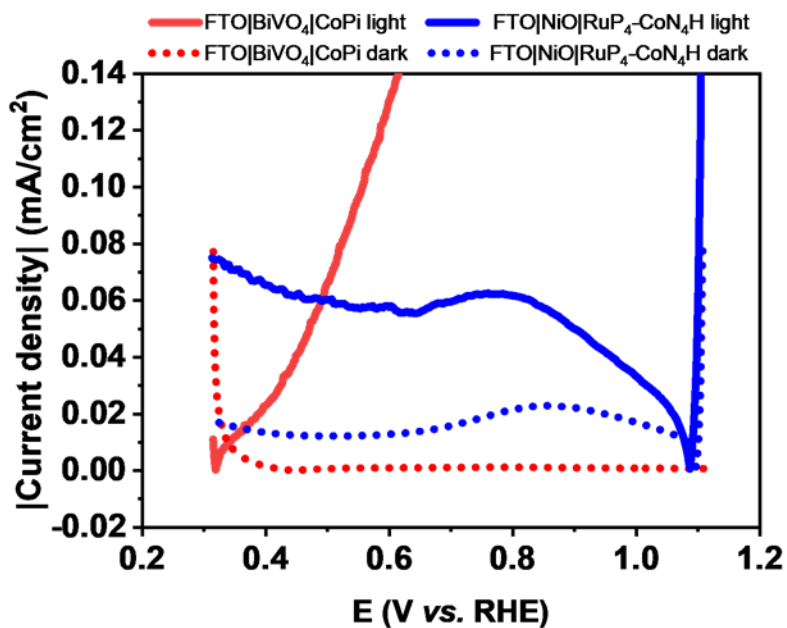


Figure 98: Prediction on the operating potential and current density of the resulted tandem cell

An overlapping of the  $|j|$ -E curves under illumination (blue straight trace for the FTO|NiO|RuP<sub>4</sub>-CoN<sub>4</sub>H photocathode and red straight trace for the FTO|BiVO<sub>4</sub>|CoPi photoanode) was observed. Therefore, the two photoelectrodes were compatible with each other in a tandem configuration. From the intersecting point, the operating potential of the resulted tandem cell was predicted to be around 0.49 V vs. RHE and the operating current density was predicted to be around 60  $\mu$ A/cm<sup>2</sup>.



#### 4.1.2. Full device assessment with bi-potentiostat and *in-situ* gas chromatography

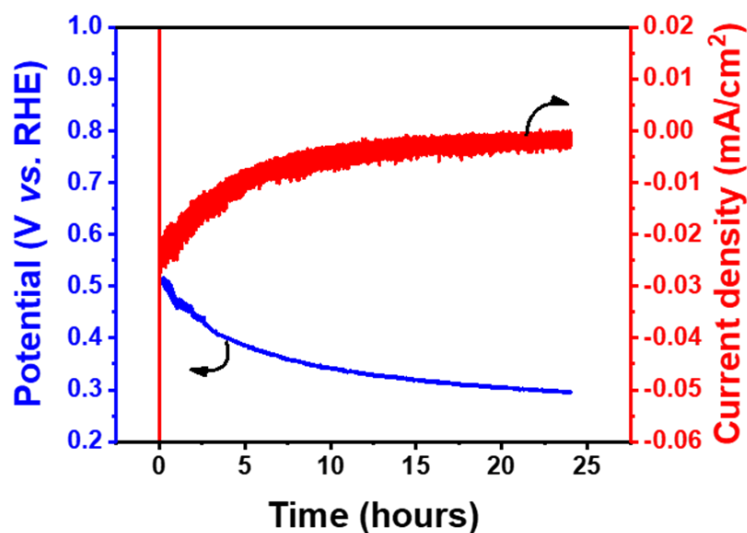


Figure 99: Evolution of the operating potential (blue) and current density of the CoPi|BiVO<sub>4</sub>|FTO-FTO|NiO|RuP<sub>4</sub>-CoN<sub>4</sub>H tandem cell under 1 sun illumination in 0.05 M NaHCO<sub>3</sub> (pH 6.6)

Upon illumination, the operating potential shared between the two photoelectrodes was recorded at 0.50 V vs. RHE, which was very close to the value of 0.49 V vs. RHE predicted from the intersecting  $|j|$ -E curves of individual photoelectrodes. This potential gradually decreased to 0.29 V vs. RHE in 24 hours (**Figure 99**, blue trace). Regarding the operating current density, an initial value of 25  $\mu\text{A}/\text{cm}^2$  was recorded, which was less than half of the predicted 60  $\mu\text{A}/\text{cm}^2$ . This was expected as the prediction through overlapping the  $|j|$ -E plots ignores various possible Ohmic drops in the true tandem system. Nevertheless, the operating current density was shown to gradually decrease over time. By the 10-hour mark, it was down to 5  $\mu\text{A}/\text{cm}^2$ , representing a 80% performance loss (**Figure 99**, red trace). After 24 hours, the current density dropped to  $\sim 2 \mu\text{A}/\text{cm}^2$ . This low final current density was likely only contributed by the NiO semiconductor.

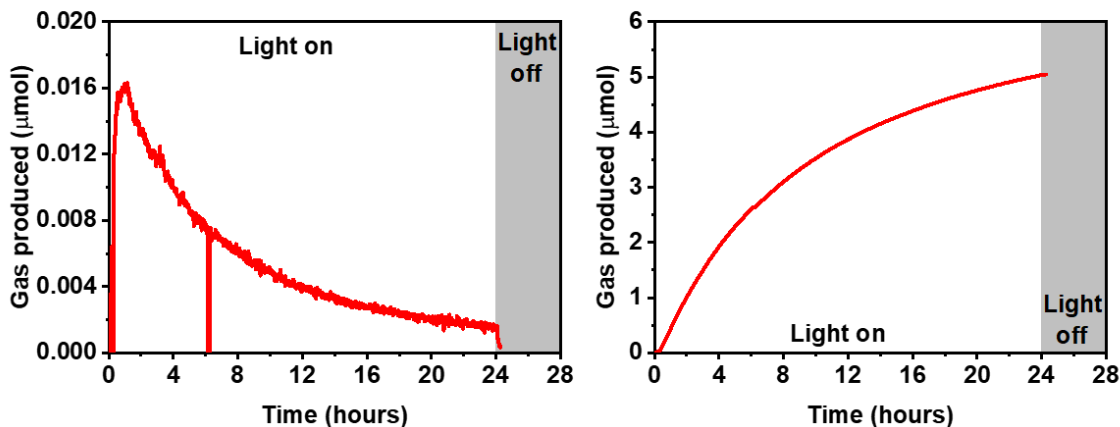


Figure 100: In-situ gas chromatography monitoring of H<sub>2</sub> generated during the bi-potentiostat assessment of the CoPi|BiVO<sub>4</sub>|FTO-FTO|NiO|RuP<sub>4</sub>-CoN<sub>4</sub>H tandem cell in real-time (left) and accumulated (right) mode

The quantification of hydrogen produced in real-time also showed a similar rate of decrement over time (**Figure 100** left). Over the course of 24 hours of continuous operation, a total of 5.05 μmol hydrogen was generated (**Figure 100** right), corresponding to a  $\eta_{\text{STH}}$  of  $4.6 \times 10^{-3}\%$  which was very close to the  $5.4 \times 10^{-3}\%$  reported for a similar hybrid tandem system made of TaON|CoO<sub>x</sub> photoanode and CuGaO<sub>2</sub>|RBG-174|CoHEC photocathode.<sup>157</sup> The Faradaic efficiency of the hydrogen evolution reaction was calculated to be 60.63%. This indicated that the photogenerated charges were not fully utilized for the reduction of proton. This decrease in Faradaic yield was likely contributed by the known reduction of NiO<sup>167</sup> as well as the reduction of O<sub>2</sub> formed at the photoanode passing through the Nafion membrane.

### 4.1.3. Post-operation individual assessment of the photoelectrodes

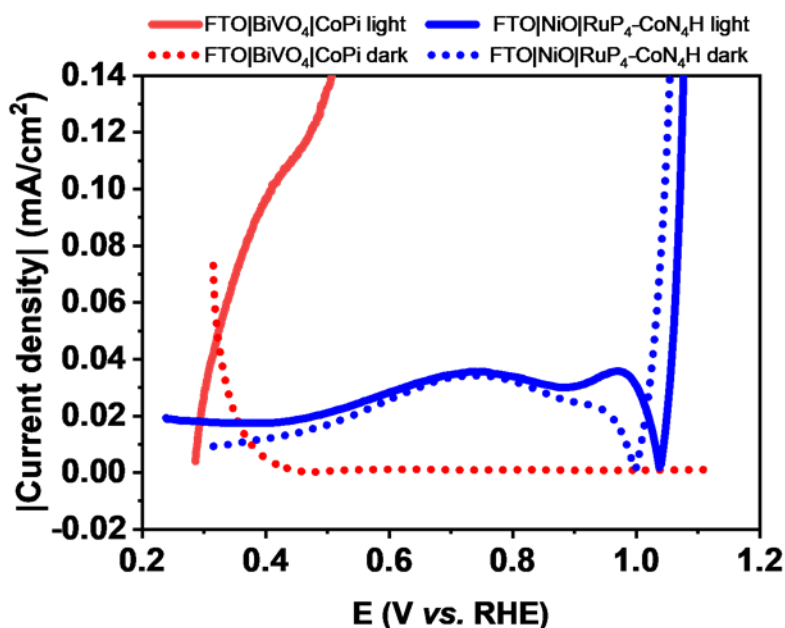


Figure 101: Post-operation verification on the operating potential and current density of the tandem cell

To verify the state of the tandem cell, an assessment of each individual photoelectrode after the photoelectrochemical operation of the cell was conducted. While the photoanode retained its activity, the photocathode was significantly degraded. Through the intersecting point of the  $|j|$ - $E$  plots, the operating potential shifted to 0.29 V vs. RHE (**Figure 101**, blue straight trace and red straight trace), which was exactly the value recorded by the bi-potentiostat monitoring system at the end of 24 hours operation experiment (**Figure 99**, blue trace). However, the operating current density determined from the  $|j|$ - $E$  curves should be  $20 \mu\text{A}/\text{cm}^2$  which is ten times higher than that recorded by the bi-potentiostat at the end of 24 hours operation experiment (**Figure 99**, red trace). We attribute this huge difference of current density to the difference of resistance between the two configurations.

## 4.2. Investigation for solar CO<sub>2</sub> reduction

We were then interested in assaying the performance of the tandem device for the CO<sub>2</sub> reduction reactions. The configuration was kept the same as the proton reduction reaction assessment, namely FTO|BiVO<sub>4</sub>|CoPi photoanode in the back and being front-illuminated, FTO|NiO|RuP<sub>4</sub>-CoN<sub>4</sub>H photocathode in the front and being back-illuminated, a Nafion membrane was used to separate the main compartment containing 0.05 M NaHCO<sub>3</sub> (pH 6.6) electrolyte. However, instead of being degassed by Ar, the electrolyte was saturated by research grade CO<sub>2</sub> gas through continuous bubbling for 15 minutes.

### 4.2.1. Individual assessment of the photoelectrodes and their compatibility

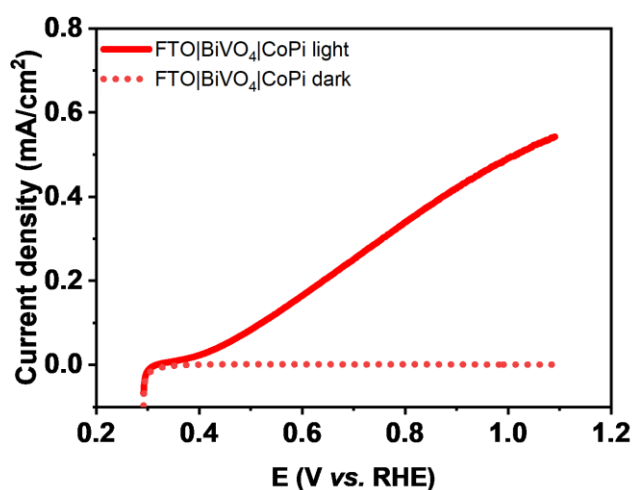


Figure 102: Photoelectrochemical assessment of FTO|BiVO<sub>4</sub>|CoPi photoanode in CO<sub>2</sub> saturated 0.05 M NaHCO<sub>3</sub> (pH 6.6)

Similar performances were obtained for the FTO|BiVO<sub>4</sub>|CoPi photoanode when it was assayed in a CO<sub>2</sub>-saturated and Ar-saturated 0.05 M NaHCO<sub>3</sub> (pH 6.6) electrolyte solution. The solar water oxidation reaction was observed at an onset potential of 400 mV vs. RHE (Figure 102).

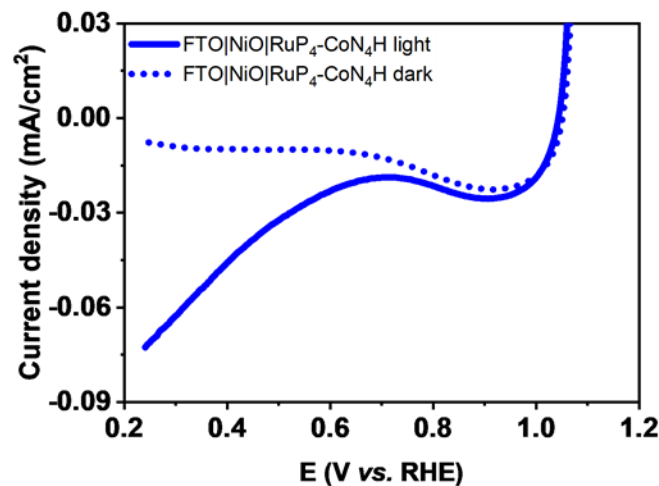


Figure 103: Photoelectrochemical assessment of FTO|NiO|RuP<sub>4</sub>-CoN<sub>4</sub>H photocathode in CO<sub>2</sub> saturated 0.05 M NaHCO<sub>3</sub> (pH 6.6)

Regarding the FTO|NiO|RuP<sub>4</sub>-CoN<sub>4</sub>H photocathode, it also exhibited similar photoactivity with an onset potential of around 450 mV vs. RHE (**Figure 103**, blue straight trace) and comparable current density. The activity in the dark was significantly lower (**Figure 103**, blue dotted trace). A reduction event characteristic to the NiO base was also observed.

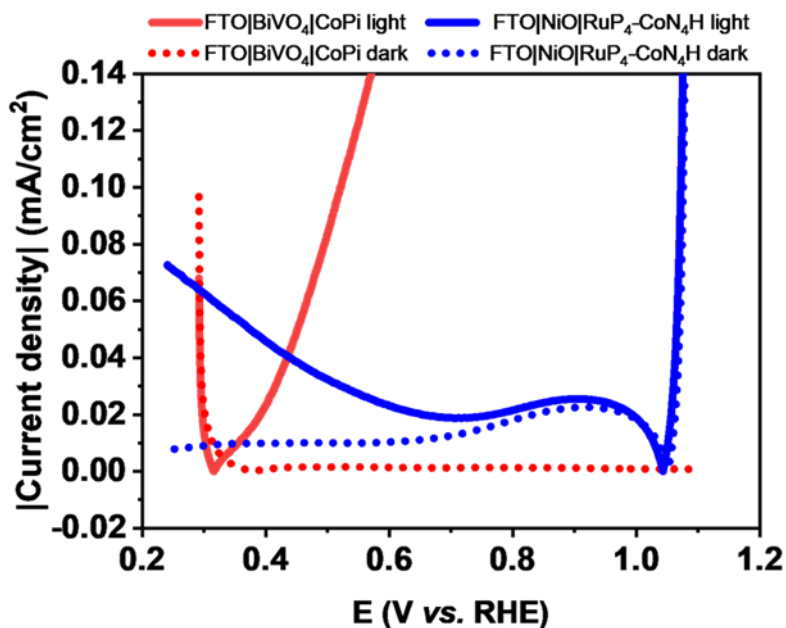


Figure 104: Prediction of the operating potential and current density of the resulted tandem cell

Thus, an overlapping of the  $|j|$ -E curves under illumination (blue straight trace for the FTO|NiO|RuP<sub>4</sub>-CoN<sub>4</sub>H photocathode and red straight trace for the FTO|BiVO<sub>4</sub>|CoPi photoanode) was observed (**Figure 104**), indicating their compatibility. From the intersecting point, the operating potential of the resulted tandem cell was predicted to be around 0.44 V vs. RHE and the operating current density was predicted to be around 41  $\mu$ A/cm<sup>2</sup>.

#### 4.2.2. Full device assessment with bi-potentiostat and gas chromatography

From the previous bi-potentiostat monitoring for proton reduction, the current density produced by the tandem setup was largely reduced in the first few hours. Combining with the observed full degradation in performance of the photocathode, we deduced that the tandem setup was largely compromised during this period. Therefore, the assessment for CO<sub>2</sub> reduction was shortened to 3 hours.

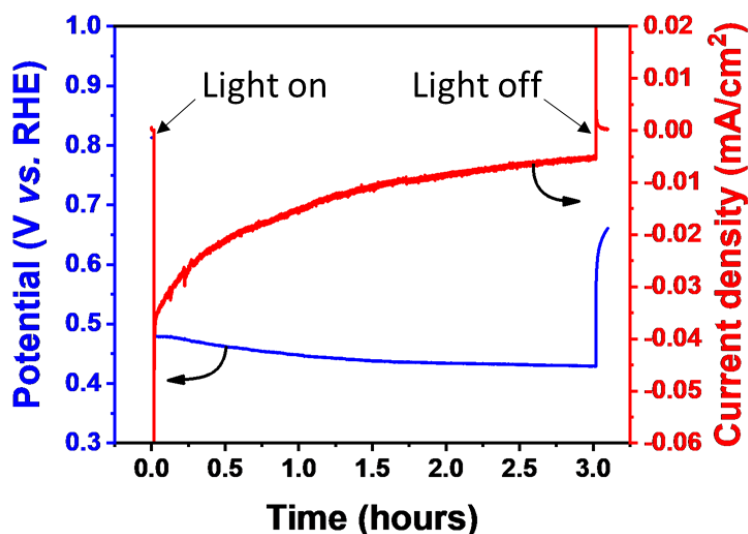


Figure 105: Evolution of the operating potential (blue) and current density of the CoPi|BiVO<sub>4</sub>|FTO-FTO|NiO|RuP<sub>4</sub>-CoN<sub>4</sub>H tandem cell under 1 sun illumination in 0.05 M NaHCO<sub>3</sub> (pH 6.6) saturated with CO<sub>2</sub>

Upon illumination, the operating potential shared between the two photoelectrodes was recorded at 0.48 V vs. RHE, which was very close to the value predicted 0.44 V vs. RHE. This potential gradually decreased to 0.43 V vs. RHE after 3 hours (**Figure 105**, blue trace). An initial operating current density of 33  $\mu\text{A}/\text{cm}^2$  was recorded, coming close to the predicted 41  $\mu\text{A}/\text{cm}^2$ . This boost in current density could be the result of the addition of CO<sub>2</sub> to the system. After 3 hours of continuous operation, it was reduced to 5  $\mu\text{A}/\text{cm}^2$  (**Figure 105**, red trace). Afterwards, illumination was cut off. After a quick surcharge period, the operating current density immediately fell to 0  $\mu\text{A}/\text{cm}^2$ , confirming that the recorded current density was indeed the result of photoactivity.

Gas sample from both compartments were injected to the gas chromatography equipped with sensors for both H<sub>2</sub> and CO. After 3 hours, 1382 nmol of CO and 319 nmol of H<sub>2</sub> were generated by the tandem cell, translating to the Faradaic efficiency of 61.59% and 14.22%, respectively.

The  $\eta_{STH}$  was calculated to be  $2.3 \times 10^{-3}\%$ , which was lower than the  $4.6 \times 10^{-3}\%$  in the proton reduction test in **section 4.1**. Nevertheless, this result has not taken into account the low activity of the degraded sample dragging down the overall  $\eta_{STH}$  over time. Indeed, if only the performance during the first 3 hours of the proton reaction in **section 4.1** was taken into consideration, the corresponding  $\eta_{STH}$  would be  $11.0 \times 10^{-3}\%$ , much higher than the  $2.3 \times 10^{-3}\%$  obtained above.

On another note, given the Gibbs free energy of the  $\text{CO}_2$  reduction reaction to CO is 257 kJ/mol,<sup>168</sup> the  $\eta_{STF}$  of the reaction can be calculated using Eq.21 to be  $11.0 \times 10^{-3}\%$ .

$$\eta_{STF} = \frac{\text{Energy stored in CO}}{\text{Total light Energy}} = \frac{\text{Amount of CO(mol)} \times 257000 \text{ (J.mol}^{-1}\text{)}}{\text{Light Power(J.s}^{-1}\text{.cm}^{-1}\text{)} \times \text{Area(cm)} \times \text{Irradiation time(s)}} \quad (\text{Eq.21})$$

Thus, the total  $\eta_{STF}$  of the tandem device for solar  $\text{CO}_2$  reduction to syngas ( $\text{CO}$  and  $\text{H}_2$  mixture) was  $13.3 \times 10^{-3}\%$ . This value was in the range with the recently reported  $17 \times 10^{-3}\%$  using a very similar hybrid tandem setup with  $\text{NiO|PRu-poly-Ru-RuCAT1}$  photocathode and  $\text{BiVO}_4|\text{CoO}_x$  photoanode from Ishitani group.<sup>168</sup> However, we also note that their system is significantly more robust thanks to the superior stability of the photocathode obtained through electrochemical polymerization of the dye molecules.

#### 4.2.3. Post-operation individual assessment of the photoelectrodes

Unfortunately, due to the head-space volume measurement required for quantifying the gas produced, the reactor had to be filled with distilled water at the end of the measurement. Therefore, the concentration of the electrolyte could not be maintained. In addition, the electrical connections were completely immersed in the liquid, posing elevated risk for photoelectrochemical measurements. For these reasons, the post-operation individual assessment of the photoelectrodes after  $\text{CO}_2$  reduction test was not performed.

## 5. Conclusions and perspectives

The hybrid tandem cell born from the collaboration between SolHyCat and CECS was shown to be able to perform both proton and CO<sub>2</sub> reduction with efficiency in the range of comparable systems. The employment of the bi-potentiostat setup was shown to be effective in real-time monitoring of various key variables of the device such as operating potential and current density. Coupled with gas chromatography, the evolution of various products was also possible, leading to the deduction of key parameters for comparison and optimization like Faradaic efficiency and solar-to-fuel efficiency.

It was shown that the current limitation of the tandem device was the degradation of the photocathode. Indeed, desorption of the dye from the semiconductor was a huge problem for the stability of the photocathode. Introduction of protective layers<sup>169</sup> or development of different anchoring method<sup>170</sup> would be able to address this problem. Alternatively, the use of novel semiconducting materials like CuGaO<sub>2</sub> that was shown to be a good alternative for NiO<sup>171,172</sup> would also have the potential to improve the activity of the photocathode.

Nevertheless, with improvements in reactor designs to minimize additional resistance of the system, more precise measurements of the operating current density could be achieved. Thus, the bi-potentiostat setup would be indispensable tool for the development, integration and optimization of future tandem cells from photoelectrodes of different origins.



# General conclusions and perspectives

Through various compromise, the initial goals of the thesis were achieved. Indeed, through the creation of two functional solar fuels generators, namely the monolithic artificial leaf and the tandem artificial leaf with performance comparable to those of the same class, we have contributed solutions to the aforementioned level 4 problem, namely building devices that work. Our second target, namely the level 3 solution, involves development of suitable experimentation to shed light to the inner-workings and provide commonly shared parameters of the devices for proper future optimization and benchmarking. This goal was reached through the realization of the versatile multi-potentiostat monitoring system coupled with *in/ex-situ* gas chromatography for the development, comparison and optimization of a wide range of solar fuels generator. Most importantly, we have successfully demonstrated the importance of collaboration in research to reach a common goal.

To elaborate, the two reference catalysts that gave rise to the dual catalysts system from the same precursor solution was each contributed from the previous works of the two groups. This has been the most important condition to realize our aim of driving down the complexity and the level of engineering required for the fabrication of the monolithic artificial leaf. Indeed, through the simultaneous light-induced assembly of the catalysts onto the triple-junction amorphous silicon solar cell, the fabrication could be done with readily available tools in a photoelectrochemistry laboratory, without the needs of complex or specialized equipment. The liberation from electrodeposition using potentiostat and clamp cells also improved greatly the size limitation of the resulted leaf. Although the novel fabrication method came with a small cost in overall performance, the resulted artificial leaf was able to function in aqueous electrolyte at neutral pH without the need of a membrane. Employing a large array of invasive and non-invasive assessment systems, the current limitation of the device was evidenced to be the inadequate protection of the delicate solar cell immersed in the electrolyte, leading to deleterious degradation of performance.

The collaboration reached a step further with the contribution of highly functional photoelectrodes from the two groups to create a viable hybrid tandem artificial leaf. With the aid of a specially designed reactor, not only the integration of the photoelectrodes were simplified, but the subsequent assessment of the resultant tandem device was also significantly streamlined. The BiVO<sub>4</sub>-based photoanode was found to be stable during the operation.

However, the fuel-forming dye-sensitized photocathode, although capable of driving both proton and CO<sub>2</sub> reduction reactions, was found to be the limiting factor of the tandem cell due to low stability.

As these two solar fuels generators are composed of various components, many strategies for improving their performance and stability can be conducted:

- For the monolithic artificial leaf, identification of novel OER, HER dual catalysts which are efficient and robust against the (electro)chemical corrosion could be the first improvement. In addition, identifying innovative catalyst deposition strategies that can properly protect the delicate 3jn-a-Si solar cell could potentially have positive effect on the longevity of the device. Advancement on the engineering of the electrical contact to avoid damaging the delicate ITO surface would also be important for integration of the multi-potentiostat assessment system.
- For the tandem artificial leaf, introduction of protective layer or development of different anchoring method could potentially prevent or reduce rate of the dye desorption process, leading to overall stability improvement of the photoelectrodes. On the performance front, researching on more efficient alternatives for the base semiconductor could have positive impact on the overall efficiency of the system. Taking advantages of the extreme tunability and versatility of organic synthesis, higher performance as well as robustness could be achieved for novel dye and catalysts complexes. Last, but not least, refinement in reactor designs could lead to improvement in overall performance of the device as well as the capability, accuracy and sensitivity of assessment systems.

Nevertheless, the successful fabrication of these two viable solar fuels generators provided two highly versatile base structures for future development and integration of novel light harvesters and catalysts. Study on the resultant devices would then be done with the equally versatile multi-potentiostat assessment system that could provide simultaneous real-time monitoring of various parameters of the components within. These systems, when adequately refined and improved, could effectively aid our progress in creating the ultimate solar fuels generator, and hopefully, a sustainable future.

# References

1. Lee R. The outlook for population growth. *Science (80- )*. 2011;333(6042):569-573. doi:10.1126/science.1208859
2. United Nations. *World Population Prospects 2019*.; 2019. <http://www.ncbi.nlm.nih.gov/pubmed/12283219>.
3. IEA. *World Energy Outlook 2019*. OECD; 2019. doi:10.1787/caf32f3b-en
4. Looney B. Statistical Review of World Energy globally consistent data on world energy markets . and authoritative publications in the field of energy. *Rev World Energy data*. 2021;70:8-20.
5. Layton BE. A comparison of energy densities of prevalent energy sources in units of joules per cubic meter. *Int J Green Energy*. 2008;5(6):438-455. doi:10.1080/15435070802498036
6. Shafiee S, Topal E. When will fossil fuel reserves be diminished? *Energy Policy*. 2009;37(1):181-189. doi:10.1016/j.enpol.2008.08.016
7. Schobert H, ed. Formation of fossil fuels. In: *Chemistry of Fossil Fuels and Biofuels*. Cambridge Series in Chemical Engineering. Cambridge: Cambridge University Press; 2013:103-131. doi:DOI: 10.1017/CBO9780511844188.009
8. Crowley TJ, Berner RA. CO<sub>2</sub> and climate change. *Science (80- )*. 2001;292(5518):870-872. doi:10.1126/science.1061664
9. Solomon S, Plattner GK, Knutti R, Friedlingstein P. Irreversible climate change due to carbon dioxide emissions. *Proc Natl Acad Sci U S A*. 2009;106(6):1704-1709. doi:10.1073/pnas.0812721106
10. Hoffert MI. Farewell to fossil fuels? *Science (80- )*. 2010;329(5997):1292-1294. doi:10.1126/science.1195449
11. McNutt M. Climate Change Impacts. *Science (80- )*. 2013;341(6145):435-435. doi:10.1126/science.1243256
12. Wheeler T, von Braun J. Climate Change Impacts on Global Food Security. *Science (80- )*. 2013;341(6145):508-513. doi:10.1126/science.1239402
13. Pecl GT, Araújo MB, Bell JD, et al. Biodiversity redistribution under climate change: Impacts on ecosystems and human well-being. *Science (80- )*. 2017;355(6332). doi:10.1126/science.aai9214
14. Doney SC, Ruckelshaus M, Emmett Duffy J, et al. Climate change impacts on marine ecosystems. *Ann Rev Mar Sci*. 2012;4:11-37. doi:10.1146/annurev-marine-041911-111611
15. Tol RSJ. The economic impacts of climate change. *Rev Environ Econ Policy*. 2018;12(1):4-25. doi:10.1093/reep/rex027
16. Calzadilla A, Rehdanz K, Betts R, Falloon P, Wiltshire A, Tol RSJ. Climate change impacts on global agriculture. *Clim Change*. 2013;120(1-2):357-374. doi:10.1007/s10584-013-0822-4
17. *Paris Agreement to the United Nations Framework Convention on Climate Change, Dec. 12, 2015, T.I.A.S. No. 16-1104*.

18. IPCC, 2018: Global Warming of 1.5°C. An IPCC Special Report on the impacts of global warming of 1.5°C above pre-industrial levels and related global greenhouse gas emission pathways, in the context of strengthening the global response to the threat of climate change and efforts to eradicate poverty. *Masson-Delmotte, V., P. Zhai, H.-O. Pörtner, D. Roberts, J. Skea, P.R. Shukla, A. Pirani, W. Moufouma-Okia, C. Péan, R. Pidcock, S. Connors, J.B.R. Matthews, Y. Chen, X. Zhou, M.I. Gomis, E. Lonnoy, T. Maycock, M. Tignor, and T. Waterfield (Eds.). In Press.*
19. Perez R, Perez M. A Fundamental Look At Supply Side Energy Reserves For The Planet. *Int Energy Agency SHC Program Sol Updat.* 2015;62(April 2009):4-6. <http://www.iea-shc.org/data/sites/1/publications/2015-11-A-Fundamental-Look-at-Supply-Side-Energy-Reserves-for-the-Planet.pdf>.
20. Schröder KP, Connon Smith R. Distant future of the Sun and Earth revisited. *Mon Not R Astron Soc.* 2008;386(1):155-163. doi:10.1111/j.1365-2966.2008.13022.x
21. Chawla R, Singhal P, Garg AK. Photovoltaic Review of all Generations: Environmental Impact and Its Market Potential. *Trans Electr Electron Mater.* 2020;21(5):456-476. doi:10.1007/s42341-020-00217-9
22. Sharma S, Jain KK, Sharma A. Solar Cells: In Research and Applications—A Review. *Mater Sci Appl.* 2015;06(12):1145-1155. doi:10.4236/msa.2015.612113
23. Khatibi A, Razi Astarai F, Ahmadi MH. Generation and combination of the solar cells: A current model review. *Energy Sci Eng.* 2019;7(2):305-322. doi:10.1002/ese3.292
24. Wright VP. *World Energy Outlook 2020.* OECD; 2020. doi:10.1787/557a761b-en
25. Stripp ST, Happe T. How algae produce hydrogen—news from the photosynthetic hydrogenase. *Dalt Trans.* 2009;(45):9960. doi:10.1039/b916246a
26. Rutherford AW. BIOCHEMISTRY: Water Photolysis in Biology. *Science (80- ).* 2004;303(5665):1782-1784. doi:10.1126/science.1096767
27. Andreiadis ES, Chavarot-Kerlidou M, Fontecave M, Artero V. Artificial photosynthesis: From molecular catalysts for light-driven water splitting to photoelectrochemical cells. *Photochem Photobiol.* 2011;87(5):946-964. doi:10.1111/j.1751-1097.2011.00966.x
28. Cavendish H. XIX. Three papers, containing experiments on factitious air. *Philos Trans R Soc London.* 1766;56:141-184. doi:10.1098/rstl.1766.0019
29. Ramachandran R, Menon RK. An overview of industrial uses of hydrogen. *Int J Hydrogen Energy.* 1998;23(7):593-598. doi:10.1016/s0360-3199(97)00112-2
30. Irvine P, Smith M, Dong Z. Hydrogen fertilizer: Bacteria or fungi? *Acta Hort.* 2004;631:239-242. doi:10.17660/ActaHortic.2004.631.30
31. Møretrø T, Fanebust H, Fagerlund A, Langsrud S. Whole room disinfection with hydrogen peroxide mist to control *Listeria monocytogenes* in food industry related environments. *Int J Food Microbiol.* 2019;292(June 2018):118-125. doi:10.1016/j.ijfoodmicro.2018.12.015
32. Pelin G, Stoica C, Pelin CE, Balasa R. High concentration hydrogen peroxide for rocket fuel applications. *INCAS Bull.* 2020;12(3):151-157. doi:10.13111/2066-8201.2020.12.3.12
33. Brown TR, Lydon MC. Testing of Paraffin-Based Hybrid Rocket Fuel Using Hydrogen Peroxide Oxidizer. *Color Sp Grant Consort.* 2005:1-8.
34. Silvera IF, Cole JW. Metallic hydrogen: The most powerful rocket fuel yet to exist. *J Phys Conf Ser.* 2010;215. doi:10.1088/1742-6596/215/1/012194

35. Sdanghi G, Maranzana G, Celzard A, Fierro V. Towards non-mechanical hybrid hydrogen compression for decentralized hydrogen facilities. *Energies*. 2020;13(12). doi:10.3390/en13123145
36. Thomas G. Overview of Storage Development DOE Hydrogen Program: Sandia National Laboratories Livermore, California. 2000:1-14.
37. Grahame A, Aguey-Zinsou KF. Properties and applications of metal (M) dodecahydro-closo-dodecaborates (Mn=1,2B12H12) and their implications for reversible hydrogen storage in the borohydrides. *Inorganics*. 2018;6(4):1-38. doi:10.3390/inorganics6040106
38. Møller KT, Jensen TR, Akiba E, Li H wen. Hydrogen - A sustainable energy carrier. *Prog Nat Sci Mater Int*. 2017;27(1):34-40. doi:10.1016/j.pnsc.2016.12.014
39. IEA. Net Zero by 2050: A Roadmap for the Global Energy Sector. 2021. <https://www.iea.org/reports/net-zero-by-2050>.
40. Dincer I, Acar C. Review and evaluation of hydrogen production methods for better sustainability. *Int J Hydrogen Energy*. 2014;40(34):11094-11111. doi:10.1016/j.ijhydene.2014.12.035
41. Palmer C, Upham DC, Smart S, Gordon MJ, Metiu H, McFarland EW. Dry reforming of methane catalysed by molten metal alloys. *Nat Catal*. 2020;3(1):83-89. doi:10.1038/s41929-019-0416-2
42. Von Wald GA, Masnadi MS, Upham DC, Brandt AR. Optimization-based technoeconomic analysis of molten-media methane pyrolysis for reducing industrial sector CO<sub>2</sub> emissions. *Sustain Energy Fuels*. 2020;4(9):4598-4613. doi:10.1039/d0se00427h
43. Schneider S, Bajohr S, Graf F, Kolb T. State of the Art of Hydrogen Production via Pyrolysis of Natural Gas. *Chemie-Ingenieur-Technik*. 2020;92(8):1023-1032. doi:10.1002/cite.202000021
44. Penner SS. Steps toward the hydrogen economy. *Energy*. 2006;31(1 SPEC. ISS.):33-43. doi:10.1016/j.energy.2004.04.060
45. Crabtree GW, Dresselhaus MS, Buchanan M V. The hydrogen economy. *Phys Today*. 2004;57(12):39-44. doi:10.1063/1.1878333
46. Marbán G, Valdés-Solís T. Towards the hydrogen economy? *Int J Hydrogen Energy*. 2007;32(12):1625-1637. doi:10.1016/j.ijhydene.2006.12.017
47. Fu SC, Zhong XL, Zhang Y, et al. Bio-inspired cooling technologies and the applications in buildings. *Energy Build*. 2020;225. doi:10.1016/j.enbuild.2020.110313
48. United Nations Environment Programme (2019). *Emissions Gap Report 2019*.; 2019. <http://www.unenvironment.org/emissionsgap>.
49. Gaurina-Međimurec N, Novak-Mavar K, Majić M. Carbon capture and storage (CCS): Technology, projects and monitoring review. *Rud Geol Naft Zb*. 2018;33(2):1-14. doi:10.17794/rgn.2018.2.1
50. Bryngelsson M, Westermarck M. CO<sub>2</sub> capture pilot test at a pressurized coal fired CHP plant. *Energy Procedia*. 2009;1(1):1403-1410. doi:10.1016/j.egypro.2009.01.184
51. Sweet W. Winner: Clean Coal - Restoring Coal's Sheen. *IEEE Spectr*. 2008;45(1):57-60. doi:10.1109/MSPEC.2008.4428318
52. Benson EE, Kubiak CP, Sathrum AJ, Smieja JM. Electrocatalytic and homogeneous approaches

- to conversion of CO<sub>2</sub> to liquid fuels. *Chem Soc Rev.* 2009;38(1):89-99. doi:10.1039/b804323j
53. Larrazábal GO, Martín AJ, Pérez-Ramírez J. Building Blocks for High Performance in Electrocatalytic CO<sub>2</sub> Reduction: Materials, Optimization Strategies, and Device Engineering. *J Phys Chem Lett.* 2017;8(16):3933-3944. doi:10.1021/acs.jpcclett.7b01380
  54. Steffen W, Richardson K, Rockström J, et al. Planetary boundaries: Guiding human development on a changing planet. *Science (80- ).* 2015;347(6223). doi:10.1126/science.1259855
  55. FUJISHIMA A, HONDA K. Electrochemical Photolysis of Water at a Semiconductor Electrode. *Nature.* 1972;238(5358):37-38. doi:10.1038/238037a0
  56. Jaegermann W, Kaiser B, Finger F, Smirnov V, Schäfer R. Design Considerations of Efficient Photo-Electrosynthetic Cells and its Realization Using Buried Junction Si Thin Film Multi Absorber Cells. *Zeitschrift fur Phys Chemie.* 2020;234(4):549-604. doi:10.1515/zpch-2019-1584
  57. McKone JR, Lewis NS, Gray HB. Will solar-driven water-splitting devices see the light of day? *Chem Mater.* 2014;26(1):407-414. doi:10.1021/cm4021518
  58. Nielander AC, Shaner MR, Papadantonakis KM, Francis SA, Lewis NS. A taxonomy for solar fuels generators. *Energy Environ Sci.* 2015;8(1):16-25. doi:10.1039/c4ee02251c
  59. Tembhurne S, Nandjou F, Haussener S. A thermally synergistic photo-electrochemical hydrogen generator operating under concentrated solar irradiation. *Nat Energy.* 2019;4(5):399-407. doi:10.1038/s41560-019-0373-7
  60. Jia J, Seitz LC, Benck JD, et al. Solar water splitting by photovoltaic-electrolysis with a solar-to-hydrogen efficiency over 30%. *Nat Commun.* 2016;7(May):1-6. doi:10.1038/ncomms13237
  61. Oikawa T, Saijo Y, Kato S, Mishima T, Nakamura T. Formation of definite GaN p-n junction by Mg-ion implantation to n--GaN epitaxial layers grown on a high-quality free-standing GaN substrate. *Nucl Instruments Methods Phys Res Sect B Beam Interact with Mater Atoms.* 2015;365:168-170. doi:10.1016/j.nimb.2015.07.095
  62. Ye F, Li C. Formation of p-n junction by plasma spraying technique to enhance the photocatalytic activity of TiO<sub>2</sub>. *J Mater Sci.* 2004;39(1):353-355. doi:10.1023/B:JMSE.0000008088.60193.50
  63. Pinaud BA, Benck JD, Seitz LC, et al. Technical and economic feasibility of centralized facilities for solar hydrogen production via photocatalysis and photoelectrochemistry. *Energy Environ Sci.* 2013;6(7):1983-2002. doi:10.1039/c3ee40831k
  64. Hisatomi T, Domen K. Reaction systems for solar hydrogen production via water splitting with particulate semiconductor photocatalysts. *Nat Catal.* 2019;2(5):387-399. doi:10.1038/s41929-019-0242-6
  65. Nishiyama H, Yamada T, Nakabayashi M, et al. Photocatalytic solar hydrogen production from water on a 100 m<sup>2</sup>-scale. *Nature.* 2021. doi:10.1038/s41586-021-03907-3
  66. Reece SY, Hamel J a., Sung K, et al. Wireless Solar Water Splitting Using Silicon-Based Semiconductors and Earth-Abundant Catalysts. *Science (80- ).* 2011;334(6056):645-648. doi:10.1126/science.1209816
  67. Nocera DG. The Artificial Leaf. *Acc Chem Res.* 2012;45(5):767-776. doi:10.1021/ar2003013
  68. Vermaas DA, Sassenburg M, Smith WA. Photo-assisted water splitting with bipolar membrane

- induced pH gradients for practical solar fuel devices. *J Mater Chem A*. 2015;3(38):19556-19562. doi:10.1039/c5ta06315a
69. Maric R, Yu H. Proton Exchange Membrane Water Electrolysis as a Promising Technology for Hydrogen Production and Energy Storage. *Nanostructures Energy Gener Transm Storage*. 2019. doi:10.5772/intechopen.78339
70. Reece SY, Nocera DG. Proton-coupled electron transfer in biology: Results from synergistic studies in natural and model systems. *Annu Rev Biochem*. 2009;78(lii):673-699. doi:10.1146/annurev.biochem.78.080207.092132
71. Radzicka A, Wolfenden R. A proficient enzyme. *Science (80- )*. 1995;267(5194):90-93. doi:10.1126/science.7809611
72. Bailar JC. "HETEROGENIZING" HOMOGENEOUS CATALYSTS. *Catal Rev*. 1974;10(1):17-36. doi:10.1080/01614947408079625
73. Collis AEC, Horváth IT. Heterogenization of homogeneous catalytic systems. *Catal Sci Technol*. 2011;1(6):912-919. doi:10.1039/c1cy00174d
74. Kakkar AK. Nano-organometallics: Heterogenizing homogeneous catalysts via thin film methodology. *Chem Rev*. 2002;102(10):3579-3588. doi:10.1021/cr010360k
75. Materna KL, Jiang J, Regan KP, Schmuttenmaer CA, Crabtree RH, Brudvig GW. Optimization of Photoanodes for Photocatalytic Water Oxidation by Combining a Heterogenized Iridium Water-Oxidation Catalyst with a High-Potential Porphyrin Photosensitizer. *ChemSusChem*. 2017;10(22):4526-4534. doi:10.1002/cssc.201701693
76. Garrido-Barros P, Gimbert-Surinifach C, Moonshiram D, et al. Electronic I-Delocalization Boosts Catalytic Water Oxidation by Cu(II) Molecular Catalysts Heterogenized on Graphene Sheets. *J Am Chem Soc*. 2017;139(37):12907-12910. doi:10.1021/jacs.7b06828
77. Charisiadis A, Giannoudis E, Pournara Z, et al. Synthesis and Characterization of a Covalent Porphyrin-Cobalt Diimine-Dioxime Dyad for Photoelectrochemical H<sub>2</sub> Evolution. *Eur J Inorg Chem*. 2021;2021(12):1122-1129. doi:10.1002/ejic.202001111
78. Coñizares P, García-Gómez J, Fernández de Marcos I, Rodrigo MA, Lobato J. Measurement of mass-transfer coefficients by an electrochemical technique. *J Chem Educ*. 2006;83(8):1204-1207. doi:10.1021/ed083p1204
79. Bard AJ, Faulkner LR. *Electrochemical Methods: Fundamentals and Applications, 2nd Edition*. John Wiley & Sons, Incorporated; 2000. <https://books.google.com.vn/books?id=hQocAAAQBAJ>.
80. Luo J, Im JH, Mayer MT, et al. Water photolysis at 12.3% efficiency via perovskite photovoltaics and Earth-abundant catalysts. *Science (80- )*. 2014;345(6204):1593-1596. doi:10.1126/science.1258307
81. Frydendal R, Paoli EA, Knudsen BP, et al. Benchmarking the Stability of Oxygen Evolution Reaction Catalysts: The Importance of Monitoring Mass Losses. *ChemElectroChem*. 2014;1(12):2075-2081. doi:10.1002/celec.201402262
82. Parsons R. The rate of electrolytic hydrogen evolution and the heat of adsorption of hydrogen. *Trans Faraday Soc*. 1958;54:1053. doi:10.1039/tf9585401053
83. She ZW, Kibsgaard J, Dickens CF, Chorkendorff I, Nørskov JK, Jaramillo TF. Combining theory and experiment in electrocatalysis: Insights into materials design. *Science (80- )*. 2017;355(6321). doi:10.1126/science.aad4998

84. Vesborg PCK, Seger B, Chorkendorff I. Recent development in hydrogen evolution reaction catalysts and their practical implementation. *J Phys Chem Lett.* 2015;6(6):951-957. doi:10.1021/acs.jpcclett.5b00306
85. Artero V. Bioinspired catalytic materials for energy-relevant conversions. *Nat Energy.* 2017;2(9):1-6. doi:10.1038/nenergy.2017.131
86. SIEGBAHN PEM. PROTON AND ELECTRON TRANSFERS IN [NiFe] HYDROGENASE. *Adv Inorg Chem.* 2004;56(04):101-125. doi:10.1016/S0898-8838(04)56004-X
87. Hinnemann B, Moses PG, Bonde J, et al. Biomimetic Hydrogen Evolution: MoS<sub>2</sub> Nanoparticles as Catalyst for Hydrogen Evolution. *J Am Chem Soc.* 2005;127(15):5308-5309. doi:10.1021/ja0504690
88. Yan Y, Xia BY, Zhao B, Wang X. A review on noble-metal-free bifunctional heterogeneous catalysts for overall electrochemical water splitting. *J Mater Chem A.* 2016;4(45):17587-17603. doi:10.1039/C6TA08075H
89. Nguyen QT, Nguyen PD, Nguyen D, et al. Novel Amorphous Molybdenum Selenide as an Efficient Catalyst for Hydrogen Evolution Reaction. *ACS Appl Mater Interfaces.* 2018;10(10):8659-8665. doi:10.1021/acsami.7b18675
90. Joe J, Yang H, Bae C, Shin H. Metal chalcogenides on silicon photocathodes for efficient water splitting: A mini overview. *Catalysts.* 2019;9(2). doi:10.3390/catal9020149
91. Zhao J, Wang J, Chen Z, Ju J, Han X, Deng Y. Metal chalcogenides: An emerging material for electrocatalysis. *APL Mater.* 2021;9(5). doi:10.1063/5.0049772
92. Benck JD, Hellstern TR, Kibsgaard J, Chakhranont P, Jaramillo TF. Catalyzing the hydrogen evolution reaction (HER) with molybdenum sulfide nanomaterials. *ACS Catal.* 2014;4(11):3957-3971. doi:10.1021/cs500923c
93. Tran PD, Tran T V., Orio M, et al. Coordination polymer structure and revisited hydrogen evolution catalytic mechanism for amorphous molybdenum sulfide. *Nat Mater.* 2016;15(June):1-8. doi:10.1038/nmat4588
94. Merki D, Vrabel H, Rovelli L, Fierro S, Hu X. Fe, Co, and Ni ions promote the catalytic activity of amorphous molybdenum sulfide films for hydrogen evolution. *Chem Sci.* 2012;3(90 C):2515. doi:10.1039/c2sc20539d
95. Karikalan N, Sundaresan P, Chen SM, Karthik R, Karuppiah C. Cobalt molybdenum sulfide decorated with highly conductive sulfur-doped carbon as an electrocatalyst for the enhanced activity of hydrogen evolution reaction. *Int J Hydrogen Energy.* 2019;44(18):9164-9173. doi:10.1016/j.ijhydene.2019.02.110
96. Chen WF, Wang CH, Sasaki K, et al. Highly active and durable nanostructured molybdenum carbide electrocatalysts for hydrogen production. *Energy Environ Sci.* 2013;6(3):943-951. doi:10.1039/c2ee23891h
97. McEnaney JM, Chance Crompton J, Callejas JF, et al. Electrocatalytic hydrogen evolution using amorphous tungsten phosphide nanoparticles. *Chem Commun.* 2014;50(75):11026-11028. doi:10.1039/c4cc04709e
98. Popczun EJ, Read CG, Roske CW, Lewis NS, Schaak RE. Highly active electrocatalysis of the hydrogen evolution reaction by cobalt phosphide nanoparticles. *Angew Chemie - Int Ed.* 2014;53(21):5427-5430. doi:10.1002/anie.201402646
99. Goff A Le, Artero V, Josselme B, et al. From hydrogenases to noble metal-free catalytic



- nanomaterials for H<sub>2</sub> production and uptake. *Science* (80- ). 2009;326(5958):1384-1387. doi:10.1126/science.1179773
100. Brazzolotto D, Gennari M, Queyriaux N, et al. Nickel-centred proton reduction catalysis in a model of [NiFe] hydrogenase. *Nat Chem*. 2016;8(11):1054-1060. doi:10.1038/nchem.2575
  101. Berggren G, Adamska A, Lambert C, et al. Biomimetic assembly and activation of [FeFe]-hydrogenases. *Nature*. 2013;499(7456):66-69. doi:10.1038/nature12239
  102. Kötzt R, Stucki S. Stabilization of RuO<sub>2</sub> by IrO<sub>2</sub> for anodic oxygen evolution in acid media. *Electrochim Acta*. 1986;31(10):1311-1316. doi:10.1016/0013-4686(86)80153-0
  103. Lee Y, Suntivich J, May KJ, Perry EE, Shao-Horn Y. Synthesis and activities of rutile IrO<sub>2</sub> and RuO<sub>2</sub> nanoparticles for oxygen evolution in acid and alkaline solutions. *J Phys Chem Lett*. 2012;3(3):399-404. doi:10.1021/jz2016507
  104. Matsumoto Y, Sato E. Electrocatalytic properties of transition metal oxides for oxygen evolution reaction. *Mater Chem Phys*. 1986;14(5):397-426. doi:10.1016/0254-0584(86)90045-3
  105. Wohlfahrt-Mehrens M, Heitbaum J. Oxygen evolution on Ru and RuO<sub>2</sub> electrodes studied using isotope labelling and on-line mass spectrometry. *J Electroanal Chem*. 1987;237(2):251-260. doi:10.1016/0022-0728(87)85237-3
  106. Kötzt R, Stucki S, Scherson D, Kolb DM. In-situ identification of RuO<sub>4</sub> as the corrosion product during oxygen evolution on ruthenium in acid media. *J Electroanal Chem*. 1984;172(1-2):211-219. doi:10.1016/0022-0728(84)80187-4
  107. Kanan MW, Nocera DG. In situ formation of an oxygen-evolving catalyst in neutral water containing phosphate and Co<sup>2+</sup>. *Science* (80- ). 2008;321(5892):1072-1075. doi:10.1126/science.1162018
  108. Friebel D, Louie MW, Bajdich M, et al. Identification of highly active Fe sites in (Ni,Fe)OOH for electrocatalytic water splitting. *J Am Chem Soc*. 2015;137(3):1305-1313. doi:10.1021/ja511559d
  109. Kim JS, Kim B, Kim H, Kang K. Recent Progress on Multimetal Oxide Catalysts for the Oxygen Evolution Reaction. *Adv Energy Mater*. 2018;8(11):1-26. doi:10.1002/aenm.201702774
  110. Suntivich J, May KJ, Gasteiger HA, Goodenough JB, Shao-Horn Y. A perovskite oxide optimized for oxygen evolution catalysis from molecular orbital principles. *Science* (80- ). 2011;334(6061):1383-1385. doi:10.1126/science.1212858
  111. Xiao D, Gregg J, Lakshmi K V., Bonitatibus PJ. Bio-Inspired Molecular Catalysts for Water Oxidation. *Catalysts*. 2021;11(9):1068. doi:10.3390/catal11091068
  112. Hori Y. Electrochemical CO<sub>2</sub> Reduction on Metal Electrodes. *Mod Asp Electrochem*. 2008;(42):89-189. doi:10.1007/978-0-387-49489-0\_3
  113. Hori Y, Wakebe H, Tsukamoto T, Koga O. Electrocatalytic process of CO selectivity in electrochemical reduction of CO<sub>2</sub> at metal electrodes in aqueous media. *Electrochim Acta*. 1994;39(11-12):1833-1839. doi:10.1016/0013-4686(94)85172-7
  114. Hansen HA, Varley JB, Peterson AA, Nørskov JK. Understanding trends in the electrocatalytic activity of metals and enzymes for CO<sub>2</sub> reduction to CO. *J Phys Chem Lett*. 2013;4(3):388-392. doi:10.1021/jz3021155
  115. Kedzierzawski P, Augustynski J. Poisoning and Activation of the Gold Cathode during

- Electroreduction of CO<sub>2</sub>. *J Electrochem Soc.* 1994;141(5):L58-L60. doi:10.1149/1.2054936
116. Raciti D, Wang C. Recent Advances in CO<sub>2</sub> Reduction Electrocatalysis on Copper. *ACS Energy Lett.* 2018;3(7):1545-1556. doi:10.1021/acsenerylett.8b00553
  117. Proppe AH, Li YC, Aspuru-Guzik A, et al. Bioinspiration in light harvesting and catalysis. *Nat Rev Mater.* 2020;5(11):828-846. doi:10.1038/s41578-020-0222-0
  118. Tinnemans AHA, Koster TPM, Thewissen DHMW, Mackor A. Tetraaza-macrocyclic cobalt(II) and nickel(II) complexes as electron-transfer agents in the photo(electro)chemical and electrochemical reduction of carbon dioxide. *Recl des Trav Chim des Pays-Bas.* 1984;103(10):288-295. doi:10.1002/recl.19841031004
  119. Kosugi K, Kondo M, Masaoka S. Quick and Easy Method to Dramatically Improve the Electrochemical CO<sub>2</sub> Reduction Activity of an Iron Porphyrin Complex. *Angew Chemie Int Ed.* 2021;60(40):22070-22074. doi:10.1002/anie.202110190
  120. Mondal B, Sen P, Rana A, Saha D, Das P, Dey A. Reduction of CO<sub>2</sub> to CO by an Iron Porphyrin Catalyst in the Presence of Oxygen. *ACS Catal.* 2019;9(5):3895-3899. doi:10.1021/acscatal.9b00529
  121. Rao H, Schmidt LC, Bonin J, Robert M. Visible-light-driven methane formation from CO<sub>2</sub> with a molecular iron catalyst. *Nature.* 2017;548(7665):74-77. doi:10.1038/nature23016
  122. Veroneau SS, Nocera DG. Continuous electrochemical water splitting from natural water sources via forward osmosis. *Proc Natl Acad Sci U S A.* 2021;118(9):1-5. doi:10.1073/pnas.2024855118
  123. Tran PD, Chiam SY, Boix PP, et al. Novel cobalt/nickel-tungsten-sulfide catalysts for electrocatalytic hydrogen generation from water. *Energy Environ Sci.* 2013;6(8):2452-2459. doi:10.1039/c3ee40600h
  124. Nguyen LN, Thuy UTD, Truong QD, Honma I, Nguyen QL, Tran PD. Electrodeposited Amorphous Tungsten-doped Cobalt Oxide as an Efficient Catalyst for the Oxygen Evolution Reaction. *Chem - An Asian J.* 2018;13(12):1530-1534. doi:10.1002/asia.201800401
  125. Cobo S, Heidkamp J, Jacques PA, et al. A Janus cobalt-based catalytic material for electro-splitting of water. *Nat Mater.* 2012;11(9):802-807. doi:10.1038/nmat3385
  126. Lin GH, Kapur M, Kainthla RC, Bockris JOM. One step method to produce hydrogen by a triple stack amorphous silicon solar cell. *Appl Phys Lett.* 1989;55(4):386-387. doi:10.1063/1.101879
  127. Rocheleau RE, Miller EL, Misra A. High-efficiency photoelectrochemical hydrogen production using multijunction amorphous silicon photoelectrodes. *Energy and Fuels.* 1998;12(1):3-10. doi:10.1021/ef9701347
  128. Miller EL, Marsen B, Paluselli D, Rocheleau R. Optimization of hybrid photoelectrodes for solar water-splitting. *Electrochem Solid-State Lett.* 2005;8(5):247-249. doi:10.1149/1.1887196
  129. Miller EL, Rocheleau RE, Khan S. A hybrid multijunction photoelectrode for hydrogen production fabricated with amorphous silicon/germanium and iron oxide thin films. *Int J Hydrogen Energy.* 2004;29(9):907-914. doi:10.1016/j.ijhydene.2003.01.003
  130. Miller EL, Rocheleau RE, Deng XM. Design considerations for a hybrid amorphous silicon/photoelectrochemical multijunction cell for hydrogen production. *Int J Hydrogen Energy.* 2003;28(6):615-623. doi:10.1016/S0360-3199(02)00144-1
  131. Lutterman DA, Surendranath Y, Nocera DG. A self-healing oxygen-evolving catalyst. *J Am*

- Chem Soc.* 2009;131(11):3838-3839. doi:10.1021/ja900023k
132. Wang X, Su R, Aslan H, et al. Tweaking the composition of NiMoZn alloy electrocatalyst for enhanced hydrogen evolution reaction performance. *Nano Energy.* 2015;12:9-18. doi:10.1016/j.nanoen.2014.12.007
  133. Shockley W, Queisser HJ. Detailed balance limit of efficiency of p-n junction solar cells. *J Appl Phys.* 1961;32(3):510-519. doi:10.1063/1.1736034
  134. Rühle S. Tabulated values of the Shockley-Queisser limit for single junction solar cells. *Sol Energy.* 2016;130:139-147. doi:10.1016/j.solener.2016.02.015
  135. De Vos A. Detailed balance limit of the efficiency of tandem solar cells. *J Phys D Appl Phys.* 1980;13(5):839-846. doi:10.1088/0022-3727/13/5/018
  136. NREL. *Best Research-Cell Efficiencies.*; 2021.
  137. Geisz JF, France RM, Schulte KL, et al. Six-junction III-V solar cells with 47.1% conversion efficiency under 143 Suns concentration. *Nat Energy.* 2020;5(4):326-335. doi:10.1038/s41560-020-0598-5
  138. Deng X. Optimization of a-SiGe based triple, tandem and single-junction solar cells. *Conf Rec IEEE Photovolt Spec Conf.* 2005:1365-1370. doi:10.1109/pvsc.2005.1488395
  139. Vijn A. *Thin - Film Silicon Technology and Manufacturing.*; 2012.
  140. Wang W, Povolny H, Du W, Liao XB, Deng X. Triple-junction a-Si solar cells with heavily doped thin interface layers at the tunnel junctions. *Conf Rec IEEE Photovolt Spec Conf.* 2002:1082-1085. doi:10.1109/pvsc.2002.1190793
  141. Müller A, Jostes R, Flemming V, Potthast R. Delocalized molecular orbitals in the trimetallic thioheteroanion [S<sub>2</sub>WS<sub>2</sub>CoS<sub>2</sub>SW<sub>2</sub>]<sup>2-</sup>: spectroscopic and cyclic voltammetric results. *Inorganica Chim Acta.* 1980;44:L33-L35. doi:10.1016/S0020-1693(00)90943-5
  142. Shao Y, Xiao X, Zhu YP, Ma TY. Single-Crystal Cobalt Phosphate Nanosheets for Biomimetic Oxygen Evolution in Neutral Electrolytes. *Angew Chemie - Int Ed.* 2019;58(41):14599-14604. doi:10.1002/anie.201909326
  143. Xi F, Bogdanoff P, Harbauer K, et al. Structural Transformation Identification of Sputtered Amorphous MoS<sub>x</sub> as an Efficient Hydrogen-Evolving Catalyst during Electrochemical Activation. *ACS Catal.* 2019;9(3):2368-2380. doi:10.1021/acscatal.8b04884
  144. Lee SC, Benck JD, Tsai C, et al. Chemical and phase evolution of amorphous molybdenum sulfide catalysts for electrochemical hydrogen production. *ACS Nano.* 2016;10(1):624-632. doi:10.1021/acsnano.5b05652
  145. Zhao Y, Wang Y, Dong Y, et al. Quasi-Two-Dimensional Earth-Abundant Bimetallic Electrocatalysts for Oxygen Evolution Reactions. *ACS Energy Lett.* 2021;6(9):3367-3375. doi:10.1021/acsenergylett.1c01302
  146. Zang M, Xu N, Cao G, et al. Cobalt Molybdenum Oxide Derived High-Performance Electrocatalyst for the Hydrogen Evolution Reaction. *ACS Catal.* 2018;8(6):5062-5069. doi:10.1021/acscatal.8b00949
  147. Laudadio ED, Bennett JW, Green CM, Mason SE, Hamers RJ. Impact of Phosphate Adsorption on Complex Cobalt Oxide Nanoparticle Dispersibility in Aqueous Media. *Environ Sci Technol.* 2018;52(17):10186-10195. doi:10.1021/acs.est.8b02324

148. Di Palma V, Zafeiropoulos G, Goldsweer T, et al. Atomic layer deposition of cobalt phosphate thin films for the oxygen evolution reaction. *Electrochem Commun.* 2019;98(October 2018):73-77. doi:10.1016/j.elecom.2018.11.021
149. van der Heide H, Hemmel R, van Bruggen CF, Haas C. X-ray photoelectron spectra of 3d transition metal pyrites. *J Solid State Chem.* 1980;33(1):17-25. doi:10.1016/0022-4596(80)90543-5
150. Chakrabarti S, Samanta S, Maikap S, Rahaman SZ, Cheng HM. Temperature-Dependent Non-linear Resistive Switching Characteristics and Mechanism Using a New W/WO<sub>3</sub>/WO<sub>x</sub>/W Structure. *Nanoscale Res Lett.* 2016;11(1). doi:10.1186/s11671-016-1602-7
151. Sarma DD, Rao CNR. XPS studies of oxides of second- and third-row transition metals including rare earths. *J Electron Spectros Relat Phenomena.* 1980;20(1):25-45. doi:https://doi.org/10.1016/S0020-1693(00)90943-5
152. Hou Y, Abrams BL, Vesborg PCK, et al. Bioinspired molecular co-catalysts bonded to a silicon photocathode for solar hydrogen evolution. *Nat Mater.* 2011;10(6):434-438. doi:10.1038/nmat3008
153. Chen Q, Fan G, Fu H, Li Z, Zou Z. Tandem photoelectrochemical cells for solar water splitting. *Adv Phys X.* 2018;3(1):863-884. doi:10.1080/23746149.2018.1487267
154. Leygraf C, Hendewerk M, Somorjai GA. Photocatalytic production of hydrogen from water by a p- and n-type polycrystalline iron oxide assembly. *J Phys Chem.* 1982;86(23):4484-4485. doi:10.1021/j100220a007
155. Ingler WB, Khan SUM. A self-driven pn- Fe<sub>2</sub>O<sub>3</sub> tandem photoelectrochemical cell for water splitting. *Electrochem Solid-State Lett.* 2006;9(4):144-146. doi:10.1149/1.2176082
156. Chen M, Liu Y, Li C, et al. Spatial control of cocatalysts and elimination of interfacial defects towards efficient and robust CIGS photocathodes for solar water splitting. *Energy Environ Sci.* 2018;11(8):2025-2034. doi:10.1039/c7ee03650g
157. Windle CD, Kumagai H, Higashi M, et al. Earth-Abundant Molecular Z-Scheme Photoelectrochemical Cell for Overall Water-Splitting. *J Am Chem Soc.* 2019;141(24):9593-9602. doi:10.1021/jacs.9b02521
158. Wu H, Irani R, Zhang K, et al. Unveiling Carrier Dynamics in Periodic Porous BiVO<sub>4</sub> Photocatalyst for Enhanced Solar Water Splitting. *ACS Energy Lett.* 2021:3400-3407. doi:10.1021/acsenergylett.1c01454
159. Kim T, Choi K. Nanoporous BiVO<sub>4</sub> Photoanodes with Dual-Layer Oxygen Evolution Catalysts for Solar Water Splitting. *Science (80- ).* 2014;343(February):990-995.
160. Kudo A, Omori K, Kato H. A novel aqueous process for preparation of crystal form-controlled and highly crystalline BiVO<sub>4</sub> powder from layered vanadates at room temperature and its photocatalytic and photophysical properties. *J Am Chem Soc.* 1999;121(49):11459-11467. doi:10.1021/ja992541y
161. Le H V., Nguyen MD, Pham YTH, et al. Decoration of AgOx hole collector to boost photocatalytic water oxidation activity of BiVO<sub>4</sub> photoanode. *Mater Today Energy.* 2021;21(April). doi:10.1016/j.mtener.2021.100762
162. Wood CJ, Summers GH, Clark CA, et al. A comprehensive comparison of dye-sensitized NiO photocathodes for solar energy conversion. *Phys Chem Chem Phys.* 2016;18(16):10727-10738. doi:10.1039/c5cp05326a

163. Queyriaux N, Giannoudis E, Lefebvre JF, Artero V, Chavarot-Kerlidou M. Synthesis of Ruthenium Tris-Diimine Photosensitizers Substituted by Four Methylphosphonate Anchoring Groups for Dye-Sensitized Photoelectrochemical Cell Applications. *Eur J Inorg Chem.* 2019;2019(15):2154-2161. doi:10.1002/ejic.201900151
164. Ligand R, Lacy DC, Mccrory CCL, Peters JC. Studies of Cobalt-Mediated Electrocatalytic CO<sub>2</sub> Reduction Using a. *Inorg Chem.* 2014;53:4980-4988.
165. Tikhomirov BP, Hopfenberg HB, Stannett V, Williams JL. Permeation, diffusion, and solution of gases and water vapor in unplasticized poly(vinylchloride). *Die Makromol Chemie.* 1968;118(1):177-188. <http://dx.doi.org/10.1002/macp.1968.021180112>.
166. Alarcón-Lladó E, Chen L, Hettick M, et al. BiVO<sub>4</sub> thin film photoanodes grown by chemical vapor deposition. *Phys Chem Chem Phys.* 2014;16(4):1651-1657. doi:10.1039/c3cp53904k
167. Kaeffer N, Massin J, Lebrun C, Renault O, Chavarot-Kerlidou M, Artero V. Covalent Design for Dye-Sensitized H<sub>2</sub>-Evolving Photocathodes Based on a Cobalt Diimine-Dioxime Catalyst. *J Am Chem Soc.* 2016;138(38):12308-12311. doi:10.1021/jacs.6b05865
168. Kamata R, Kumagai H, Yamazaki Y, Higashi M, Abe R, Ishitani O. Durable photoelectrochemical CO<sub>2</sub> reduction with water oxidation using a visible-light driven molecular photocathode. *J Mater Chem A.* 2021;9(3):1517-1529. doi:10.1039/d0ta07351b
169. Chandrasekaran S, Kaeffer N, Cagnon L, et al. A robust ALD-protected silicon-based hybrid photoelectrode for hydrogen evolution under aqueous conditions. *Chem Sci.* 2019;10(16):4469-4475. doi:10.1039/c8sc05006f
170. Zhang L, Cole JM. Anchoring groups for dye-sensitized solar cells. *ACS Appl Mater Interfaces.* 2015;7(6):3427-3455. doi:10.1021/am507334m
171. Kumagai H, Sahara G, Maeda K, Higashi M, Abe R, Ishitani O. Hybrid photocathode consisting of a CuGaO<sub>2</sub> p-type semiconductor and a Ru(II)-Re(i) supramolecular photocatalyst: Non-biased visible-light-driven CO<sub>2</sub> reduction with water oxidation. *Chem Sci.* 2017;8(6):4242-4249. doi:10.1039/c7sc00940b
172. Renaud A, Chavillon B, Le Pleux L, et al. CuGaO<sub>2</sub>: A promising alternative for NiO in p-type dye solar cells. *J Mater Chem.* 2012;22(29):14353-14356. doi:10.1039/c2jm31908j
173. O'Reilly JE. Oxidation-reduction potential of the ferro-ferricyanide system in buffer solutions. *BBA - Bioenerg.* 1973;292(3):509-515. doi:10.1016/0005-2728(73)90001-7

# Supporting information

## 1. Materials

### 1.1. Chemicals

Unless otherwise stated, all the chemicals were purchased from Sigma-Aldrich and utilized without additional purification.

### 1.2. Transparent conducting oxides (TCO)

Fluorine-doped tin oxide (FTO TEC 10, 7-10  $\Omega/\text{sq}$ ) and indium tin oxide (ITO SOL 12, 12  $\Omega/\text{sq}$ ) films were purchased from SOLEMS. Prior to being used, the pieces were cut to appropriate size with a common glass cutting bench then cleaned by sonication for 15 minutes each in soapy water, deionized water, ethanol, acetone and completed by 30 minutes in a UV-Ozone cleaner. When necessary, the working surface area was limited by thermal tapes.

### 1.3. Nafion membrane

Nafion membrane (NRE-212, 0.05mm thick,  $\geq 0.92$  meq/g exchange capacity) was purchased from Alfa Aesar. The membrane was cut to appropriate size using a typical art scissor and thoroughly soaked in MilliQ water before use.

## 2. Equipment

### 2.1. Ag/AgCl 3 M KCl reference electrode

Possessing simple structure as well as low fabrication cost compared to other reference electrodes, Ag/AgCl in KCl was widely utilized in (photo)electrochemistry laboratories. However, its potential was shown to be shifting over time, either through ingestion of foreign elements in the KCl solution during operation, or blockage of the Vycor glass frit. Therefore, for optimum accuracy, our Ag/AgCl 3M KCl reference electrode was calibrated daily to obtain the  $E^0_{\text{Ag/AgCl}}$  and all recorded potentials were accordingly converted to reversible hydrogen (RHE) electrode through **Eq.19**.

The calibration process was performed using an SP-300 potentiostat from Biologic in typical three-electrode mode. A freshly polished glassy carbon rod was used as the working

electrode. The reference electrode was the Ag/AgCl 3M KCl that needed to be calibrated. The counter electrode was a Pt wire. The electrolyte was a 10 mM equimolar solution of potassium ferro-ferricyanide ( $K_3/K_4[Fe(CN)_6]$ ) in 0.1 M phosphate buffer (pH 7) with oxidation potential ( $E^0_{Fe^{3+}/Fe^{2+}}$ ) at 0.4247 V vs. NHE<sup>173</sup>. A cyclic voltammetry was performed with scan rate of 100 mV/s and scan range from -0.4 V to 0.8 V vs. ref. In this range, a redox couple for the  $Fe^{3+}/Fe^{2+}$  conversion was clearly observed. The value for this redox couple versus the Ag/AgCl 3M KCl that needed to be calibrated ( $E_{Fe^{3+}/Fe^{2+}}$ ) was then deduced from the mean position of the two peaks. Afterwards, the potential of the Ag/AgCl 3M KCl that needed to be calibrated would be calculated by the following equation:

$$E^0_{Ag/AgCl} = E^0_{Fe^{3+}/Fe^{2+}} - E_{Fe^{3+}/Fe^{2+}} \quad (\text{Eq. 22})$$

## 2.2. Electrochemical setup

All (photo)electrochemical measurements were performed with a SP-300 potentiostat from Biologic controlled by the included EC-Lab software. Measurements were done either in the typical three-electrode configuration or in two-electrode configuration, upon which, the banana plugs for the reference and counter electrodes were connected together.

## 2.4. Illumination system

All following components were purchased from Newport. The illumination source was a Xenon arc lamp set at 280 W. To better simulate the sun light, an air mass 1.5 global (AM1.5G) filter was used. The light intensity was then calibrated to 100 mW/cm<sup>2</sup> (1 sun) with a photodiode.

## 3. Fabrication of FTO|BiVO<sub>4</sub>|CoPi photoanode

### *Electrodeposition of BiOI film*

Firstly, a BiOI film was prepared by electrodeposition on FTO according to Le *et al.*<sup>161</sup> from CECS group. To prepare the electrolyte solution, 1.494 g KI was added to 20 mL of deionized (DI) water (0.45 M). To this colorless solution, 0.388 g Bi(NO<sub>3</sub>)<sub>3</sub> was added (0.04 M), yielding an opaque red suspension. HNO<sub>3</sub> 1 M was added slowly to adjust the pH to 1.7, upon which the suspension turned to a clear red solution. To complete, 0.216 g of p-benzoquinone dissolved in 8 mL of ethanol absolute was added to the electrolyte solution. A 1 x 4 cm FTO piece with a working area limited with thermal tape to 1 x 3 cm was used as

working electrode in a typical three-electrode configuration. The reference electrode was a Ag/AgCl 3 M KCl and the counter electrode was a Pt wire. The FTO electrode was held at -0.1 V vs. Ag/AgCl until a total charge density of  $150 \text{ mC}\cdot\text{cm}^{-2}$  was recorded to ensure uniform film thickness between samples. The resulted bright red film was washed gently under a stream of DI water and dried with nitrogen before the next step.

#### ***Fabrication of BiVO<sub>4</sub> film from the BiOI film***

On the surface of the electrodeposited BiOI film was dropped 120  $\mu\text{L}$  of a deep green solution of 0.5 M VO(acac)<sub>2</sub> in DMSO. The electrode was heated at 80°C on a hot plate to remove the majority of DMSO before annealing in a flat oven. The thermal annealing used the following four steps ramp: RT-100°C (30 minutes), 100°C (60 minutes), 100°C – 400°C (180 minutes), 400°C (60 minutes). After cooling down, the resultant orange electrode was submerged gently in a 1M NaOH solution for 30 minutes to remove all excess VO(acac)<sub>2</sub>, yielding a bright yellow film. The FTO|BiVO<sub>4</sub> electrode was then washed with DI water and dried under nitrogen.

#### ***Electrodeposition of CoPi cocatalyst on the BiVO<sub>4</sub> film***

The FTO|BiVO<sub>4</sub> was used as the working electrode of a potentiostat in a typical three electrode configuration with Ag/AgCl 3 M KCl reference electrode and a Pt wire counter electrode. Chronoamperometry was used to hold the electrode at 1.1 V vs. Ag/AgCl in a 0.5 mM solution of Co(NO<sub>3</sub>)<sub>2</sub> in 0.1 M phosphate buffer (pH 7) until a charge density of 50 mC/cm<sup>2</sup> passed through.

## **4. Characterization techniques**

### **4.1. Gas chromatography (GC)**

#### **4.1.1. Micro gas chromatography in automatic sampling mode**

Gas chromatography in automatic sampling mode was performed with a micro gas chromatography (microGC) model S3000 from SRA Instruments equipped with a thermal conductivity detector (TCD). Research grade argon (Ar) gas was used as carrier gas for the elution and injection process as well as the reference for the TCD. The injection interval was set to be 92 seconds. Prior to measurements, calibration was done with the aid of an electrochemical setup using a potentiostat in conventional three-electrode mode. For improved



accuracy, the calibration should be performed using the same reactor as the desired measurements. The working and counter electrodes were both Pt wires while the reference electrode was a Ag/AgCl 3M KCl. Chronopotentiometry mode was utilized to yield a constant 1 mA current circulating between the two Pt wire for 24 hours, generating a constant rate of hydrogen and oxygen evolution. The process was constantly monitored by the gas chromatography in continuous sampling mode. The obtained response was then normalized with the total charges passing through the Pt wires taking into account that their Faradaic efficiency was 100%. Based on this response, subsequent measurements would then be quantified accordingly.

This method is more suitable for systems that can yield enough gaseous products to cause increased pressure in the reactor. In addition, with the constant bubbling of Ar, the desired products dissolved in the electrolyte would also be largely removed, improving the accuracy of the assessment.

#### **4.1.2. Gas chromatography in single injection mode**

Gas chromatography in single injection mode was performed with a Clarus 580 from Perkin Elmer equipped with a molecular sieve 5 Å column (30m – 0.53 mm) along with a flame ionization detector (FID) for CO detection as well as a TCD for H<sub>2</sub> detection. The chromatograph used research grade nitrogen (N<sub>2</sub>) as carrier gas. Prior to measurements, a calibration curve was obtained from separate injections of a fixed amount (50µL) of carefully prepared gaseous mixture of N<sub>2</sub> and the desired product (i.e. CO or H<sub>2</sub>). Subsequent measurements would be done with the same injection volume to quantify the desired gaseous product. The total amount of gaseous product generated inside the reactor would be deduced from careful measurement of the head space.

Since the reactor was completely isolated from the environment, this method is more suitable for systems yielding small amount of gaseous products with negligible effect to the overall pressure of the system. In addition, quantification of the dissolved products in the electrolyte is challenging, resulting in having to employ additional equipment. However, with its simple operation and high sensitivity to a wide range of detectable gases, it remains as one of the most frequently used method for gas detection.

#### **4.2. Inductively coupled plasma-optical emission spectroscopy (ICP-OES)**

ICP-OES (also known as ICP-AES: Inductively Coupled Plasma Atomic Emission Spectrometry) was performed with an ICPE-9000 from Shimadzu. Sample digestion was done in concentrated HNO<sub>3</sub> then diluted with MilliQ water.

#### **4.3. Scanning Electron Microscopy and energy-dispersive X-ray spectroscopy (SEM & EDX)**

SEM and EDX measurements were performed with a Carl Zeiss AG - ULTRA 55 with gun voltages of 5 or 10 keV. Carbon tape was used to secure the samples as well as improving their conductivity to the holder.

#### **4.4. X-ray photoelectron spectroscopy (XPS)**

X-ray photoelectron spectroscopy (XPS) was performed using a VG ESCALAB 220i-XL system (Thermo Scientific Theta Probe) with the X-ray source being a monochromatic Al Ka (1,486.6 eV). Calibration of the binding energy was done with adventitious carbon having 1s binding energy of 284.65 eV. Deconvolution of the signal was done with CasaXPS program using a Shirley background and Lorentzian distribution. Various reference parameters from NIST XPS database were also utilized.

## Abstract

In addition to the mature renewable electricity production, solar fuels production possibly combined with fuel cells devices promises a sustainable and environmentally friendly solution to answer both the global ever-increasing energy demand and the damages to the biosphere brought by the abuse of fossil fuels. Countless efforts have been made in improving the individual materials and components required to drive the overall water splitting for solar H<sub>2</sub> fuel production. However, the ultimate goal of this research field is the fabrication of operational devices and prototypes. Through the collaboration between the two laboratories in France and Vietnam, we successfully construct two types of unassisted solar fuels generators. The first device is a monolithic integrated PV-electrolyzer in artificial leaf configuration, which was made famous by D. Nocera (Harvard University), that is capable of producing hydrogen fuel through direct solar water splitting. The leaf features a pair of water electrolysis catalysts deposited on a commercial triple junction silicon solar cell through a novel self-assembly approach from a single deposition solution. The second device is a tandem hybrid photoelectrochemical cell based on a dye-sensitized photocathode and a BiVO<sub>4</sub>-based photoanode that can produce syngas without any external bias. Performance study of the devices was done employing an operando setup comprises of multiple potentiostats coupled with gas chromatography. It was shown that the artificial leaf exhibits comparable performance to the similar but more complex to fabricate one featured by D. Nocera. However, the degradation of the light harvesting unit in the electrolyte is a big problem and suitable protection is required to increase the overall stability of the device. For the tandem device, the photocathode is currently the limiting component due to desorption of the dye from the corresponding electrode. Nevertheless, the successful fabrication of the devices and the implementation of an experimental setup to monitor their important parameters during operation is a prominent milestone for future improvements.

## Résumé

En parallèle de la production d'électricité renouvelable, la production de carburants solaires, éventuellement combinée à leur conversion ultérieure via des piles à combustible, est une solution durable et respectueuse de l'environnement à la fois pour répondre à la demande énergétique mondiale toujours croissante et éviter les dommages causés à la biosphère par l'utilisation de combustibles fossiles. De nombreux efforts ont été accomplis pour améliorer les composants individuels et matériaux capable d'effectuer les réactions conduisant à la production de tels carburants solaires. Cependant, l'objectif de ce champ de recherche reste la fabrication de dispositifs et prototypes opérationnels. Grâce à la collaboration entre deux laboratoires en France et au Vietnam, nous avons construit avec succès deux types de générateurs autonomes de carburants solaires. Le premier dispositif monolithique est un photo-électrolyseur intégré selon une configuration de feuille artificielle telle que popularisée par D. Nocera (Université d'Harvard) capable de produire de l'hydrogène par décomposition solaire directe de l'eau. La feuille renferme des catalyseurs bimétalliques d'anode et de cathode différents mais déposés en une seule étape grâce à la mise au point d'une solution de dépôt unique sur une cellule solaire commerciale à triple jonction en silicium. Le deuxième dispositif est une cellule photoélectrochimique tandem hybride qui renferme une photocathode à colorant et une photoanode à base de vanadate de bismuth qui, combinées, produisent sous irradiation du gaz de synthèse sans autre biais externe. L'étude des performances des dispositifs a été réalisée via leur instrumentation utilisant plusieurs potentiostats couplés à la chromatographie en phase gazeuse. Il a été montré la feuille artificielle atteint des performances comparables à d'autres dispositifs similaires décrit par D. Nocera mais plus compliqués à fabriquer. Cependant, la dégradation du composant photovoltaïque au contact de l'électrolyte est un gros problème et une protection appropriée sera nécessaire pour augmenter la stabilité globale du dispositif. Pour la cellule photoélectrochimique tandem, la photocathode limite actuellement les performances du dispositif en raison de la désorption du colorant de l'électrode. Néanmoins, la fabrication des dispositifs opérationnels et la mise au point d'une configuration expérimentale pour mesurer leurs paramètres de fonctionnement est une étape importante en vue d'améliorations futures de tels prototypes.